

Die approbierte Originalversion dieser  
Dissertation ist in der Hauptbibliothek der  
Technischen Universität Wien aufgestellt und  
zugänglich.

<http://www.ub.tuwien.ac.at>



The approved original version of this thesis is  
available at the main library of the Vienna  
University of Technology.

<http://www.ub.tuwien.ac.at/eng>



**TECHNISCHE  
UNIVERSITÄT  
WIEN**

Vienna University of Technology

PhD THESIS

# **Development of wear resistant coatings based on complex metallic alloys for functional application**

supervised by

**Ao.Univ.Prof. Dipl.-Ing. Dr.techn. Christoph EISENMENGER-SITTNER**

Institute of Solid State Physics E138

Thin film group

Submitted at Vienna University of Technology

Faculty of Physics

by

**Dipl. Ing. Wolfgang Vollinhofer**

Matr.Nr. e0325126

Zwölfergasse 8/6/17, 1150 Wien

Vienna, January 2012

# Kurzfassung

Da eine fortschreitende Abnutzung von Maschinenkomponenten zu einem drastischen Anstieg an Energieverbrauch und Kosten führt, hat die Entwicklung neuer, hoch abnutzungsresistenter Materialien große Bedeutung für verschiedenste industrielle Anwendungen. Ihre einzigartige Kombination von mechanischen, elektrischen und thermischen Eigenschaften macht komplexe Metallverbindungen (CMAs), insbesondere das quasikristalline  $\text{Al}_{59}\text{Cu}_{25.5}\text{Fe}_{12.5}\text{B}_3$  und  $\text{AlMgB}_{14}$  zu vielversprechenden und kosteneffizienten Materialien für abnutzungsresistente Schutzschichten.

Zur Abscheidung von  $\text{Al}_{59}\text{Cu}_{25.5}\text{Fe}_{12.5}\text{B}_3$  und  $\text{AlMgB}_{14}$  Schichten mittels Magnetron Sputtern, wurde ein geeignetes Beschichtungssystem konstruiert. Entsprechende Targets wurden durch Heißpressen eines Elementarpulvergemisches hergestellt. Zur Herstellung von  $\text{Al}_{59}\text{Cu}_{25.5}\text{Fe}_{12.5}\text{B}_3$  Targets konnte zusätzlich das kommerziell erhältliche Pulver *St Gobain Cristome F1* verwendet werden. Zur Schichtabscheidung wurden verschiedene Substrate wie: Hartmetall WC-Co, Stahl K600 und K890, epitaktisches Si und keramisches  $\text{Al}_2\text{O}_3$  verwendet. Um die Haftbarkeit zu verbessern und übermäßige Diffusion zu vermeiden, wurden folgende Materialien als mögliche Zwischenschicht getestet: Chrom (Cr), Kupfer (Cu), Titan (Ti), Mangan (Mn) und Nickel (Ni). Zur Optimierung der Schichteigenschaften wurden die Beschichtungsleistung, der Substrat-Target Abstand, der Arbeitsgasdruck, die Substrattemperatur und die Bias Spannung variiert. Die Targets und die abgeschiedenen Schichten wurden mit folgenden Methoden analysiert: Induktiv-gekoppelte-Plasma Massen Spektroskopie (ICP-MS), Energiedispersive Röntgenspektroskopie (EDS), Rasterelektronenmikroskop (SEM), Röntgen Diffraktometrie (XRD), Transmissionselektronenmikroskopie (TEM), Rasterkraftmikroskop (AFM).

Während die  $\text{AlMgB}$  Targets aus 90 %  $\text{AlMgB}_{14}$  Phase und etwa 10 %  $\text{Al}_2\text{MgO}_4$  bestehen, enthalten die bei 600 °C auf WC-Co Hartmetall abgeschiedenen Schichten nur eine amorphe Bor Phase. Auch ein nachträgliches Erhitzen auf 900 °C bewirkt nicht die Ausbildung einer kristallinen  $\text{AlMgB}_{14}$  Schicht. Der Beschichtungsprozess mit RF Magnetron Sputtern beinhaltet auch einige technische Schwierigkeiten wie: Bruch-/Rissbildung in den  $\text{AlMgB}$  Targets auch bei niedriger Beschichtungsleistung ( $3.8 \text{ W/cm}^2$ ) und sehr niedrige Beschichtungsraten (20 nm/min für eine Beschichtungsleistung von  $15.2 \text{ W/cm}^2$ ).

$\text{AlCuFeB}$  Targets mit der chemischen Zusammensetzung von  $\text{Al}_{59}\text{Cu}_{25.5}\text{Fe}_{12.5}\text{B}_3$  aber ohne die quasikristalline Struktur konnten durch Heißpressen bei niedrigen Temperaturen hergestellt werden. Da die Targets nur aus metallischen Phasen bestehen, kann DC Magnetron Sputtern zur Schichtabscheidung verwendet werden. Mit diesen Targets können  $\text{AlCuFeB}$  Schichten, bestehend aus 40 % quasikristalliner  $\text{AlCuFe}$  Phase und 60 %  $\text{Al}_{50}\text{Cu}_{40}\text{Fe}_{10}$   $\beta$  Phase abgeschieden werden. Die Schichten bestehen aus einer  $\text{Al}_{50}\text{Cu}_{40}\text{Fe}_{10}$   $\beta$  Phasen Matrix, in der quasikristalline Körner mit einem Durchmesser von etwa 10 nm eingebettet sind. Die  $\text{AlCuFeB}$  Schichten haften gut auf den verschiedenen Substraten. Jedoch zeigen sich auf Si, ab einer Schichtdicke von etwa 1  $\mu\text{m}$ , Ablösungserscheinungen. Die  $\text{AlCuFeB}$  Schichten weisen günstige Eigenschaften für die Nanoimprint Lithographie (NIL) auf und können daher als potentielle abnutzungsresistente Schutzschichten in diesem Bereich angesehen werden. Bei Abspanversuchen mit Aluminium konnte die Lebensdauer des Abspannwerkzeuges gegenüber einer kommerziell verfügbaren  $\text{TiB}_2$  Schutzschicht erhöht werden.

# Abstract

As growing abrasion and wear causes a drastic increase of energy consumption and costs, the development of new, high abrasion resistant materials with a very low friction coefficient is important for various industrial applications in a short as well as in a long-term timescale. Because of their unique combination of mechanical, electrical and thermal characteristics complex metallic alloys (CMAs), especially the quasicrystalline  $\text{Al}_{59}\text{Cu}_{25.5}\text{Fe}_{12.5}\text{B}_3$  and  $\text{AlMgB}_{14}$  are regarded as promising, cost-effective materials for protective coatings.

For deposition of  $\text{Al}_{59}\text{Cu}_{25.5}\text{Fe}_{12.5}\text{B}_3$  and  $\text{AlMgB}_{14}$  films from hot pressed targets by magnetron sputtering an appropriate deposition system was constructed.  $\text{AlMgB}_{14}$  targets were produced by hot pressing an elemental powder mixture. For producing  $\text{Al}_{59}\text{Cu}_{25.5}\text{Fe}_{12.5}\text{B}_3$  targets commercially available powder *St Gobain Cristome F1* and elemental powder mixtures could be used. For depositing  $\text{Al}_{59}\text{Cu}_{25.5}\text{Fe}_{12.5}\text{B}_3$  and  $\text{AlMgB}_{14}$  coatings, the following substrates were chosen: hard metal WC-Co, steel K600, steel K890, epitaxial Si and ceramic  $\text{Al}_2\text{O}_3$ . To provide a gradual change of the thermal expansion coefficient and avoid diffusion between the coating and substrate, the following materials were tested as possible interlayer: Chrome (Cr), Copper (Cu), Titanium (Ti), Manganese (Mn) and Nickel (Ni). To optimize the coating characteristics deposition parameters like deposition power, substrate – target distance, working gas pressure, substrate temperature and bias voltage were varied. The targets and the deposited coatings were analyzed by: Inductively Coupled Plasma Mass Spectroscopy (ICP-MS), Energy Dispersive X-Ray Spectroscopy (EDS), Scanning Electron Microscope (SEM), X-Ray Diffraction (XRD), Transmission Electron Microscope (TEM) und Atomic Force Microscope (AFM).

While  $\text{AlMgB}$  targets consisting of 90 %  $\text{AlMgB}_{14}$  phase and about 10 %  $\text{Al}_2\text{MgO}_4$  could be produced, the  $\text{AlMgB}$  coatings deposited on WC-Co hard metal substrates at 600 °C consist of mainly amorphous boron. Also 900 °C post annealing does not cause the development of a crystalline  $\text{AlMgB}_{14}$  phase. During RF magnetron sputter deposition also technical problems are encountered, like crack formation in the  $\text{AlMgB}$  targets even for very low power densities (3.8 W/cm<sup>2</sup>) and very low deposition rates (20 nm/min for a power density of 15.2 W/cm<sup>2</sup>).

$\text{AlCuFeB}$  targets that exhibit the  $\text{Al}_{59}\text{Cu}_{25.5}\text{Fe}_{12.5}\text{B}_3$  composition but not the quasicrystalline structure could be produced by low temperature hot pressing. Since these targets contain only metallic phases they can be used for DC magnetron sputter deposition. With these targets  $\text{AlCuFeB}$  coatings, which exhibit 40 % quasicrystalline  $\text{AlCuFe}$  phase and 60 %  $\text{Al}_{50}\text{Cu}_{40}\text{Fe}_{10}$   $\beta$  phase can be deposited. The coating microstructure consists of an  $\text{Al}_{50}\text{Cu}_{40}\text{Fe}_{10}$   $\beta$  phase matrix, in which quasicrystalline grains with sizes of about 10 nm are embedded. Adhesion of the  $\text{AlCuFeB}$  coatings is very good on steel K600 and K890 as well as on ceramic  $\text{Al}_2\text{O}_3$ . On WC-Co and Si the  $\text{AlCuFeB}$  adhesion is good for thin coatings (~500 nm) but delamination occurs when the film thickness exceeds 1  $\mu\text{m}$ . The  $\text{AlCuFeB}$  coatings were found to exhibit favourable characteristics for nanoimprint lithography and thus can be regarded as promising candidates as wear protective films for this method. During Aluminum turning tests cutting inserts with the  $\text{AlCuFeB}$  coatings outperform cutting inserts with a commercially available  $\text{TiB}_2$  coating.

# Table of contents

<b>1. Introduction</b>	<b>1</b>
1.1 Motivation . . . . .	1
1.2 Definition of objectives . . . . .	3
<b>2. Fundamentals &amp; state of the art</b>	<b>4</b>
2.1 Complex metallic alloys (CMAs) . . . . .	4
2.2 AlMgB <sub>14</sub> . . . . .	5
2.2.1 Influence of impurities . . . . .	7
2.2.2 Electrical resistivity . . . . .	8
2.3 Al <sub>59</sub> Cu <sub>25.5</sub> Fe <sub>12.5</sub> B <sub>3</sub> . . . . .	10
2.3.1 Influence of impurities . . . . .	15
2.3.2 Electrical resistivity . . . . .	16
2.4 Magnetron sputtering . . . . .	20
2.4.1 RF magnetron sputtering . . . . .	21
2.4.2 Alloys and compounds . . . . .	22
2.5 Interface formation and film growth . . . . .	24
2.5.1 Adsorption and desorption on solid surfaces . . . . .	24
2.5.2 Interface formation . . . . .	26
2.5.3 Intrinsic and thermal stress . . . . .	29

<b>3. Experimental</b>	<b>30</b>
3.1 Deposition geometry and substrate holder . . . . .	30
3.2 Residual gas analysis . . . . .	35
3.3 Targets . . . . .	38
3.4 Substrates . . . . .	47
3.5 Interface . . . . .	53
3.6 Chemical analysis (EDS) . . . . .	55
3.7 Microstructure analysis (XRD) . . . . .	61
<b>4. Results</b>	<b>66</b>
4.1 AlMgB <sub>14</sub> . . . . .	66
4.1.1 Targets . . . . .	66
4.1.2 Coatings . . . . .	71
4.1.3 Post annealing . . . . .	73
4.1.4 Interface and adhesion . . . . .	77
4.1.4 Microhardness . . . . .	81
4.2 AlCuFeB ceramic targets . . . . .	82
4.2.1 Targets . . . . .	82
4.2.2 Coating composition . . . . .	87
4.2.3 Coating microstructure . . . . .	90
4.2.4 Coating interface . . . . .	93
4.3 AlCuFeB shifted composition targets . . . . .	96
4.3.1 Targets . . . . .	96
4.3.2 Coatings . . . . .	98

4.4	AlCuFeB metallic targets	102
4.4.1	Targets	102
4.4.2	Deposition power	109
4.4.3	Working distance (target – substrate distance)	113
4.4.4	Substrate temperature	116
4.4.5	Working gas pressure	118
4.4.6	Bias voltage	121
4.4.7	Optimised AlCuFeB coatings	123
4.4.8	Electrical resistivity	137
4.4.9	Interlayer	142
4.4.10	Nano-imprint-lithography (NIL)	156
4.4.11	Cutting inserts	164
<b>5.</b>	<b>Discussion</b>	<b>167</b>
5.1	AlMgB <sub>14</sub> targets	167
5.1.1	Targets	167
5.1.2	Coatings	168
5.2	AlCuFeB ceramic targets	171
5.2.1	Targets	171
5.2.2	Coatings	173
5.3	AlCuFeB shifted composition targets	174
5.4	AlCuFeB metallic targets	175
5.4.1	Targets	175
5.4.2	Coatings	177
5.4.3	Optimised coatings	180

5.4.4	Electrical resistivity	183
5.4.5	Interlayer	185
5.4.6	Nano-imprint-lithography (NIL)	187
5.4.5	Cutting insert	189
<b>6.</b>	<b>Conclusion</b>	<b>190</b>
6.1	AlMgB <sub>14</sub>	190
6.2	AlCuFeB ceramic targets <sub>4</sub>	191
6.3	AlCuFeB shifted composition targets <sub>4</sub>	192
6.4	AlCuFeB metallic targets	192
<b>7.</b>	<b>Final summary</b>	<b>195</b>
<b>8.</b>	<b>Acknowledgements</b>	<b>196</b>
<b>9.</b>	<b>References</b>	<b>197</b>
	<b>Appendix</b>	<b>201</b>

# 1. Introduction

## 1.1 Motivation

Complex Metallic Alloys (CMAs), especially the Al-Cu-Fe-B and Al-Mg-B system, offer a unique combination of high hardness and wear resistance, low friction, low tendency for adhesion/sticking, low surface energy, good corrosion resistance, and thermal expansion coefficients intermediate between those of metals and of ceramics. These properties are not driven by grain sizes and interfaces, but they result directly from the formation of giant unit cells or even no unit cell at all in aperiodic crystals. The use of these CMAs as bulk components in structural applications is limited by their brittleness. A promising approach for eliminating the drawback of bulk CMAs is their use as CMA-based surface coatings, to take advantage of their excellent tribological properties in the field of wear. Transferring the outstanding properties of the two selected CMA-systems to coatings, the following applications and impacts are feasible:

- Automotive industry: Reduction of friction e.g.: prolonged lifetime of pistons, cylinders and engine
- Aerospace industry: Reduction of costs for maintenance because of reduced abrasion and longer usage times between services e.g.: turbines' lifetime, aircrafts' landing gear parts
- Oil and mining industry e.g.: drilling and cutting machines and valves for pumps
- Material processing: Reduction of production/machining costs and increased productivity e.g.: grinding, cutting, drilling and polishing
- Improvement of the efficiency in forming/shaping processes (e.g.: extrusion, forming, stamping, moulding) by using coated injection moulding dies
- Si master mold with anti-sticking layer for nano-imprint-lithography and hot embossing with higher wear resistance and less sticking to thermoplastic resins
- Microelectronics and MEMS (Micro-Electro-Mechanical Systems):  
Production of electrical components for usage in severe environments (mechanical load, radiation, corrosion, high temperatures) e.g.: cutting silicon-wafer, electrical conductive, wear resistant probe for microchips
- Substitution of hazardous chemicals in fretting resistant parts and wear/corrosion resistant components



The economic need for advanced wear resistant coatings is mainly driven by:

- The pressure of high manufacturing costs in Europe compared to East and Far East countries
- A continuous reduction of production/machining costs and increased productivity (increased life time can be achieved by coated tools for cutting, extruding, forming, moulding, nano-imprinting or stamping)
- A continuous growing importance of energy saving and energy efficient industrial processes
- The reduction of costs for maintenance especially in the aerospace industry
- The reduction of the used cooling lubricants or even dry machining
- The reduction of chemical pollution by lubricants and metals from wear in air, water and ground

The aim of this work is to evaluate and to develop possible magnetron sputtering based  $\text{Al}_{59.5}\text{Cu}_{25.3}\text{Fe}_{12.5}\text{B}_3$ , and  $\text{AlMgB}_{14}$  coating deposition processes for industrial applications. Besides the production of targets and coatings with the necessary chemical composition, microstructure and homogeneity, the examination of the adhesion and interface quality of the coatings on different substrate types is of special interest. Concepts like bias sputtering, pulsed sputtering and interlayer films were followed to improve the coating - substrate interface and the coating toughness. Additionally the coating characteristics were investigated according to the specific needs of two selected industrial applications: coatings for nano-imprint-lithography stamps and coatings for hard metal cutting inserts.

## 1.2 Definition of objectives

The major scientific objectives of this work can be summarized as follows:

- To verify the possibility of a magnetron-sputtering based coating deposition for the two CMA material systems  $\text{Al}_{59.5}\text{Cu}_{25.3}\text{Fe}_{12.5}\text{B}_3$ , and  $\text{AlMgB}_{14}$
- To develop an appropriate deposition processes (target composition, substrate preparation and deposition and/or post-annealing parameters)
- To analyze the chemical composition and the crystallographic structure of the deposited coatings
- To study the relationship between different PVD processing parameters and the coating characteristics
- To identify and design interfaces with high adhesion strength (diffusion zones, interlayer) between the CMA coatings and different substrates

## 2. Fundamentals & state of the art

### 2.1 Complex metallic alloys (CMAs)

Complex metallic alloys (CMAs) are intermetallic compounds characterized by:

- Large unit cells (up to thousands of atoms)
- Presence of well-defined atom clusters, frequently of icosahedral point group symmetry
- Occurrence of inherent disorder in the ideal structure
- Distinct differences in physical properties and behaviour with respect to regular metallic alloys

CMAs, especially the Al-Cu-Fe-B and Al-Mg-B systems offer:

- A unique combination of high hardness and wear resistance
- Low friction and surface energy
- Good corrosion resistance
- Thermal expansion coefficients intermediate between those of metals and of ceramics

Due to the unusual combination of properties CMAs possess high potential for technological application. As the use of CMA bulks in structural applications is very unlikely due to their brittleness, CMA-based surface coatings indicate a promising approach to take advantage of their excellent tribological properties. It's expected that enhancing ductility, while preserving the attractive mechanical surface is possible by PVD deposition [1-4].

## 2.2 AlMgB<sub>14</sub>

AlMgB<sub>14</sub> exhibits the following characteristics:

- Non-cubic, complex structure [5]
- Hardness between 32 – 35 GPa [6] (pure, nano-crystalline AlMgB<sub>14</sub>)
- Additives can increase the hardness, e.g.: by adding 5 – 70 wt% TiB<sub>2</sub> a hardness of 35 – 46 GPa can be achieved [6]
- Fracture toughness of 3 – 4 MPam<sup>1/2</sup> [7]
- Additives and impurities cause changes in the electrical characteristics [8-10]
- Good electric (semi)conductor [10,11]
- Low chemical reactivity, even at high temperatures up to 1300 °C with Ti [12]
- Insoluble in hydrochloric acid (HCl) and ammonium hydroxide (NH<sub>4</sub>OH) [9]
- High resistance to abrasive wear [13]
- Comparatively cost efficient production due to low cost of constituents

In comparison to other hard materials, AlMgB<sub>14</sub> has a unit cell with high complexity and low symmetry. The structure is based on four covalently bonded B<sub>12</sub> icosahedra positioned in a body-centred orthorhombic unit cell (Imam space group) with 64 atoms (see Figure 2.1). The four B<sub>12</sub> icosahedra are arranged in distorted, close-packed layers and positioned at (0.25, 0.25, 0.25), (0.25, 0.75, 0.25), (0.75, 0.25, 0.75) and (0.75, 0.75, 0.75). The other eight B atoms lie outside of the icosahedra and are bonded to the icosahedra B atoms, the Al and Mg atoms. The intericosahedral Al atoms occupy a fourfold position at (0.250, 0.750, 0.250), whereas the intericosahedral Mg atoms occupy a fourfold position at (0.250, 0.359, 0) [5,6,14].

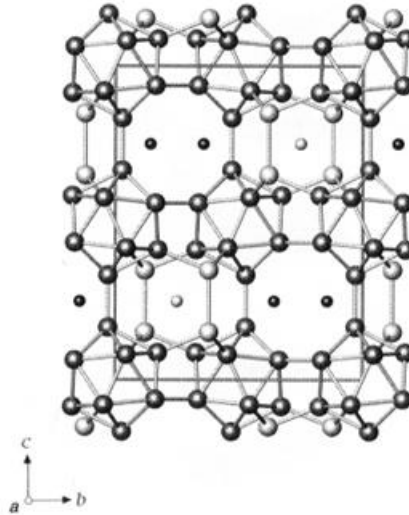


Figure 2.1 Structure of  $\text{AlMgB}_{14}$  as seen along the  $a$  axis (orthorhombic, space group  $\text{Imam}$ ) [5]  
 Lattice parameters:  $a = 0.5848 \text{ nm}$ ,  $b = 0.8112 \text{ nm}$ ,  $c = 1.0312 \text{ nm}$   
 Small circles stand for Mg (dark) and Al (gray) atoms. The less dark circles linking to the icosahedral apical atoms are isolated boron atoms

The unique electrical and mechanical characteristics of the material are thought to result from complex interactions within each icosahedron (intraicosahedral bonding), combined with interactions between the icosahedra (intericosahedral bonding). The high hardness of  $\text{AlMgB}_{14}$  is probably caused by the covalent intraicosahedral B-B bonding. As the B-B bonding within the  $\text{B}_{12}$  icosahedra has an electron deficit, it is assumed that the Al and Mg atoms provide their valence electrons to the B network and thus contribute to a completely occupied valence band of the  $\text{B}_{12}$  icosahedra and to stronger B-B bonds [14,15].

According to band structure calculations the electrical resistance and the hardness of  $\text{AlMgB}_{14}$  should reach a maximum when the valence band is fully occupied and the Fermi level lies in a band gap. Since the electronic states at the Fermi level can be changed vastly by doping, it can be expected that production process parameters (e.g.: cooling rate, additives) not only induce microstructure changes but also influence transport characteristics like the electric resistance [8-10,16].

### 2.2.1 Influence of impurities

AlMgB<sub>14</sub> contains in general 2 – 3 wt% impurities, mostly Al<sub>2</sub>MgO<sub>4</sub>. If the sample is highly contaminated these impurities can amount up to 30 wt% [8]. The high number of various impurities and phases that might occur in AlMgB<sub>14</sub> samples makes a reliable mechanical, electrical and thermal characterization difficult. As those characteristics depend on the nano-crystalline structure, the amount and composition of phases and impurities have an enormous influence on the properties of AlMgB<sub>14</sub>. In general, the hardness of AlMgB<sub>14</sub> decreases with an increasing amount of Al<sub>2</sub>MgO<sub>4</sub>, Fe<sub>3</sub>O<sub>4</sub> and FeB (see Figure 2.2). All those impurities have a lower intrinsic hardness than AlMgB<sub>14</sub>, which might cause the reduction of hardness [6,8,17].

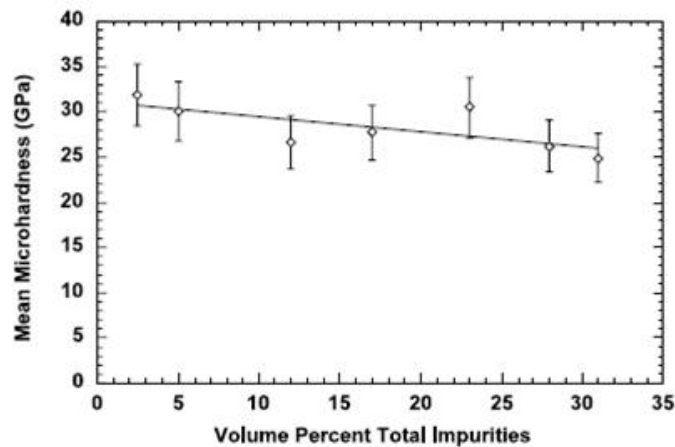


Figure 2.2 A plot of the average microhardness as a function of the total volume percent of Al<sub>2</sub>MgO<sub>4</sub>, Fe<sub>3</sub>O<sub>4</sub>, and FeB impurity phases in AlMgB<sub>14</sub>. Error bars indicate one standard deviation [8].

Oxygen impurities can substantially change the microstructure of AlMgB<sub>14</sub>. If the oxygen impurities exceed ~12 at% the formation of single phase AlMgB<sub>14</sub> is prohibited. This is due to the oxidation of Al, Mg and B that is energetically more favourable than the formation of a crystalline AlMgB<sub>14</sub> phase. O reacts with Al and Mg to Al<sub>2</sub>MgO<sub>4</sub> spinell and with Fe impurities to Fe<sub>3</sub>O<sub>4</sub>. A two or multiple phase structure develops. The strong B-B bonds are replaced by weaker B-O bonds which leads to a reduced hardness. Mostly the O impurities are caused by the contact of the materials with the atmosphere during the production process or because of O impurities in the B, Al and Mg powders that are used for production. [6,8,15,17-19].

### 2.2.2 Electrical resistivity

The electrical resistivity of  $\text{AlMgB}_{14}$  is significantly lower than the one of other ultra-hard materials. This is due to a high carrier concentration and low carrier mobility. Measurements of the electrical resistance using the 4-point probe technique and the Van der Pauw method lead to vastly different results. This is caused by the impurities of the samples (particularly Fe), whereby the samples with the lowest Fe impurities show the highest and the samples with the most Fe impurities the lowest electrical resistance. Furthermore the electrical resistance depends on temperature (see Figure 2.3). In the following the typical ranges of several electrical properties of  $\text{AlMgB}_{14}$  are given [8,9,11,18,20]:

- Electrical resistance:  $\sim 7 \cdot 10^{-5}$  (high amount of Fe) to  $\sim 50 \Omega\text{m}$  (low amount of Fe)
- Hall coefficient:  $-0.001194$  to  $-0.0065625 \text{ cm}^3/\text{C}$
- Carrier mobility:  $0.08125$  to  $0.1676 \text{ cm}^2/\text{Vs}$
- Carrier density  $n(p)$ :  $3.792 \cdot 10^{20}$  to  $5.872 \cdot 10^{21} \text{ cm}^{-3}$

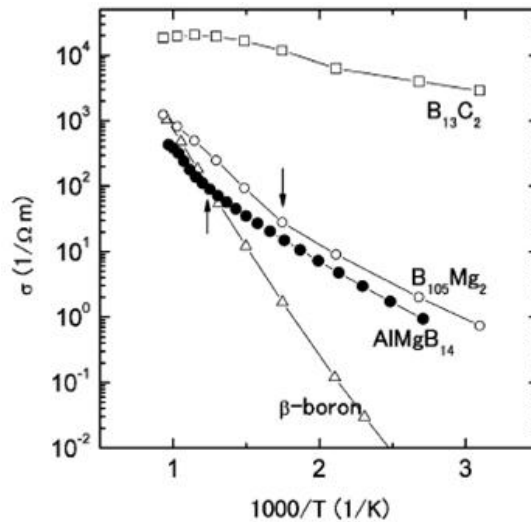


Figure 2.3: Temperature dependence of the electrical conductivity of  $\text{AlMgB}_{14}$  [11]

For  $\text{AlMgB}_{14}$  the electrical resistance reduces about 5 orders of magnitude with an increasing content of  $\text{Al}_2\text{MgO}_4$ ,  $\text{Fe}_3\text{O}_4$  and FeB (see Figure 2.4). This effect is far greater than a simple rule of mixture would predict, since these impurities are not highly conductive materials [8].

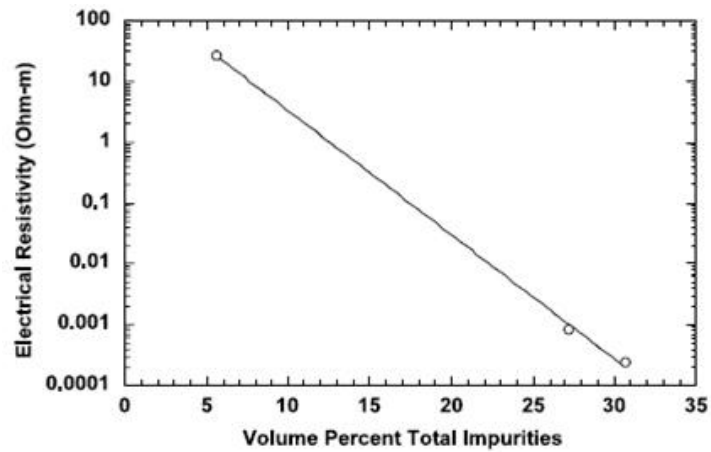


Figure 2.4: A plot of the electrical resistivity in  $\text{AlMgB}_{14}$  as a function of the total volume percent of  $\text{Al}_2\text{MgO}_4$ ,  $\text{Fe}_3\text{O}_4$ , and FeB impurity phases. The electrical resistivity of single crystal, high purity  $\text{AlMgB}_{14}$  has been reported to be  $50 \Omega\text{m}$  [8].



## 2.3 $\text{Al}_{59}\text{Cu}_{25.5}\text{Fe}_{12.5}\text{B}_3$

Quasicrystals are multicomponent alloy phases, which exhibit fascinating atomic structures and very unusual physical and transport properties. While the classical rules of crystallography only allow arrangements of atoms with 2-, 3-, 4- and 6-fold symmetries, quasicrystals exhibit 5-, 8-, 10- and 12-fold symmetries. In contrast to traditional crystals which have planes of atoms arranged periodically (translational symmetry), quasicrystals have aperiodically assembled planes. Nevertheless, quasicrystals exhibit a long-range order and the positions of the atoms can be predicted [21]. The structure of traditional crystals can be obtained by filling a two-dimensional space without voids or overlaps, which is only possible using rectangles, triangles, squares and hexagons. Other rotational symmetries such as 5-fold or any  $n$ -fold beyond 6 are not compatible with this classical definition of a crystal. To obtain the atomic structures of quasicrystals the mathematical framework of a higher-dimensional space has to be used, by cutting the higher dimensional space with an object of lower dimension and projecting the structures from higher dimensional space onto the lower dimensional object [4,21,22]. One way of understanding the nature of atomic order in quasicrystals is to assume that order is dictated by a rule other than periodicity, as in a non-periodic mathematical construction. Two types of constructions are commonly used [23]:

1) Fibonacci sequence (one-dimensional)

A sequence of objects is generated according to the following rule:  $n_i = n_{i-1} + n_{i-2}$   
(see Figure 2.5).





<u>Starting point: L</u>		
<u>Result:</u>		<u>Number of objects in the chain, N</u>
L		1
LS		2
LSL		3
LSLLS		5
LSLLSLSL		8
LSLLSLSLLS		13
• • •		• • •

Figure 2.5 Results of generating a Fibonacci sequence [23]

## 2) Penrose tiling (two/three-dimensional)

In Figure 2.6 an example, where the two objects are rhombi can be seen. If those rhombi are assembled according to specific matching rules, they can cover the entire two-dimensional plane.

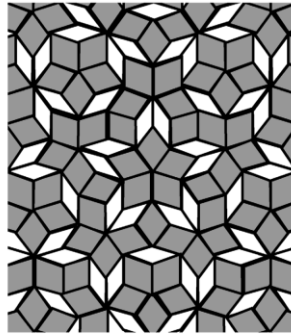


Figure 2.6 Penrose tiling constructed of two types of rhombi (gray and white) [23]

While many quasicrystals that can be found in binary mixtures of aluminium or titanium alloys with a transition metal are metastable and irreversibly transform into equilibrium crystalline structures upon heating, some ternary quasicrystals are stable up to their melting temperature. They belong to an equilibrium phase diagram and are of special interest since thermodynamic equilibrium and reversibility of the formation conditions also implies that they may be prepared by conventional metallurgy techniques such as casting, gas atomization and thermal spraying. Especially the AlCuFe system, showing thermal stability together with the availability and low cost of the constituents, was examined concerning industrial applications [1,3,21].

The useful physical and chemical properties of quasicrystals imply:

- Hardness of about 790 – 800 Vickers units [2] respectively 7.5 – 9 GPa [26]
- High Young's modulus  $E \approx 100$  GPa [2,3]
- Low adhesion and sticking forces [2,24]
- Reduced surface energy [3,24]
- Low friction coefficient [2,24]
- High wear resistance [2]
- Good corrosion, oxidation and chemical resistance [3,21,25]
- Low electrical and thermal conductivity [26]
- Thermal expansion coefficient of  $14.0 - 19.0 \cdot 10^{-6} \text{ K}^{-1}$  [21]

The quasicrystalline AlCuFe phase exists only at a very sharply defined composition around  $\text{Al}_{62}\text{Cu}_{25.5}\text{Fe}_{12.5}$ , with a compositional range of existence of not more than 2 or 3 at% for each component (see Figure 2.7).

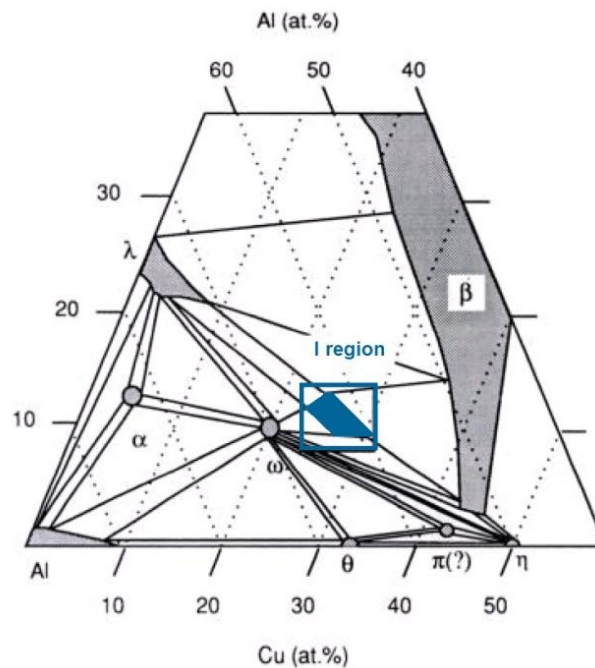


Figure 2.7 Overall compositions of phases in the Al-rich parts of the ternary AlCuFe alloy systems at 750 °C. [27]

The temperature dependent AlCuFe phase diagram (see Figure 2.8) reveals that the AlCuFe quasicrystalline phase exists only in a restricted temperature range between 650 °C and 850 °C. Its widest extension range is at about 750 °C whereas it shrinks dramatically with decreasing temperature. Thus precise technical conditions in the production process are required, restricting the use of classic metallurgical techniques. While the temperature-time profile is critical in view of preparing quasicrystalline  $\text{Al}_{62}\text{Cu}_{25.5}\text{Fe}_{12.5}$ , the mode of pressure application is not very important [3,28-31].

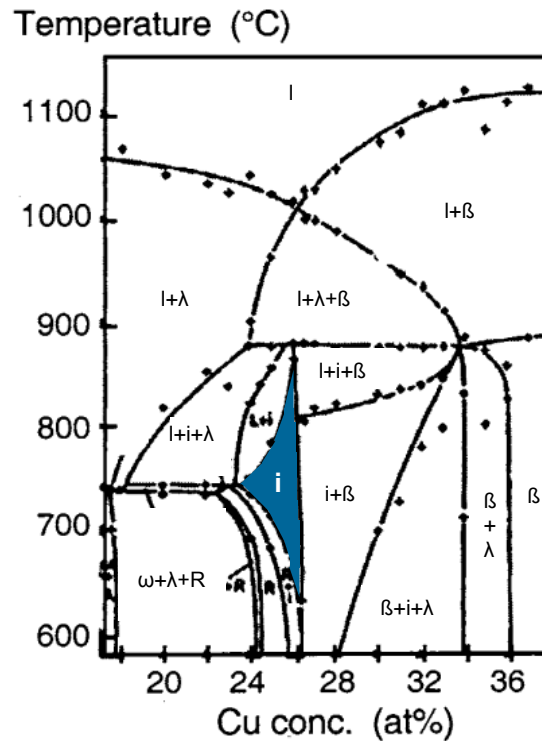


Figure 2.8 Temperature dependent AlCuFe phase diagram [32]

In the Al–Cu–Fe system addition, or partial substitution, of new chemical species allows to enhance some properties of the quasicrystal. For instance substituting a few atomic percent of boron (< 7 at%) to Al atoms in  $\text{Al}_{62}\text{Cu}_{25.5}\text{Fe}_{12.5}$  induces precipitates embedded in the icosahedral AlCuFe matrix. Although these boron phases are hardly detected by XRD (volume ratio lower than 1 %), they result in a three times larger yield stress, higher fracture strength, increased hardness and a lower coefficient of friction. Hence, the quaternary Al–Cu–Fe–B is a better choice for tribological applications than the more classical Al–Cu–Fe [1,3].

The electronic structure and properties of Al-based intermetallics with complex structures (systems with large unit cells), particularly AlCuFe compounds cannot be explained by the free-electron model. The AlCuFe compounds show a pseudo-gap which forms at the Fermi level ( $E_F$ ) in the partial Al DOS, particularly the Al 3p and Al 3 s,d distributions. The pseudo-gap results from the strong interaction between Al p-d states and the transition metals' d states in the middle of the valence band. The contribution of Al 3p states to the total binding energy for a large variety of AlCuFe compounds shows a sharp minimum for the quasicrystalline structures. Thus the pseudo-gap is not a signature of quasicrystalline order, but its depth and width are maximized for the quasicrystalline structure. [21,33,34] Compared to approximants with close chemical composition, AlCuFe quasicrystals display the following characteristics, which can be related to the maximized pseudo-gap:

- Quasicrystals display the lowest surface energy, the surface energy of  $\text{Al}_{59}\text{Cu}_{25.5}\text{Fe}_{12.5}\text{B}_3$  is estimated as  $44 \text{ mJ/m}^2$  [2,3,24]. (Teflon  $20 \text{ mJ/m}^2$ , stainless steel  $60 \text{ J/m}^2$ , Si  $1.1 \text{ J/m}^2$ , WC-Co  $1.7 \text{ J/m}^2$ )
- Quasicrystals exhibit the lowest coefficient of friction ( $\mu = 0.04 \pm 0.05$  with diamond [2] and  $\mu = 0.20 \pm 0.05$  with WC-Co [24]). This is probably due to the absence (or decrease) of chemical bonding at the common interface and the unfavourable matching of atomic lattices of a crystalline indenter and of a quasicrystal [24].
- Quasicrystals show the highest electrical resistivity (about  $2000 - 4000 \mu\Omega \text{ cm}$ ) caused by the reduced density of states and the very low effective number of carriers. For AlCuFe alloys, strong variations in electrical resistivity values with slight changes in composition are seen, which can be attributed to differences in the structural state [21,33,35,36].
- Heat conduction is very much reduced, even up to the melting temperature at typically  $1200 \text{ K}$ . [21]

### 2.3.1 Influence of impurities

According to literature the presence of C, O and N strongly influences the formation the icosahedral AlCuFe phase. If the C, O or N contamination is large enough, the formation of multiphase structures instead of a single phase icosahedral AlCuFe region has been observed. Carbon contamination can transform the single phase icosahedral region to an icosahedral and an  $\text{Al}_{50}\text{Cu}_{40}\text{Fe}_{10}$   $\beta$  phase and with increasing C content to three phases (i,  $\beta$  and  $\omega$ ) [28]. Oxidation at temperatures between 500 °C and 800 °C of quasicrystalline AlCuFe causes the development of an amorphous aluminium oxide layer and/or  $\gamma\text{-Al}_2\text{O}_3$  oxide and with ongoing Al loss, the icosahedral phase transforms to a  $\beta$  phase [37] and/or to a  $\lambda\text{-Al}_{13}\text{Fe}_4$  phase [38]. Nitridation at temperatures between 600 °C and 700 °C causes the formation of hexagonal AlN and with progressive depletion of Al a phase transformation from icosahedral AlCuFe to a  $\beta$  and  $\lambda$  phase occurs [1].

### 2.3.2 Electrical resistivity

For AlCuFe quasicrystals drastic changes of the electrical resistivity with concentration and structural quality are reported [21,33,35,36]. Adding defects/impurities leads to a decrease of resistivity, which is opposite to the classical Matthiessen rule for impurities dissolved in metals. Since impurities increase electron scattering at grain boundaries, an increase of resistivity with an increasing amount of impurities is common for metals and metal alloys. Figure 2.9 shows the temperature dependent electrical resistivity for AlCuFe and AlCuFeB samples with different microstructures.

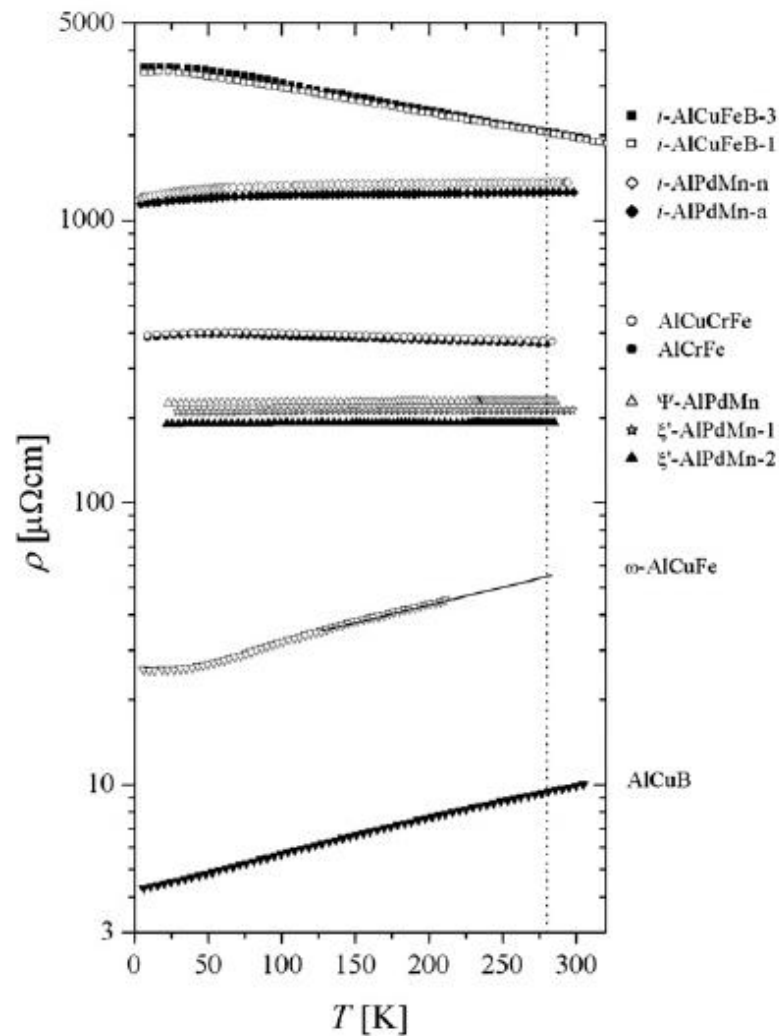


Figure 2.9 Temperature dependent electrical resistivity for different AlCuFe and AlCuFeB samples [35]

While the electrical resistivity of  $\omega$ -AlCuFe ( $26 - 50 \mu\Omega \text{ cm}$ ) lies within the range characteristic of simple alloys, quasicrystalline AlCuFeB shows a considerably larger electrical resistivity of  $2070 \mu\Omega \text{ cm}$  at room temperature and a negative temperature coefficient ( $(\rho_{4K} - \rho_{280K}) / \rho_{280K} = 70 \%$ ) [35].

In Figure 2.10 the variation of the electrical conductivity with temperature is displayed for quasicrystalline AlCuFe samples with four slightly different compositions ( $a = \text{Al}_{62.5}\text{Cu}_{25}\text{Fe}_{12.5}$ ,  $b = \text{Al}_{63}\text{Cu}_{24.5}\text{Fe}_{12.5}$ ,  $c = \text{Al}_{62}\text{Cu}_{25.5}\text{Fe}_{12.5}$ ,  $d = \text{Al}_{62.5}\text{Cu}_{25}\text{Fe}_{12.5}$ ) and of different quality (1 = samples with structural defects and additional phases, 2 = samples with structural defects, 3 = pure, high quality samples).

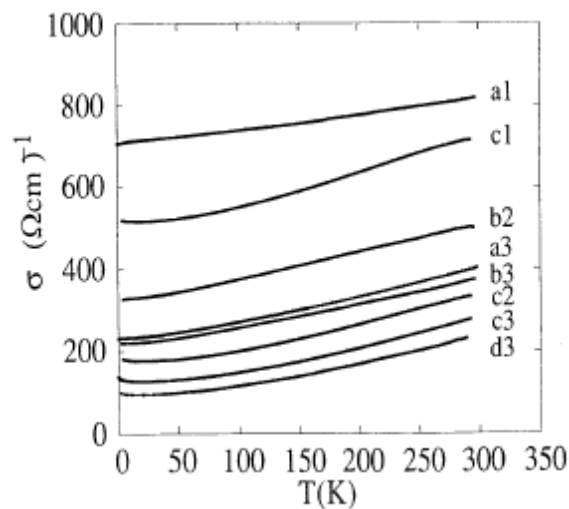


Figure 2.10 Conductivity as a function of temperature for samples ( $a = \text{Al}_{62.5}\text{Cu}_{25}\text{Fe}_{12.5}$ ,  $b = \text{Al}_{63}\text{Cu}_{24.5}\text{Fe}_{12.5}$ ,  $c = \text{Al}_{62}\text{Cu}_{25.5}\text{Fe}_{12.5}$ ,  $d = \text{Al}_{62.5}\text{Cu}_{25}\text{Fe}_{12.5}$ ) with different qualities (1 = samples with structural defects and additional phases, 2 = samples with structural defects, 3 = pure, high quality samples) [36]

For all compositions, the pure, high quality samples exhibit the highest electrical resistivity/lowest electrical conductivity. The electrical resistivity ranges from  $1200 \mu\Omega \text{ cm}$  to  $1700 \mu\Omega \text{ cm}$  for samples with structural defects and additional phases, from  $2000 \mu\Omega \text{ cm}$  to  $3400 \mu\Omega \text{ cm}$  for samples with structural defects but without additional phases and from  $2800 \mu\Omega \text{ cm}$  to  $5000 \mu\Omega \text{ cm}$  for pure, high quality samples [36]. Figure 2.11 shows the temperature-dependent conductivity of quasicrystalline  $\text{Al}_{62.5}\text{Cu}_{25}\text{Fe}_{12.5}$  thin films deposited on sapphire substrates [39]. In contrast to metal and metal alloy films, the conductivity of the deposited quasicrystalline  $\text{Al}_{62.5}\text{Cu}_{25}\text{Fe}_{12.5}$  films increases with decreasing film thickness.



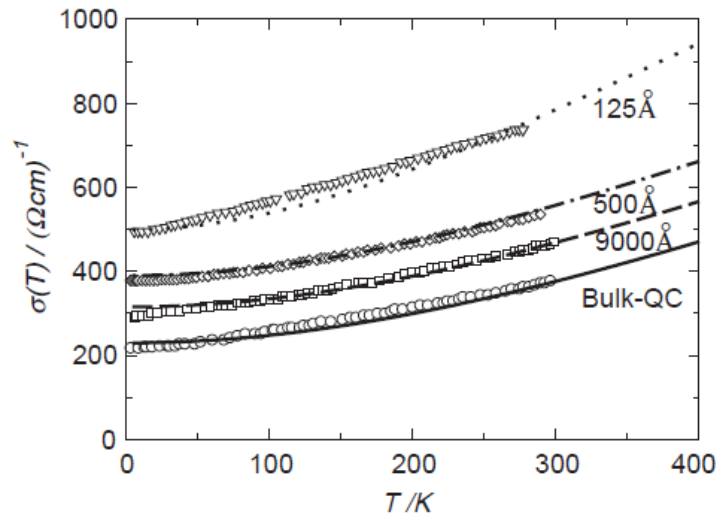


Figure 2.11 Temperature-dependent conductivity of quasicrystalline  $\text{Al}_{62.5}\text{Cu}_{25}\text{Fe}_{12.5}$  thin films with different film thicknesses [39]

Several mathematical models to describe the temperature dependence of the electrical conductivity of quasicrystalline AlCuFe can be found in literature [40-42] and will be shortly described in the following. The electrical conductivity of AlCuFe quasicrystals can be written as a temperature independent term that is strongly dependent on the structural quality and composition of the AlCuFe sample and a temperature dependent term. If a two band model consisting of electrons and holes (see Relation 2.1) and a constant mobility for each carrier type is assumed, the temperature dependence of the electrical conductivity can be described by an increase of the carrier densities due to excitation over a pseudogap  $E_G$  (see Relation 2.2) [40,41]:

$$\sigma(T) = e^2 \left( \frac{\tau_e n_e}{m_e^*} + \frac{\tau_h n_h}{|m_h^*|} \right) \quad (2.1)$$

$e = 1.602176487 \cdot 10^{-19}$  As... unit charge

$n_e/n_h$  ... electron/hole density

$m_e/m_h$ ... electron/hole effective mass

$\tau_e/\tau_h$ ... electron/hole scattering time

$$n_{e,h} = n_{e0,h0} + C e^{-E_G/k_B T} \quad (2.2)$$

$k_B$ ... Boltzmann constant  
 $E_G$ ... pseudogap

The experimental data can then be simply fitted using Relation 2.3 [41,40].

$$\sigma(T) = \sigma_{4K} + A e^{BT} \quad (2.3)$$

$\sigma_{4K}$ ... residual (temperature independent) conductivity of the system  
 $A$ ... Fitting parameter  
 $B$ ... Fitting parameter

A more sophisticated conductivity model (see Relation 2.4 and Relation 2.5) consisting of a metal-like  $\sigma_{ML}$  and a semiconductor-like  $\sigma_{SCL}$  component can be applied to consider the temperature dependence of the carrier's mobility [42].

$$\sigma(T) = \sigma_{ML} + \sigma_{SCL} \quad (2.4)$$

$\sigma(T)$ ... temperature dependent conductivity  
 $\sigma_{ML}$ ... metal-like component  
 $\sigma_{SCL}$ ... semiconductor-like component

$$\sigma_{ML} = \sigma_0 + BT^{1/2} \quad (2.5)$$

$$\sigma_{SCL} = A_1 T^{\alpha_1} e^{-460/T} + A_2 T^{\alpha_2} e^{-2700/T}$$

$\sigma_0$ ... residual (temperature independent) conductivity of the system  
 $\alpha_1 = 0.4$ ... fitting parameter  
 $\alpha_2 = 1.6$ ... fitting parameter  
 $A_1$ ... fitting parameter  
 $A_2$ ... fitting parameter

Since the electrical conductivity of quasicrystals depends strongly on the chemical composition and the microstructure, electrical resistivity measurements can be used as an easy method to estimate the quality of quasicrystalline materials. Because of the maximized pseudo-gap at the Fermi level, the electrical conductivity of quasicrystals can be described by semiconductor-like models.

## 2.4 Magnetron sputtering

Details about the technical implementation and scientific background on the sputtering process, interface formation, nucleation and film growth and the microstructure of sputter deposited films can be found in [43,44] and are shortly summarised in the following.

Sputtering is a process whereby material is dislodged and ejected from the surface of a solid (source of coating material = target) due to the momentum exchange associated with surface bombardment by heavy inert gas ions. Sputter deposition is a vacuum coating process and the ion bombardment is provided by igniting an electric glow discharge (abnormal glow discharge) so that ionization of the working gas (ionized gas = plasma) is produced in the region adjacent to the target. The target is made the negative electrode (cathode) so that its surface is bombarded by the positive ions from the plasma and the substrate is made the anode. The sputtered material is ejected primarily in atomic form and the substrates are positioned in front of the target so that they intercept the flux of sputtered atoms. The incident ions produce a cascade of collisions primarily within a region extending about 1 nm below the target surface. Beside other interaction processes, a part of the kinetic energy of the incident particle is transferred to the target particles leading to the emission of one or more atoms from the target. The sputter yield is defined as the number of target atoms ejected per incident particle and depends on the target species, the bombarding species, the energy of the bombarding species and their angle of incidence. Sputtering apparatuses are generally calibrated to determine the deposition rate under given operating conditions. Magnetron sputtering sources use a magnetic field to trap the electrons on magnetic field lines (circular motion) and thus force them to make the collisions required to maintain the plasma. The magnetic field is of such strength that it affects the plasma electrons but not the ions. Compared to conventional sputtering sources, the efficiency of the ionization mechanisms is considerably increased. Thus magnetron sputtering sources can provide intense plasma discharges offering high deposition rates at low working gas pressures, moderate voltages and low substrate heating. The most important characteristic of the sputtering process is its universality. Since the coating material is passed into vapour phase by a mechanical (momentum exchange) rather than a chemical or thermal process, virtually any material is a candidate coating. DC methods are generally used for sputtering metals, while RF potential must be applied to the target when sputtering non-conducting materials. Alloys and compounds can generally be sputter-deposited while preserving their compositions.

### 2.4.1 RF magnetron sputtering

DC magnetron sputtering cannot be used to sputter non-conducting materials because of charge accumulation on the target surface. This difficulty can be overcome by using radio frequency (RF) sputtering, which can be used to deposit conducting, semiconducting and insulating coatings. For RF sputtering, the target is capacitively coupled to the plasma and an alternating voltage is applied. The electrodes reverse cathode-anode roles on each half-cycle and the discharge is operated at a sufficiently high frequency (low MHz range) so that the massive ions cannot follow the temporal variations in the applied potential. Due to the higher mobility of the electrons, significantly more electron current flows when the target is on a positive potential than does ion current flow when the target is on negative potential. Because capacitive coupling requires that there must not be a DC current flow, the net current to the target in each RF cycle must be zero. Accordingly a negative bias must form such that the electron current on the positive side of the cycle becomes equal to the ion current on the negative side (see Figure 2.12). The negative bias is approximately equal to the zero-to-peak voltage of the RF signal and therefore can be made large enough to produce sputtering.

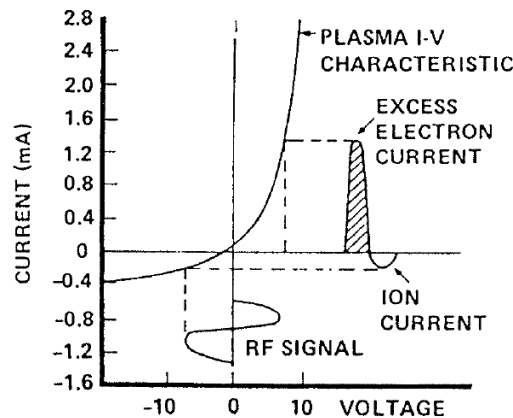


Figure 2.12: Schematic illustration of the development of a negative bias when a RF potential is capacitively coupled to a target [43]

Besides the technically more complicated and complex implementation of RF processes, RF magnetron sputtering is also energetically less economic compared to DC magnetron sputtering.

### 2.4.2 Alloys and compounds

Since sputter deposition is a process during which single atoms are ejected from the target material, chemical bondings and molecules are sputtered in fractions (e.g.:  $\text{Ta}_2\text{O}_5 \rightarrow \text{Ta}, \text{TaO}$  and  $\text{O}$ ) Nevertheless, one important advantage of the sputtering process is that the vapour flux produced tends to have the chemical composition of the originating solid. Thus the composition of a sputtered film tends to be that of the target if [43]:

- The target is maintained sufficiently cool to avoid diffusion of the constituents
- The target does not decompose
- Reactive contaminants are not present
- The gas phase transport of the components is the same
- The sticking coefficients for the components on the substrate are the same

Nevertheless, the details of the sputtering interaction on multicomponent materials are complex and poorly understood. When sputtering is first initiated from a homogeneous target composed of species having different individual sputtering yields or masses, the sputtered flux will in general be rich in one of the constituents. To achieve the correct composition an adjustment period is needed. During this period, the compositions of the species in a surface layer adjust so that the product of the effective sputtering yield times surface concentration for each species is proportional to its concentration in the target (see Figure 2.13) [43].

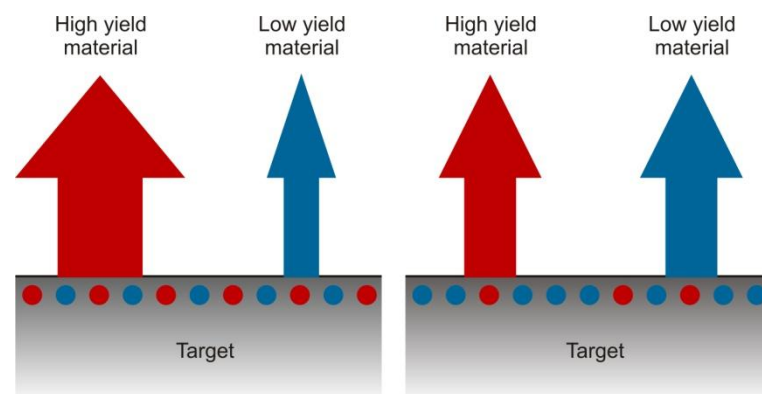


Figure 2.13: Schematic illustration of the modification in surface composition that occurs during sputtering of a homogenous multispecies material [43]

It is obvious that diffusion from the bulk would restock the reduced concentrations of high yield materials in the altered layer and thus must be avoided. The thickness and composition of the altered layer depend on the target material and sputtering conditions. A change in sputtering conditions will in general require an adjustment of the altered layer. It is important to note that the effective sputtering yield of a constituent in an alloy or compound will not be the same as that constituent itself, because of the different binding energy and the different atomic masses involved in the collision sequence. A similar situation appears, if deposition is done from a two-phase alloy in which the phases have significantly different sputtering yields. The inhomogeneous sputtering yield over the surface will cause the development of an irregular surface topography (cones). After an incubation period, when an equilibrium surface has developed, the sputtered material flux will become identical to the target. Nevertheless, the irregular surface topography may cause the overall yield to be considerably lower than what might be expected on the basis of the yields of the primary target constituents. Particular caution must be exercised when targets with poor electrical or thermal conductivity are used. Since concentrated heating occurs under the plasma ring, poor thermal conductivity leads to high surface temperatures and may result in the loss of volatile constituents by evaporation or sublimation.

## 2.5 Interface formation and film growth

Details and scientific background on interface formation, nucleation and film growth and the microstructure of sputter deposited films can be found in [43,44] and are shortly summarised in the following.

A solid interface is defined as a small number of atomic layers that separate two well defined phases and where the properties differ significantly from those of the bulk materials it separates. Examples would be a coating on a substrate, which is separated by a substrate-coating interface from the bulk of the substrate or a grain boundary between two single-crystalline grains inside a solid state body. The surface of a solid is a particular simple type of interface, at which the solid is in contact with the atmosphere or any kind of gas or vacuum. Since on a real surface reconstruction and defects (adatoms, interstitials, kinks, vacancies, steps, terraces) are always present, an ideal surface with complete translational symmetry cannot exist. Due to the different electron orbitals and the type of chemical bonding, defects cause local variations in important surface quantities such as binding energy, coordination, electronic states, etc. Thus the defect structure of a surface influences the interface development and other coating properties like adhesion and is crucial for coating deposition.

### 2.5.1 Adsorption and desorption on solid surfaces

A fresh, clean surface is usually very reactive towards particles, atoms and molecules, impinging on it. As all kinds of adsorbed particles form an ad-layer on the topmost atomic layers of the solid, the real surfaces exposed to atmosphere are very complex and not well defined systems. Thus the preparation of a clean and uncontaminated surface is required to create a well defined interface in a controlled way. Among others, techniques to clean substrate surfaces under vacuum conditions are: heating, ion bombardment and chemical reactive cleaning

Adsorption and desorption are the two processes, which determine the macroscopic coverage on a solid surface exposed to a gas. The bonding of an adsorbed atom or molecule on a solid surface may be chemical, van der Waals, electrostatic or a combination of these types. The adsorption rate depends on the number of particles striking the surface per second and on the so-called sticking coefficient, which is the probability that an impinging particle sticks to the substrate. The rate  $v_g$  at which particles impinge on a surface located in an environment with a vapour pressure  $p$  (per unit area and time) is given by:

$$v_g = \frac{p}{\sqrt{2\pi mk_B T}} \quad (2.6)$$

*p*... vapour pressure [Pa]  
*m*... mass of impinging gas particles  
*k<sub>B</sub>*... Boltzmann's constant  
*T*... temperature in Kelvin

Then the number of coating particles impinging on the surface can be estimated as:

$$v_c = \frac{\rho \cdot a_w}{m_c} \quad (2.7)$$

*ρ*... density of the coating material  
*a<sub>w</sub>*... deposition rate  
*m<sub>c</sub>*... mass of the coating material particles

And the ratio of impinging gas particles (*v<sub>g</sub>*) to coating particles (*v<sub>c</sub>*) is given by:

$$\frac{v_g}{v_c} = \frac{m_c p}{a_w \rho \sqrt{2\pi m k_B T}} \quad (2.8)$$

*p*... vapour pressure [Pa]  
*m<sub>c</sub>*... mass of the coating material particles  
*a<sub>w</sub>*... deposition rate  
*ρ*... density of the coating material  
*m*... mass of impinging gas particles  
*k<sub>B</sub>*... Boltzmann's constant  
*T*... temperature in Kelvin

Relation 2.8 can be used to estimate the O and C impurities, which are incorporated in the deposited AlCuFeB and AlMgB coatings due to the residual gas of the vacuum chamber. Since impurities have a significant influence on the characteristics of AlMgB<sub>14</sub> and quasicrystalline AlCuFeB (see Section 2.21 and Section 2.3.1), the estimation of incorporated impurities is of high interest.



### 2.5.2 Interface formation

The interfacial region between a coating and a surface determines many physical and electrical properties of the couple. These include: contact resistance, contact noise, acoustic coupling, electron trapping and recombination, thermal conductance and film adhesion. Adhesion or adhesive strength is a macroscopic property that depends on the bonding across the interfacial region, local stresses and the adhesive failure mode. The failure mode depends on the type of stress to which the interfacial region is subjected:

- Mechanical loading (tensile, shear, fatigue)
- Thermal (high, low temperatures, cycling)
- Chemical environment (chemical and/or electrochemical corrosion)
- Electrical environment

Good adhesion is promoted by:

- Strong atom-atom bonding within the interfacial region
- Low local stress levels
- Absence of easy deformation or fracture modes
- No long-term degradation modes

These characteristics depend on the nature of the interfacial region, which in turn depends on the interactions between the deposited material and the surface.

When atoms impinge on a surface, they transfer kinetic energy to the substrate lattice and become loosely bonded adatoms. An adatom might immediately re-evaporate or diffuse along the surface. This diffusing particle may re-evaporate or adsorb, particularly at special sites like edges or other defects. The incorporated atoms readjust their positions within the lattice by bulk/surface diffusion processes. Nucleation of more than one adsorbed particle might occur and the nuclei growth mode determines the effective interfacial contact area, the development of voids, the defect morphology and the amount of diffusion and reaction between the deposited atoms and substrate material. The final macroscopic state of the system is not necessarily the most stable one, since it is kinetically determined.

The interface between two solids might be: crystalline/crystalline or amorphous/crystalline. Both types of interfaces can be classified as:

- Mechanical interface  
The mechanical interface is characterised by mechanical interlocking of the film material with a rough surface. Often deposition of a film on a rough surface gives a porous film due to the geometrical shadowing effect.
- Monolayer-to-monolayer interface  
The monolayer-to-monolayer interface is characterised by an abrupt change from the film material to the substrate material in a distance of the order of the separation between atoms (2 to 5 Å). It usually occurs, when there is no diffusion and little chemical reaction between the deposited atoms and the substrate surface.
- Compound interface  
The compound interface is characterised by a constant composition layer, many lattice parameters thick, created by chemical interaction of the film and substrate material.
- Diffusion type of interface  
The diffusion type of interface is characterised by a gradual change in composition, intrinsic stress, and lattice parameters across the interfacial region. If there is a difference in diffusion rates of the film atoms and the substrate atoms, porosity may be formed in the interfacial region.
- Pseudo-diffusion type of interface  
The pseudo-diffusion type of interface occurs under energetic situations such as ion bombardment, for materials that are normally insoluble. Ion bombardment prior to film deposition may increase the interfacial solubility by creating very high concentrations of point defects or stress gradients or both which will enhance diffusion.

The type of interfacial region formed during deposition depends on the substrate surface morphology, contamination, chemical interactions, the energy available during interface formation, and the nucleation behaviour of the depositing atoms. Thermodynamic considerations can yield limiting conditions for the formation of the particular interface, but not all thermodynamically possible phases will necessarily occur in reality because of kinetic limitations such as activation energies for nucleation. Thus phase diagrams can give useful information about the expected properties of certain solid/solid interfaces. For

example, a requirement for the formation of a smooth gradual interface at the temperature  $T_0$  is a binary phase diagram, which allows complete mixing of the two components (see Figure 2.14 a). In contrast, a phase diagram as in Figure 2.14 b allows mixing of the two components at temperature  $T_0$  only between two specific concentrations. Outside this concentration range, only the phases I and II exist.

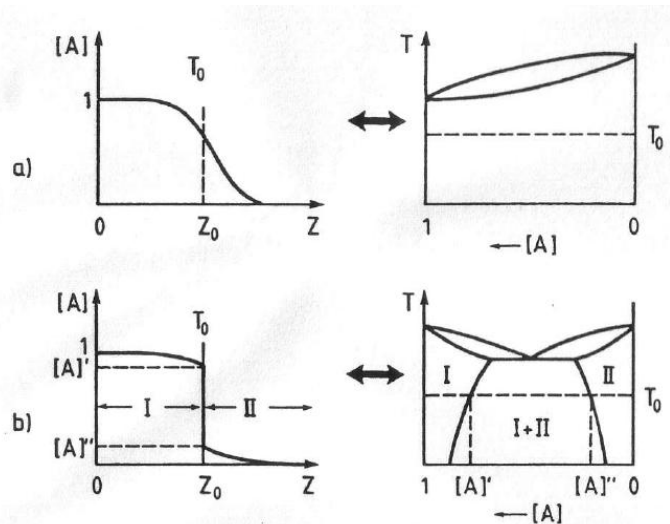


Figure 2.14 Phase diagram (right) and concentration versus depth ( $z$ ) plots (left) for two materials A and B. The two materials have been brought in contact at a temperature  $T_0$  and after a certain reaction time the interface at  $z_0$  (left) might be gradual (a) or more or less sharp (b) depending on the phase diagram (right). The phase diagram in (a) allows complete mixing of A and B, whereas in (b) the phase diagram allows the existence of two separate phases I and II and mixing of I and II at the particular temperature  $T_0$  only between the concentrations  $[A]'$  and  $[A]''$  [44]

When depositing metals on metals, a diffusion type interface region with metallic bonds is ideal because of the gradual change in composition and stress across the interface. Such interfaces are promoted by elevated substrate temperatures, which enhance diffusion, but are prevented by oxide or other contamination layers that can act as diffusion barriers. Compound interface regions are also promoted by elevated substrate temperature but have the disadvantage that they are brittle. Thus only a thin compound layer is desirable.

### 2.5.3 Intrinsic and thermal stress

All sputtered coatings are in a state of stress. The total stress  $\sigma = \sigma_i + \sigma_T$  is composed of an intrinsic stress  $\sigma_i$  and a thermal stress  $\sigma_T$ . The thermal stress is caused by differences in the thermal expansion coefficients of the coating and substrate materials and can be calculated according to the following relation:

$$\sigma_T = E_S(\alpha_C - \alpha_S)(T_D - T_M) \quad (2.9)$$

$E_S$ ... elasticity modulus of the coating

$\alpha_C$ ... thermal expansion coefficient of the coating

$\alpha_S$ ... thermal expansion coefficient of the substrate

$T_D$ ... temperature during deposition

$T_M$ ... temperature during measurement

The intrinsic stress  $\sigma_i$  is caused by atoms, which are out of position with respect to the minimum in the inter-atomic force field and by impurity incorporations. Compressive stresses ( $\sigma > 0$ ) develop when the atoms are in closer proximity to one another, tensile stresses ( $\sigma < 0$ ) develop when atoms are further apart than they would be under more equilibrium circumstances. For low melting point materials, deposition conditions will generally involve sufficiently high temperature values so that the intrinsic stresses are significantly reduced by recovery during the coating growth. Thermal stresses are therefore of primary importance for such materials. Stress relief can occur by annealing the coatings after deposition. Higher melting point materials are generally deposited at sufficiently low temperatures ( $< 1/4$  of the melting point) so that the intrinsic stresses dominate over the thermal stresses. For thin films ( $< 500$  nm) the intrinsic stresses are generally constant throughout the coating thickness. The interfacial bond must withstand the shear forces associated with the accumulated intrinsic stresses throughout the coating, as well as the thermal stresses. Since the intrinsic stress contribution increases with coating thickness it can be the cause of premature interface cracking, and poor adhesion for coatings exceeding critical values of thickness, which may be as low as 100 nm.

A good adhesion of functional coatings on the substrate is of significant importance for technical applications, thus the interface between the deposited coating and the substrate, as well as the intrinsic and thermal stresses are of special interest. The deposition parameters will be optimised to minimize the stresses in the coatings, to develop a desired interface and therefore to guarantee good adhesion.

## 3. Experimental

### 3.1 Deposition geometry and substrate holder

For deposition of  $\text{Al}_{59}\text{Cu}_{25.5}\text{Fe}_{12.5}\text{B}_3$  and  $\text{AlMgB}_{14}$  films from hot pressed targets by magnetron sputtering a substrate holder was constructed, which allows concentric positioning of the substrates above the magnetron sputtering source (*AJA International ST20*) and to arbitrarily vary the substrate - sputtering source distance (see Figure 3.1 a, b). The engineering drawings of the substrate holder can be found in the Appendix A-I. To heat the substrate during deposition and ion etching, the substrate holder contains a cartridge heater (*Loysch KG HP000H*), with a diameter of 10 mm and a length of 40 mm. The cartridge heater is operated at 230 V AC and allows a maximum operation power of 315 W. The cartridge heater contains a type-L thermocouple (Fe - CuNi), which allows temperature measurement within a range of  $-200\text{ }^\circ\text{C}$  to  $+900\text{ }^\circ\text{C}$ . The cables of the cartridge heater were insulated using  $\text{Al}_2\text{O}_3$  tubes (*FRIATEC Degusit AL23 F160-11030-00005*) with an outer diameter of 3.0 mm, an inner diameter of 1.6 mm and a length of 5 mm. The head of the substrate holder is made of Copper (Cu) to guarantee a fast and homogenous heat distribution and a good thermal contact with the substrates. To implement a thermal and electrical insulation of the substrate holder's head from the guiding rod, a *Macor* (Corning, NY, USA – 46 wt%  $\text{SiO}_2$ , 17 wt% MgO, 16 wt%  $\text{Al}_2\text{O}_3$ , 10 wt%  $\text{K}_2\text{O}$ , 7 wt%  $\text{B}_2\text{O}_3$ , 4 wt% F) ring was placed between the substrate holder's head and the guiding rod. Therefore plasma-etching treatment of the substrates before sputtering and bias-sputtering is possible.

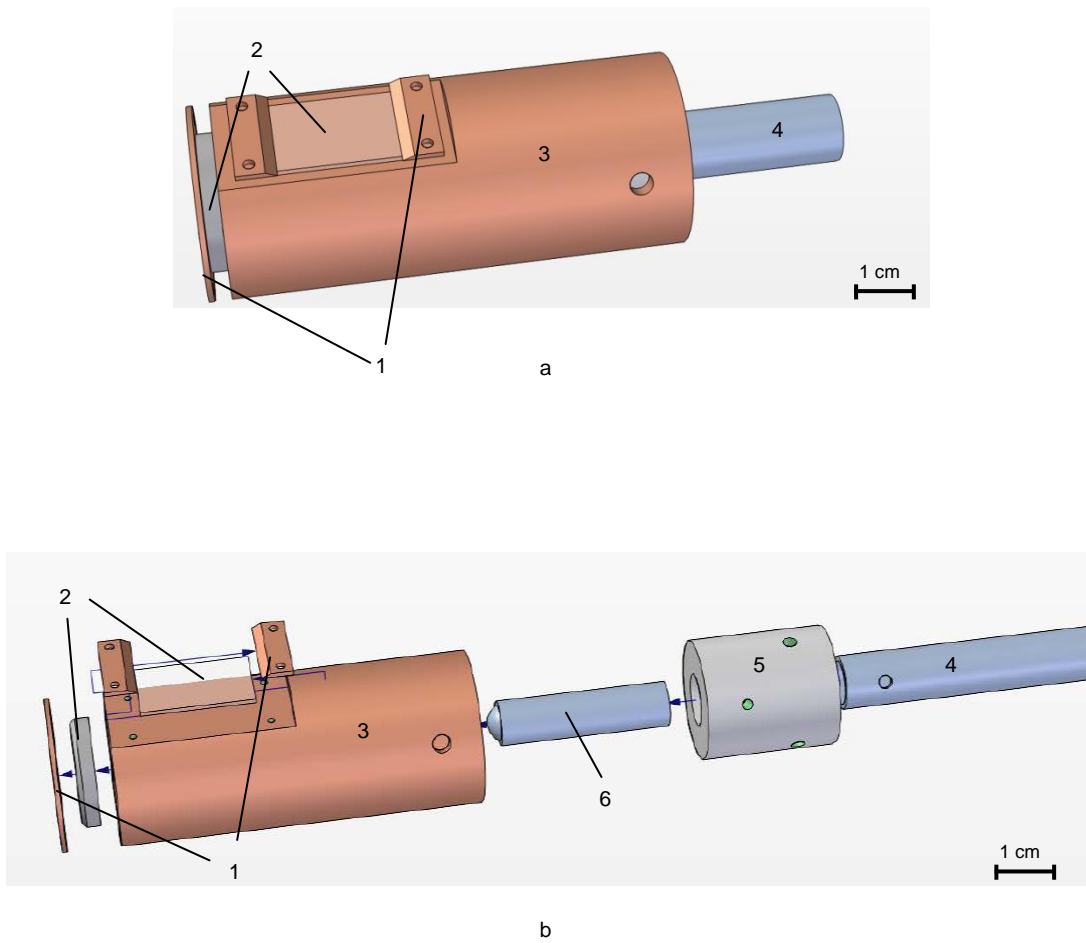


Figure 3.1 Substrate holder  
1 – Substrate mounting clips  
2 – Substrates  
3 – Copper head  
4 – Stainless steel guiding rod  
5 – *Macor* ring  
6 – Cartridge heater (*Loysch KG HP000H*)

Figure 3.2 shows the temperature curve of the substrate holder and the corresponding least square fit ( $T = 243.3 \times t^{0.38}$ ) for heating up from room temperature to 600 °C.

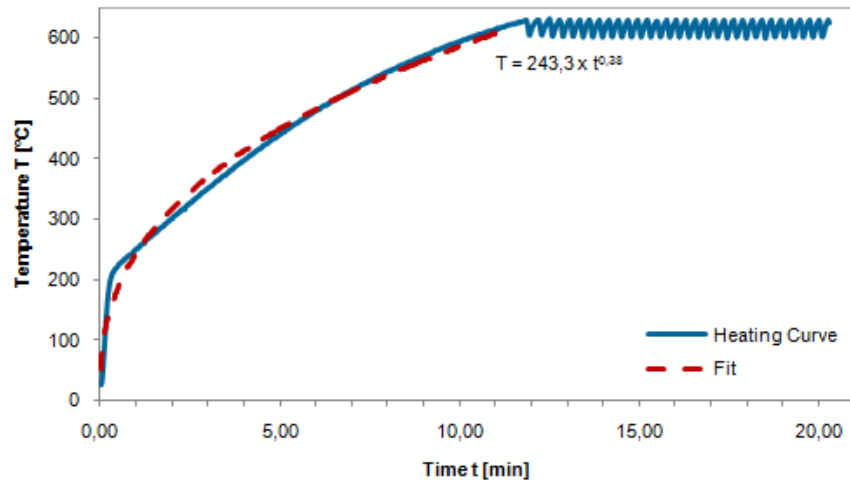


Figure 3.2 Heating curve of the substrate holder for heating up from 25 °C to 600 °C  
The oscillations after a heat time of 10 min at about 600 °C result from the PID temperature controller

Figure 3.3 shows the temperature curve of the substrate holder and the corresponding least square fit ( $T = 508 \times t^{-0.4}$ ) for cooling down from 600 °C to room temperature.

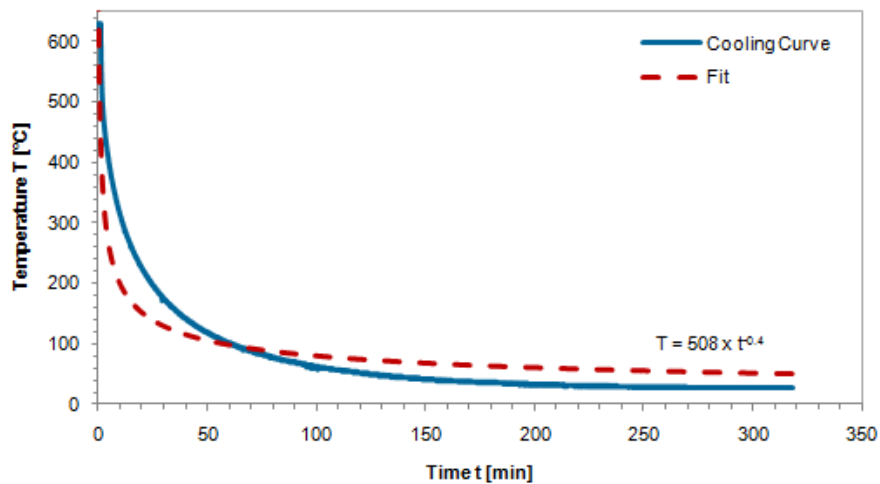


Figure 3.3 Cooling curve of the substrate holder, when cooling down from 600 °C to 25 °C

The substrate temperature was kept constant during deposition by using a PID temperature controller *Eurotherm 3216*. To minimize thermal stress in the coatings, the cooling rate was limited to 3 °C / min. Figure 3.4 represents the circuit diagram of the temperature control unit. Since the *Eurotherm 3216* has to be operated in-phase, a lamp dismantled from a phase tester is used to indicate if the power cable is connected in-phase. The heating power is provided by an adjustable AC power supply (0 - 250 V, max. 12 A).

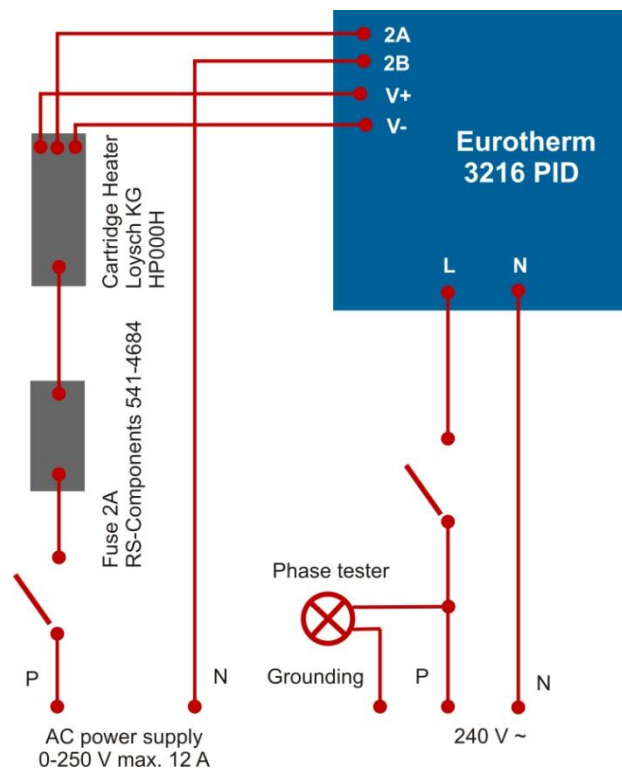


Figure 3.4 Circuit diagram of the *Eurotherm 3216* PID temperature controller

Figure 3.5 shows the deposition geometry of the vacuum chamber. The substrate-target distance (working distance) was about 3 cm for depositing the  $\text{AlMgB}_{14}$  films. For deposition of the  $\text{AlCuFeB}$  samples the working distance was varied between 1 – 10 cm. During ion-etching and heating up prior deposition a shutter can be placed between the substrate and the sputtering source, to avoid contamination of the target by impurities sputtered from the substrate (ion-etching) or out-gassing (heating up).



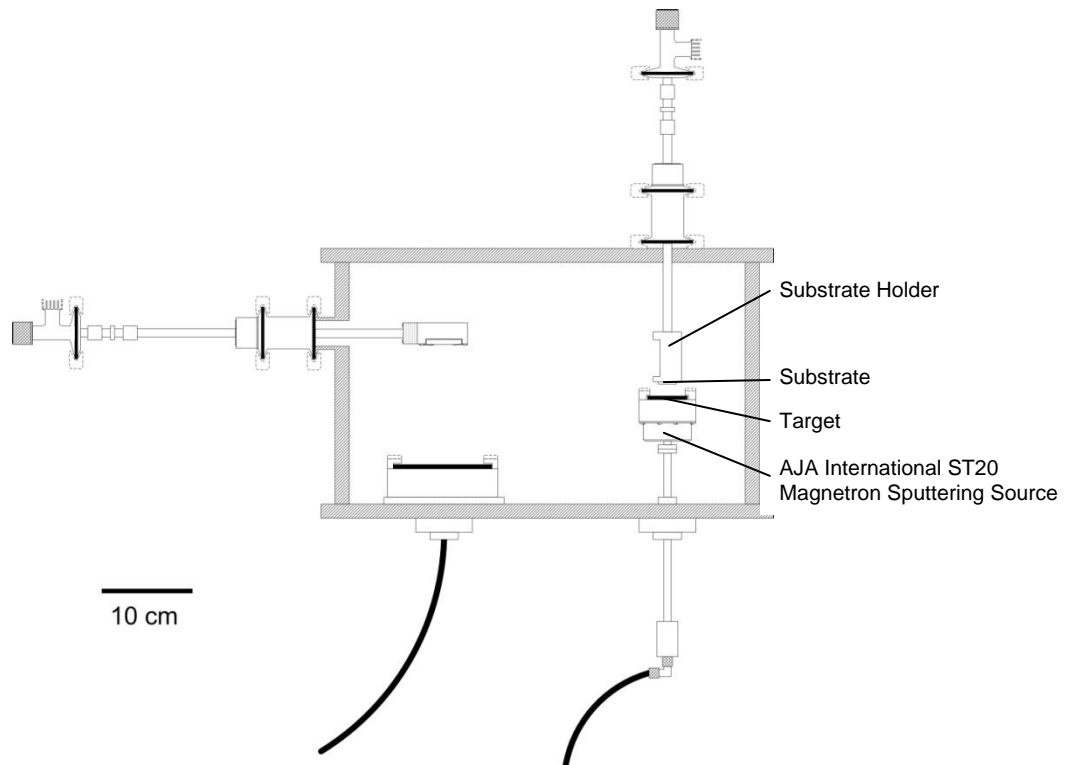


Figure 3.5 Deposition geometry of the vacuum chamber  
The target illustrated at the left hand side was only used for deposition of interlayer materials

The base pressure of the vacuum chamber is  $\sim 1.5 \times 10^{-7}$  mbar, the working gas pressure (Ar) is controlled using a *MKS Type 1179B Mass Flow Controller* and a *179B Mass Flow Meter*. Deposition from targets with metallic character was done using a DC power supply *ELAN DCS-55 4 kW*. For targets with poor conductivity, a RF power supply *Hüttinger PFG 600 RF (13.56 MHz)* in combination with a *Hüttinger HF matchbox PFM 1500 A* was used. By water-cooling the targets are kept at room temperature during deposition. The deposition rates were determined by measuring the film thickness with a *Taylor Hobson Surtronic 3+* profilometer for a known deposition time. Post annealing was done under vacuum conditions ( $1 \cdot 10^{-6}$  mbar) but in a separate vacuum chamber, so that samples had to be exposed to atmosphere between deposition and post annealing.

## 3.2 Residual gas analysis

As explained in Section 2.2.1 and Section 2.3.1, impurities can have strong effects on the microstructure development of AlCuFe and AlMgB coatings. As summarized in Section 2.5 contamination, especially on the substrate surface can crucially influence interface formation and thus coating qualities like adhesion. To minimize the impurities incorporated in the deposited coatings, the production of target materials with a low impurity content and the preparation of an uncontaminated substrate surface is crucial. Furthermore, it is important to identify and quantify the particles, which might get adsorbed on the sample surface before and during coating deposition because of the residual gas in the vacuum chamber and impurities contained in the working gas (Ar). The residual gas in the vacuum chamber was analyzed with a quadrupole mass analyzer *Alcatel Multi-Turboquad*. Analysis of the residual gas was done with a steel K600 substrate mounted for deposition. Figure 3.6 represents the mass spectrum of the vacuum system when a steel K600 substrate is mounted for deposition. If the substrate is not heated and if no Ar pressure is applied, the base pressure is  $\sim 1.5 \cdot 10^{-7}$  mbar and the residual gas consists mostly of hydrogen H ( $\sim 45\%$ ) and water vapour H<sub>2</sub>O ( $\sim 35\%$ ). Also hydroxide OH ( $\sim 9\%$ ) and carbon monoxide CO ( $\sim 7\%$ ) can be observed. C contributes with 0.1% and O with 0.8% to the residual gas. H represents the main constituent of the residual gas, since it is not well transported by turbomolecular pumps. Heating the substrate to 600 °C causes an increase of pressure to  $1.0 \cdot 10^{-6}$  mbar. In relation to the total residual gas pressure, the H ( $\sim 75\%$ ) and O ( $\sim 3\%$ ) content increases, while the content of H<sub>2</sub>O ( $\sim 13\%$ ), OH ( $\sim 4\%$ ) and CO ( $\sim 3\%$ ) decreases. Applying  $2.0 \times 10^{-3}$  mbar Ar does neither introduce new impurities nor result in a significant change of the residual gas composition.

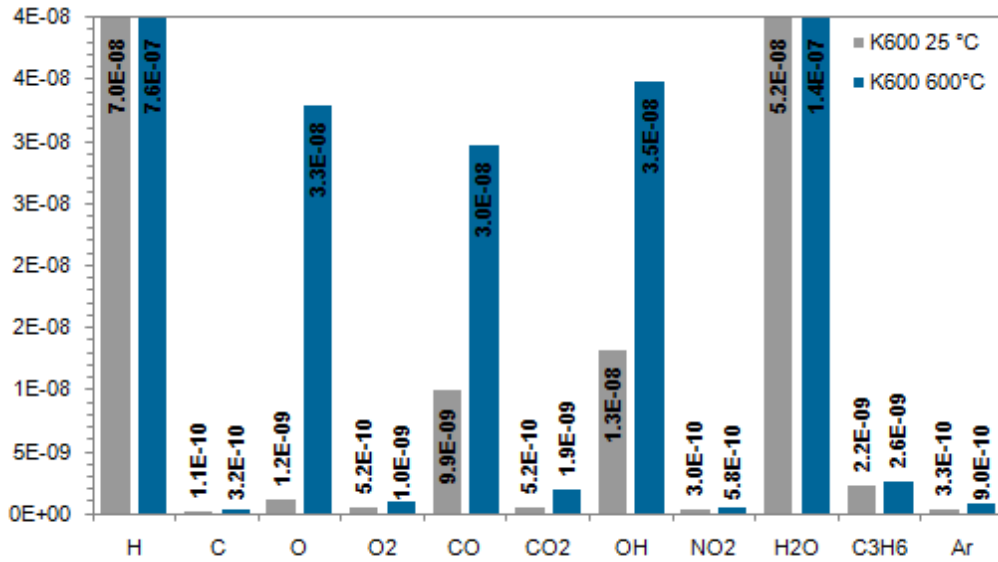


Figure 3.6 Residual gas analysis of the vacuum system with a steel K600 substrate mounted for deposition

Relation 2.8 in Section 2.5.1 can be used to estimate the ratio of impinging gas particles to coating particles. Beside the deposition rate and the density of the coating material, also the mass of the coating material particles is needed. With the atomic mass of the single constituents a weighted mean atomic mass for the target composition is calculated. Table 3.1 lists the atomic masses of the target constituents and the mean atomic mass for the two target compositions in atomic mass units ( $u=1.660538782 \cdot 10^{-27}$  kg).

Table 3.1 Atomic masses for the target constituents and the weighted mean atomic mass for the target compositions ( $u=1.660538782 \cdot 10^{-27}$  kg)

Elements/Target Composition	Al	Cu	Fe	Mg	B	Al <sub>59</sub> Cu <sub>25.5</sub> Fe <sub>12.5</sub> B <sub>3</sub>	AlMgB <sub>14</sub>
Atomic mass [u]	26.98	63.55	55.85	24.31	10.81	39.37	12.66

Table 3.2 lists the estimated C and O impurity content of coatings deposited on substrates heated to 600 °C, which is caused by the residual gas. The composition of the residual gas and the partial gas pressures of the single constituents were chosen according to the measured spectra (Figure 3.6). Different deposition rates ranging from 5 nm/min to 200 nm/min were chosen for the two material systems  $\text{Al}_{59}\text{Cu}_{25.5}\text{Fe}_{12.5}\text{B}_3$  and  $\text{AlMgB}_{14}$ .

Table 3.2 C and O content caused by the residual gas of the vacuum chamber

Deposition Rates	$\text{Al}_{59}\text{Cu}_{25.5}\text{Fe}_{12.5}\text{B}_3$		$\text{AlMgB}_{14}$	
	C [at%]	O [at%]	C [at%]	O [at%]
5 nm/min	0.8	6.8	0.5	3.8
10 nm /min	0.4	3.4	0.2	1.9
50 nm/min	0.1	0.7	0.05	0.4
100 nm/min	0.04	0.3	0.02	0.2
200 nm/min	0.02	0.2	0.01	0.1

According to these considerations the deposition rate achieved should be at least about 50 nm/min in order to keep the impurity content caused by the residual gas negligibly small.

### 3.3 Targets

For coating deposition different AlCuFeB and AlMgB<sub>14</sub> hot pressed targets were produced at *RHP-Technology GmbH & Co. KG* by Hot Uniaxial Pressing (HUP) (see Figure 3.7). Hot pressing was done under Ar atmosphere using different hot pressing parameters and different powders.

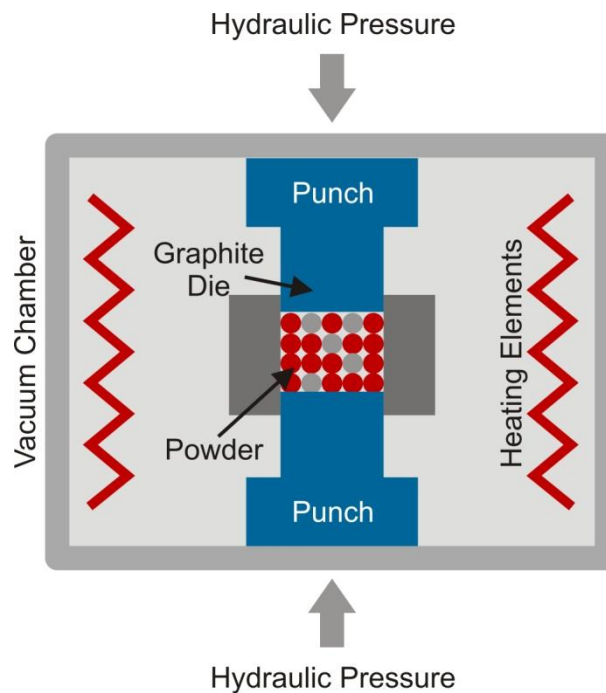


Figure 3.7 Schematic illustration of the Hot Uniaxial Press (HUP) used for target production

If the targets show high brittleness and/or a low resistance to thermal shock and temperature gradients, cracking of the targets can occur during magnetron sputter deposition. An optimisation of the hot pressing conditions can help to achieve full densification of the pressed powders and thus to avoid crack development. A possible subsequent heat treatment or slow cooling down after hot pressing can reduce the crack formation as well.

Since no commercial powder supplier was available for  $\text{AlMgB}_{14}$ , the  $\text{AlMgB}_{14}$  targets were produced by hot pressing an elemental powder mixture. The powder mixture was produced by mechanical milling elemental Al, Mg and B powders weighted out according to the  $\text{AlMgB}_{14}$  composition. The following two target types were used for magnetron sputter deposition:

#### **AlMgB with amorphous B**

An elemental powder mixture produced using amorphous B, was 30 MPa hot pressed at 1500 °C for 2 h 30 min. The targets produced with amorphous B have a density of about 1.66 g/cm<sup>3</sup>, which is considerably less than the theoretical maximum of 2.66 g/cm<sup>3</sup> [8,17].

#### **AlMgB with crystalline B**

An elemental powder mixture produced using crystalline B, was 30 MPa hot pressed at 1500 °C for 2 h 30 min. The targets produced with crystalline B have a density of about 1.96 g/cm<sup>3</sup>, which is significantly less than the theoretical maximum of 2.66 g/cm<sup>3</sup> [8,17].

For producing AlCuFeB targets commercially available powder *St Gobain Cristome F1* and elemental powder mixtures could be used. The following types of targets were used for magnetron sputter deposition:

#### **AlCuFeB ceramic targets**

AlCuFeB targets that exhibit the  $\text{Al}_{59}\text{Cu}_{25.5}\text{Fe}_{12.5}\text{B}_3$  composition and the quasicrystalline structure were produced by 30 MPa hot pressing for 1 h at 700 °C. Three different types of powders were used: *St Gobain Cristome F1* powder with particle sizes ranging from 10 - 70 μm, *St Gobain Cristome F1* powder with particle sizes between 40 - 70 μm and an elemental powder mixture. The elemental powder mixture was produced by mechanical milling elemental Al, Cu, Fe and B powders weighted out according to the  $\text{Al}_{59}\text{Cu}_{25.5}\text{Fe}_{12.5}\text{B}_3$  composition. The quasicrystalline  $\text{Al}_{59}\text{Cu}_{25.5}\text{Fe}_{12.5}\text{B}_3$  targets exhibit ceramic characteristics like high brittleness as well as low thermal and electrical conductivity, which is probably due to the quasicrystalline  $\text{Al}_{59}\text{Cu}_{25.5}\text{Fe}_{12.5}\text{B}_3$  phase that develops. The quasicrystalline  $\text{Al}_{59}\text{Cu}_{25.5}\text{Fe}_{12.4}\text{B}_3$  targets have a density between 4.66 to 4.80 g/cm<sup>3</sup>, which is close to the values found in literature of 4.7 g/cm<sup>3</sup> [43].

### **AlCuFeB shifted composition targets**

Applying higher deposition powers to quasicrystalline  $\text{Al}_{59}\text{Cu}_{25.5}\text{Fe}_{12.5}\text{B}_3$  targets leads to a shift in the chemical composition of the deposited coatings. To compensate this composition shift, the following targets with an altered chemical composition were produced by 30 MPa hot pressing at 700 °C for 1 h:

- $\text{Al}_{61}\text{Cu}_{24.3}\text{Fe}_{11.8}\text{B}_{2.9}$  (*St Gobain Cristome F1 10* - 70  $\mu\text{m}$  powder + Al)
- $\text{Al}_{58.5}\text{Cu}_{24.8}\text{Fe}_{12.1}\text{B}_{4.8}$  (*St Gobain Cristome F1 10* - 70  $\mu\text{m}$  powder +  $\text{AlB}_2$ )
- $\text{Al}_{44.8}\text{Cu}_{33.5}\text{Fe}_{18.7}\text{B}_3$  (*St Gobain Cristome F1 10* - 70  $\mu\text{m}$  powder + Cu + Fe)
- $\text{Al}_{44.8}\text{Cu}_{33.5}\text{Fe}_{18.7}\text{B}_3$  (Elemental powder mixture )

### **AlCuFeB metallic targets**

AlCuFeB targets which exhibit the  $\text{Al}_{59}\text{Cu}_{25.5}\text{Fe}_{12.5}\text{B}_3$  composition but not the quasicrystalline structure were produced by 30 MPa hot pressing of an elemental powder mixture for 1 h at 500 °C. The elemental powder mixture was produced by mechanical milling elemental Al, Cu, Fe and B powders weighted out according to the  $\text{Al}_{59}\text{Cu}_{25.5}\text{Fe}_{12.5}\text{B}_3$  composition. Because of the lower hot pressing temperatures, the quasicrystalline phase cannot develop and the targets show metallic behaviour, such as good thermal and electrical conductivity, as well as magnetism. The metallic AlCuFeB targets have a density of about 4.10  $\text{g}/\text{cm}^3$ , which is slightly lower than the density of the quasicrystalline AlCuFeB targets.

Since impurities may have strong effects on the microstructure development of AlCuFe (see Section 2.3.1) and AlMgB coatings (Section 2.2.1), it's important to use high quality powders with as little impurities as possible. Especially critical is the oxygen content of the elemental powders, because they exhibit high oxygen affinity. Table 3.3 summarizes the characteristics (particle size and shape, impurities) of the powders used for target production. Back Scattered High Resolution Scanning Electron Microscope (HR-SEM) images of the powders can be seen in Figure 3.8 to Figure 3.11. The powder impurities have been estimated using Energy Dispersive X-Ray Spectroscopy (EDS). Compared to the *St Gobain Cristome F1* powder, the elemental powders contain significantly more O and C impurities. Besides the O and C impurities also other types of impurities occur. By adding the impurities of the elemental powders weighted according to the target composition, the contamination of the produced targets can be estimated. According to these considerations the AlMgB<sub>14</sub> targets are expected to contain 3 at% O and 15 at% C and the AlCuFeB targets produced with elemental powders to contain 5 at% O, 6 at% C and 1 at% N. If no impurities are incorporated during hot pressing, the AlCuFeB targets produced with *St Gobain Cristome F1* powder are expected to exhibit no significant contamination.

Table 3.3 Characteristics of the powders used for target production

Powder	Particle size [ $\mu\text{m}$ ]	Particle shape	Impurities [at%]						
			C	O	N	B	Fe	Si	Mg
Al (ECKA Granules)	10 - 350	elongated/oval long fibre-like particles	1	4	-	-	-	-	-
Cu (ECKA Granules)	1 - 90	Irregular leaf-like morphology	12	5	-	-	-	-	-
Fe (Dr. Fritsch)	3- 70	oval shaped	8	7	8	20	-	-	-
Mg (ECKA Granules)	100 – 1000	oval shaped clefts present	8	4	-	-	-	-	-
Crystalline B (ABCR)	2- 100	irregular shaped sharp-edged	12	1	-	-	-	-	-
Amorphous B (ABCR)	0.5 – 10	irregular shaped	16	2	-	-	-	-	1
AIB <sub>2</sub> (ABCR)	1 – 25	irregular shaped two different phases	9	4	-	-	11	3	-
St. Gobain Cristome F1 Al <sub>59</sub> Cu <sub>25.5</sub> Fe <sub>12.4</sub> B <sub>3</sub>	10 – 70	elliptic/circle shaped low porosity three different phases B precipitates	0.2	0.1	-	-	-	-	-
St. Gobain Cristome F1 Al <sub>59</sub> Cu <sub>25.5</sub> Fe <sub>12.4</sub> B <sub>3</sub>	40 – 70	elliptic/circle shaped high porosity three different phases B precipitates	0.2	0.1	-	-	-	-	-



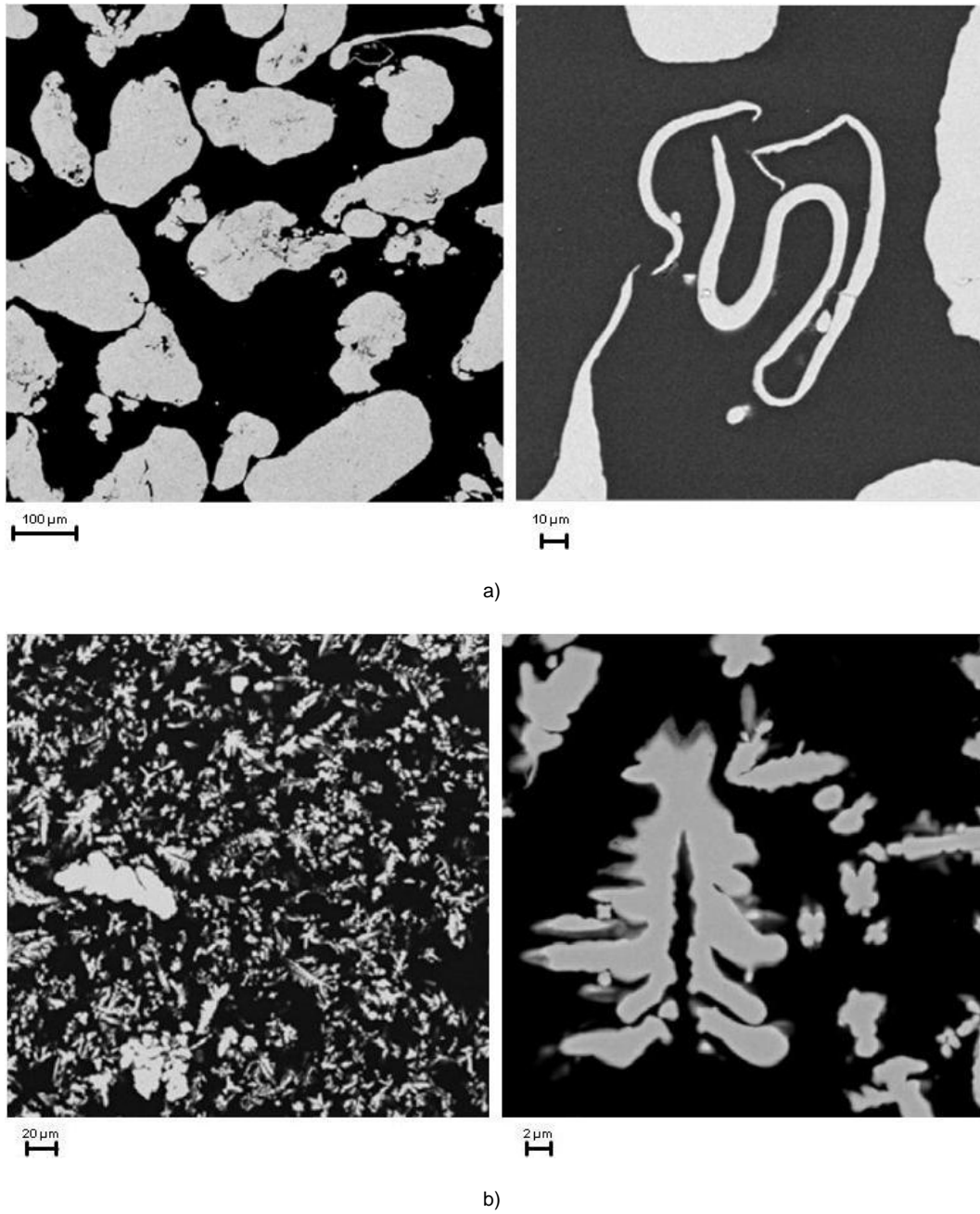


Figure 3.8 Back Scattered HR-SEM images of the powders used for target production

- a) elemental Al
- b) elemental Cu

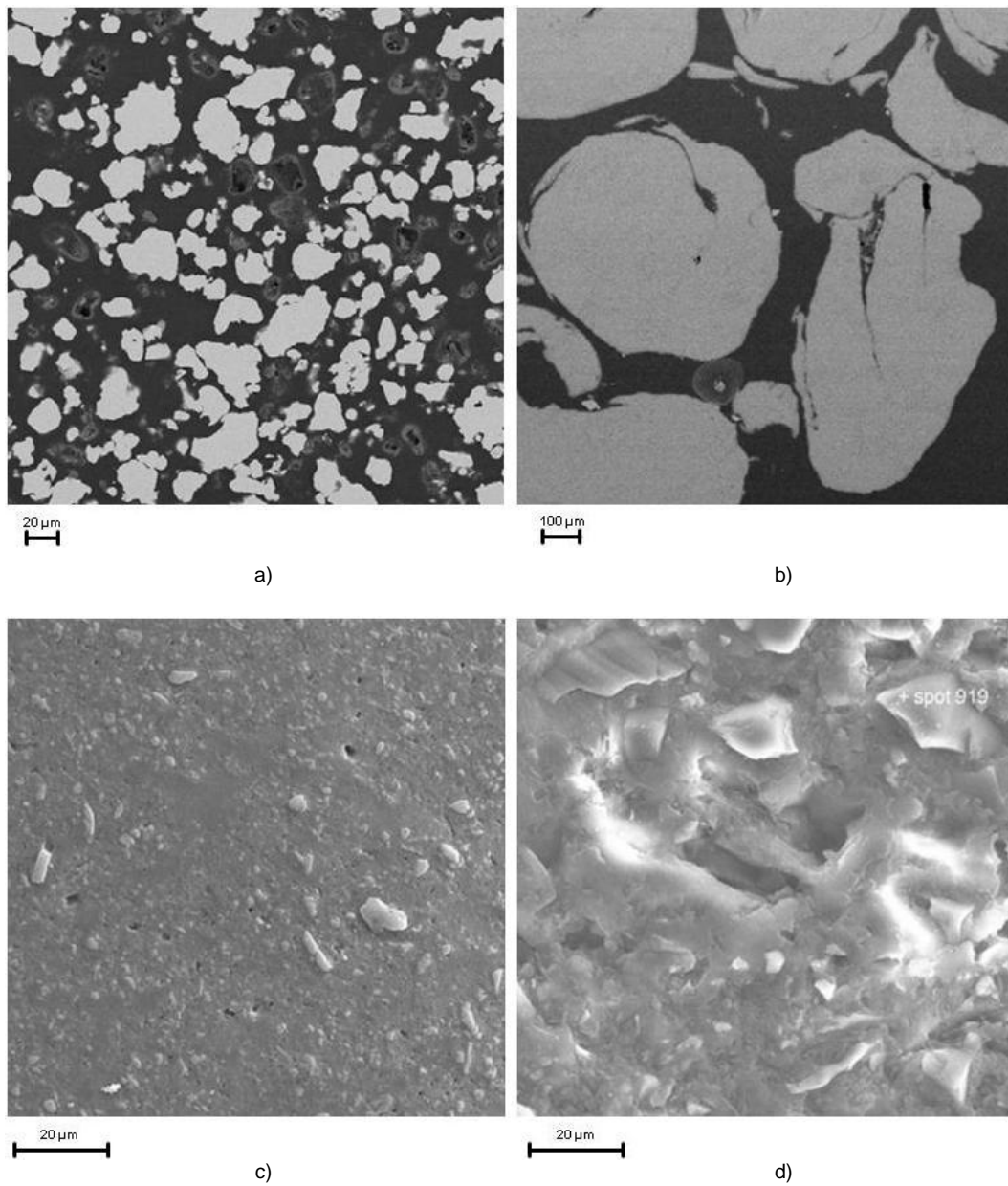


Figure 3.9 Back Scattered HR-SEM images of the powders used for target production

- a) elemental Fe
- b) elemental Mg
- c) amorphous B
- d) crystalline B

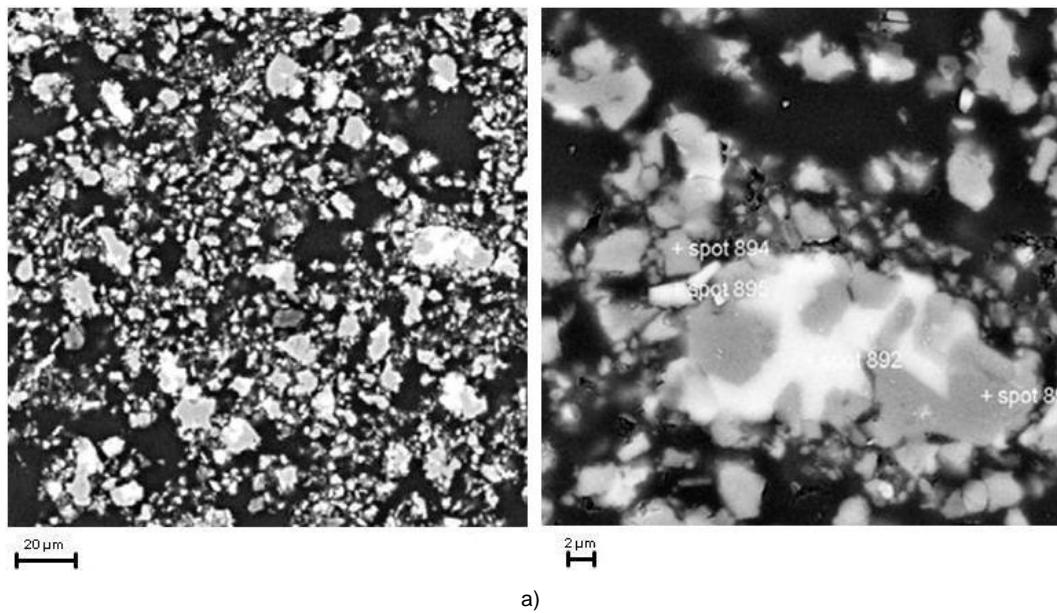


Figure 3.10 Back Scattered HR-SEM images of the  $AlB_2$  powder used for target production

Figures 3.11 a) b) represent Back Scattered High Resolution Scanning Electron Microscope (HR-SEM) images of the *St Gobain Cristome F1 10 – 70 µm* and *St Gobain Cristome F1 40 – 70 µm* powders. Figure 3.11 c) shows a high magnification HR-SEM image of one of the elliptic/circle shaped particles of the *St Gobain Cristome F1* powders. Three different phases (white, gray, black) can be clearly recognized. EDS results indicate that B accumulates mainly in precipitates (black stabs)

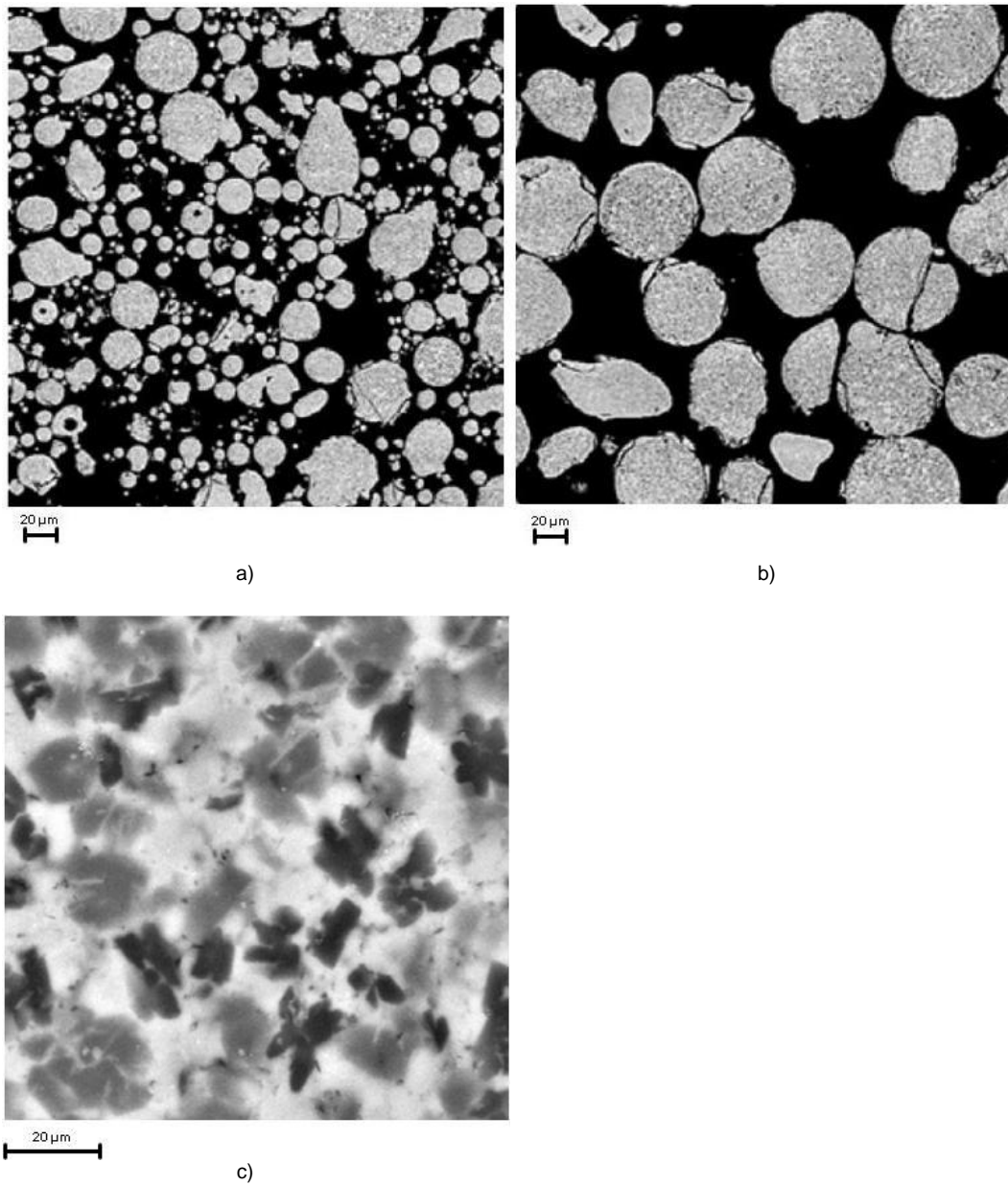


Figure 3.11 Back Scattered HR-SEM images of the powders used for target production

- a) *St Gobain Cristome F1* 10 – 70 μm
- b) *St Gobain Cristome F1* 40 – 70 μm
- c) Three phases of the elliptic/circle shaped particles of the *St Gobain Cristome F1* powders

All targets produced have a diameter of about 50 mm and a thickness of about 5 mm. Before the targets were used for coating deposition, they were subjected to an adjustment treatment for 3 x 15 min. During the adjustment treatment the targets were operated under the same process parameters as during coating deposition. This process should ensure that surface impurities of the targets are removed and that an equilibrium surface has developed before coating deposition is started. During deposition all targets were kept at room temperature by water-cooling of the magnetron sputtering source.

### 3.4 Substrates

Table 3.4 lists the different substrate types that were chosen for coating deposition. Besides the melting point, the chemical composition, the coefficient of thermal expansion and the surface roughness, which was measured with a *Taylor Hobson Surtronic 3+* profilometer and also potential applications are listed.

Table 3.4 Substrate types used for coating deposition

	Composition [wt%]	Melting point [°C]	Hardness [HV]	Thermal expansion coefficient [ $10^{-6} \text{ K}^{-1}$ ]	Average roughness Ra [nm]	Applications
WC-Co K10	94 WC 6 Co	2200	1200	5	$4.0 \pm 1.5$	cutting tools drilling tools
Steel K600	93.34 Fe 0.48 C 0.23 Si 0.40 Mn 1.30 Cr 0.25 Mo	> 870	435 – 623	11 - 14	$155.4 \pm 26.2$	coining tools cutlery dry hobbing tools, cold-shear blades
Steel K890	81.9 Fe 0.85 C 0.55 Si 0.45 Mn 4.35 Cr 2.80 Mo 2.10 V 2.55 W 4.50 Co	> 1180	615 – 864	10 - 13	$220.6 \pm 19.4$	cutting blanking cold forming compaction warm forging
Epitaxial Si n-doped	Si (1 0 0) As, P	1420	980	3	$0.6 \pm 0.2$	nano-imprint lithography
Al995	99.5 Al <sub>2</sub> O <sub>3</sub>	2050	1500	7 – 9	$519.2 \pm 29.4$	thermal insulator electrical insulator high temperature applications

All substrates except the Si substrates are disc-shaped, with a diameter of 24 mm and a thickness of about 4 mm (see Figure 3.12). The Si substrates are rectangular with a length of 20 mm, a width of 10 mm and a thickness of about 1 mm. Before usage all substrates were cleaned in an ultrasonic acetone and ethanol bath for 15 min each.

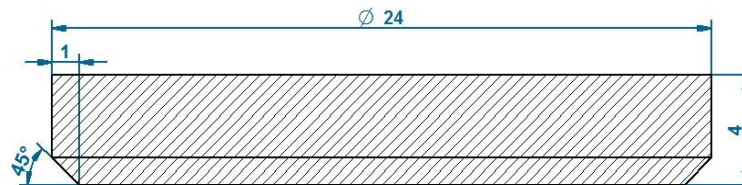


Figure 3.12 Dimensions of the disc-shaped substrates. Measures are given in mm.

Figure 3.13 shows the XRD pattern of the WC-Co K10 substrates, with the characteristic WC and Co peaks.

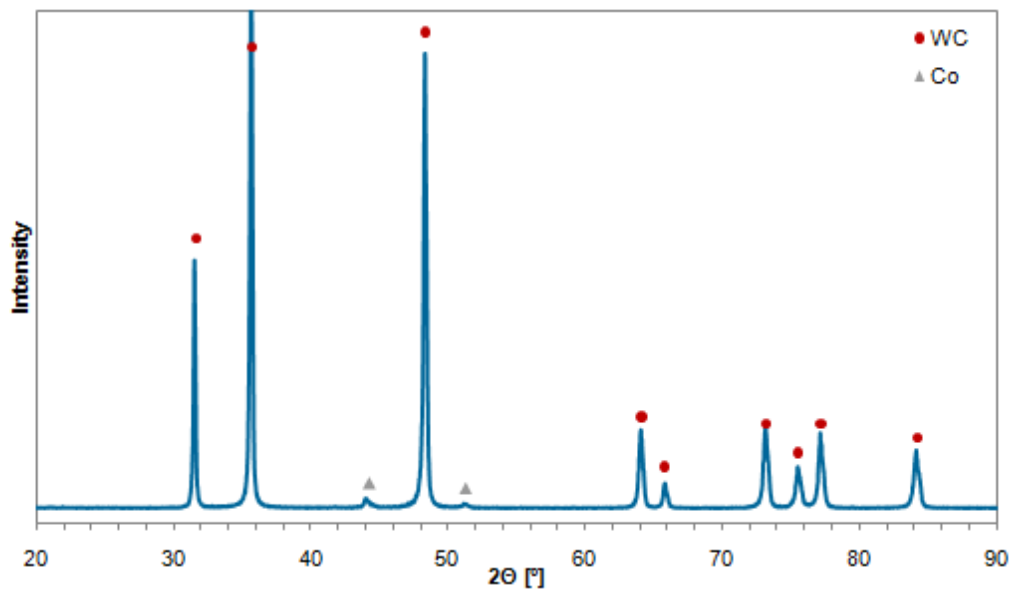


Figure 3.13 XRD pattern of the WC-Co K10 substrate (Cu anode  $\lambda = 1.542 \text{ \AA}$ )

Figure 3.14 represents the XRD pattern of the K600 steel substrate. The most prominent peaks are the ones of Fe, FeC and Cr.

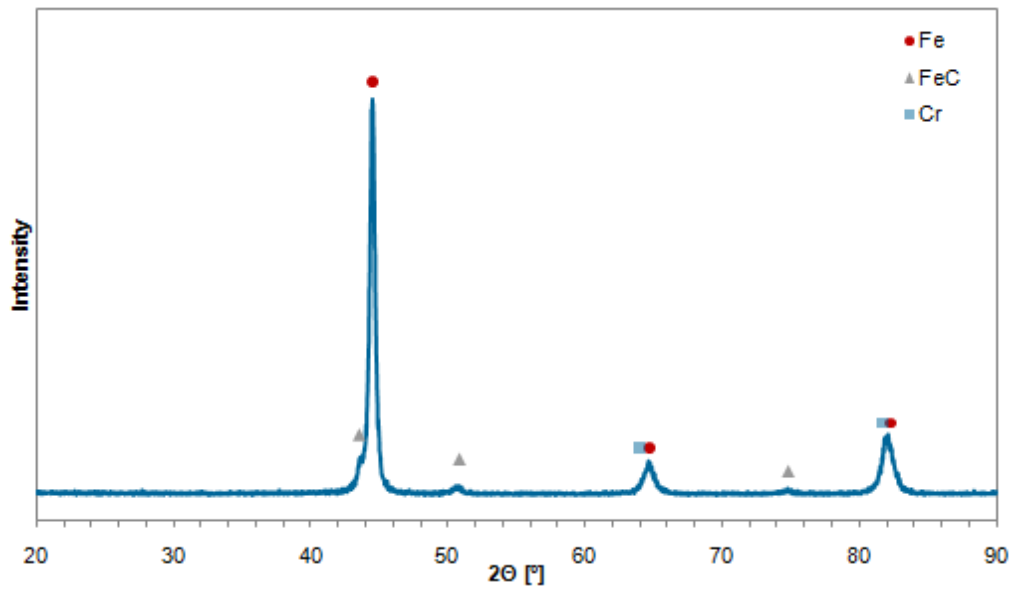


Figure 3.14 XRD pattern of the Steel K600 substrate (Cu anode  $\lambda = 1.542 \text{ \AA}$ )

Figure 3.15 displays the XRD pattern of the K890 steel substrate. The most prominent peaks are the ones of Fe, FeC, Vanadium Carbide ( $V_8C_7$ ), FeCr and  $Fe_7C_3$ .



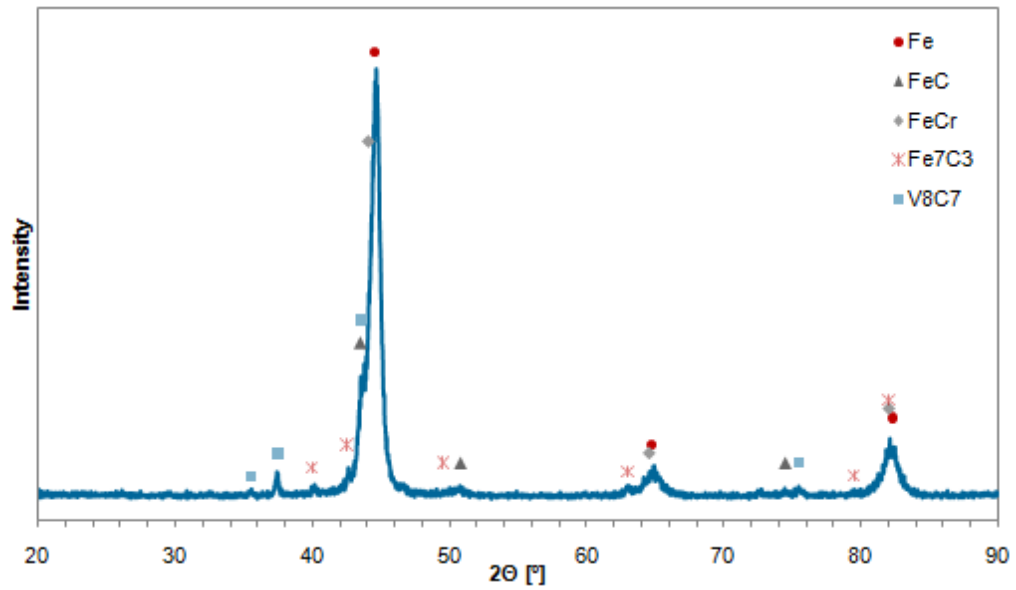


Figure 3.15 XRD pattern of the Steel K890 substrate (Cu anode  $\lambda = 1.542 \text{ \AA}$ )

Figure 3.16 exhibits the XRD pattern of the Si (1 0 0) substrate. Besides the Si peaks, also a SiO<sub>2</sub> (native oxide of the Si wafer) and P (n-type doping) peak appears.

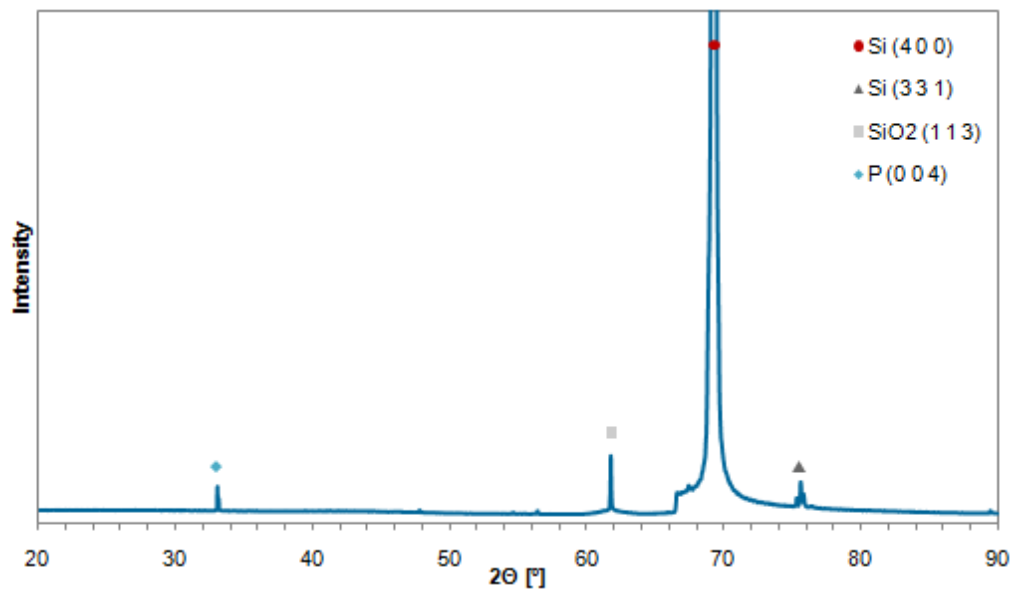


Figure 3.16 XRD pattern of the Si substrate (Cu anode  $\lambda = 1.542 \text{ \AA}$ )

According to the XRD measurement, the Al995 substrate represents a pure  $\text{Al}_2\text{O}_3$  phase (see Figure 3.17).

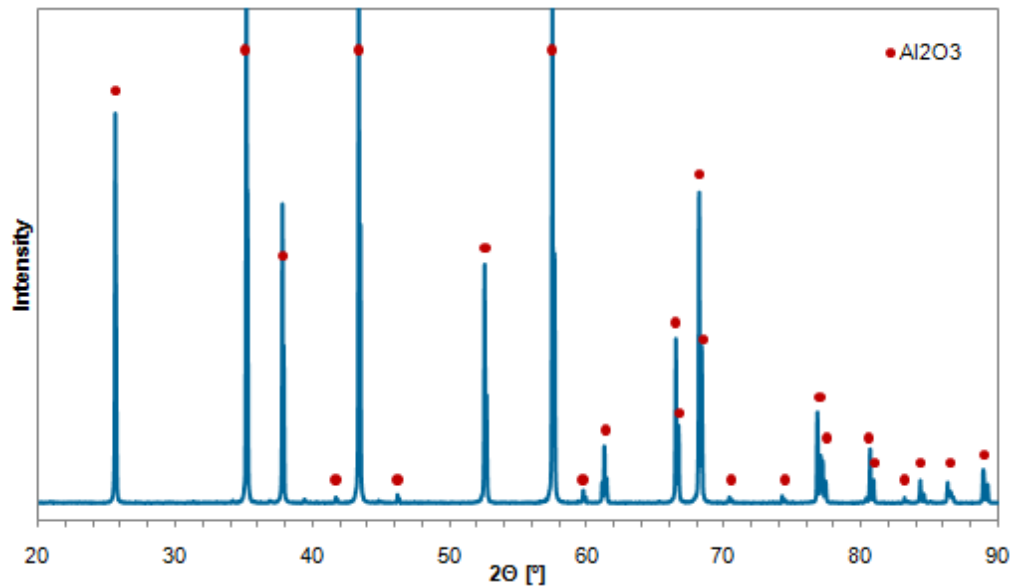


Figure 3.17 XRD pattern of the Al995 substrate (Cu anode  $\lambda = 1.542 \text{ \AA}$ )

Using Relation 2.9 (see Section 2.5.3) the thermal stresses between the deposited coatings and the substrates can be estimated. The thermal expansion coefficients of the substrates are listed in Table 3.4. For quasicrystalline AlCuFe the thermal expansion coefficient is between  $14.0$  and  $19.0 \cdot 10^{-6} \text{ K}^{-1}$  [21,45]. For  $\text{AlMgB}_{14}$  a value of  $9 \cdot 10^{-6} \text{ K}^{-1}$  can be found in literature [46]. The elastic modulus of quasicrystalline AlCuFe is about 100 GPa [2,3] and the one of  $\text{AlMgB}_{14}$  is about 210 GPa [47,48]. Table 3.5 lists the calculated thermal stresses for  $\text{AlMgB}_{14}$  and  $\text{Al}_{59}\text{Cu}_{25.5}\text{Fe}_{12.5}\text{B}_3$  coatings deposited on 600 °C substrates and cooled down to room-temperature ( $\sim 25 \text{ °C}$ ).

Table 3.5 Thermal stresses at room-temperature (25 °C) of  $\text{AlMgB}_{14}$  and  $\text{Al}_{59}\text{Cu}_{25.5}\text{Fe}_{12.5}\text{B}_3$  coatings deposited

Substrate	Thermal stress [GPa]	
	$\text{AlMgB}_{14}$	$\text{Al}_{59}\text{Cu}_{25.5}\text{Fe}_{12.5}\text{B}_3$
WC-Co K10	0.49	0.66
Steel K600	-0.43	0.23
Steel K890	-0.30	0.29
Si	0.73	0.78
A995	0.12	0.49

According to the calculated thermal stresses, it can be expected that adhesion problems occur for the following coating - substrate combinations, when deposition is done at 600 °C:  $\text{AlMgB}_{14}$  on Si,  $\text{Al}_{59}\text{Cu}_{25.5}\text{Fe}_{12.5}\text{B}_3$  on Si and  $\text{Al}_{59}\text{Cu}_{25.5}\text{Fe}_{12.5}\text{B}_3$  on WC-Co K10. Furthermore the low surface roughness of the Si (0.6 nm) and WC-Co (4 nm) substrates does not promote mechanical interlocking of the coating material with the substrate surface.

Because of the low thermal stress and the comparatively high surface roughness, which promotes mechanical interlocking, good adhesion can be expected for  $\text{Al}_{59}\text{Cu}_{25.5}\text{Fe}_{12.5}\text{B}_3$  coatings deposited on Steel K600 and Steel K890 as well as for  $\text{AlMgB}_{14}$  coatings deposited on ceramic  $\text{Al}_2\text{O}_3$  and Steel K890. Of course other parameters (e.g.: diffusion, chemical reaction, impurities, defect sites) beside surface roughness and thermal stress may have a strong influence on the interface formation and thus on adhesion (see Section 2.5).

### 3.5 Interface

Interfacial problems are mainly related to formation of diffusion based brittle interlayers and weak adhesion. To provide an improved adhesion at the interface, DC Ion etching was applied prior to deposition. Ion etching was performed by biasing the substrate negatively (700 V) relative to the plasma potential, using an inert gas (Ar) pressure of  $60 \cdot 10^{-3}$  mbar

The effects of Ion-etching include [43,44]:

1) Surface cleaning

Coating adhesion is improved by removing surface contamination, which forms diffusion barriers and precludes bond formation. The degree of surface cleanliness that can be obtained is generally limited by the purity of the working gas and out gassing from the chamber walls.

2) Defect production

If the transferred energy exceeds about 25 eV, a lattice atom may be displaced to an interstitial site and a point defect is formed (damage threshold). For less than 25 eV, the energy will all appear as heat. The combination of thermal agitation and displacement will result in the formation of dislocation networks, which increase the nucleation density and thereby minimize the formation of interface voids.

3) Crystallographic disruption

If the defects produced by ion bombardment are sufficiently immobile, the surface crystallography will be disrupted into an amorphous structure.

4) Surface morphology changes

Ion bombardment of a surface results in a wide variety of topographic changes in both crystalline and amorphous surfaces giving increased surface roughness and more nucleation sites.

To influence the film-substrate interface ion bombardment can be done also during deposition (bias sputtering). Ion bombardment of a film during deposition may cause physical mixing of the near surface regions by non-diffusion type mechanisms due to implantation of high energy particles, backscattering of sputtered atoms and recoil implantation of surface atoms. Physical mixing of the near-surface material results in a "pseudodiffusion" layer where the mixing occurs without the need for solubility or diffusion.

Transition layers might help to reduce the intensity of the strains at the interface. These interlayers should provide a gradual change of the thermal expansion coefficient and avoid diffusion between the coatings and substrates. As shown in Section 3.4, high thermal stresses are expected for the following coating - substrate combinations, when deposition is done at 600 °C: AlMgB<sub>14</sub> on Si, Al<sub>59</sub>Cu<sub>25.5</sub>Fe<sub>12.5</sub>B<sub>3</sub> on Si and Al<sub>59</sub>Cu<sub>25.5</sub>Fe<sub>12.5</sub>B<sub>3</sub> on WC-Co K10. Promising candidates for an interlayer are thus materials with a thermal expansion coefficient intermediate between Si ( $3 \cdot 10^{-6} \text{ K}^{-1}$ ), WC-Co ( $5 \cdot 10^{-6} \text{ K}^{-1}$ ) and quasicrystalline AlCuFeB ( $14.0 - 19.0 \cdot 10^{-6} \text{ K}^{-1}$ ) and AlMgB<sub>14</sub> ( $9 \cdot 10^{-6} \text{ K}^{-1}$ ). Table 3.6 lists the materials, which were tested as a possible interlayer.

Table 3.6 Possible interlayer materials and their thermal expansion coefficient (values taken from [49])

Material	Coefficient of thermal expansion [ $10^{-6} \text{ K}^{-1}$ ]
Chrome (Cr)	6.6
Copper (Cu)	9.8
Titanium (Ti)	9.8
Manganese (Mn)	13.0
Nickel (Ni)	13.0

### 3.6 Chemical analysis (EDS)

As there is no accurate phase diagram available for AlMgB<sub>14</sub>, no error margins for the composition can be defined and a composition as close as possible is targeted. As no quaternary phase diagram of the AlCuFeB system is available, the desired composition to obtain quasicrystalline Al<sub>59</sub>Cu<sub>25.5</sub>Fe<sub>12.5</sub>B<sub>3</sub> is normalized to the AlCuFe phase diagram. This is a valid simplification, since the quasicrystalline Al<sub>59</sub>Cu<sub>25.5</sub>Fe<sub>12.5</sub>B<sub>3</sub> is obtained by substitution of 3 at% Al in the quasicrystalline Al<sub>62</sub>Cu<sub>25.5</sub>Fe<sub>12.5</sub> phase by boron atoms. These boron atoms are located outside the icosahedral unit cell, forming a second phase (precipitates) with Al, Cu and Fe [3]. Thus the boron atoms do not affect the formation of the icosahedral Al<sub>59</sub>Cu<sub>25.5</sub>Fe<sub>12.5</sub>B<sub>3</sub> phase and a margin of error for the chemical composition can be defined with the help of the AlCuFe phase diagram. (see Figure 2.7 and Figure 2.8 in Section 2.3). The margin of error in the quasicrystalline AlCuFe composition approximately can be given as Al<sub>62</sub>Cu<sub>25.5</sub>Fe<sub>12</sub>. (at%), with  $\pm 2.5$  at% Al,  $\pm 3.5$  at% Cu,  $\pm 1.5$  at% Fe. If the chemical composition of the formed phase differs too much from the Al<sub>62</sub>Cu<sub>25.5</sub>Fe<sub>12</sub> composition, other crystallographic phases ( $\beta$ ,  $\omega$ ,  $\lambda$ ) will form, which exhibit less favourable tribological properties as the icosahedral phase. Thus high accuracy in the chemical composition is necessary to reach the correct Al<sub>59</sub>Cu<sub>25.5</sub>Fe<sub>12.5</sub>B<sub>3</sub> phase, which also requires a precise chemical analysis of the deposited coatings. Energy Dispersive X-Ray Spectroscopy (EDS) is a well known and reliable technique for chemical analysis, which allows comparatively fast access to sample compositions. While EDS does not require extensive sample preparation, it is limited in accuracy for quantification. Especially for elements with low atomic number (Z) like boron (Z=5) quantification becomes problematic. The reason lies within two phenomena [50,51]:

#### 1) Emission of x-rays

For elements with  $Z < 30$  the emission of Auger electrons is more likely than the emission of characteristic x-rays that are detected by EDS. This can be seen by calculating the ratio of the x-ray yield to the Auger yield, given by the following relationship:

$$\frac{Y_{x\text{-ray}}}{Y_{Auger}} = (-6.4 \cdot 10^{-2} + 3.4 \cdot 10^{-2} Z - 1.03 \cdot 10^{-6} Z^3)^4 \quad (3.1)$$

*Z... atomic number*

*Y<sub>x-ray</sub>... yield for x-ray emission*

*Y<sub>Auger</sub>... yield for Auger electron emission*

The ratio between x-ray and Auger yield is especially low for B (2 order of magnitudes lower than for Al, Fe and Cu), which means that B hardly emits any characteristic x-rays (see Table 3.7).

Table 3.7 Ratio between x-ray and Auger yield for B, Al, Fe, Cu

Element (atomic number)	$Y_{x\text{-ray}}/Y_{\text{Auger}}$
B (Z=5)	0.000126
Al (Z=13)	0.0199
Fe (Z=26)	0.4135
Cu (Z=29)	0.6471

## 2) Self absorption of characteristic x-rays

On their way to the detector, the emitted characteristic x-rays have to pass through the sample, where they can get absorbed by the sample constituents. The characteristic x-ray lines and the according energies used for EDS element analysis are listed in Table 3.8 for Al, Cu, Fe, Mg and B (values taken from the EDS measurement software EDAX Genesis Spectrum 5.21, EDAX Inc.).

Table 3.8 Characteristic x-ray lines and the according energies used for EDS element analysis (values taken from the measurement software)

Element	Line	Wavelength $\lambda$ [nm]	Energy [eV]
Al	K $\alpha$	0.832	1490
Al	K $\beta$	0.795	1560
Cu	K $\alpha$	0.154	8050
Cu	K $\beta$	0.139	8910
Fe	K $\alpha$	0.176	7050
Fe	K $\beta$	0.194	6400
Mg	K $\alpha$	0.992	1250
Mg	K $\beta$	0.961	1290
B	K $\alpha$	6.53	190

Table 3.9 shows the calculated [50,51] x-ray absorption coefficients of Al, Fe, Cu, Mg and B for the characteristic x-ray lines listed in Table 3.8. If the absorption coefficients are displayed relative to the highest absorption coefficients that occurs (Table 3.10), it is obvious that the absorption for the B K $\alpha$  line is considerably higher than for all other lines. As a consequence only B atoms, which are located on the surface, contribute to the measured EDS spectra. Furthermore the vast differences in the B K $\alpha$  absorption coefficients of the different coating constituents (very high for Al and Mg, very small for Cu and Fe) cause a strong dependence of the B peaks on the chemical environment of the B atoms. For example, if a boron atom is located next to Al atoms, its peak will very likely be absorbed and thus be missing in the EDS spectra.

Table 3.9 Absorption coefficients of the coating constituents for the different characteristic X-rays

Element	Line	Absorption coefficients [cm <sup>-1</sup> ]				
		Al	Cu	Fe	Mg	B
Al	K $\alpha$	1089.6	45913.2	27640.6	6917.1	889.0
Al	K $\beta$	11538.5	40671.6	24637.8	6206.0	777.1
Cu	K $\alpha$	135.5	459.3	2338.5	70.9	5.0
Cu	K $\beta$	100.4	346.0	1797.2	52.3	3.7
Fe	K $\alpha$	200.0	665.0	420.4	105.1	7.5
Fe	K $\beta$	265.0	870.8	553.8	139.8	10.1
Mg	K $\alpha$	1738.9	72821.5	42691.6	917.6	1468.6
Mg	K $\beta$	1597.7	67059.4	39513.9	840.8	1343.1
B	K $\alpha$	524126.2	8.6	7.5	405438.2	129148.1



Table 3.10 Relative absorption coefficients of the coating constituents for the different characteristic X-rays

Element	Line	Absorption coefficients [%]				
		Al	Cu	Fe	Mg	B
Al	K $\alpha$	0.21	8.76	5.27	1.32	0.17
Al	K $\beta$	2.20	7.76	4.70	1.18	0.15
Cu	K $\alpha$	0.03	0.09	0.45	0.01	0.00
Cu	K $\beta$	0.02	0.07	0.34	0.01	0.00
Fe	K $\alpha$	0.04	0.13	0.08	0.02	0.00
Fe	K $\beta$	0.05	0.17	0.11	0.03	0.00
Mg	K $\alpha$	0.33	13,89	8.15	0.18	0.28
Mg	K $\beta$	0.30	12,79	7.54	0.16	0.26
B	K $\alpha$	100	0.00	0.00	77.36	24.64

Because of the unreliable quantification and the small B content of the  $\text{Al}_{59}\text{Cu}_{25.5}\text{Fe}_{12.5}\text{B}_3$  samples, their boron content was not determined by EDS but assumed to be 3 at%. This is regarded as a valid simplification, since the B atoms do not affect the formation of the icosahedral  $\text{Al}_{59}\text{Cu}_{25.5}\text{Fe}_{12.5}\text{B}_3$  phase. To improve the quantification accuracy, a reference  $\text{Al}_{59}\text{Cu}_{25.5}\text{Fe}_{12.5}\text{B}_3$  sintered bulk was prepared by *Centre National de la Recherche Scientifique CNRS, France* with *St Gobain Cristome F1* 10-70  $\mu\text{m}$  powder and examined by ICP-MS (Inductively Coupled Plasma Mass Spectroscopy) at the *Austrian Institute of Technology AIT*. ICP-MS is a highly sensitive analytical technique capable of very accurate quantitative analysis at concentrations below one part in  $10^{12}$ . Afterwards an EDS measurement of the same reference sample was done and correction factors for the EDS system (*FEI Quanta 200 FEG*) were calculated (see Table 3.11). Due to the high boron content of  $\text{AlMgB}_{14}$  (87.5 at%), the amount of boron in the  $\text{AlMgB}_{14}$  targets and coatings could be assessed by EDS.

Table 3.11 Correction factors for the EDS measurements (*FEI Quanta 200 FEG*), determined by analysing the composition of a  $\text{Al}_{59}\text{Cu}_{25.5}\text{Fe}_{12.5}\text{B}_3$  sintered bulk reference by ICP-MS and EDS

	Al	Cu	Fe
Correction factors [wt%]	0.976	1.051	0.945

Figure 3.18 shows the composition of the  $\text{Al}_{59}\text{Cu}_{25.5}\text{Fe}_{12.5}\text{B}_3$  reference bulk in at% as measured and after applying the correction factors.

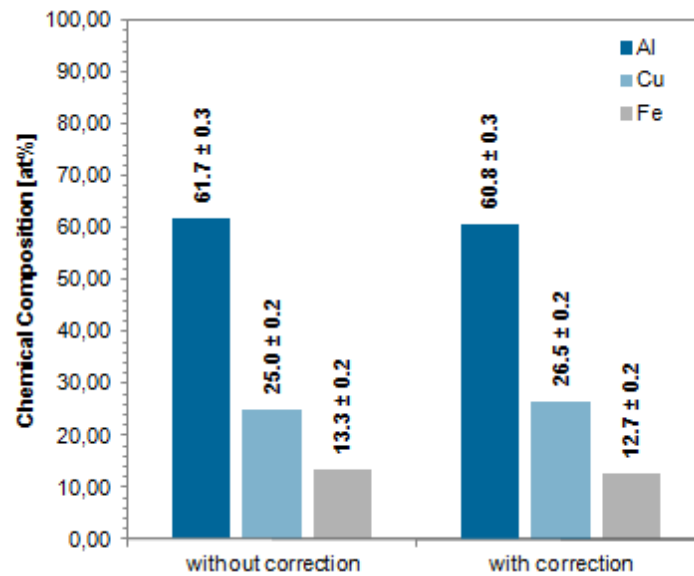


Figure 3.18 Chemical composition of the  $\text{Al}_{59}\text{Cu}_{25.5}\text{Fe}_{12.5}\text{B}_3$  reference sample in at% as measured and after applying the correction factors

To investigate the target and coating compositions, EDS measurements of 5 areas of  $0.78 \text{ mm}^2$  on each target/coating were made (see Figure 3.19). While the mean value of the five  $0.78 \text{ mm}^2$  areas represents the average coating composition, the standard deviation, gives information about the homogeneity of the targets and coatings.

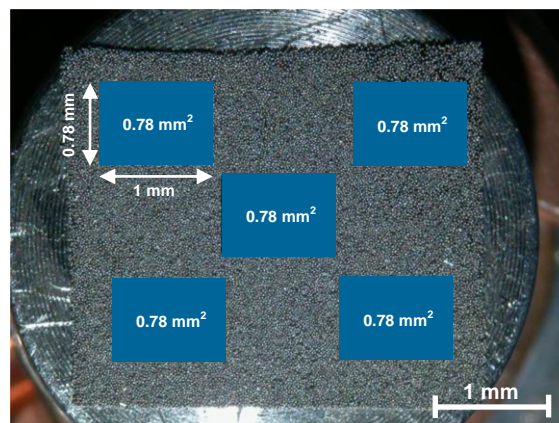


Figure 3.19 EDX mapping of targets and coatings

EDS measurements were done with a *FEI Quanta 200 FEG*, using the operating parameters listed in Table 3.12. All coatings examined by EDS had a thickness of at least 5  $\mu\text{m}$ . On all EDS results, the correction factors listed in Table 3.11 were applied. While the results for the AlCuFeB samples were normalized to 97 at%, the results for the AlMgB samples were normalized to 100 at%.

Table 3.12 EDS parameters used for chemical analysis of the targets and coatings (FEI Quanta 200 FEG)

Area of analysis	Magnification	Accelerating voltage	Aperture	Spot size	Dead time	Working distance	Acquisition time
5 x 0.78 mm <sup>2</sup>	350 x	20 kV	30 $\mu\text{m}$	4	25-30 %	11 mm	50 s

### 3.7 Microstructure analysis (XRD)

To reach the desired microstructure, coatings can be heated during deposition or after deposition (post annealing). Besides heating the microstructure of deposited films can also be modified by ion bombardment during deposition (bias sputtering). Bias sputtering is the process of maintaining a negative bias on the substrate during deposition. It is particularly effective when the sputter cleaning process (ion etching) is simply continued after the formal coating process has been started (usually at reduced bias potential). Ion bombardment of a film during deposition may cause [43,44]:

- 1) Temperature rise  
Most of the energy of bombarding particles appears as surface heating.
- 2) Enhanced diffusion  
The high defect concentration and temperature of the near surface region will enhance the diffusion rates.
- 3) Morphology  
Increased surface mobility, enhanced bulk diffusion and enhanced recrystallisation will affect the morphology of the deposited films.
- 4) Crystallography  
Ion bombardment on uncooled substrates yields typical high temperature structures, by creating nucleation sites for arriving coating atoms, or by eroding surface roughness peaks and redistributing material into valleys.
- 5) Physical properties  
Ion bombardment during deposition may increase intrinsic stress by forcing atoms into non-equilibrium sites or may decrease stress by enhancing stress relief mechanisms such as diffusion and recrystallisation.
- 6) Preferential removal of loosely bound atoms  
Bias sputtering at low ion energies (<200 eV) is often used to improve the purity of growing coatings by removing loosely bonded impurity atoms. The process is effective because such atoms have a high sputtering yield and thus are preferentially sputtered by the low energy ions.

The disadvantage of bias sputtering is that it may change the chemical content of the coating by preferential sputtering and that inert gas ions tend to become incorporated in the deposited coatings (few atomic percents), which might cause blistering of the coating.

The crystallographic structure of the  $\text{Al}_{59}\text{Cu}_{25.5}\text{Fe}_{12.5}\text{B}_3$  and  $\text{AlMgB}_{14}$  targets and coatings was examined by X-Ray Diffraction (XRD). For XRD an X-ray spectrometer *Philips X'Pert* with a *Philips PW 3020/60* generator, a *Philips PW 3050/60* goniometer and a Cu anode ( $\lambda = 1.542 \text{ \AA}$ ) was used. All films analysed by XRD had a thickness of at least  $5 \mu\text{m}$ .

XRD can be used to characterise the crystallographic structure, crystallite size (grain size), and preferred orientation in polycrystalline samples. Unknown substances are commonly identified by comparing the measured diffraction data against a database maintained by the International Centre for Diffraction Data. XRD is based on the elastic scattering of x-rays from the electron clouds of the individual atoms in the system, whereby the scattered intensity of an x-ray beam hitting a sample as a function of incident and scattered angle is observed. For diffraction applications, only short wavelength X-rays (hard X-rays) in the range of a few angstroms to 0.1 angstrom (1 keV – 120 keV) are used. Because the wavelength of x-rays is comparable to the size of atoms, they are ideally suited for probing the structural arrangement of atoms and molecules in a wide range of materials. In laboratory instruments X-rays are generally produced by X-ray tubes using Cu, Mo or Co targets. X-rays primarily interact with electrons in atoms. When X-ray photons collide with electrons, some photons from the incident beam will be deflected away from the direction where they originally travel. If the wavelength of these scattered X-rays does not change, only momentum is transferred in the scattering process (no energy loss) and the process is called elastic scattering (Thompson Scattering). Diffracted waves from different atoms can interfere with each other and if the atoms are arranged periodically, the diffracted waves will consist of sharp interference maxima (peaks) with the same symmetry as in the distribution of atoms. Periodically arranged atoms can be considered to form different sets of lattice planes in the crystal, with an interplane distance of  $d$ . If an incident X-ray beam (wavelength  $\lambda$ ) interacts with those lattice planes, the condition for a diffraction peak to occur is simply the Bragg's law:

$$2d \sin \theta = n\lambda \quad (3.2)$$

*d... distance between lattice planes*

*$\theta$ ... scattering angle*

*n... integer representing the order of the diffraction peak*

*$\lambda$ ... x-ray wavelength*

Thus the peaks in an X-ray diffraction pattern are directly related to the atomic distances and measuring the diffraction pattern allows to deduce the distribution of atoms in a material. While the peak positions are indicative of the crystal structure and symmetry of the contributing phase, peak intensities represent the total scattering from each plane in the phase's crystal structure, and are related to both the structure and composition of the phase. The peak broadening in diffraction patterns can be related to crystallite sizes less than  $\sim 0.5 \mu\text{m}$ . To correlate the crystallite size to the broadening of a peak, the Scherrer equation can be used:

$$\tau = \frac{K\lambda}{\beta \cos\theta} \quad (3.3)$$

$\tau$ ... mean grain size

$K$ ... shape factor

$\lambda$ ... x-ray wavelength

$\beta$ ... line broadening at half the maximum intensity in radians

$\theta$ ... Bragg angle

The shape factor  $K$  is a constant and has a typical value of about 0.9, but varies with the actual shape of the crystallite. Because a variety of factors can contribute to the width of a diffraction peak, the Scherrer formula provides only a lower bound for the grain size. Besides crystallite size, inhomogeneous strain within the crystal lattice and instrumental effects influence peak broadening. More details on X-ray diffraction can be found in [52-55].

To determine if the targets and the deposited coatings contain the icosahedral  $\text{Al}_{59}\text{Cu}_{25.5}\text{Fe}_{12.5}\text{B}_3$  phase, the XRD pattern of the reference  $\text{Al}_{59}\text{Cu}_{25.5}\text{Fe}_{12.5}\text{B}_3$  bulk prepared by CNRS (see Figure 3.20) was used. Further an  $\text{Al}_{50}\text{Cu}_{40}\text{Fe}_{10}$   $\beta$  phase (see Figure 3.20) reference sample produced by CNRS was used to determine the existence of the  $\beta$  phase, which is important since the tribological properties of the  $\beta$  phase are less favourable than the one of the icosahedral phase.

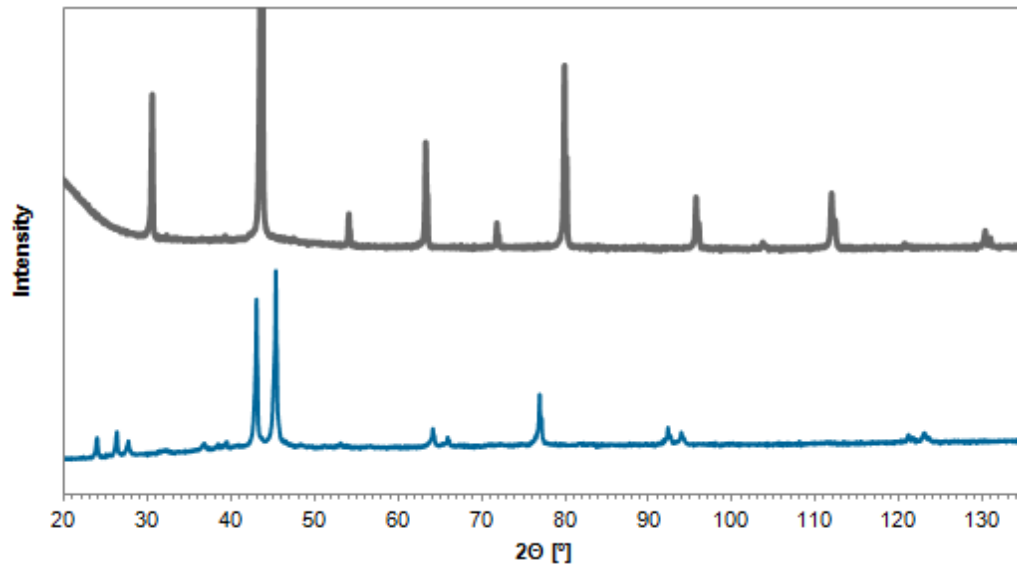


Figure 3.20 XRD pattern of the quasicrystalline  $\text{Al}_{59}\text{Cu}_{25.5}\text{Fe}_{12.5}\text{B}_3$  reference sample and the  $\text{Al}_{50}\text{Cu}_{40}\text{Fe}_{10}$   $\beta$  phase (Cu anode  $\lambda = 1.542 \text{ \AA}$ )

The XRD pattern of the reference sample is in agreement with results found in literature [2] (see Figure 3.21)

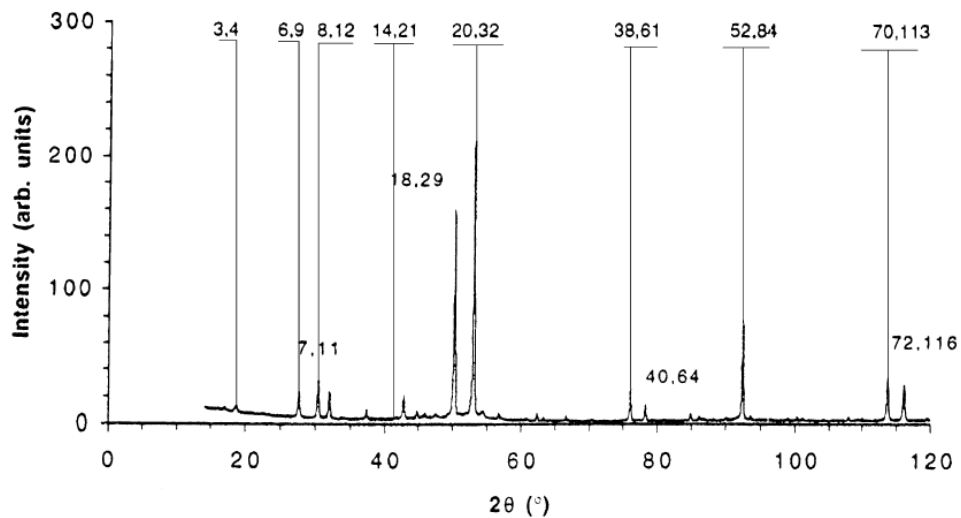


Figure 3.21 X-ray diffraction pattern Co anode ( $\lambda = 1.7889 \text{ \AA}$ ) obtained from the polished surface of a  $\text{Al}_{59}\text{Cu}_{25.5}\text{Fe}_{12.5}\text{B}_3$  sinter bulk [2]

Since no  $\text{AlMgB}_{14}$  reference sample was available, XRD patterns found in literature [9,18] had to be used as a reference for identifying the  $\text{AlMgB}_{14}$  phase in the targets and the deposited coatings (see Figure 3.22).

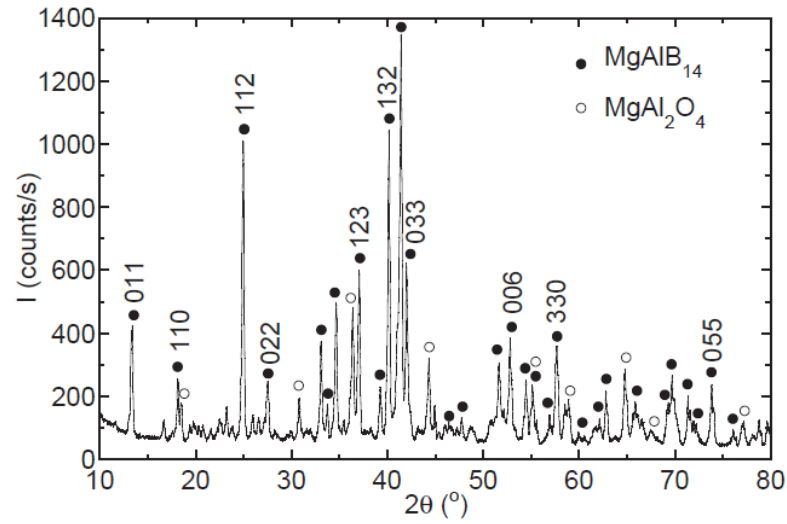


Figure 3.22 XRD pattern of  $\text{AlMgB}_{14}$  (Cu anode  $\lambda = 1.542 \text{ \AA}$ ) [9]



## 4. Results

### 4.1 AlMgB<sub>14</sub>

#### 4.1.1 Targets

Two AlMgB targets with amorphous and two with crystalline boron were produced and used for coating deposition. The average chemical composition of the targets produced with amorphous B is  $4.9 \pm 0.7$  at% Al,  $4.2 \pm 0.1$  at% Mg,  $90.9 \pm 0.8$  at% B. The average chemical composition of the targets produced with crystalline B is  $4.5 \pm 0.9$  at% Al,  $4.4 \pm 0.2$  at% Mg,  $91.1 \pm 1.1$  at% B. The targets show  $\sim 7$  at% O and  $\sim 7$  at% C on the surface. Figure 4.1 compares the average target compositions, measured by EDS with the nominal AlMgB<sub>14</sub> composition.

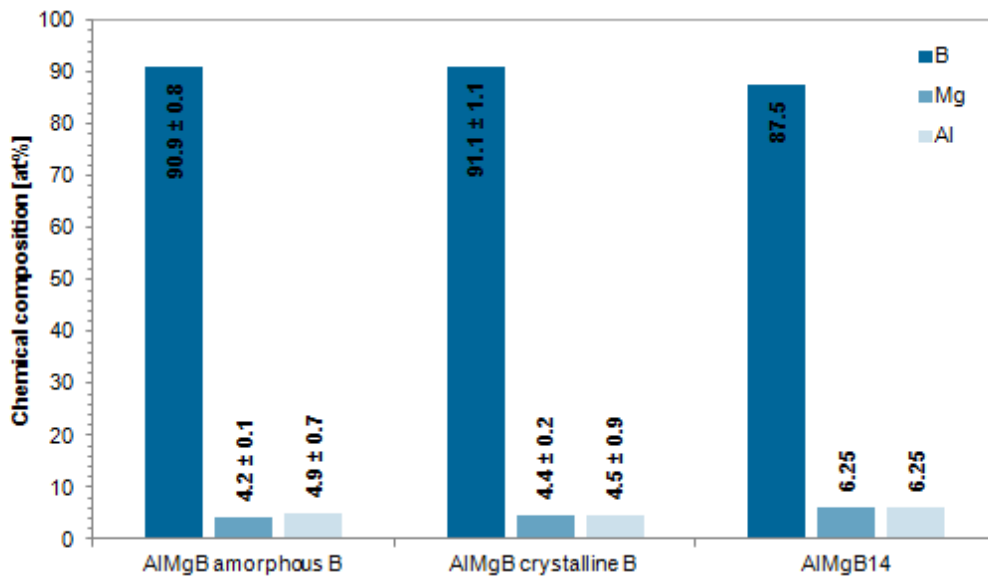


Figure 4.1 Chemical composition of the AlMgB targets in comparison with the nominal AlMgB<sub>14</sub> composition

Figure 4.2 and Figure 4.3 show Scanning Electron Microscope (SEM) images with different magnification of the AlMgB target surfaces. The AlMgB target surfaces exhibit a very high surface roughness and a high density of pores, with diameters up to some micrometers. For both types of boron powder (amorphous and crystalline) the AlMgB targets show surface features, which are similar to those of the crystalline B powder (see Figure 3.9 d in Section 3.3).

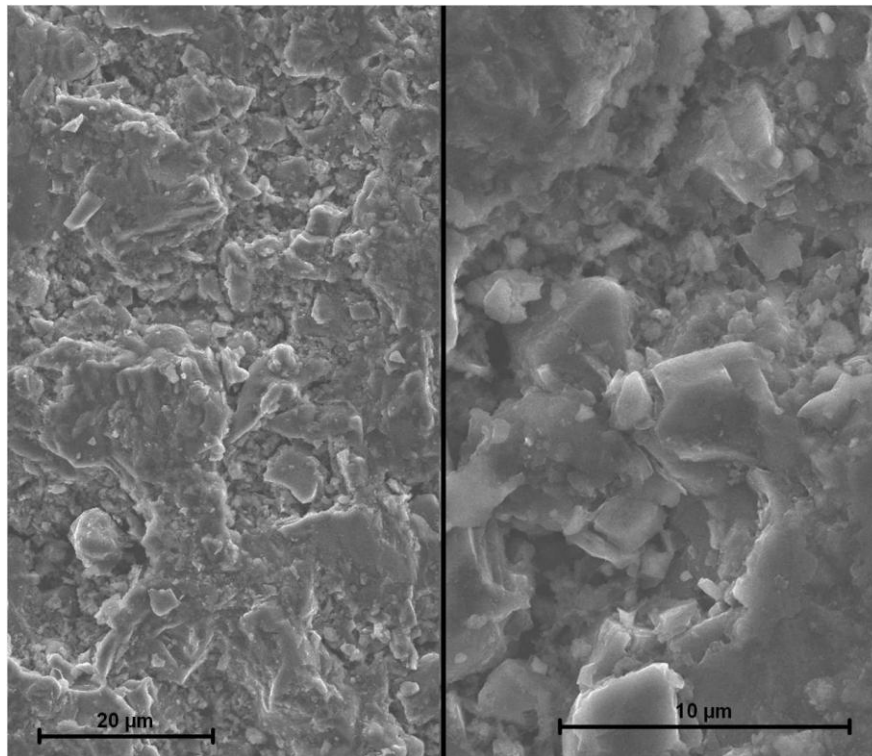


Figure 4.2 Surface of the AlMgB target with amorphous boron (secondary electron SEM)

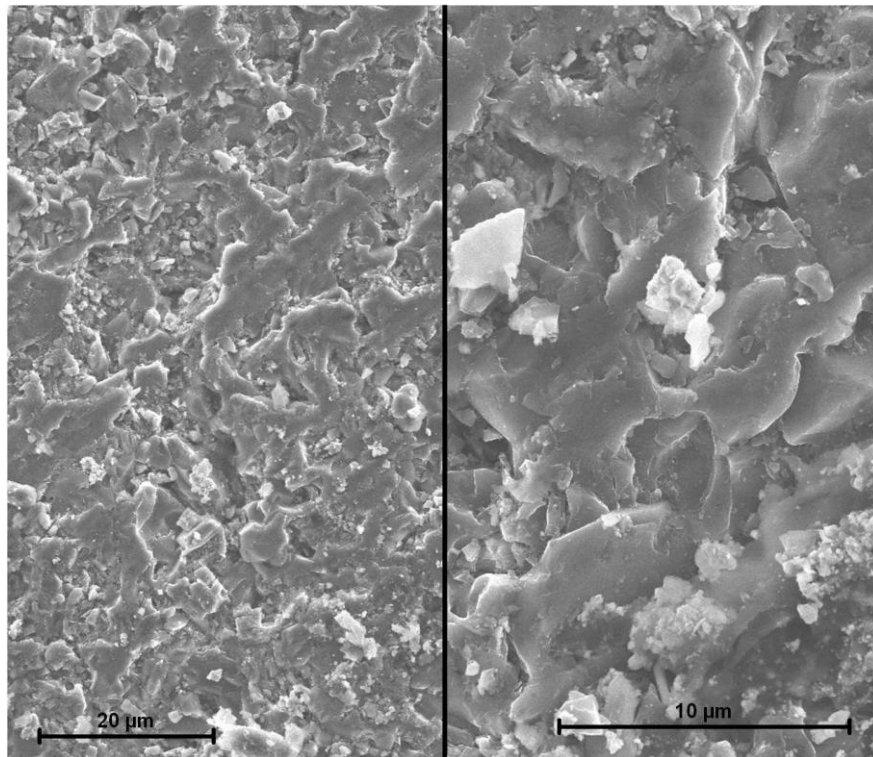


Figure 4.3 Surface of the AlMgB target with crystalline boron (secondary electron SEM)

The cross section images (Figure 4.4 and Figure 4.5) of the AlMgB targets exhibit two different phases. According to EDS measurements, the composition of the light gray phase corresponds to the  $\text{Al}_2\text{MgO}_4$  composition, while the dark gray phase exhibits approximately the  $\text{AlMgB}_{14}$  composition. The  $\text{Al}_2\text{MgO}_4$  phase is present in the form of particles with diameters less than  $3\ \mu\text{m}$ , which are homogeneously distributed throughout the target. The cross section images of the AlMgB targets reveal very porous structures. The target with amorphous B shows a higher density of pores than the target produced with crystalline B.

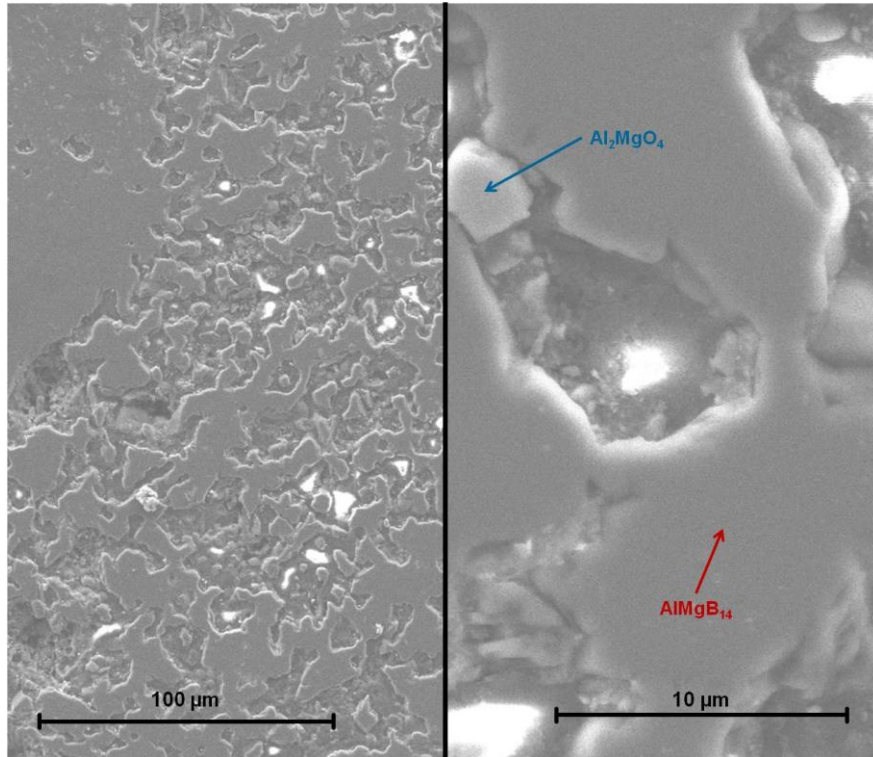


Figure 4.4 Cross section of the AIMgB target with amorphous boron (secondary electron SEM)

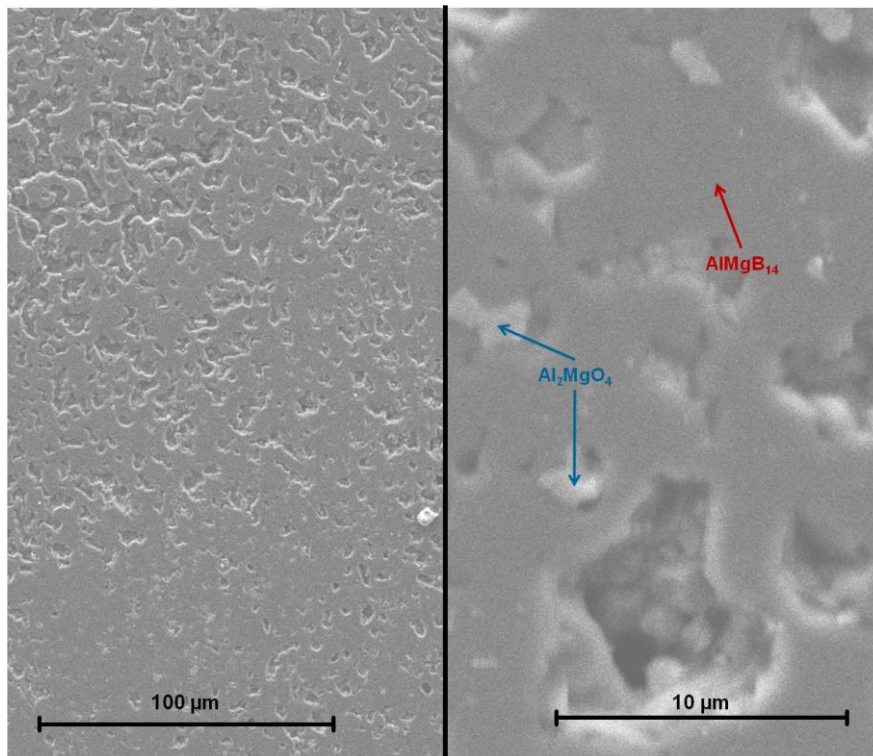


Figure 4.5 Cross section of the AIMgB target with crystalline boron (secondary electron SEM)

Figure 4.6 shows the XRD pattern of the two AlMgB target types from 20° to 90°. Both targets contain the AlMgB<sub>14</sub> phase as well as an Al<sub>2</sub>MgO<sub>4</sub> phase.

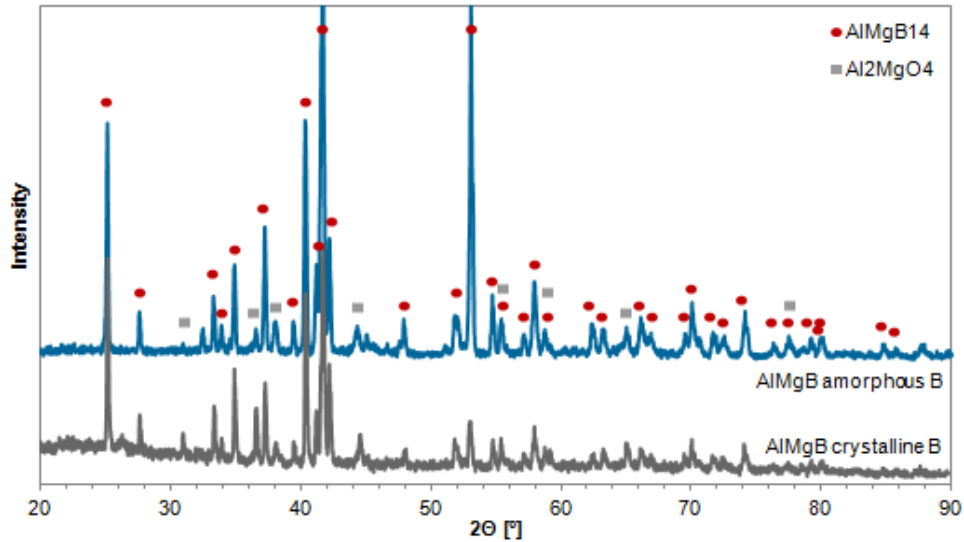


Figure 4.6 XRD pattern of the AlMgB targets

Since the AlMgB targets show a high electrical resistivity (1.13 Ωm), RF magnetron sputtering has to be used for coating deposition. During deposition all AlMgB targets suffer from crack formation, which occurs even if the applied deposition power does not exceed 25 W (3.8 W/cm<sup>2</sup>). Crack formation is more severe for the targets produced with crystalline boron (see Figure 4.7).

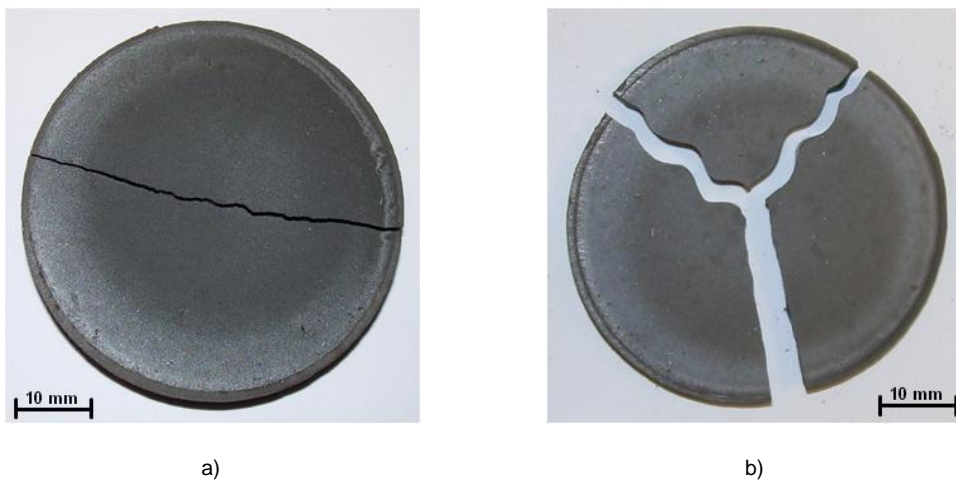


Figure 4.7 Crack formation in the AlMgB targets  
 a) Target produced with amorphous B after applying 25 W (3.8 W/cm<sup>2</sup>)  
 b) Target produced with crystalline B after applying 25 W (3.8 W/cm<sup>2</sup>)

### 4.1.2 Coatings

Because the AlMgB targets exhibit a low electrical conductivity, RF magnetron sputtering has to be used for coating deposition. The Ar pressure was  $4 \cdot 10^{-3}$  mbar, which represents the lowest working gas pressure for which a stable plasma could be achieved. All coatings used for EDS and XRD measurements had a thickness of  $\sim 5 \mu\text{m}$ . The substrate – target distance was 3 cm. For both AlMgB target types, the deposition rates achieved are very low. In a range of 25 W RF ( $3.8 \text{ W/cm}^2$ ) to 100 W RF ( $15.2 \text{ W/cm}^2$ ) the deposition rate ( $D$ ) increases linearly with the applied deposition power ( $P$ ) (see Figure 4.8). For the AlMgB targets with amorphous boron the following relation can be obtained by a linear fit:  $D = 2.5 \text{ nm/min} + 0.19 \text{ nm}/(\text{min W}) P$  and for the targets with crystalline B:  $D = -2 \text{ nm/min} + 0.24 \text{ nm}/(\text{min W}) P$ . Because of the very low deposition rates at low deposition powers, all AlMgB coatings were deposited using 100W RF ( $15.2 \text{ W/cm}^2$ ). In order to avoid more severe crack formation, not more than 100 W RF was applied.

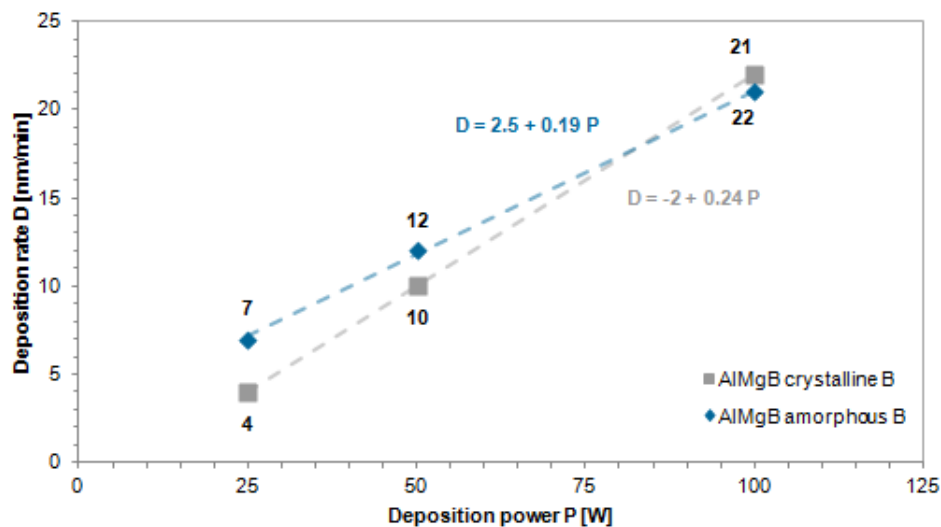


Figure 4.8 Deposition rate in dependence on the deposition power for the AlMgB targets

The coatings deposited using an AlMgB target with amorphous B show an average composition of  $2.7 \pm 0.8$  at% Al,  $1.4 \pm 0.6$  at% Mg,  $95.9 \pm 1.4$  at% B. Compared to the target the coatings show 2.2 at% less Al, 2.8 at% less Mg and 5 at% more B (see Figure 4.9). The coating deposited with 25 W ( $3.8 \text{ W/cm}^2$ ) contains the most O ( $\sim 9$  at%) and C ( $\sim 2.5$  at%). The amount of O and C impurities decreases with increasing deposition power/deposition rate. A comparison of the measured O and C amount with the estimated impurity content can be found in Section 5.1.2.

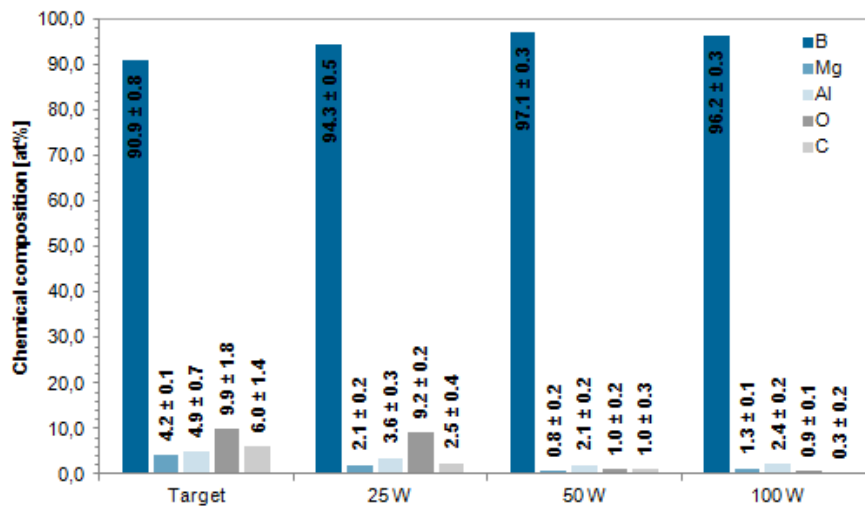


Figure 4.9 Chemical composition of coatings deposited on Si substrates at 25 °C using an AIMgB target with amorphous B

The coatings deposited using an AIMgB target with crystalline B exhibit an average composition of:  $1.7 \pm 0.3$  at% Al,  $0.7 \pm 0.4$  at% Mg,  $97.6 \pm 1.2$  at% B. In comparison with the target composition, the coatings exhibit 3.6 at% less Al, 3.8 at% less Mg and 7.4 at% more B. The coatings contain about 1.1 at% C and 1.5 at% O. No dependence of the coating composition or the impurity content on the deposition power can be observed. (see Figure 4.10)

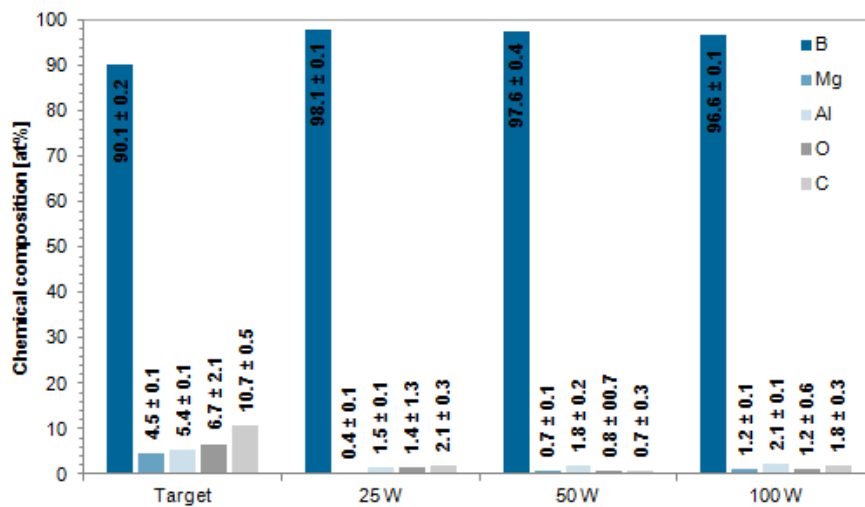


Figure 4.10 Chemical composition of coatings deposited on Si substrates at 25 °C using an AIMgB target with crystalline B

### 4.1.3 Post annealing

Figure 4.11 compares the chemical composition of AlMgB coatings deposited on WC-Co heated to 600 °C in the as deposited state and after 3 h post annealing at 900 °C under vacuum conditions ( $1 \cdot 10^{-6}$  mbar). Post annealing significantly increases the C content of the coatings. While the as deposited coatings contain about 2 at% C, the samples post annealed at 900 °C exhibit 25 - 45 at% C.

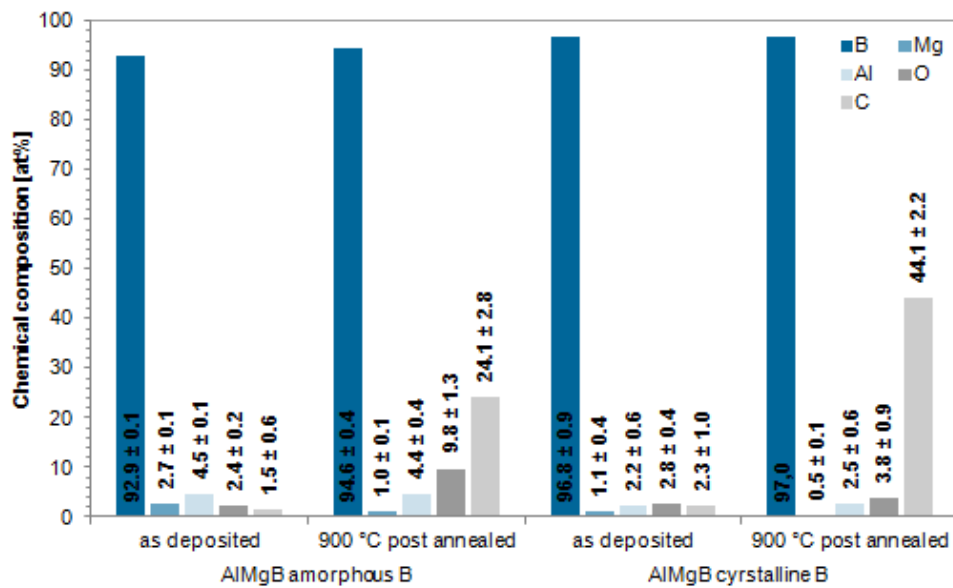


Figure 4.11 Chemical composition of coatings deposited on WC-Co substrates heated to 600 °C before and after 3 h post annealing at 900 °C under vacuum conditions ( $1 \cdot 10^{-6}$  mbar)

The coatings deposited on WC-Co substrates heated to 600 °C exhibit a flat and featureless surface. There are no different phases distinguishable and the coating seems to be very homogenous (see Figure 4.12 and Figure 4.13). After 3 h post annealing at 900 °C under vacuum conditions ( $1 \cdot 10^{-6}$  mbar) the surface appears very rough, showing a two phase structure. EDS measurements suggest that the white phase might be  $\text{AlB}_2$ , while the dark phase consists of B, C and O and thus might represent amorphous boron. (see Figure 4.14 and Figure 4.15)



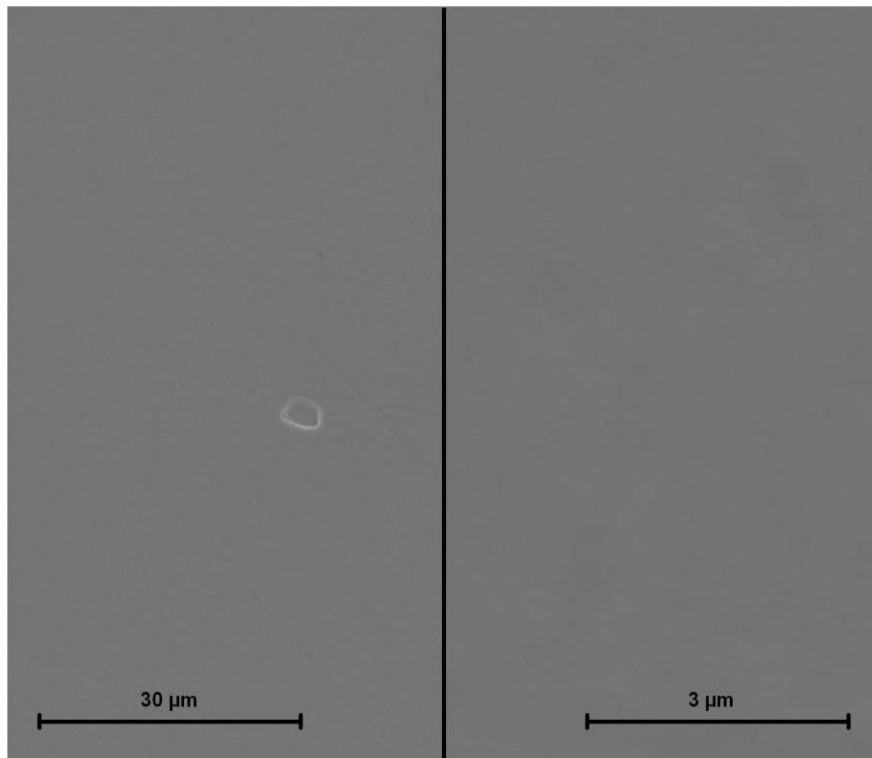


Figure 4.12 Surface of a coating deposited on a WC-Co substrate heated to 600 °C using an AlMgB target with amorphous boron (secondary electron SEM)

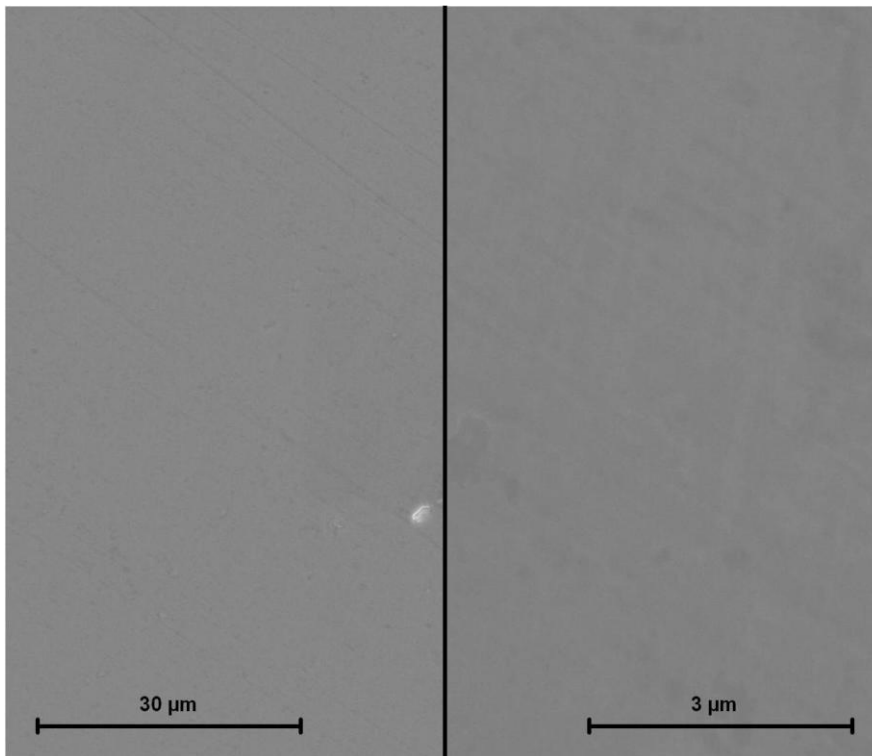


Figure 4.13 Surface of a coating deposited on a WC-Co substrate heated to 600 °C using an AlMgB target with crystalline boron (secondary electron SEM)

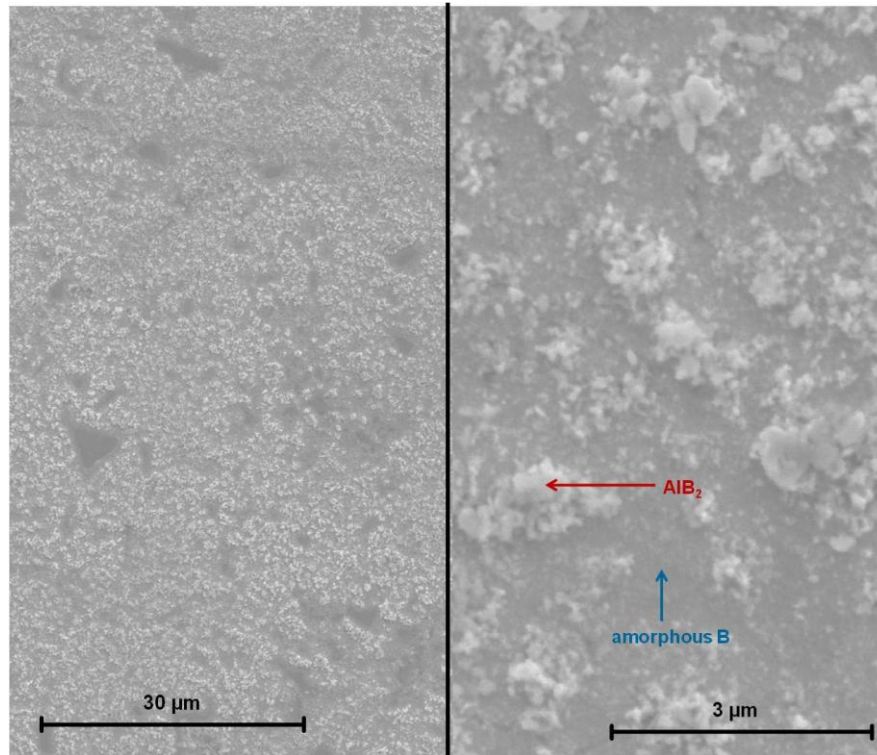


Figure 4.14 Surface of a coating post annealed at 900 °C deposited on a WC-Co substrate heated to 600 °C using an AlMgB target with amorphous boron (secondary electron SEM)

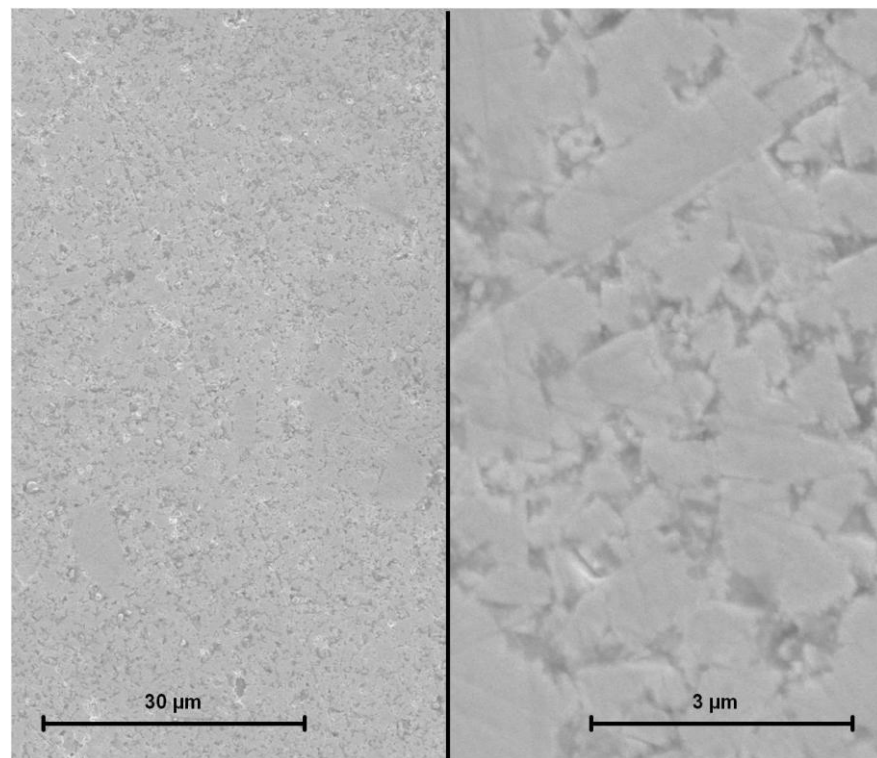


Figure 4.15 Surface of a coating post annealed at 900 °C deposited on a WC-Co substrate heated to 600 °C using an AlMgB target with crystalline boron (secondary electron SEM)

In the XRD pattern of the coatings deposited on WC-Co substrates heated to 600 °C, only the peaks of the WC-Co substrate are visible, suggesting that the deposited coatings consist mainly of amorphous boron (see Figure 4.16).

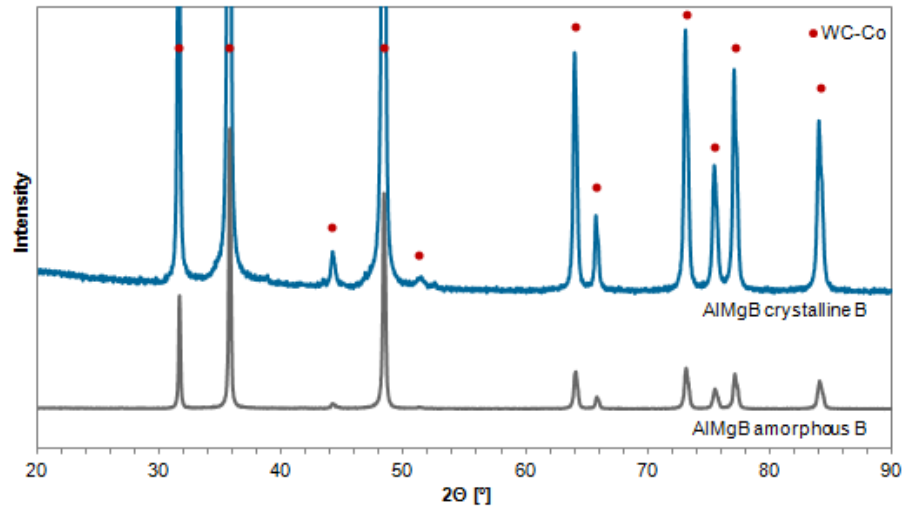


Figure 4.16 XRD pattern of AIMgB coatings deposited on WC-Co substrates heated to 600 °C using 100 W RF

If post annealing at 900 °C is applied for 3 h under vacuum, an  $\text{AlB}_2$  phase develops. For the coatings deposited using an AIMgB target with amorphous B also a  $\text{CoWB}$  phase appears (see Figure 4.17).

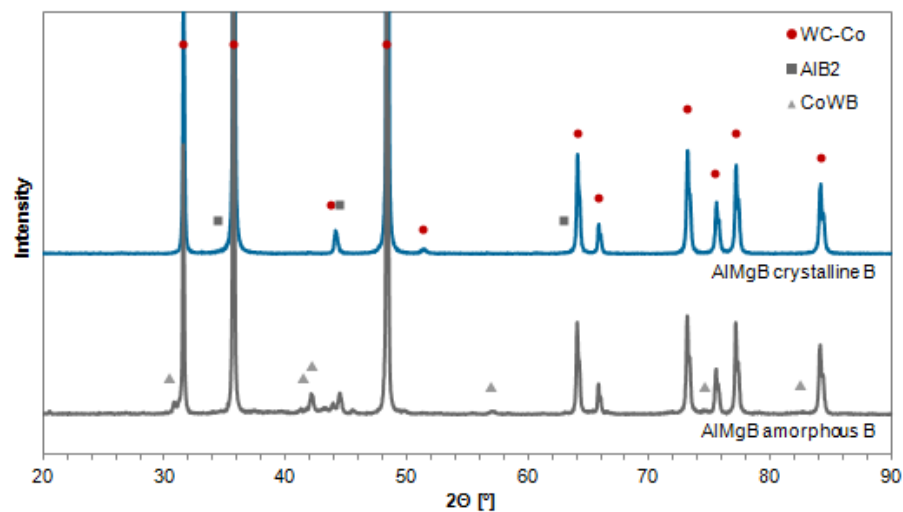


Figure 4.17 XRD pattern of AIMgB coatings deposited on WC-Co substrates heated to 600 °C using 100 W RF deposition power after applying 900 °C post annealing for 3h under vacuum

#### 4.1.4 Interface and adhesion

A monolayer-to-monolayer interface develops between the WC-Co substrates and the AlMgB coatings deposited at 600 °C, where little diffusion and chemical reaction between the deposited atoms and the substrate seems to occur. The deposited coatings appear very homogenous without any cracks or pores (see Figure 4.18). The EDS line scan shows that the Al, Mg and B content stays approximately constant throughout the coating. Hardly any W or Co diffuses into the coating (see Figure 4.19). After applying post annealing at 900 °C, the interface still exhibits a monolayer-to-monolayer characteristic, although the interface region appears a bit less sharp. The coating still looks very homogenous without any cracks or pores (see Figure 4.20). The EDS line scan confirms that the Al, Mg and B distribution is even more homogenous than for the as-deposited coatings and that the region of W diffusion is increased causing a less sharp substrate coating interface (see Figure 4.21). While the O content is approximately the same as found for the as-deposited coatings, the C content of the post annealed coatings is significantly increased and equals approximately the C content found in the WC-Co substrate. The C content is not measured in the EDS cross section line scans (see Figure 4.19 and Figure 4.21) because the preparation method (polishing) and the bonding agent introduce significant C contamination. Thus the C content determined by the EDS cross section line scans is not reliable. Since the C content of AlMgB coatings deposited on Si substrates does not increase during the post annealing process, it can be assumed that high temperature diffusion from the WC-Co substrate is responsible for the significantly increased C content.

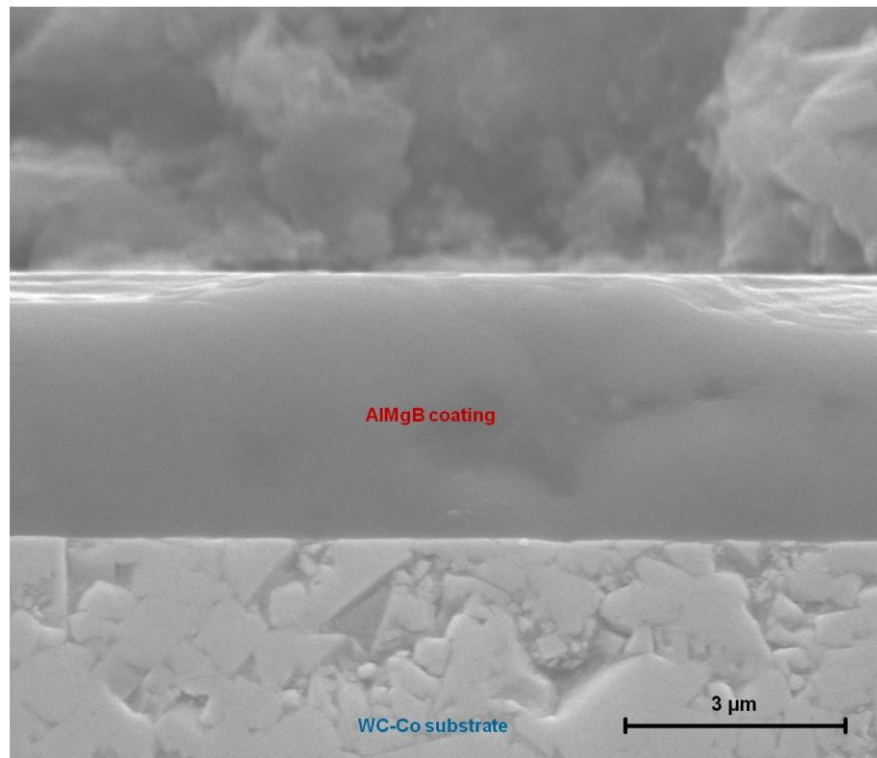


Figure 4.18 Cross section of an AlMgB coating deposited on a WC-Co substrate heated to 600 °C using a target with crystalline boron (secondary electron SEM)

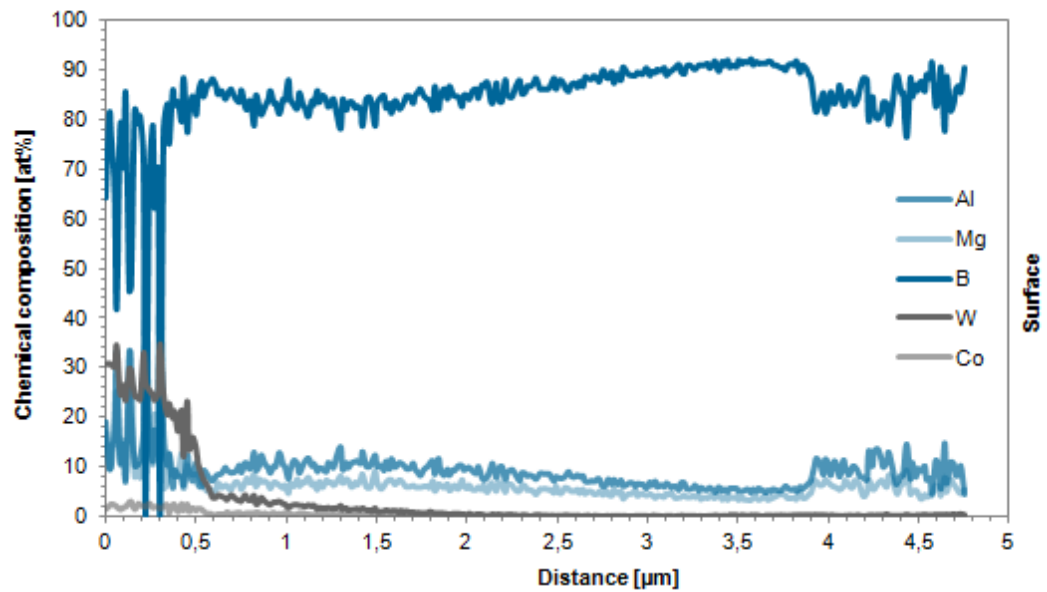


Figure 4.19 EDS line scan of an AlMgB coating deposited on a WC-Co substrate heated to 600 °C using a target with crystalline boron

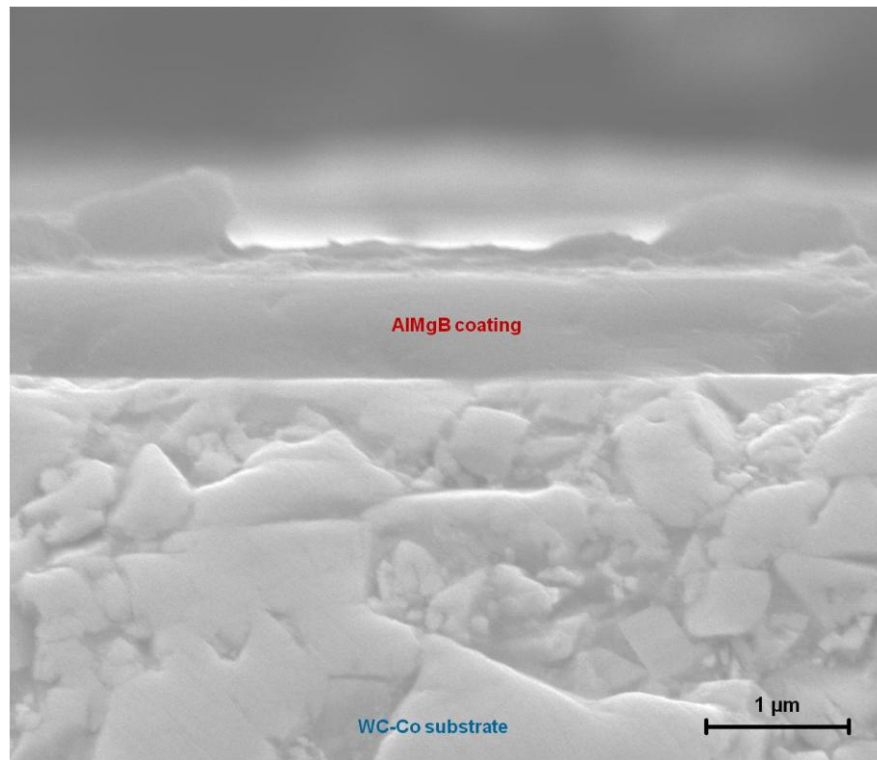


Figure 4.20 Cross section of an AlMgB coating deposited on a WC-Co substrate heated to 600 °C using a target with amorphous boron after applying post annealing at 900 °C for 3h (secondary electron SEM)

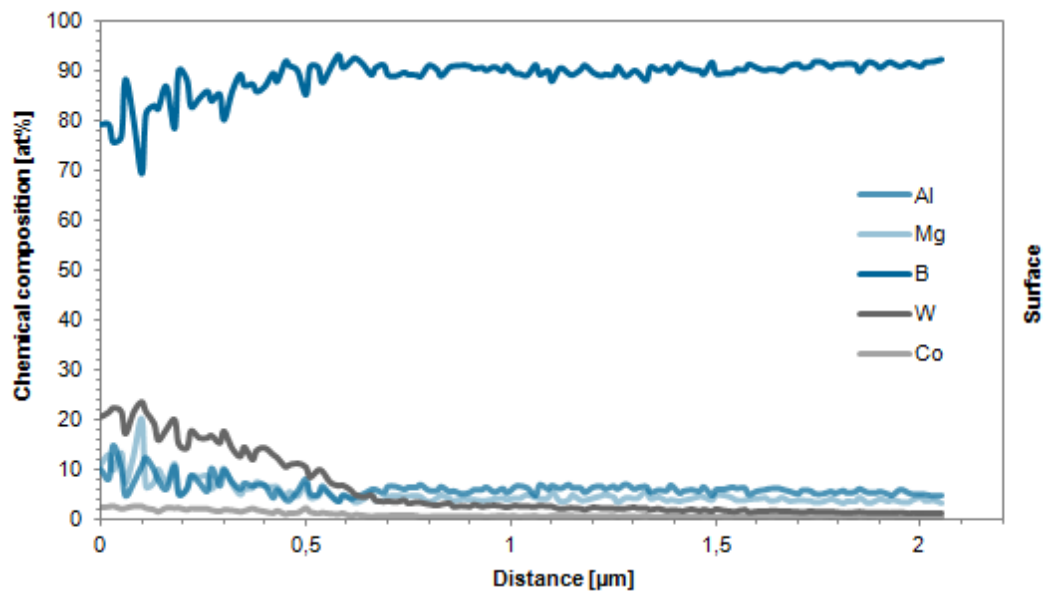


Figure 4.21 EDS line scan of an AlMgB coating deposited on a 600 °C heated WC-Co substrate using a target with amorphous boron after applying post annealing at 900 °C for 3h

While the adhesion of AlMgB coatings deposited on WC-Co substrates heated to 600 °C is good, delamination can be observed for 3 µm thick coatings after post annealing is applied at 900 °C for 3 h in vacuum (see Figure 4.22).

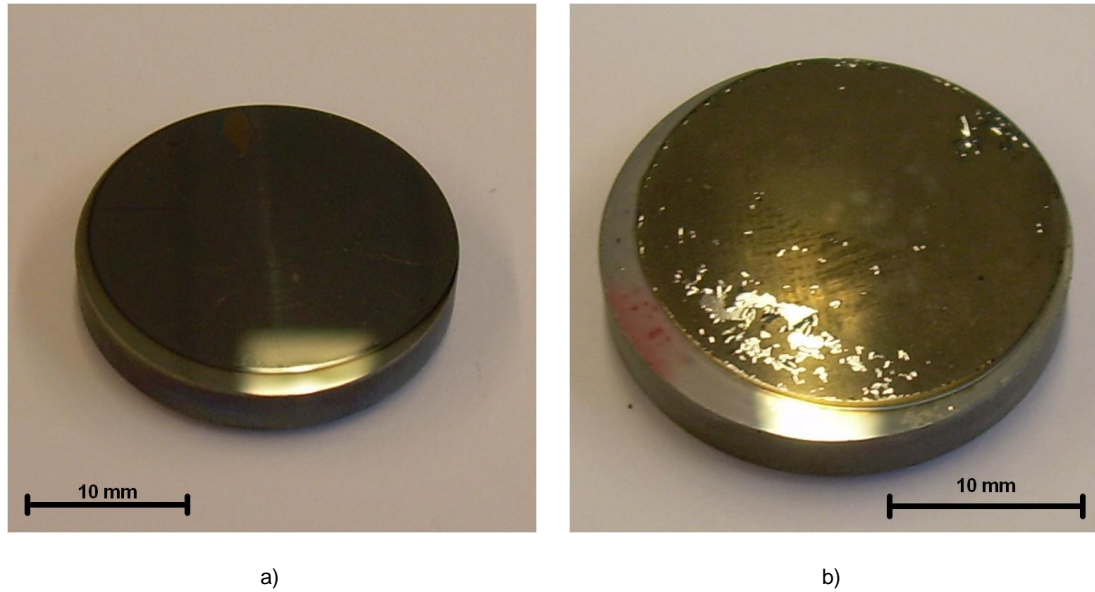


Figure 4.22 Comparison of two 3 µm coatings deposited on WC-Co substrates heated to 600 °C using an AlMgB target with amorphous B, 100 W RF deposition power and a working gas pressure of  $4 \cdot 10^{-3}$  mbar  
a) As deposited  
b) After post annealing at 900 °C for 3h under vacuum

#### 4.1.5 Microhardness

The hardness of AlMgB coatings was measured using a *Reichert-Jung* micro-hardness tester *Micro-Duromat 4000*. The test load was 222.4 N (50 Pond), the images for measurement analysis were taken with a magnification of 50x. The hardness of the WC-Co K10 substrates was measured as  $1712 \pm 252$  HV. The AlMgB coatings were 3  $\mu\text{m}$  thick and deposited on WC-Co substrates heated to 600 °C using a target with amorphous and one with crystalline B. Hardness was measured for as-deposited coatings and after applying post annealing at 900 °C for 3 h under vacuum conditions ( $1 \cdot 10^{-6}$  mbar). The AlMgB coatings deposited using a target with amorphous boron exhibit a hardness of about 2455 HV and the coatings deposited using a target with crystalline B show a hardness of about 2136 HV. The difference between the as-deposited and 900 °C post annealed samples is not significant, although the hardness of the as-deposited coatings tends to be slightly higher than the one of the coatings post annealed at 900 °C. The hardness of pure, nano-crystalline AlMgB<sub>14</sub> ranges between 32 – 35 GPa (3200 HV – 3600 HV) [6].

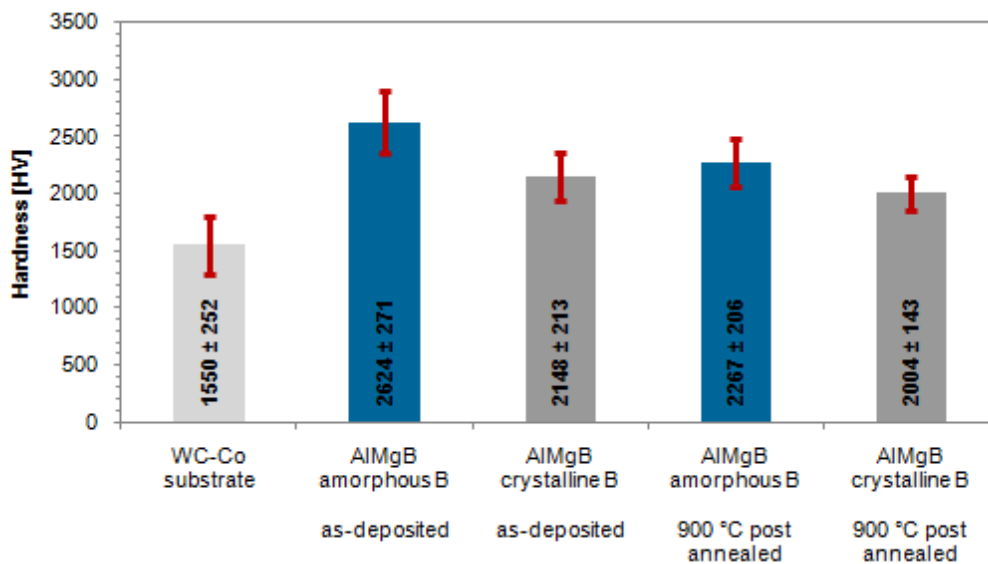


Figure 4.23 Hardness of the WC-Co substrate and 3  $\mu\text{m}$  AlMgB coatings deposited on WC-Co substrates heated to 600 °C. Hardness measured for as deposited and coatings post annealed at 900 °C



## 4.2 AlCuFeB ceramic targets

### 4.2.1 Targets

AlCuFeB targets that exhibit the  $\text{Al}_{59}\text{Cu}_{25.5}\text{Fe}_{12.5}\text{B}_3$  composition and the quasicrystalline structure were produced with three different types of powders: *St Gobain Cristome F1* powder with particles sizes ranging from 10 – 70  $\mu\text{m}$ , *St Gobain Cristome F1* powder with particle sizes between 40 - 70  $\mu\text{m}$  and an elemental powder mixture. With each powder type, three targets were produced, analysed and tested. Figure 4.24 shows the average chemical composition of the different target types measured by EDS and normalized to 97 at% (B atoms do not affect the formation of the quasicrystalline phase, see Section 3.6). The average chemical composition of the targets produced with the *St Gobain Cristome F1* powders corresponds to the powder composition and thus with the nominal  $\text{Al}_{59}\text{Cu}_{25.5}\text{Fe}_{12.5}\text{B}_3$  composition. The standard deviation is about  $\pm 0.5$  at%, which is very low. The O content determined by EDS is 4 at%. The targets produced with an elemental powder mixture show small deviations from the nominal  $\text{Al}_{59}\text{Cu}_{25.5}\text{Fe}_{12.5}\text{B}_3$  composition ( $\sim 3$  at%) and a higher standard deviation (about 3 at%). Compared to the targets produced with *St. Gobain Cristome F1* powders, the targets produced with elemental powders show a significantly higher amount of oxygen impurities (19 at%)

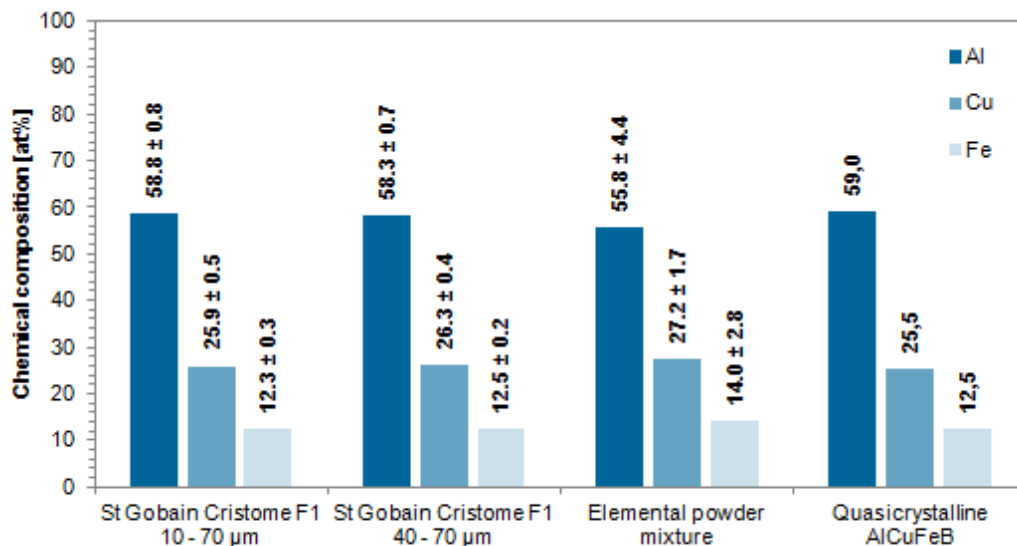


Figure 4.24 Chemical composition of the ceramic AlCuFeB targets in comparison with the  $\text{Al}_{59}\text{Cu}_{25.5}\text{Fe}_{12.5}\text{B}_3$  composition

The targets produced with *St. Gobain Cristome F1* powders exhibit a very homogenous structure, with quite complex surface features (see Figure 4.25). Black particles with diameters  $< 1 \mu\text{m}$ , which contain boron can be observed at grain boundaries as well as within the grains. EDS measurements suggest that the needle shaped B precipitates represent  $\text{AlFeB}_2$ , while the oval shaped B precipitates might be  $\text{AlB}_{12}$ . Additionally white stabs occur, which are enriched in Fe (about 5 - 13 at% more Fe than the target average). The structure of the *St. Gobain Cristome F1* powder particles is not preserved (see Figure 3.11 c in Section 3.3).

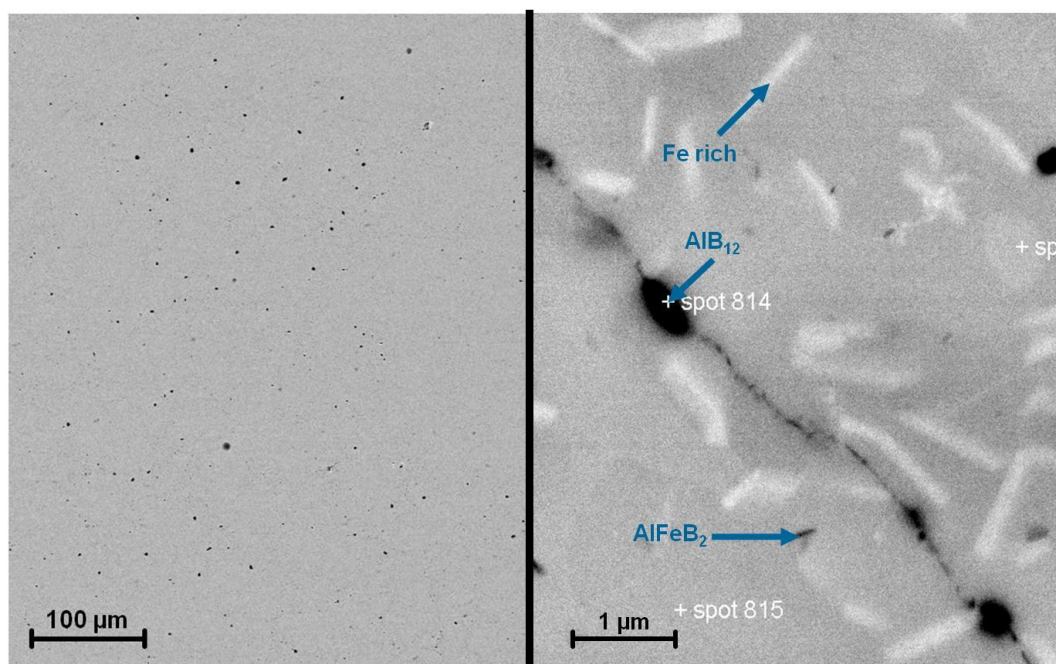


Figure 4.25 Back scattered HRSEM images of a target produced with *St. Gobain Cristome F1* 40 – 70  $\mu\text{m}$  powder

Targets produced with elemental powders show different surface features (see Figure 4.26). B particles (black areas) with diameters up to 25  $\mu\text{m}$  can be observed, which do not dissolve in the matrix. The chemical composition of the white areas corresponds to the nominal  $\text{Al}_{59}\text{Cu}_{25.5}\text{Fe}_{12.5}\text{B}_3$  composition. The dominating bright gray area probably represents an  $\text{Al}_{50}\text{Cu}_{40}\text{Fe}_{10}$   $\beta$  phase and the dark gray areas represent Al+Fe rich (Cu poor) phases.

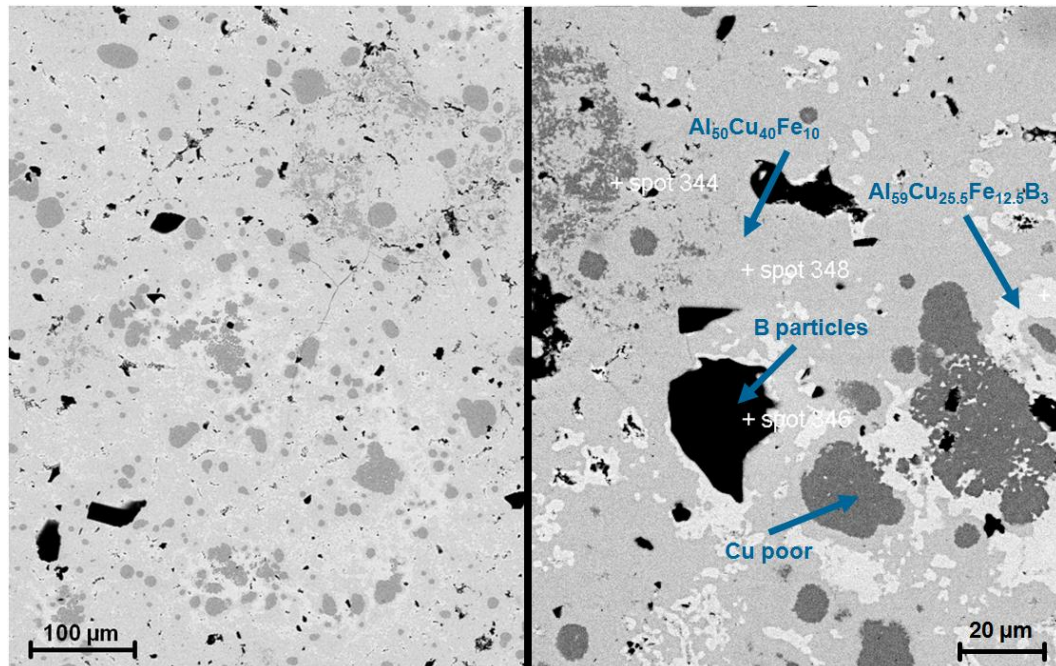


Figure 4.26 Back scattered HRSEM images of a target produced with elemental powders

Figure 4.27 shows the XRD pattern of the  $\text{Al}_{59}\text{Cu}_{25.5}\text{Fe}_{12.5}\text{B}_3$  reference sample and the  $\text{Al}_{50}\text{Cu}_{40}\text{Fe}_{10}$   $\beta$  phase in comparison with the XRD pattern of the three different target types from  $20^\circ$  to  $60^\circ$ . The targets produced with elemental powders consist of about 70 %  $\text{Al}_{50}\text{Cu}_{40}\text{Fe}_{10}$   $\beta$  phase and 30 % icosahedral AlCuFe phase (estimated by XRD peak intensities). For the targets produced with *St. Gobain Cristome F1* powder only peaks corresponding to the icosahedral AlCuFe phase appear. For all three target types as well as for the reference sample, the characteristic quasicrystalline AlCuFe peaks show shoulders (see Figure 4.28). The nature of these shoulders is discussed in Section 5.2.2.

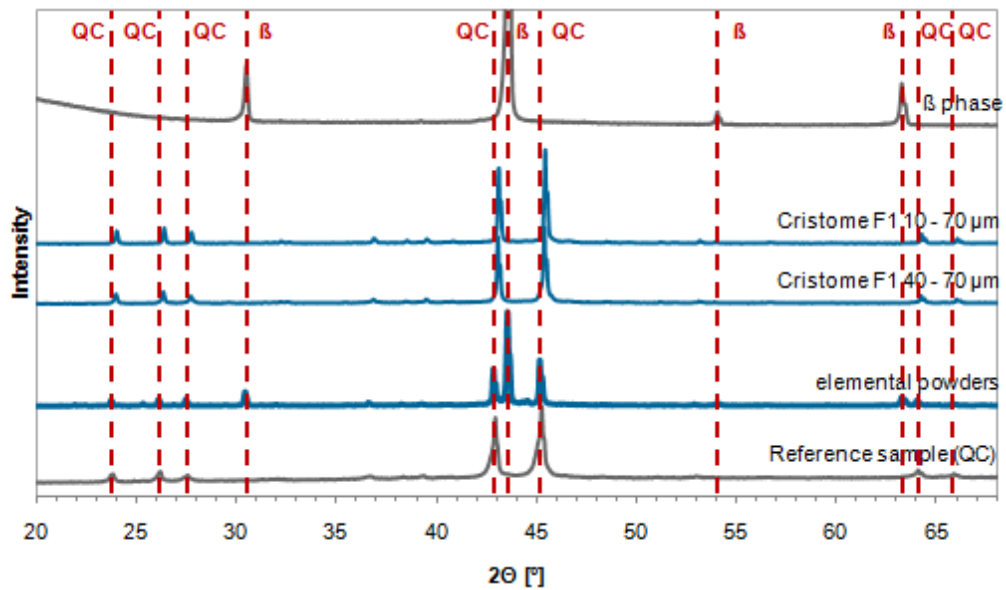


Figure 4.27 XRD pattern of the three target types in comparison with the XRD pattern of the quasicrystalline  $\text{Al}_{59}\text{Cu}_{25.5}\text{Fe}_{12.5}\text{B}_3$  reference sample and the  $\text{Al}_{50}\text{Cu}_{40}\text{Fe}_{10}$   $\beta$  phase (Cu anode  $\lambda = 1.542 \text{ \AA}$ )

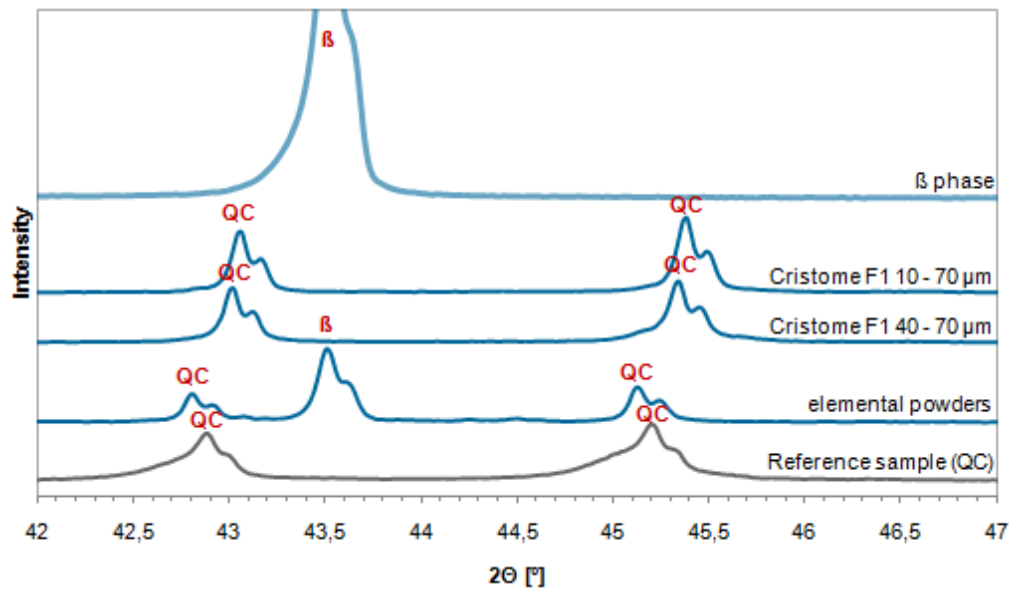


Figure 4.28 Zoom into the XRD pattern of the three target types in comparison with the XRD pattern of the quasicrystalline  $\text{Al}_{59}\text{Cu}_{25.5}\text{Fe}_{12.5}\text{B}_3$  reference sample and the  $\text{Al}_{50}\text{Cu}_{40}\text{Fe}_{10}$   $\beta$  phase (Cu anode  $\lambda = 1.542 \text{ \AA}$ )

The electrical resistivity of the targets produced with *St. Gobain Cristome F1* powders was measured as  $96.4 \mu\Omega\text{m} \pm 4.0 \mu\Omega\text{m}$ . The targets produced with the elemental powders exhibit a resistivity of  $15.0 \mu\Omega\text{m} \pm 5.2 \mu\Omega\text{m}$ . Because of the poor electrical conductivity RF magnetron sputtering had to be applied. During deposition all target types suffer from crack formation. This crack formation occurs even if the applied deposition power does not exceed  $25 \text{ W}$  ( $3.8 \text{ W/cm}^2$ ) and proceeds further if the deposition power is increased. Using pulsed magnetron sputtering (frequency  $100 \text{ Hz}$ , reverse time  $2 \mu\text{s}$ ) does not prevent crack formation (see Figure 4.29).

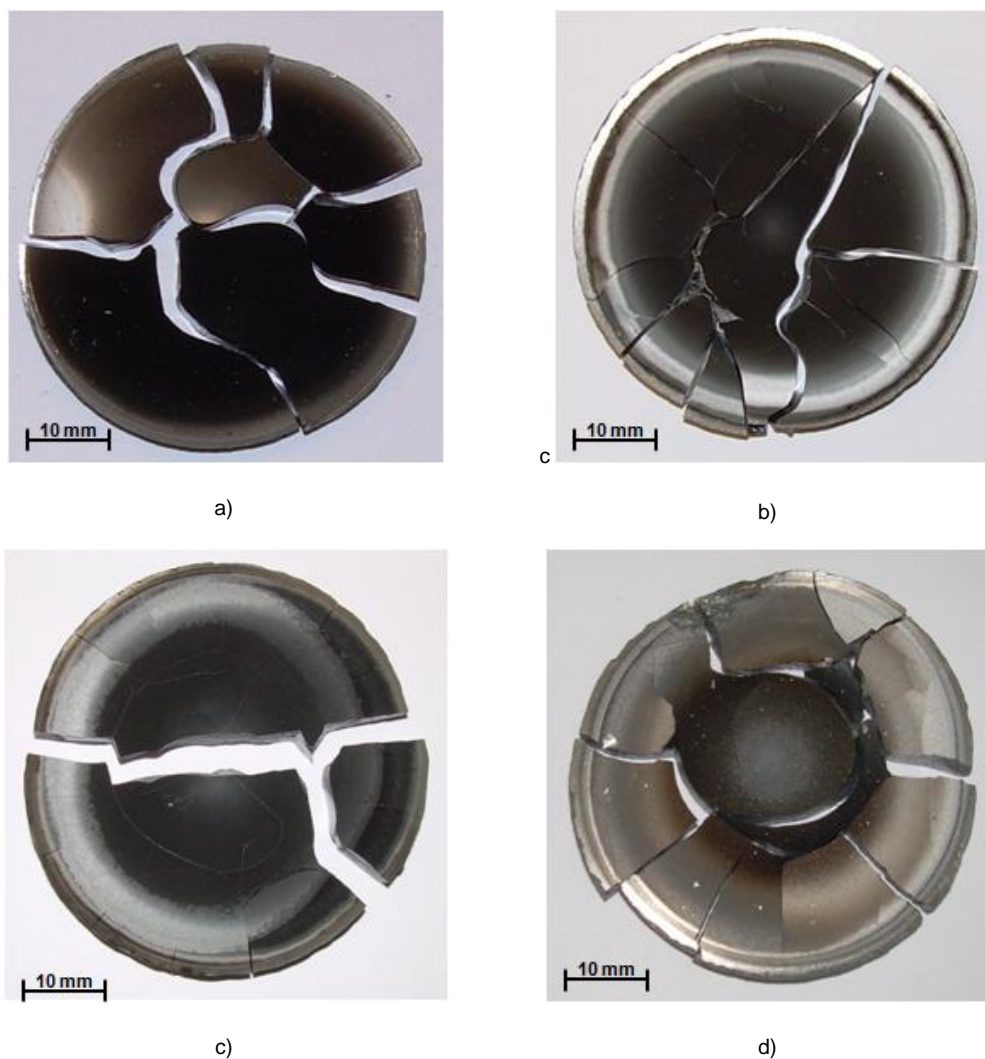


Figure 4.29 Ceramic  $\text{Al}_{59}\text{Cu}_{25.5}\text{Fe}_{12.5}\text{B}_3$  targets after deposition

- Target produced with *St. Gobain Cristome F1* 10-70  $\mu\text{m}$  powder after applying 50 W RF
- Target produced with *St. Gobain Cristome F1* 40-70  $\mu\text{m}$  powder after applying 300 W RF
- Target produced with elemental powders after applying 25 W RF
- Target produced with *St. Gobain Cristome F1* 10-70  $\mu\text{m}$  powder after applying 100 W pulsed magnetron sputtering (frequency 100 Hz, reverse time  $2 \mu\text{s}$ )

### 4.2.2 Coating composition

Since the quasicrystalline AlCuFeB targets exhibit ceramic characteristics, RF magnetron sputtering had to be used for coating deposition. The Ar pressure was varied between  $1.5 \cdot 10^{-3}$  mbar and  $15 \cdot 10^{-3}$  mbar and the deposition power between 25 W ( $3.8 \text{ W/cm}^2$ ) and 300 W ( $45 \text{ W/cm}^2$ ). The deposition rate  $D$  is independent of the powders used for target production and increases linearly with the deposition power  $P$  from 21 nm/min (25 W) to 252 nm/min (300 W) with  $D = -4.8 \text{ nm/min} + 0.8 \text{ nm/(min W)} P$  (see Figure 4.30). The film thickness of all samples was 5  $\mu\text{m}$  and film deposition was done on natively oxidized (1 0 0) Si substrates, with a substrate – target distance of 5 cm.

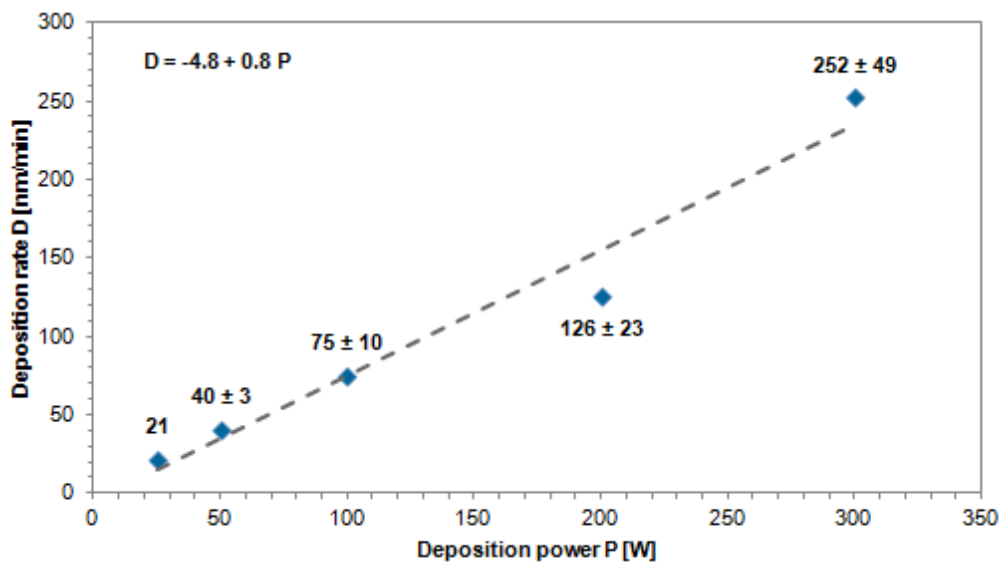


Figure 4.30 Deposition rate in dependence of the deposition power. The applied working gas pressure was  $4 \cdot 10^{-3}$  mbar

Independent of the powders used for target production, a dependence of the coating composition on the deposition power and the working gas pressure could be observed. If a deposition power of more than 50 W is applied, the Al content increases approximately linearly while the Fe and Cu content decrease. Figure 4.31 shows the Al content of coatings deposited using the three different target types in dependence on the deposition power. The applied working gas (Ar) pressure was  $4 \cdot 10^{-3}$  mbar. Averaging over all three target types, the following relation can be given:  $Al [\text{at}\%] = 60.0(\pm 2.5) \text{ at}\% + 57(\pm 13.5) \cdot 10^{-3} \text{ at}\%/\text{W} \cdot P [\text{W}]$ .

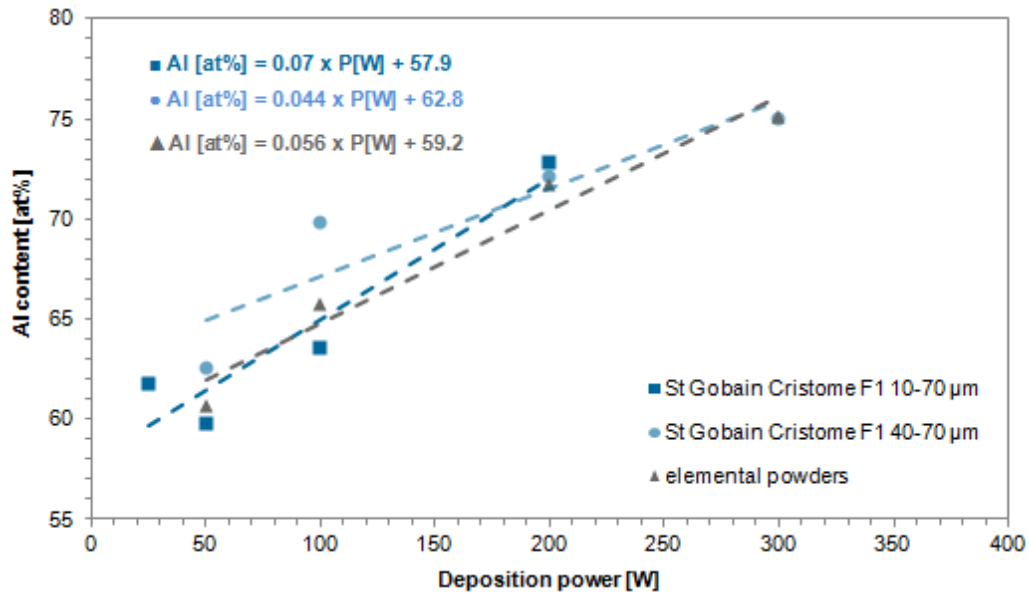


Figure 4.31 Al content of the deposited films in dependence on the applied deposition power for all three target types used. The applied working gas pressure was  $4 \cdot 10^{-3}$  mbar

If the deposition power is kept constant (50 W), it can be observed that the deposited coatings contain  $\sim 7$  at% less Al as well as  $\sim 5$  at% more Cu and  $\sim 2$  at% more Fe than the corresponding target, if a working gas pressure below  $4.0 \cdot 10^{-3}$  mbar is applied. If a pressure of  $4.0 \cdot 10^{-3}$  mbar or more is applied, the coatings exhibit  $\sim 2$  at% more Al,  $\sim 1$  at% less Cu and 1 at% less Fe than the target. Figure 4.32 shows the chemical compositions of coatings deposited using a target produced with *St. Gobain Cristome F1* 10 – 70  $\mu\text{m}$  powder in dependence on the working gas pressure. This effect could be verified with the other target types. In contrast to the applied deposition power and working gas pressure, the post annealing temperature (up to 600 °C) was found not to influence the chemical composition of the coatings.

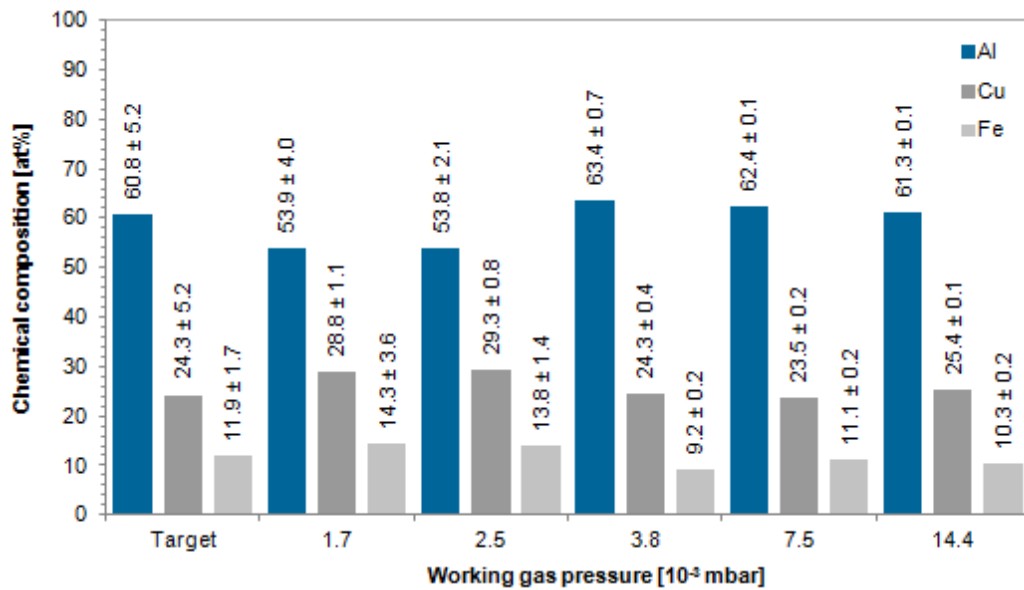


Figure 4.32 Chemical composition of AlCuFeB coatings in dependence on the working gas pressure. Deposited using a target produced with St. Gobain Cristome F1 10 – 70  $\mu\text{m}$  powder. The applied deposition power was 50 W.

Even if the deposition power and the working gas pressure are kept constant at 50 W RF and  $4 \cdot 10^{-3}$  mbar, the coating composition statistically varies in a range of  $\pm 4$  at% Al,  $\pm 3$  at% Cu and  $\pm 2$  at% Fe, with an average coating composition of: 61 at% Al, 25 at% Cu and 11 at% Fe. The average coating composition lies within the icosahedral area, but due to the composition variations, also coating compositions outside this area are possible (see Figure 4.33). The O content of the coatings is about 2 at% and the C content about 3 at%.



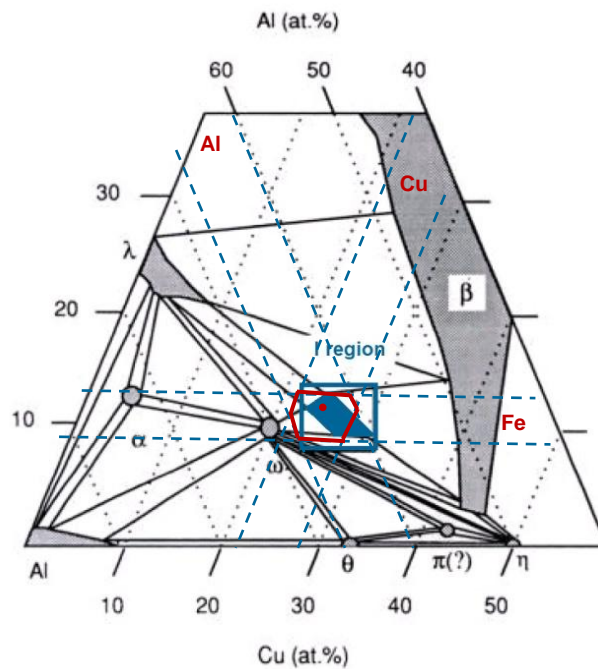


Figure 4.33 Average coating composition (red dot) displayed in the Al-Cu-Fe phase diagram at 750 °C [27]  
 Dashed blue lines = area of Al, Cu, Fe variation, Full red lines = area of coating composition variation

### 4.2.3 Coating microstructure

Figure 4.34 shows the XRD pattern of AlCuFeB coatings deposited using a ceramic target, a working gas pressure of  $4 \cdot 10^{-3}$  mbar and a deposition power of 50 W. XRD was done for an as-deposited coating and for coatings after applying 5 min to 3 h post annealing at 600 °C in vacuum ( $1 \cdot 10^{-6}$  mbar). For the as-deposited coating only a broad peak, corresponding to an amorphous structure occurs. Post annealing at 600 °C for 5 - 15 min or less leads to the development of mostly  $\text{Al}_{50}\text{Cu}_{40}\text{Fe}_{10}$   $\beta$  phase (~60 %). When the post annealing time is increased from 5 – 15 min to 30 – 45 min the content of  $\text{Al}_{50}\text{Cu}_{40}\text{Fe}_{10}$   $\beta$  phase decreases from ~60 % to ~35 %. With a further increase of post annealing time to 3 h, the amount of  $\beta$  phase can be reduced to ~25 % (see Figure 4.35). To exclude that the  $\beta$  phase formation is specific for Si substrates, a 5  $\mu\text{m}$  coating was deposited on a WC-Co hard metal substrate and post annealed at 600 °C for 3 h. For this sample, the development of the  $\beta$  phase could be observed as well. The quasicrystalline diffraction peaks show shoulders, which become less significant for longer post annealing times (see Figure 4.36). A certain degree of peak broadening exists also after 3 h of post annealing.

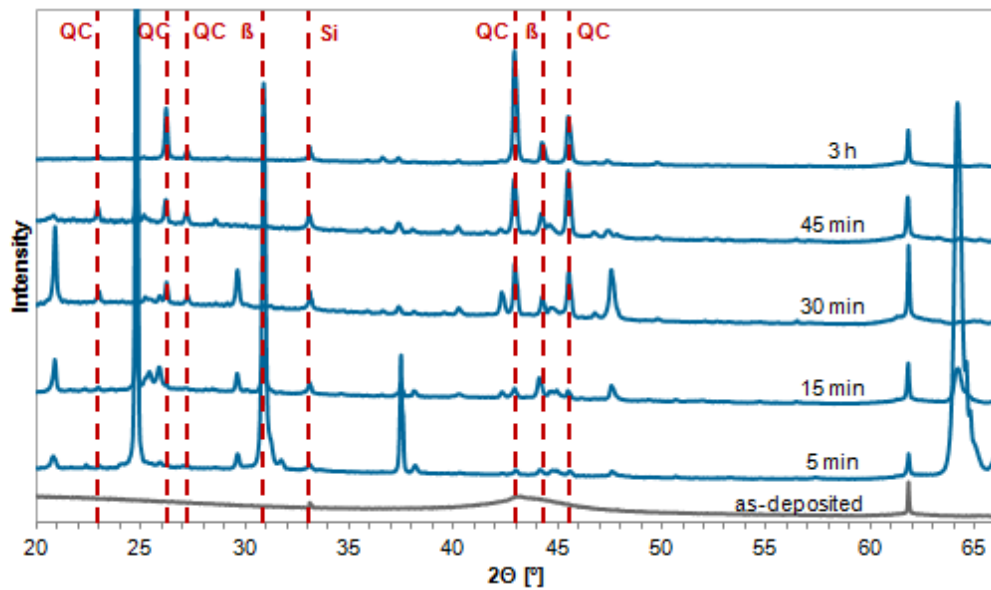


Figure 4.34 XRD pattern of room-temperature deposited coatings, as-deposited and after applying 600 °C post annealing for 5 min to 3 h. (Cu anode  $\lambda = 1.542 \text{ \AA}$ ) The applied working gas pressure was  $4 \cdot 10^{-3}$  mbar and the deposition power 50 W.

QC = quasicrystalline AlCuFe,  $\beta = \text{Al}_{50}\text{Cu}_{40}\text{Fe}_{10}$   $\beta$  phase, Si = Si substrate

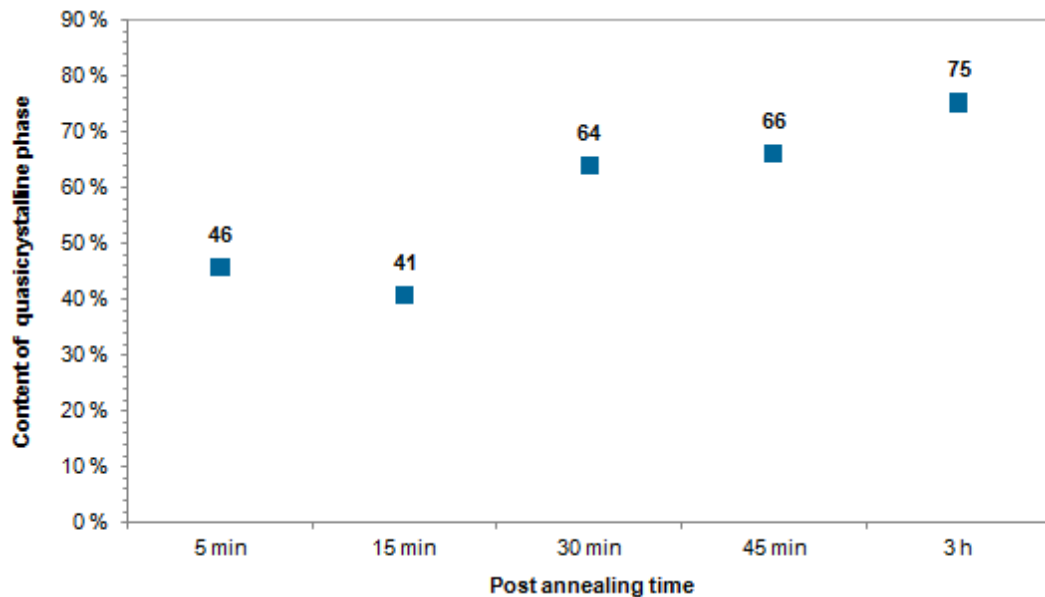


Figure 4.35 Amount of quasicrystalline phase in the deposited AlCuFeB coatings in dependence on the post annealing time. The amount of quasicrystalline phase was estimated using the XRD peak intensities. (Cu anode  $\lambda = 1.542 \text{ \AA}$ )

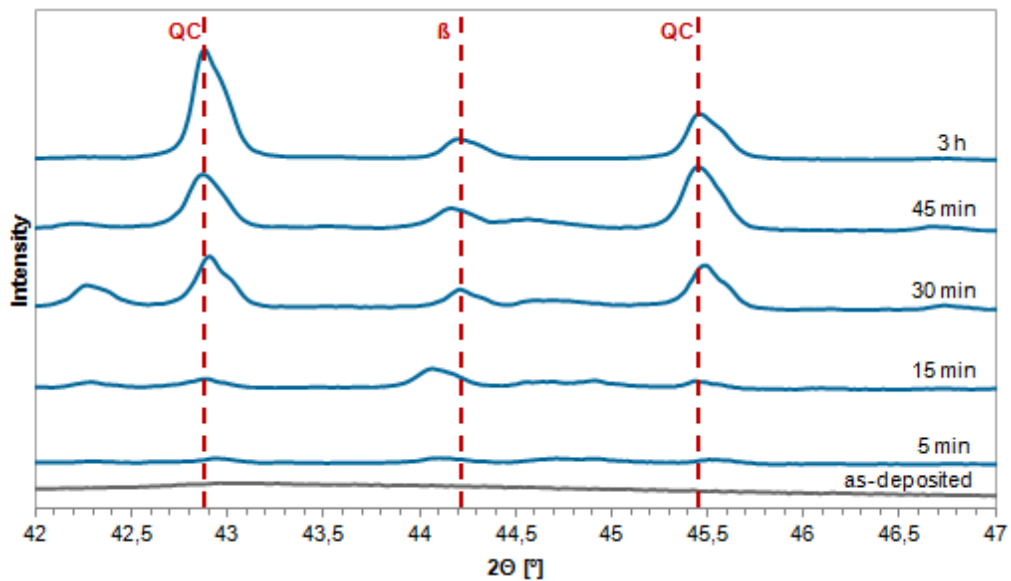


Figure 4.36 XRD pattern of coatings deposited at room-temperature, as-deposited and after applying 600 °C post annealing for 5 min to 3 h. (Cu anode  $\lambda = 1.542 \text{ \AA}$ )  
The applied working gas pressure was  $4 \cdot 10^{-3}$  mbar and the deposition power 50 W

QC = quasicrystalline AlCuFe,  $\beta = \text{Al}_{50}\text{Cu}_{40}\text{Fe}_{10}$   $\beta$  phase, Si = Si substrate

The amount of quasicrystalline phase as displayed in Figure 4.35 was estimated by using the XRD peak intensities as shown in Figure 4.36. The average intensity  $QC^*$  of the two main peaks corresponding to quasicrystalline AlCuFeB at 42.86° and 45.18° (QC in Figure 4.36) was set in relation to the main peak corresponding to the  $\beta$  phase at 43.34° ( $\beta$  in Figure 4.36):

$$\text{Amount of quasicrystalline phase} = \frac{QC^*}{QC^* + \beta} \cdot 100 \quad (4.1)$$

$QC^*$ ...average intensity of the two main XRD peaks corresponding to quasicrystalline AlCuFeB  
 $\beta$ ...intensity of the main XRD peak corresponding to the  $\text{Al}_{50}\text{Cu}_{40}\text{Fe}_{10}$   $\beta$  phase

#### 4.2.4 Coating interface

For the as-deposited coating (working gas pressure:  $4 \cdot 10^{-3}$  mbar, deposition power: 50 W), the surface roughness is very low and the interface is very homogenous (see Figure 4.37). EDS line scans (see Figure 4.38) show that Fe, Cu and Al are uniformly distributed throughout the coating. With this analytical method, no B precipitates as in the targets can be recognized. The Si substrate – coating interface exhibits a sharp monolayer-to-monolayer characteristic without any significant diffusion and mechanical interlocking. Nevertheless, according to EDS line scans Si diffuses from the interface towards the surface of the coating, where about 6 at% Si can be found. An O content of about 5 at% can be found throughout the coating. The sample post annealed at 600 °C for 1 h exhibits a very high surface roughness and cracks propagate from the surface through the coating into the substrate. The interface is very inhomogeneous and small pores have developed. Obviously high temperature diffusion occurred and the development of a compound interface, with chemical interaction of the film and substrate is likely. The EDS line scan shows that Si is present throughout the coating and that Si rich phases with ~55 at% Si (dark areas) form on the interface, inside the coating and close to the surface (see Figure 4.37). An O content of about 5 at% can be found throughout the coating.

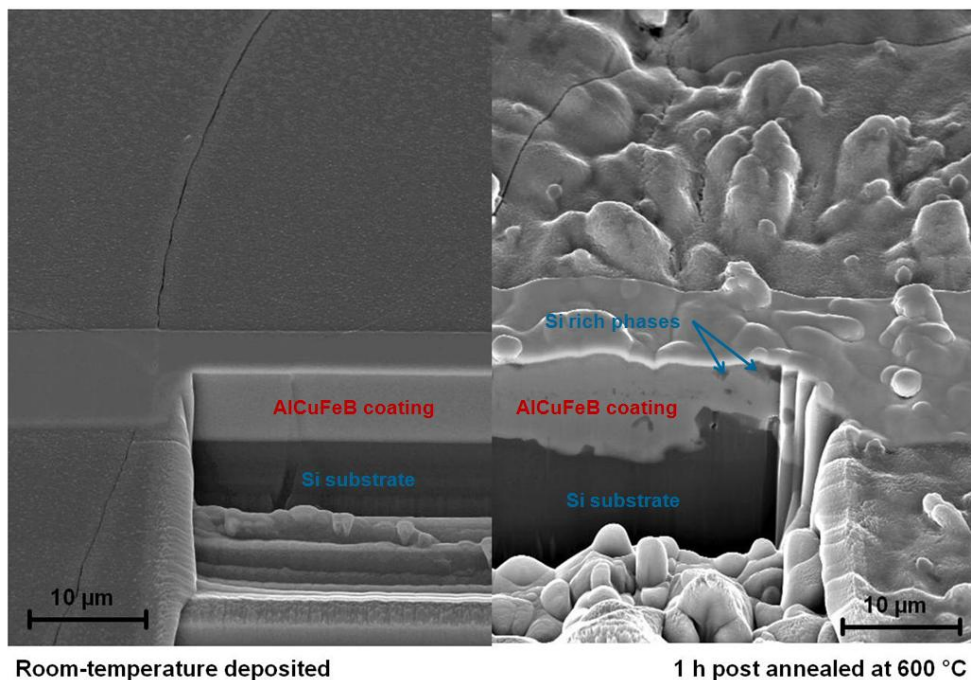


Figure 4.37 Secondary Electron image of FIB cross sections of coatings deposited at room-temperature using a target produced with *St. Gobain Cristome F1 10 - 70 μm* powders, as-deposited (working gas pressure:  $4 \times 10^{-3}$  mbar, deposition power: 50 W) and after 1 h post annealing at 600 °C

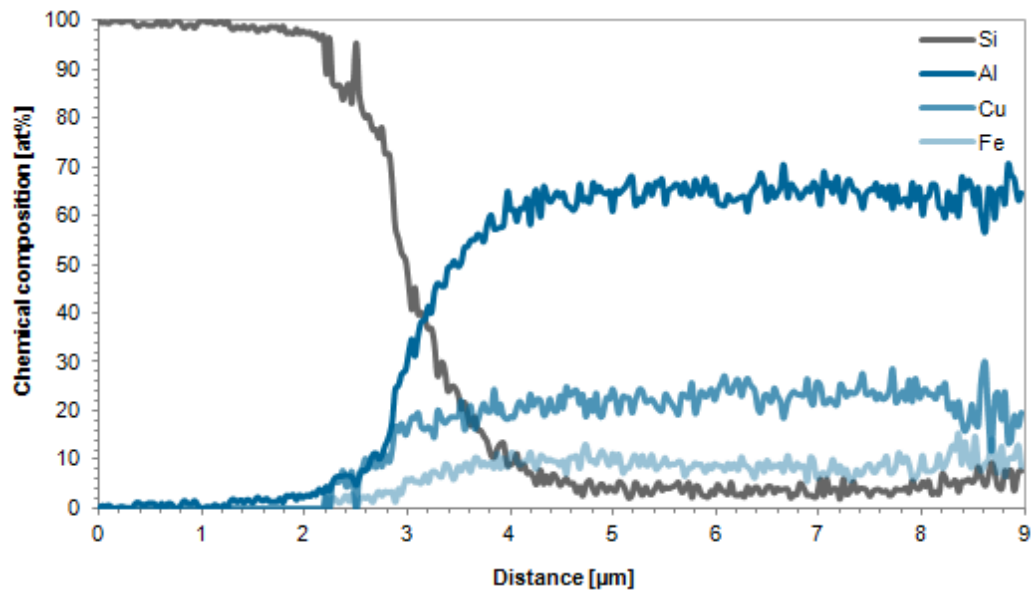


Figure 4.38 EDS line scan of a coating deposited at room-temperature using a target produced with *St. Gobain Cristome F1 10* - 70 μm powders, a working gas pressure of  $4 \cdot 10^{-3}$  mbar and a deposition power of 50 W

An overview of the coating surface shows that 600 °C post annealing causes coating delamination all over the coating surface. Higher magnification reveals that the coating delamination as well as the crack formation is induced by buckles with diameters of  $24.4 \pm 3.7$  μm (see Figure 4.39).

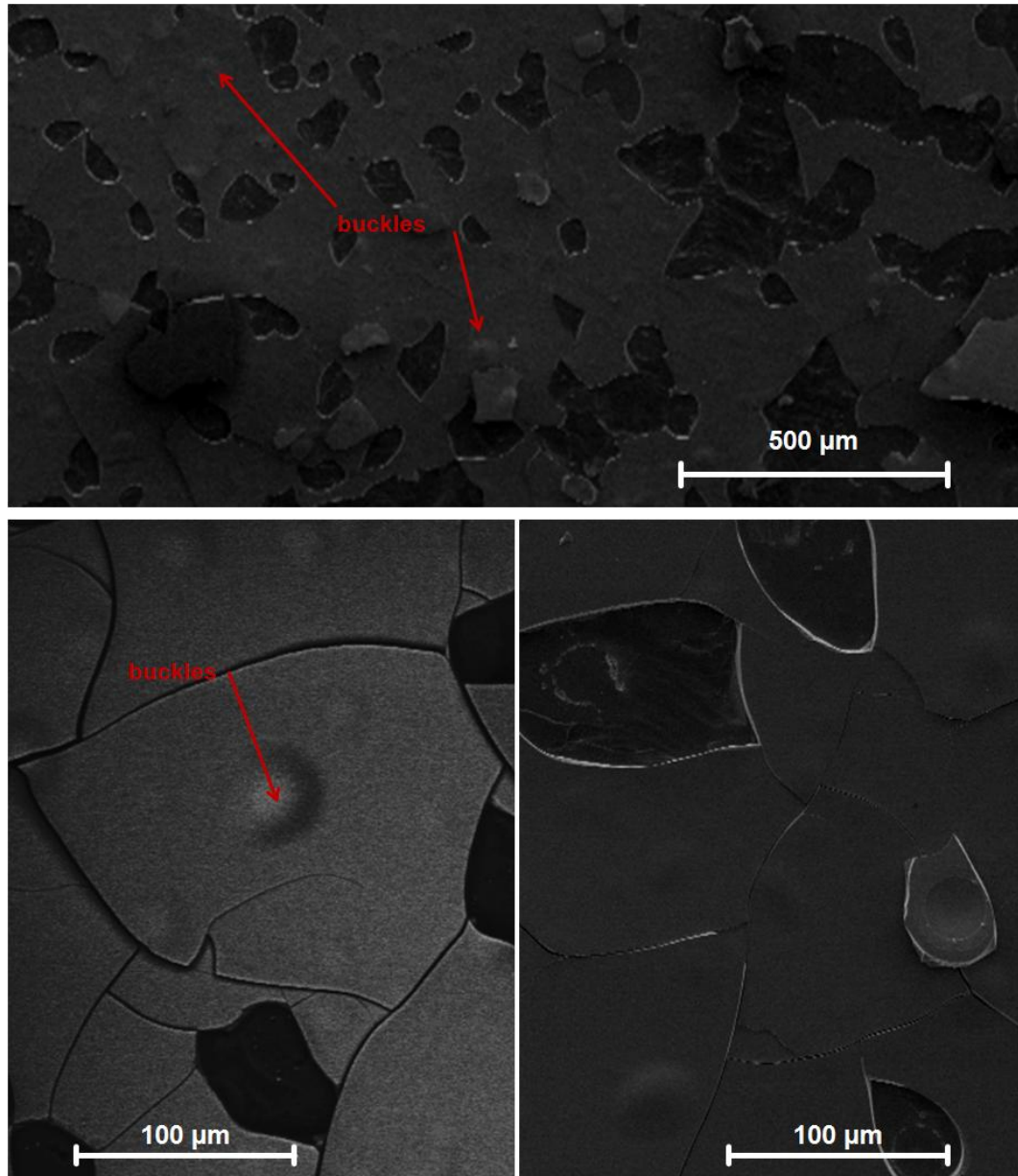


Figure 4.39 Back scattered HRSEM images of a coating deposited at room-temperature, using a target produced with *St. Gobain Cristome* F1 10 - 70 μm, a working gas pressure of  $4 \cdot 10^{-3}$  mbar and a deposition power of 50 W powders after 1 h post annealing at 600 °C

### 4.3 AlCuFeB shifted composition targets

#### 4.3.1 Targets

Applying a deposition power over 50 W on quasicrystalline  $\text{Al}_{59}\text{Cu}_{25.5}\text{Fe}_{12.5}\text{B}_3$  targets leads to a shift in the chemical composition of the deposited coatings. While the Al content is linearly increasing with the deposition power, the Fe and Cu content decrease (see Section 4.2.2). To compensate the observed composition shift, the following targets with an altered chemical composition were produced (see Figure 4.40):

- $\text{Al}_{61}\text{Cu}_{24.3}\text{Fe}_{11.8}\text{B}_{2.9}$  (*St Gobain Cristome F1* 10 - 70  $\mu\text{m}$  powder + Al)
- $\text{Al}_{58.5}\text{Cu}_{24.8}\text{Fe}_{12.1}\text{B}_{4.8}$  (*St Gobain Cristome F1* 10 - 70  $\mu\text{m}$  powder +  $\text{AlB}_2$ )
- $\text{Al}_{44.8}\text{Cu}_{33.5}\text{Fe}_{18.7}\text{B}_3$  (*St Gobain Cristome F1* 10 - 70  $\mu\text{m}$  powder + Cu + Fe)
- $\text{Al}_{44.8}\text{Cu}_{33.5}\text{Fe}_{18.7}\text{B}_3$  (Elemental powder mixture)

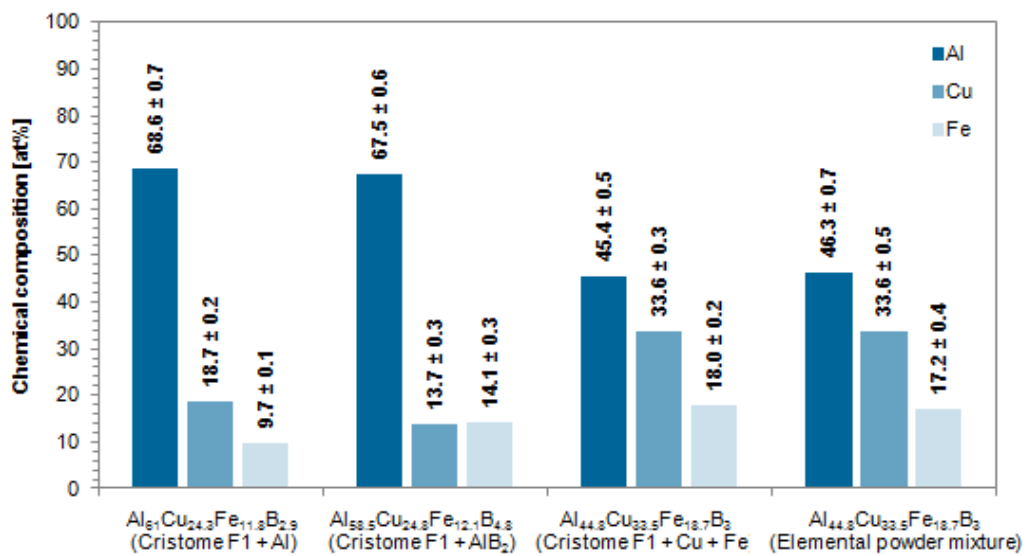


Figure 4.40 Chemical composition of the AlCuFeB shifted targets

The measured composition of the shifted composition AlCuFeB targets with *St Gobain Cristome F1* 10 – 70  $\mu\text{m}$  powder and additional Al and AlB<sub>2</sub> deviates from the composition of the initial powder composition. Both targets contain about 8 at% more Al and about 8 at% less Cu than the powder composition. The composition of the shifted composition AlCuFeB targets produced with an elemental powder mixture and with *St Gobain Cristome F1* 10 – 70  $\mu\text{m}$  powder and additional Cu + Fe corresponds with the initial powder composition. The shifted composition targets suffer from crack formation if a deposition power of more than 100 W is applied (see Figure 4.41).

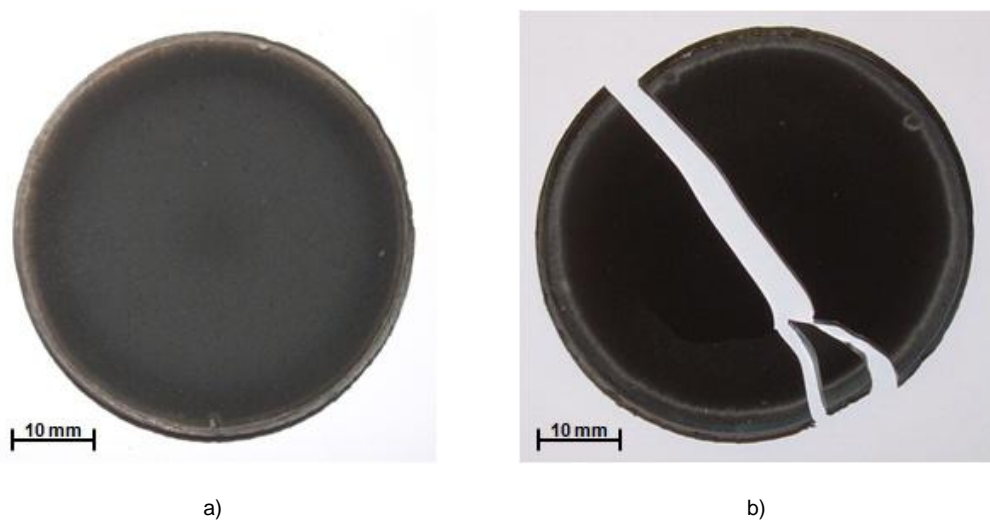


Figure 4.41 Shifted composition AlCuFeB targets after deposition  
a)  $\text{Al}_{44.8}\text{Cu}_{33.5}\text{Fe}_{18.7}\text{B}_3$  (*St Gobain Cristome F1* 10 - 70  $\mu\text{m}$  powder + Cu + Fe) after applying 100 W  
b)  $\text{Al}_{44.8}\text{Cu}_{33.5}\text{Fe}_{18.7}\text{B}_3$  (*St Gobain Cristome F1* 10 - 70  $\mu\text{m}$  powder + Cu + Fe) after applying 200 W



### 4.3.2 Coatings

For coating deposition from the shifted composition targets, RF magnetron sputtering and a working gas pressure of  $2 \cdot 10^{-3}$  mbar was used. The deposition rate  $D$  increases linearly with the applied deposition power  $P$  with  $D = 12.4 \text{ nm/min} + 0.4 \text{ nm/(min W)} P$  (see Figure 4.42).

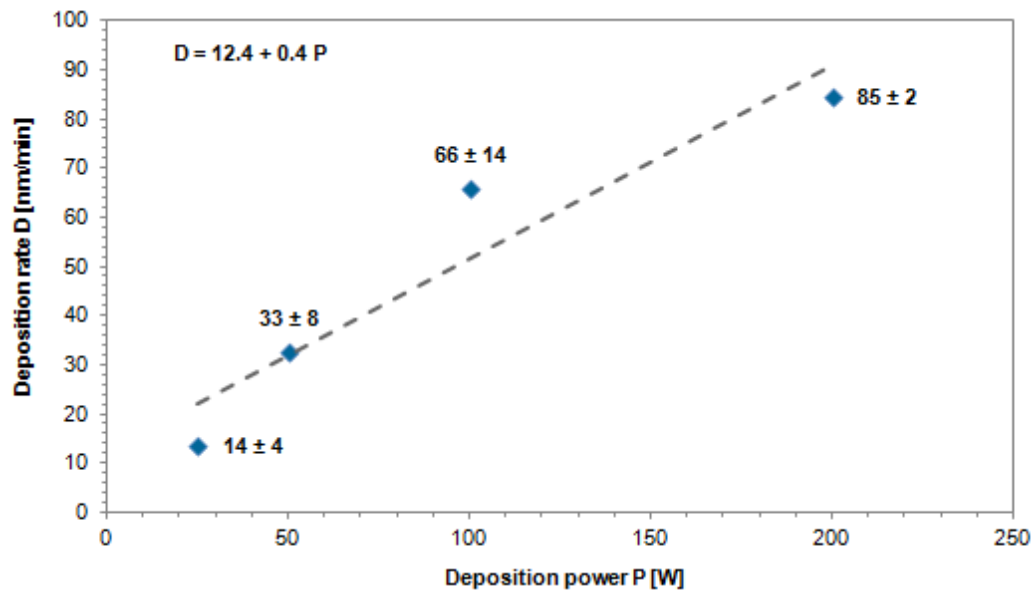


Figure 4.42 Deposition rate in dependence of the deposition power

The film thickness of all deposited samples was  $5 \mu\text{m}$  and film deposition was done on Si substrates, with a substrate-target distance of 5 cm. If a deposition power between 25 W and 200 W is applied, the target composition is reproduced and the coatings exhibit the same composition as the shifted composition targets (see Figure 4.43 and Figure 4.44).

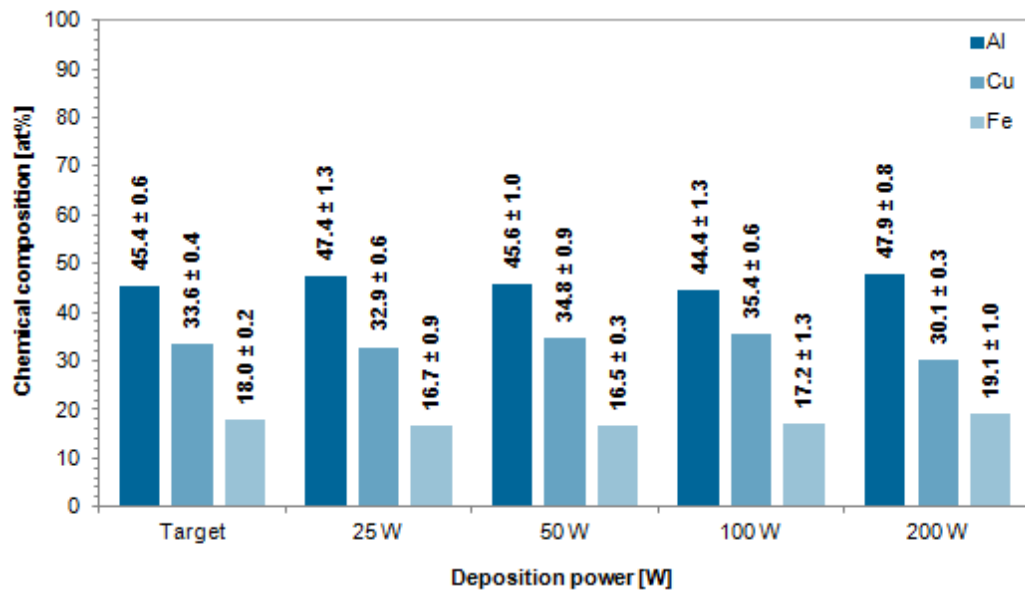


Figure 4.43 Chemical compositions of AlCuFeB coatings in dependence of the deposition power. Deposited using target  $\text{Al}_{44.8}\text{Cu}_{33.5}\text{Fe}_{18.7}\text{B}_3$  (St Gobain Cristome F1 10 - 70  $\mu\text{m}$  powder + Cu + Fe) and a working gas pressure of  $2 \cdot 10^{-3}$  mbar

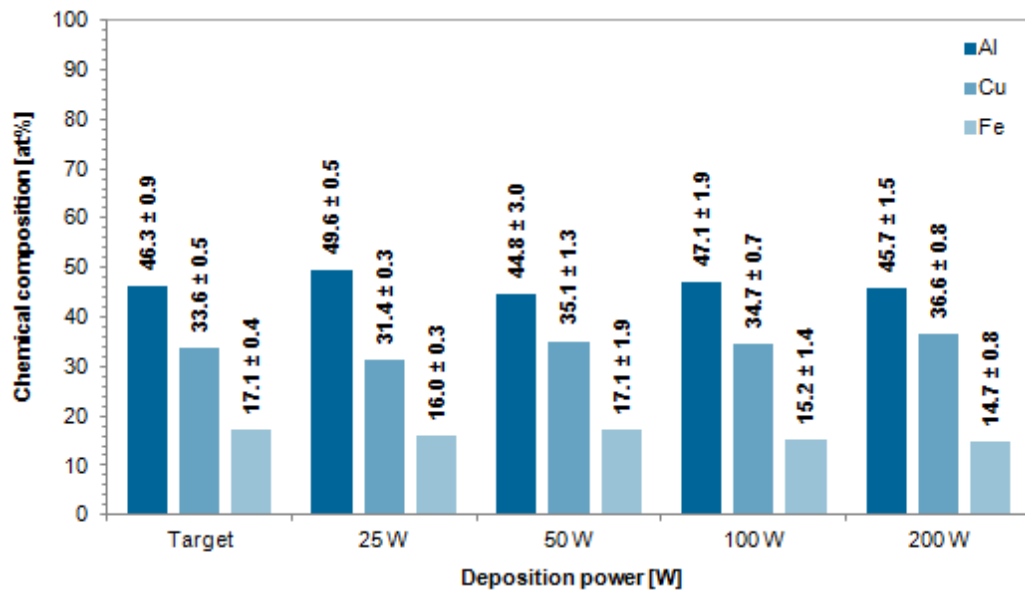


Figure 4.44 Chemical compositions of AlCuFeB coatings in dependence of the deposition power. Deposited using target  $\text{Al}_{44.8}\text{Cu}_{33.5}\text{Fe}_{18.7}\text{B}_3$  (Elemental powder mixture) and a working gas pressure of  $2 \cdot 10^{-3}$  mbar

Also the substrate temperature does not influence the coating composition in a range from 25 °C to 400 °C (see Figure 4.45 and Figure 4.46)

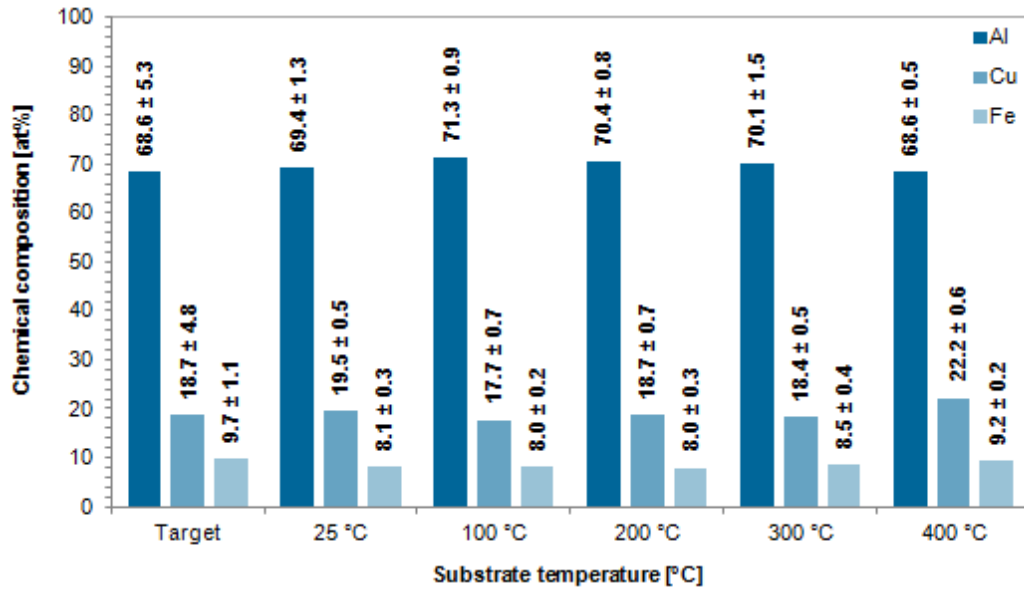


Figure 4.45 Chemical compositions of AlCuFeB coatings in dependence of the substrate temperature. Deposited using target  $\text{Al}_{61}\text{Cu}_{24.3}\text{Fe}_{11.8}\text{B}_{2.9}$  (*St Gobain Cristome F1 10 - 70 μm powder + Al*), a working gas pressure of  $2 \cdot 10^{-3}$  mbar and a deposition power of 100 W

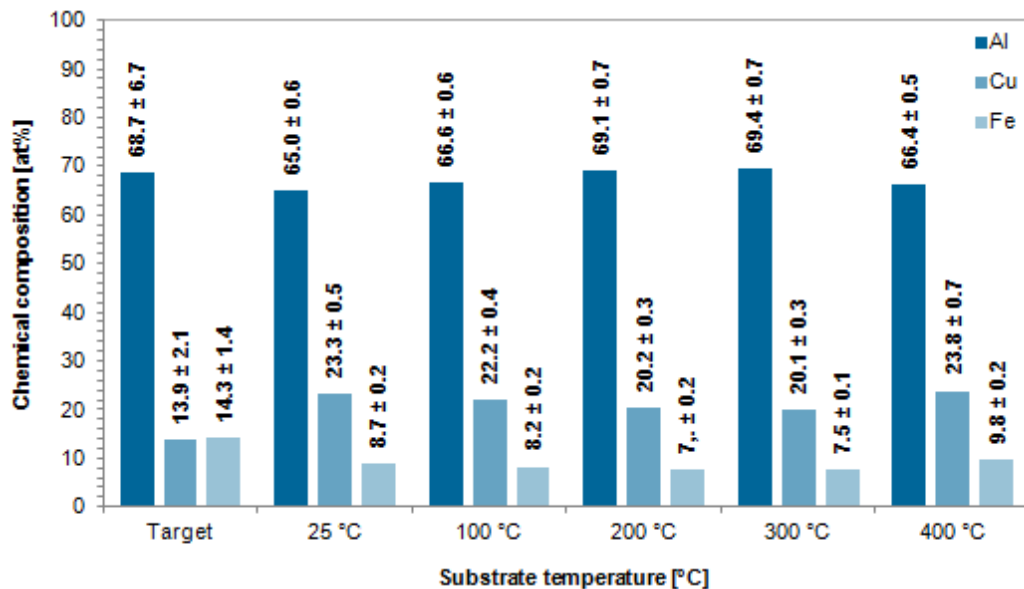


Figure 4.46 Chemical compositions of AlCuFeB coatings in dependence of the substrate temperature. Deposited using target  $\text{Al}_{61}\text{Cu}_{24.3}\text{Fe}_{11.8}\text{B}_{2.9}$  (*St Gobain Cristome F1 10 - 70 μm powder + AlB<sub>2</sub>*), a working gas pressure of  $2 \cdot 10^{-3}$  mbar and a deposition power of 100 W

By using targets with a shifted chemical composition, the crack formation in the targets during the deposition process could be prevented. Thus higher deposition powers, with respect to the ceramic AlCuFeB targets can be applied and reasonable deposition rates can be achieved. Since the target composition is reproduced in the coatings, this kind of targets cannot be used for deposition of AlCuFeB coatings, which exhibit the chemical composition necessary for the formation of the quasicrystalline phase. To overcome the problem of crack formation in the targets and to deposit coatings with the nominal composition of quasicrystalline AlCuFeB, targets were produced by hot pressing at lower temperatures (~500 °C), using an elemental powder mixture that exhibits the  $\text{Al}_{59}\text{Cu}_{25.5}\text{Fe}_{12.5}\text{B}_3$  composition.

## 4.4 AlCuFeB metallic targets

### 4.4.1 Targets

AlCuFeB targets which exhibit the  $\text{Al}_{59}\text{Cu}_{25.5}\text{Fe}_{12.5}\text{B}_3$  composition but not the quasicrystalline structure were produced with an elemental powder mixture. Since densification of the *St Gobain Cristome F1* powders is not possible at hot pressing temperatures lower than 700 °C and because the powder particles itself exhibit the quasicrystalline characteristics, the *St Gobain Cristome F1* powders were not used to produce targets that exhibit metallic characteristics. The average chemical composition of the AlCuFeB metallic targets shows about 5 at% more Al, 2.5 at% less Cu and 2.5 at% less Fe than the nominal  $\text{Al}_{59}\text{Cu}_{25.5}\text{Fe}_{12.5}\text{B}_3$  composition (see Figure 4.47). The standard deviation is about  $\pm 1.0$  at%. The target exhibits about 15 at% O and 14 at% C on the surface.

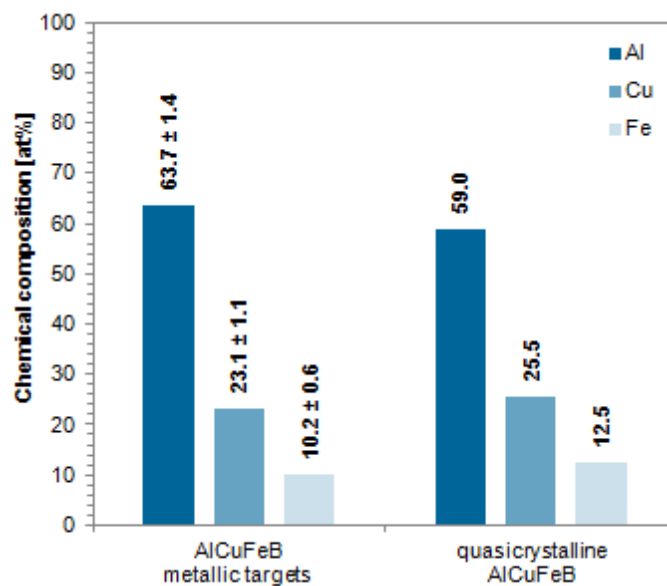


Figure 4.47 Average chemical composition of the metallic targets normalized to 97 at% in comparison with the nominal quasicrystalline AlCuFeB composition

The surface of the metallic targets is mostly flat, with some pores and rough areas (see Figure 4.48).

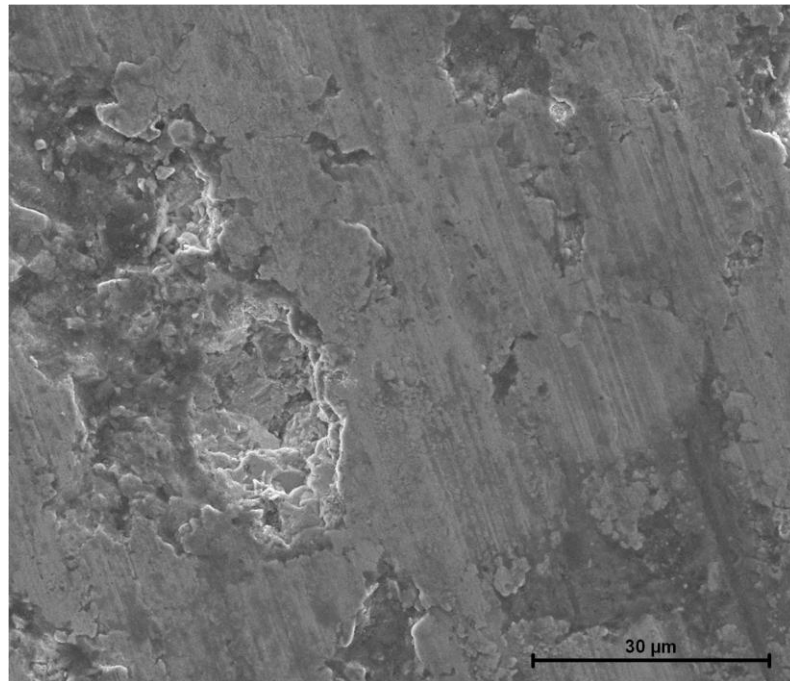


Figure 4.48 Surface of the AlCuFeB metallic targets (secondary electron SEM)

Boron does not dissolve in the target matrix and occurs in the form of B precipitates, which are uniformly allocated throughout the target (see Figure 4.49). Higher magnification (Figure 4.50) shows small pores that occur homogeneously throughout the target. By EDS and XRD seven different phases could be identified. According to the surface ratio, the dominating phases are AlCu, Al<sub>2</sub>Cu and Al<sub>7</sub>Cu<sub>2</sub>Fe. The pure Fe phase occurs as oval/round shaped islands, while the pure Al phase forms elongated areas. The shapes of the pure Al and Fe phase are similar to the corresponding powder particle shapes. The different phases seem to be homogeneously distributed.

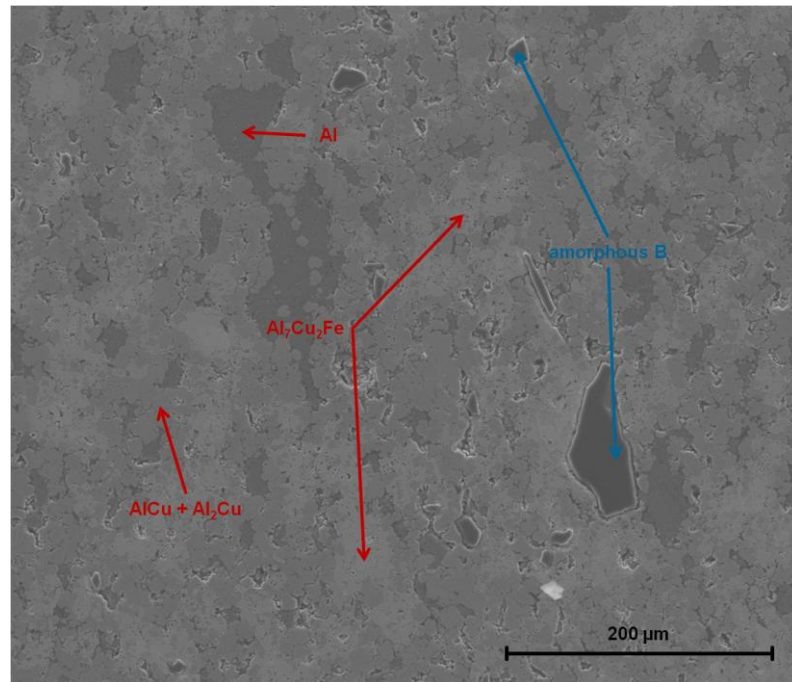


Figure 4.49 Cross section of the AlCuFeB metallic targets (secondary electron SEM)

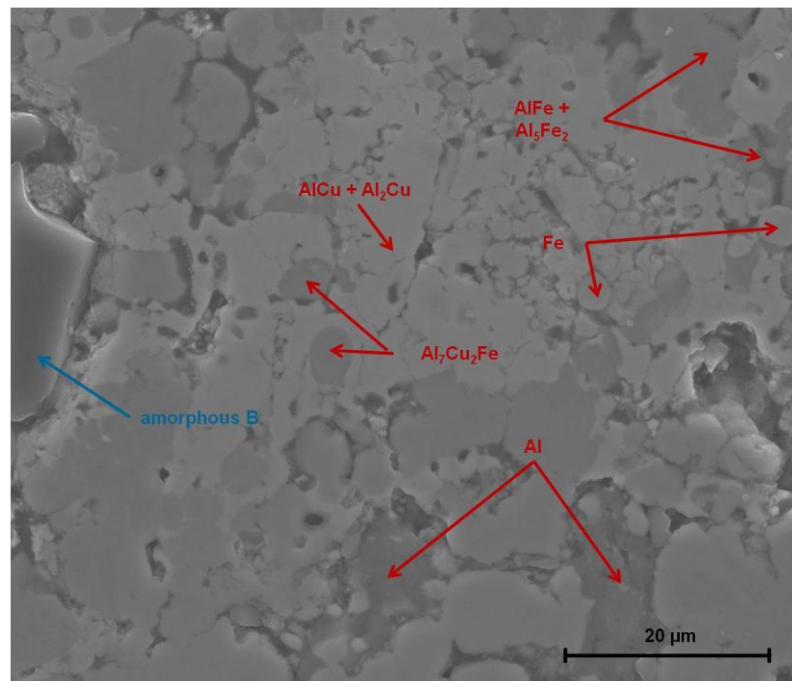


Figure 4.50 Cross section of the AlCuFeB metallic targets (secondary electron SEM)

Figure 4.51 shows the XRD pattern of the AlCuFeB metallic targets from 20° to 90°. The complex pattern consists of peaks caused by the seven phases identified in SEM cross section images in combination with EDS.

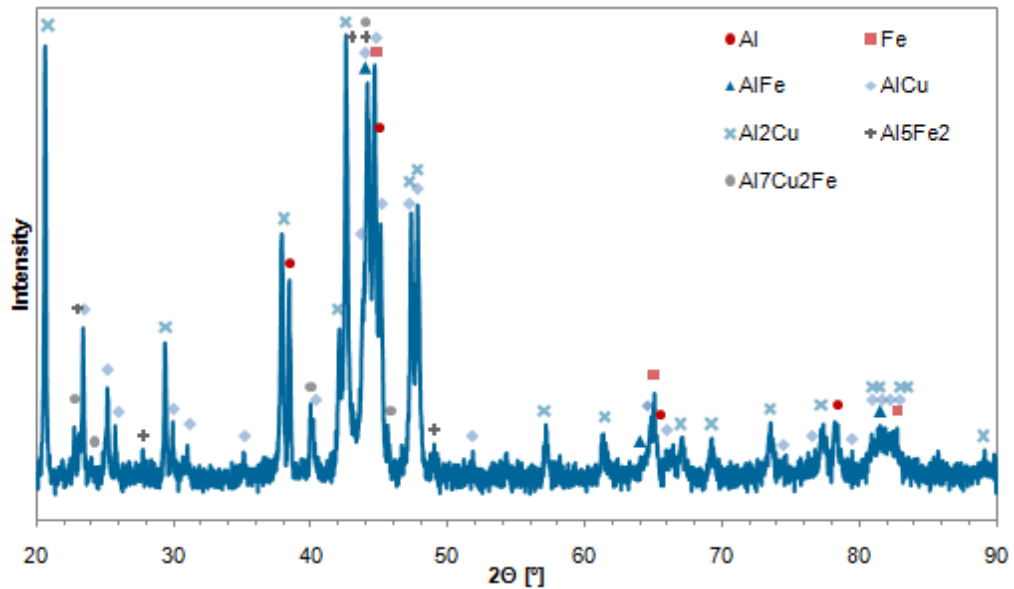


Figure 4.51 XRD pattern of the AlCuFeB metallic targets

Since the electrical conductivity of the metallic targets is good ( $1.12 \mu\Omega\text{m} \pm 0.06 \mu\Omega\text{m}$ ) DC magnetron sputtering can be applied. The metallic targets do not show any crack formation when a deposition power between 25 W and 300 W is applied (see Figure 4.52)



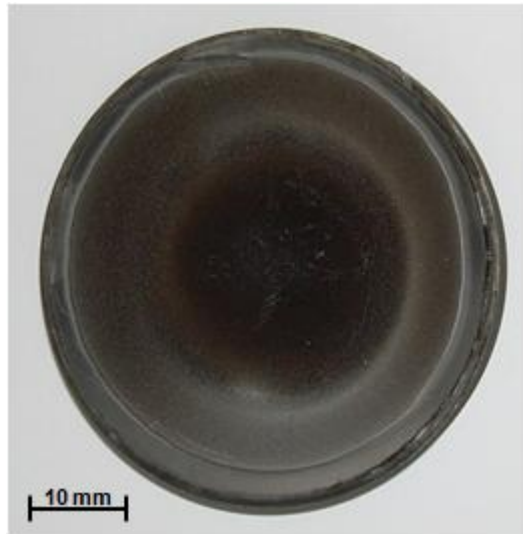


Figure 4.52 AlCuFeB metallic target after a total usage time of 80 h operated at 100 W in average and at a maximum deposition power of 300 W

During a usage time of 80 h the chemical composition of the metallic target (measured on the target surface) stays approximately constant, with an average composition of:  $64.4 \pm 1.9$  at% Al,  $23.3 \pm 2.0$  at% Cu and  $9.3 \pm 0.7$  at% Fe (see Figure 4.53). The O and C impurities found on the target surface significantly decrease from  $\sim 17$  at% O and  $\sim 13$  at% C to  $\sim 6$  at% O and  $\sim 3$  at% C after 5 min of operation (see Figure 4.54). The target was operated with 100 W and a working gas pressure of  $2 \cdot 10^{-3}$  mbar. While the chemical composition of the target measured on its surface is approximately constant after an operating time of 5 min, the chemical composition of the deposited coatings ( $5 \mu\text{m}$  on Si substrates) needs a condition time of 1 h to stay constant at:  $62.8 \pm 0.4$  at% Al,  $28.8 \pm 0.8$  at% Cu and  $8.5 \pm 1.1$  at% Fe. For operating times below 1 h, the deposited coatings exhibit a significant excess of Al and a deficit of Cu (see Figure 4.55) as well as significant O ( $\sim 30$  at%) and C ( $\sim 5$  at%) impurities, which decrease to  $\sim 5$  at% O and  $\sim 1$  at% C after 1 h of operation (see Figure 4.56).

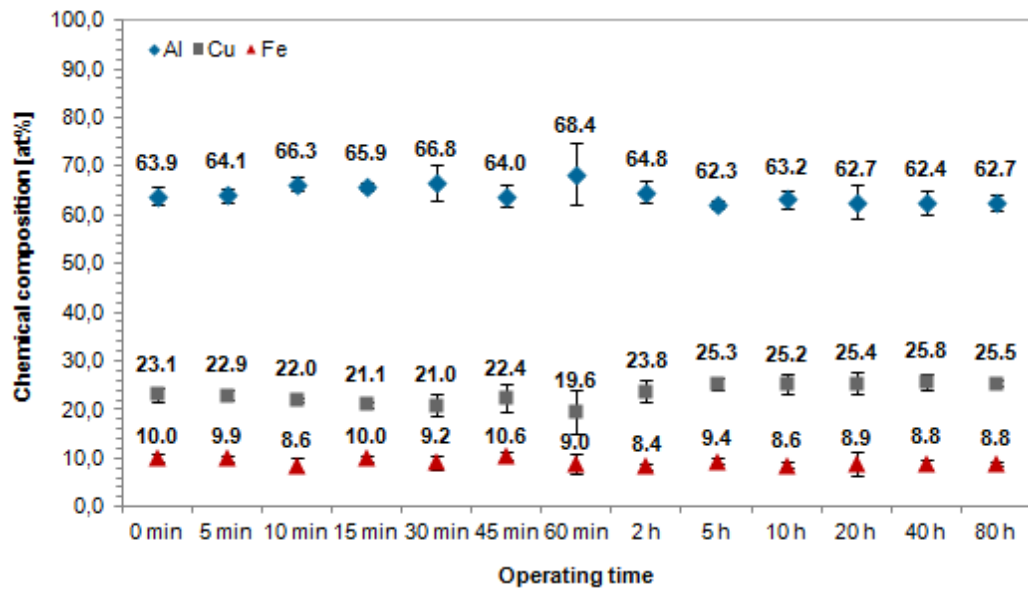


Figure 4.53 Chemical composition (EDS on surface) of the AlCuFeB metallic target in dependence on the usage time

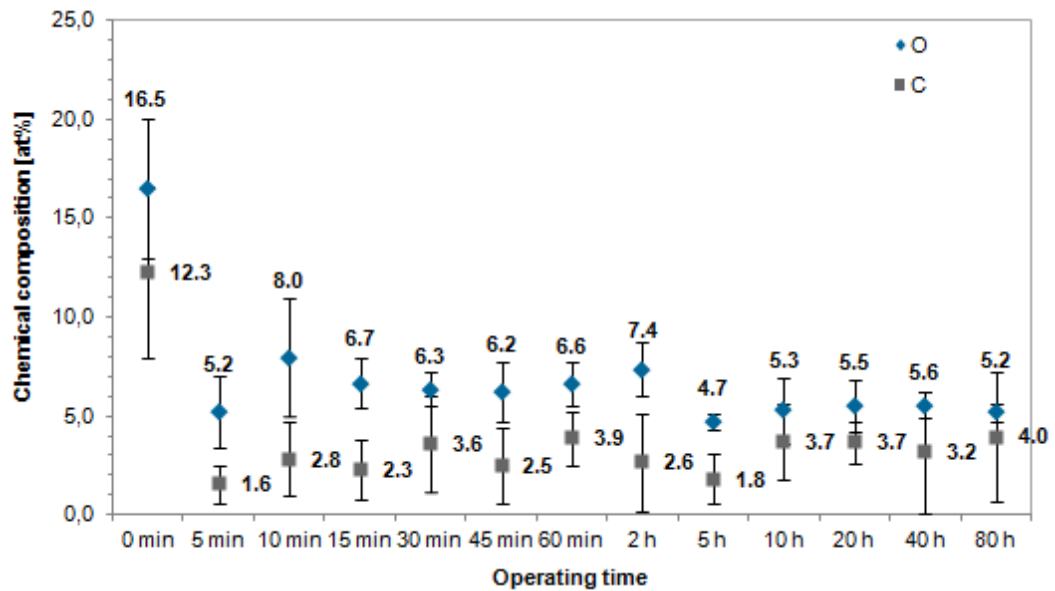


Figure 4.54 C and O impurities of the AlCuFeB metallic target (EDS on surface) in dependence on the usage time

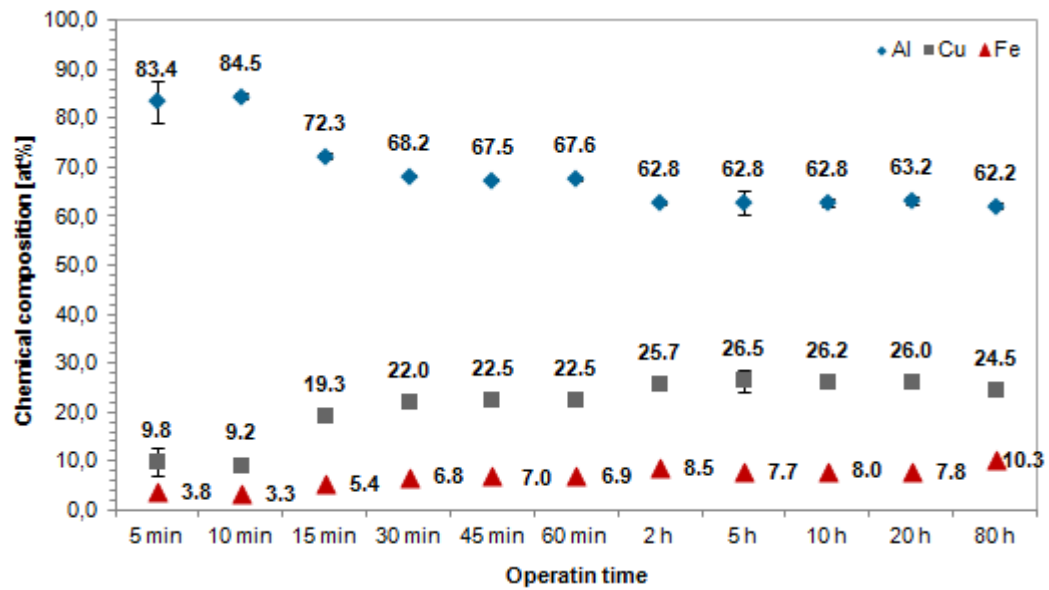


Figure 4.55 Chemical composition of the AlCuFe coatings deposited using a metallic target in dependence on the usage time

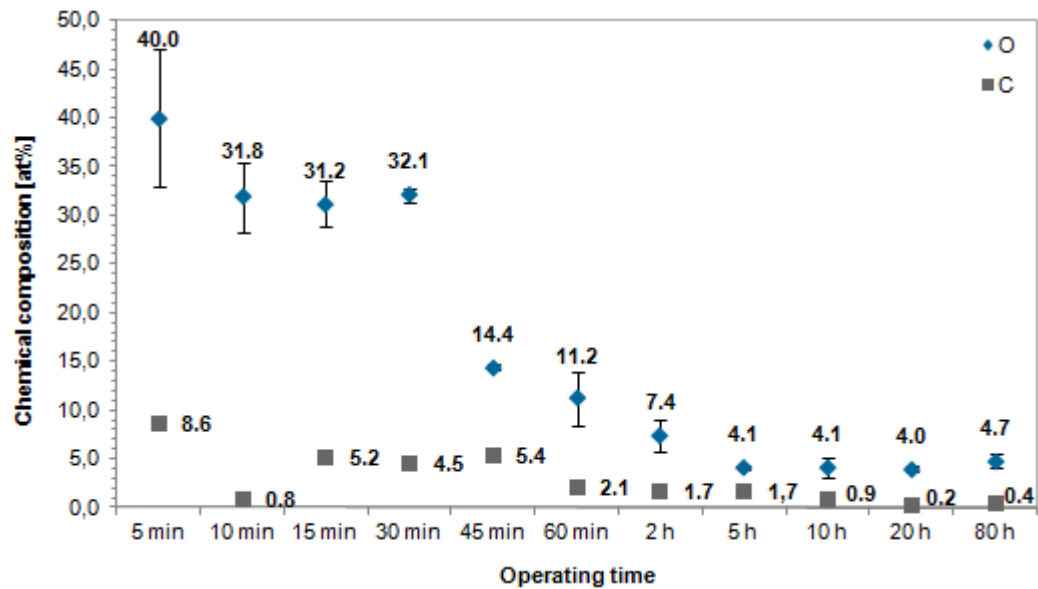


Figure 4.56 C and O impurities of the AlCuFe coatings deposited using a metallic target in dependence on the usage time

#### 4.4.2 Deposition power

Using DC magnetron sputtering, AlCuFeB coatings were deposited on Si substrates heated to 600 °C to study the influence of the deposition power on the coating composition and microstructure. The film thickness of all samples was 5 μm, the substrate – target distance 3 cm and the working gas pressure was  $2 \cdot 10^{-3}$  mbar. The achieved deposition rates are reasonable for industrial applications (see Figure 4.57). From 25 W (3.8 W/cm<sup>2</sup>) to 200 W (30.4 W/cm<sup>2</sup>) the deposition rate  $D$  increases linearly with the applied deposition power  $P$  with  $D = 24.3 \text{ nm/min} + 0.73 \text{ nm}/(\text{min W}) P$ . If more than 200 W (30.4 W/cm<sup>2</sup>) are applied, the deposition rate starts to decrease.

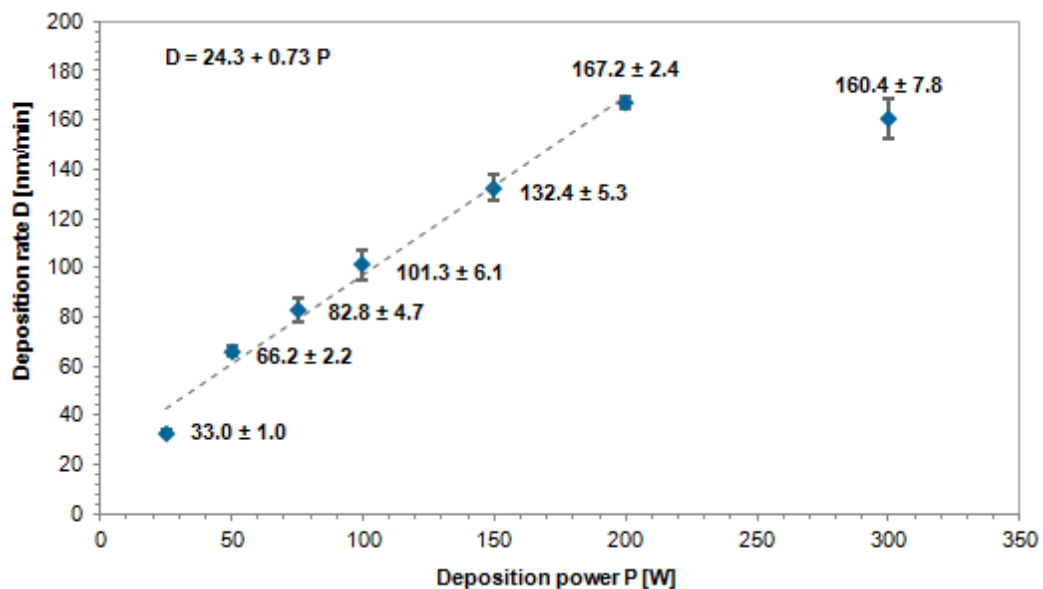


Figure 4.57 Deposition rate in dependence on the deposition power for AlCuFeB metallic targets

If a deposition power of less than 200 W (30.4 W/cm<sup>2</sup>) is applied, the coating composition statistically varies about: Al  $63.7 \pm 1.7$  at%, Cu  $24.0 \pm 1.4$  at%, Fe  $9.4 \pm 0.5$  at%, which corresponds very well with the composition of the target used: Al  $64.2 \pm 2.3$  at%, Cu  $22.0 \pm 1.5$  at%, Fe  $10.9 \pm 0.8$  at. If a deposition power of 200 W (30.4 W/cm<sup>2</sup>) or more is applied, The Al content significantly increases to ~80 at%, while the Cu content decreases to ~8 at% (see Figure 4.58).

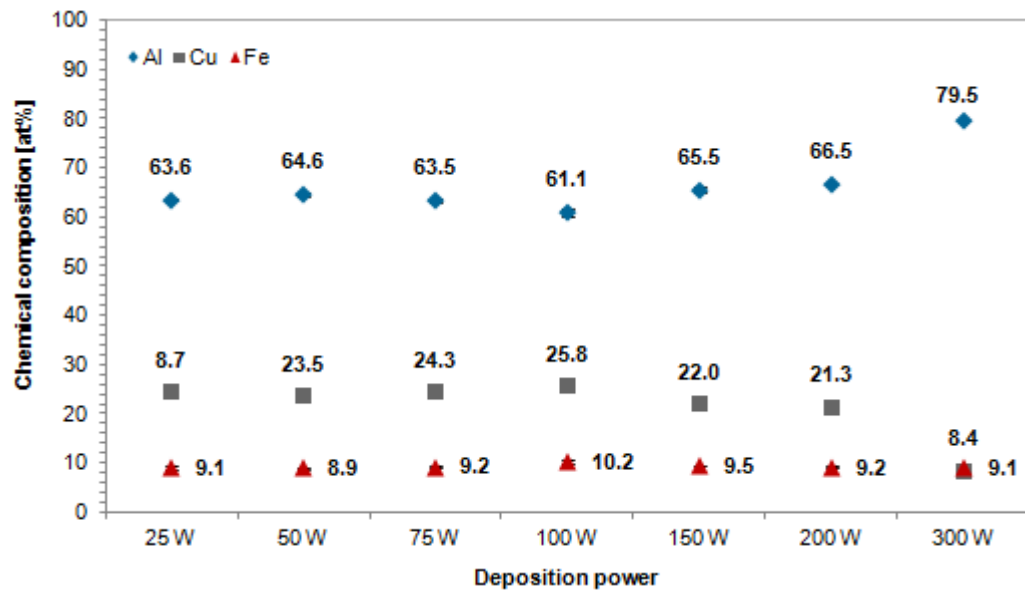


Figure 4.58 Coating composition in dependence on the deposition power for AlCuFeB metallic targets

The C content measured on the coating surface decreases from about 5 at% for a deposition power of 25 W ( $3.8 \text{ W/cm}^2$ ) to  $\sim 2$  at% for deposition powers of more than 50 W ( $7.6 \text{ W/cm}^2$ ) (see Figure 4.59). The O content measured on the coating surface is about 6 at% for deposition powers up to 200 W ( $30.4 \text{ W/cm}^2$ ). For 300 W ( $45.6 \text{ W/cm}^2$ ) the O content increases to about 12 at%. Up to a deposition power of 150 W ( $22.8 \text{ W/cm}^2$ ) practically no Si can be found on the coating surface. With higher deposition powers an increasing content of Si can be found on the coating surface:  $\sim 3$  at% for 200 W ( $30.4 \text{ W/cm}^2$ ) and  $\sim 15$  at% for 300 W ( $45.6 \text{ W/cm}^2$ ).

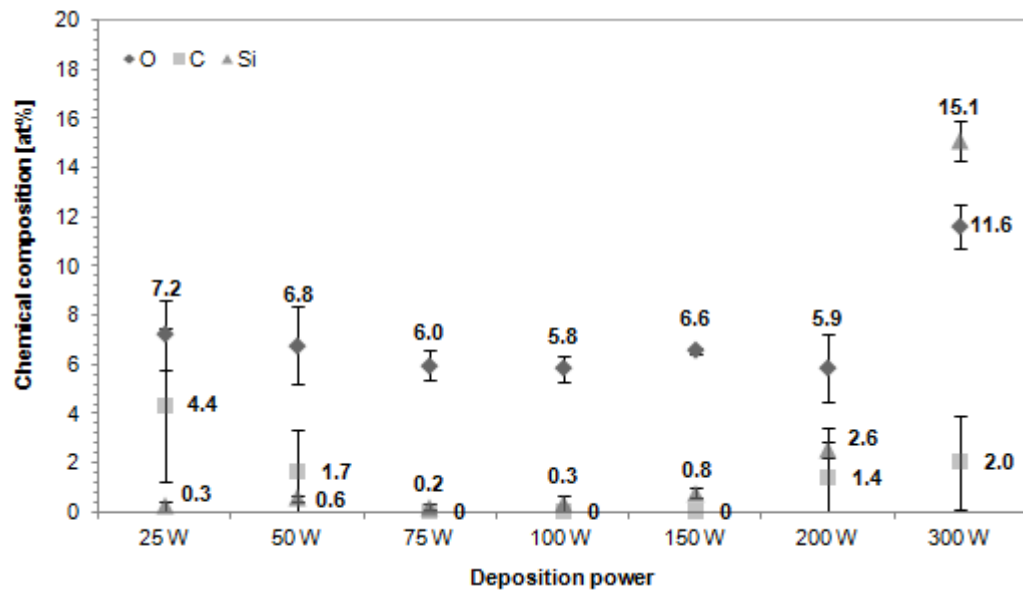


Figure 4.59 O, C and Si content on the coating surface in dependence on the deposition power for AlCuFeB metallic targets

If deposition is done on Si substrates heated to 600 °C, the intensity of the quasicrystalline AlCuFe peaks (QC) is maximized if a deposition power of 200 W is applied (see Figure 4.60). A maximum content of quasicrystalline phase (~45%) is achieved for a deposition power of 200 W. Applying more than 200 W reduces the intensities of the quasicrystalline AlCuFe peaks (QC) and peaks originating from the Si substrates (Si) appear (see Figure 4.61).

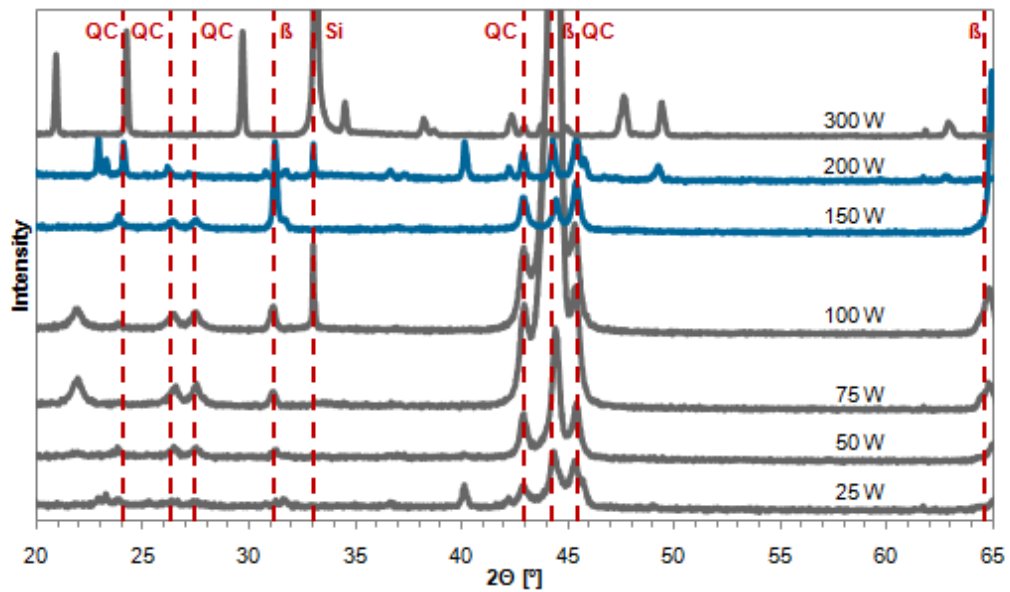


Figure 4.60 XRD pattern of AlCuFeB coatings in dependence on the applied deposition power (Cu anode  $\lambda = 1.542 \text{ \AA}$ )

QC = quasicrystalline AlCuFe,  $\beta = \text{Al}_{50}\text{Cu}_{40}\text{Fe}_{10}$   $\beta$  phase, Si = Si substrate

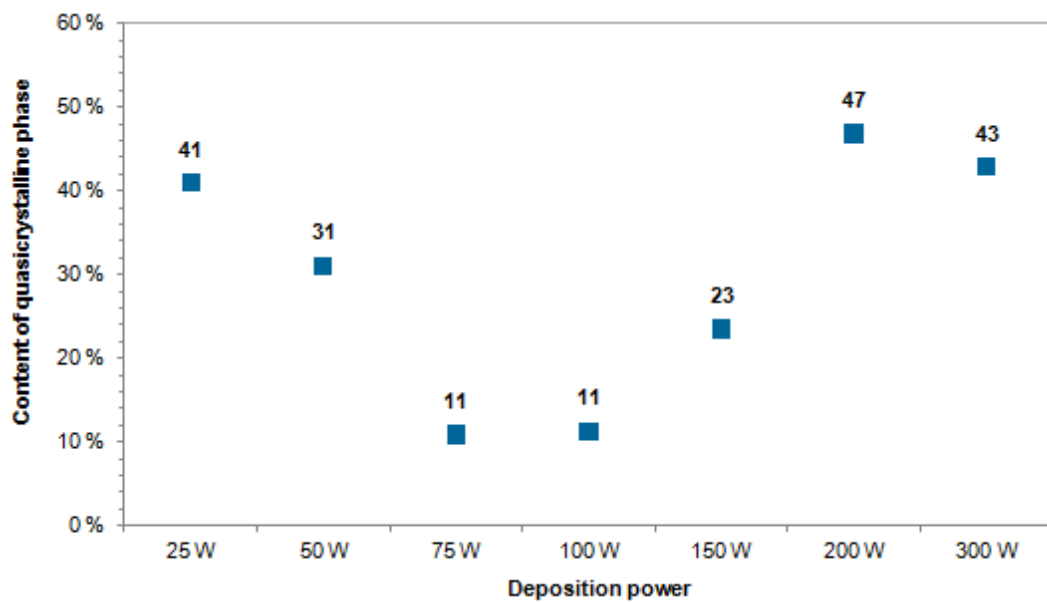


Figure 4.61 Amount of quasicrystalline phase in the deposited AlCuFeB coatings in dependence on the deposition power. The amount of quasicrystalline phase was estimated using the XRD peak intensities, see Relation 4.1 (Cu anode  $\lambda = 1.542 \text{ \AA}$ ).

#### 4.4.3 Working distance (target – substrate distance)

Using DC magnetron sputtering, AlCuFeB coatings were deposited on Si substrates heated to 600 °C to study the influence of the target – substrate distance (working distance) on the coating composition and microstructure. The film thickness of all samples was 5  $\mu\text{m}$ , the deposition power was 200 W (30.4 W/cm<sup>2</sup>) and the working gas pressure was  $10 \cdot 10^{-3}$  mbar. Figure 4.62 shows the measured deposition rate in dependence on the working distance in comparison with results of a simulation based on purely geometric considerations (gas phase scattering is neglected) [74].

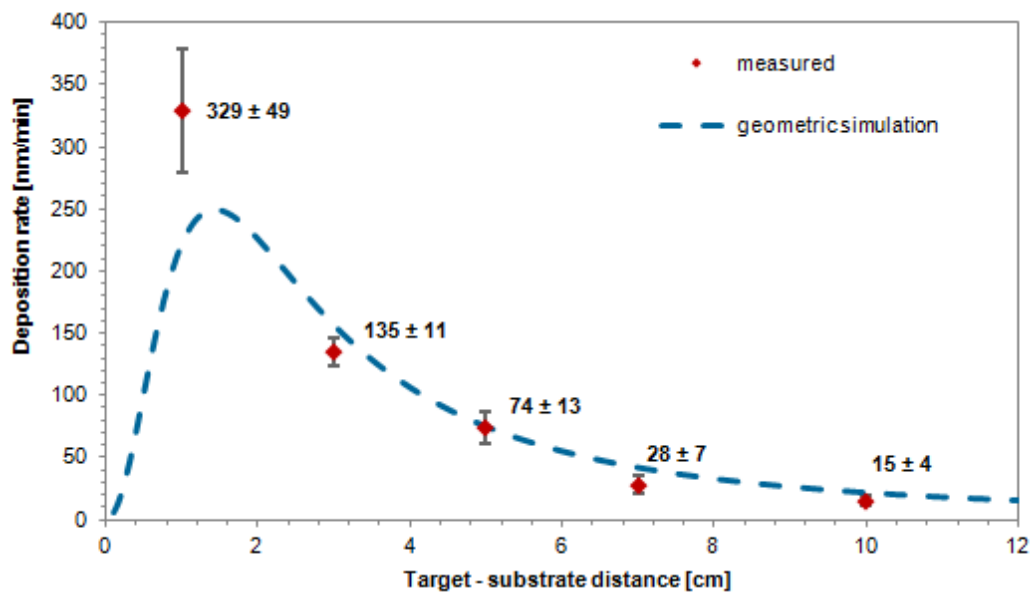


Figure 4.62 Deposition rate in dependence on the deposition power for AlCuFeB metallic targets

Within the error of measurement the chemical composition of the target is reproduced for target – substrate distances up to 5 cm (see Figure 4.63). For higher working distances, the Al content of the coatings slightly decreases ( $\sim 2\text{at}\%$ ). None of the deposited coatings showed a significant Si content on the surface. Within the error of measurement, the O and C content of the deposited coatings is independent of the working distance. In average the coatings exhibit 1 at% O and 5 at% C.



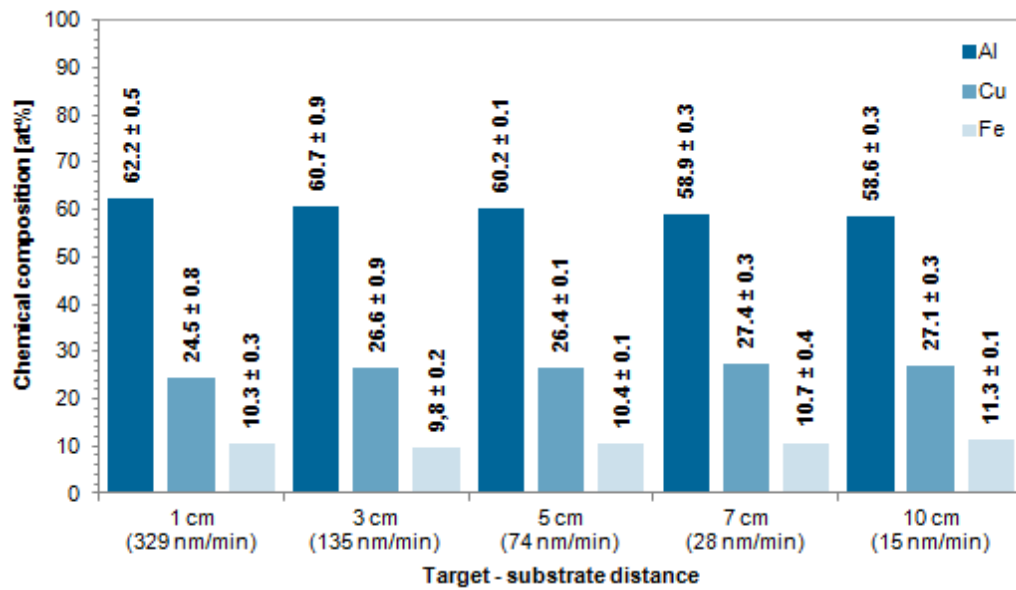


Figure 4.63 Coating composition in dependence on the target – substrate distance

If deposition is done on Si substrates heated to 600 °C, the intensity of the quasicrystalline AlCuFe peaks (QC) and the amount of quasicrystalline phase are maximized if the working distance is 3 cm (deposition rate 135 nm/min). For higher and lower working distances, the  $\text{Al}_{50}\text{Cu}_{40}\text{Fe}_{10}$   $\beta$  phase ( $\beta$ ) content increases (see Figure 4.64 and Figure 4.65).

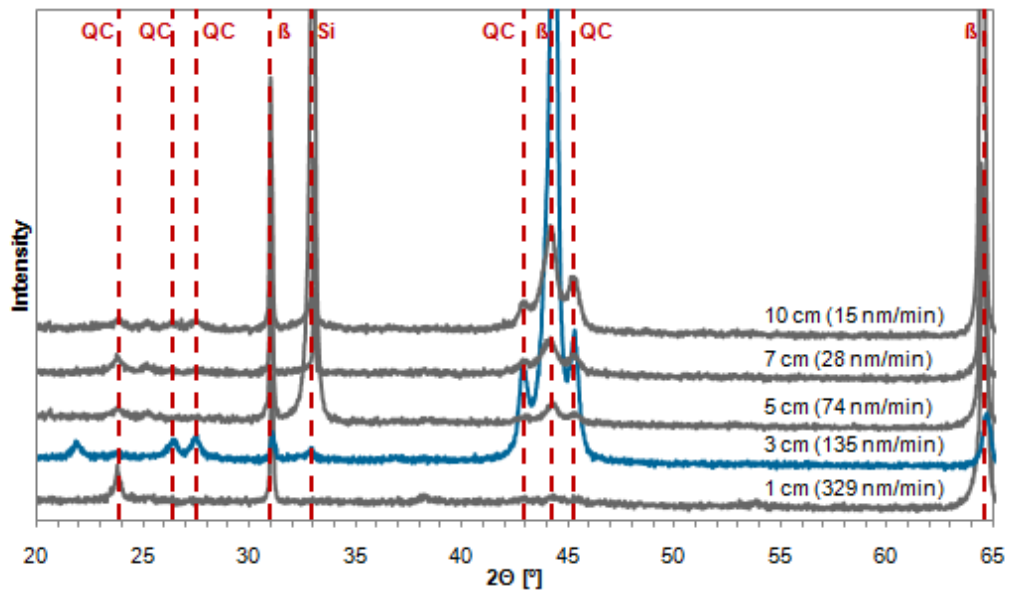


Figure 4.64 XRD pattern of AlCuFeB coatings in dependence on the working distance (Cu anode  $\lambda = 1.542 \text{ \AA}$ ).

QC = quasicrystalline AlCuFe,  $\beta = \text{Al}_{50}\text{Cu}_{40}\text{Fe}_{10}$   $\beta$  phase, Si = Si substrate

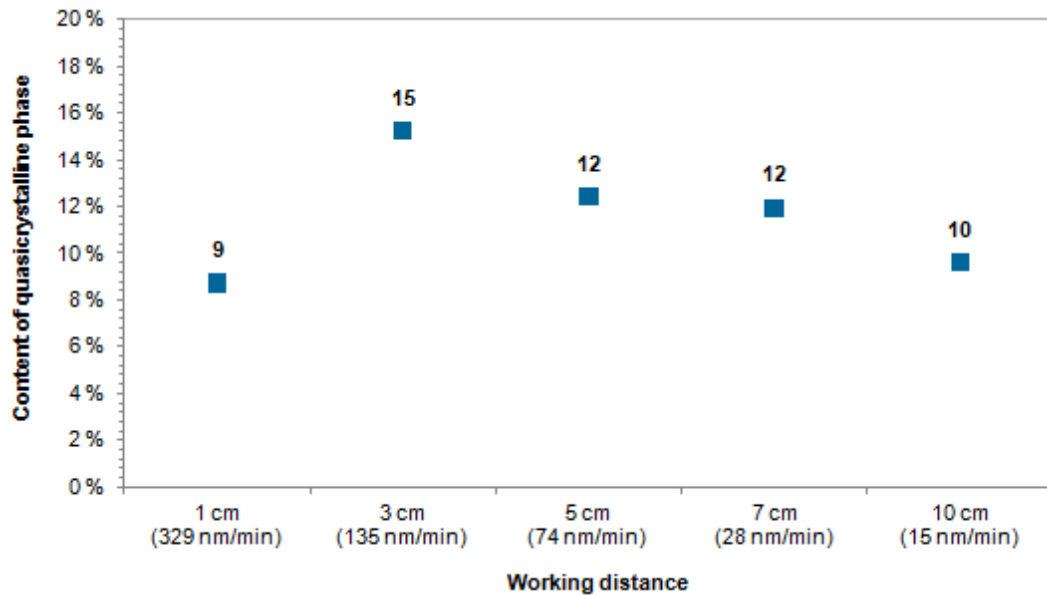


Figure 4.65 Amount of quasicrystalline phase in the deposited AlCuFeB coatings in dependence on the working distance. The amount of quasicrystalline phase was estimated using the XRD peak intensities, see Relation 4.1 (Cu anode  $\lambda = 1.542 \text{ \AA}$ ).

#### 4.4.4 Substrate temperature

To study the influence of the substrate temperature on the coating composition and microstructure, AlCuFeB coatings were deposited on heated Si substrates. The film thickness of all samples was 5  $\mu\text{m}$ , the deposition power was 200 W (30.4 W/cm<sup>2</sup>), the working distance was 3 cm and the working gas pressure was  $10 \cdot 10^{-3}$  mbar. No influence of the substrate temperature during deposition on the coating composition could be found (see Figure 4.66). The average coating composition is: Al  $63.8 \pm 1.1$  at%, Cu  $23.2 \pm 0.7$  at%, Fe  $10.1 \pm 0.4$  at%, which corresponds very well with the composition of the target used: Al  $64.2 \pm 2.3$  at%, Cu  $22.0 \pm 1.5$  at%, Fe  $10.9 \pm 0.8$  at. On the coating surface, no C was detected and an O content of  $\sim 7$  at% was found.

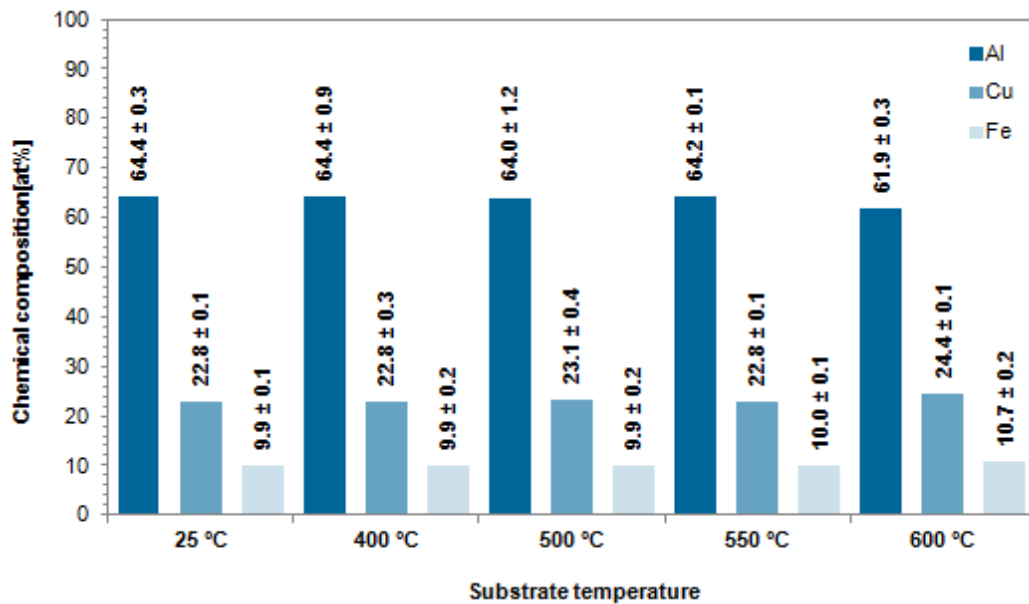


Figure 4.66 AlCuFeB coating composition in dependence on the substrate temperature

For deposition on substrate at room temperature, amorphous coatings develop. For substrate temperatures below 500 °C only a broad Al peak is visible in the XRD pattern. If a substrate temperature of 550 °C is applied, the quasicrystalline phase starts to develop (see Figure 4.67).

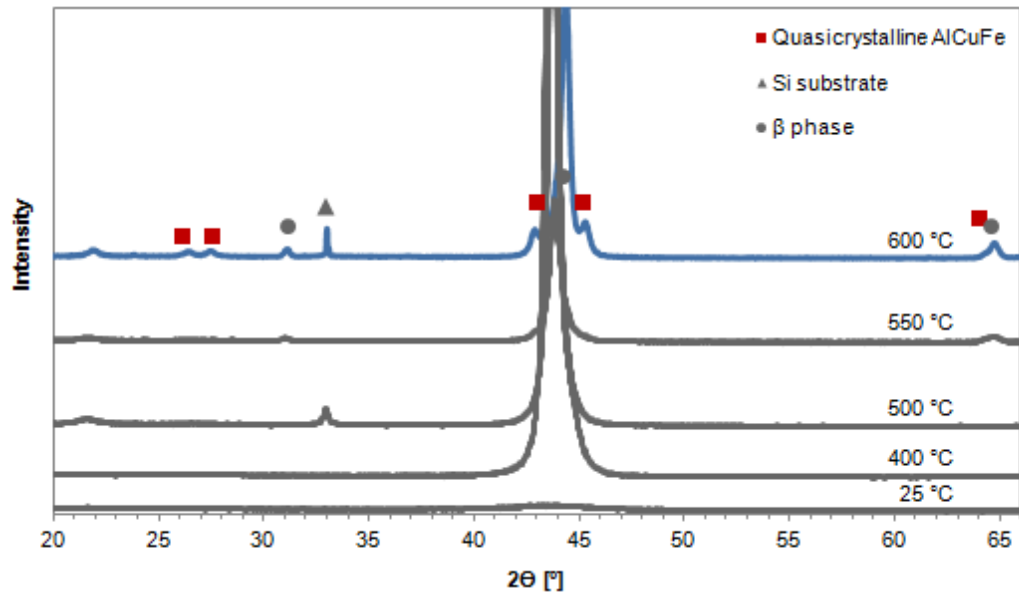


Figure 4.67 XRD pattern of AlCuFeB coatings in dependence on the substrate temperature

#### 4.4.5 Working gas pressure

To study the influence of the working gas pressure on the coating composition and microstructure, AlCuFeB coatings were deposited on Si substrates heated to 600 °C. The film thickness of all samples was 5  $\mu\text{m}$ , the deposition power was 100 W (30.4 W/cm<sup>2</sup>) and the working distance was 5 cm. The working gas pressure was varied between  $2 \cdot 10^{-3}$  mbar and  $20 \cdot 10^{-3}$  mbar. Within this range and the chosen working distance, the deposition rate seems not to be influenced by the working gas pressure (see Figure 4.68).

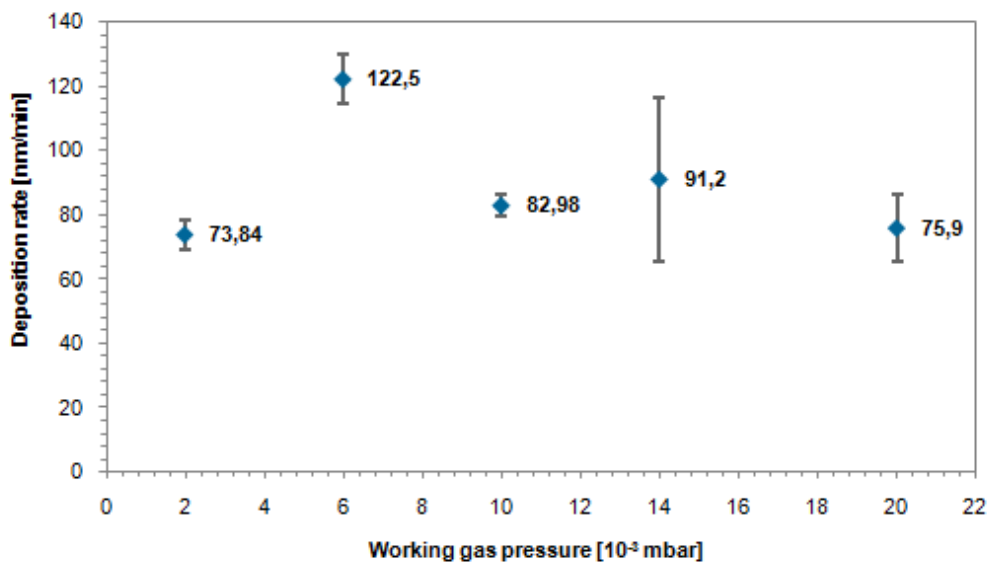


Figure 4.68 Deposition rate in dependence on the working gas pressure for AlCuFeB metallic targets

Within the error of measurement, the working gas pressure does not influence the chemical composition of the deposited coatings in a range of  $2 \cdot 10^{-3}$  to  $20 \cdot 10^{-3}$  mbar (see Figure 4.69). The coating composition statistically varies about: Al  $63.5 \pm 0.6$  at%, Cu  $22.7 \pm 0.6$  at%, Fe  $10.8 \pm 0.6$  at%, which corresponds very well with the composition of the target used: Al  $64.2 \pm 2.3$  at%, Cu  $22.0 \pm 1.5$  at%, Fe  $10.9 \pm 0.8$  at. The oxygen content on the coating surface is about 6 at% and the C content about 3 at%, both are independent of the applied working gas pressure. No Si can be found on the coating surface.

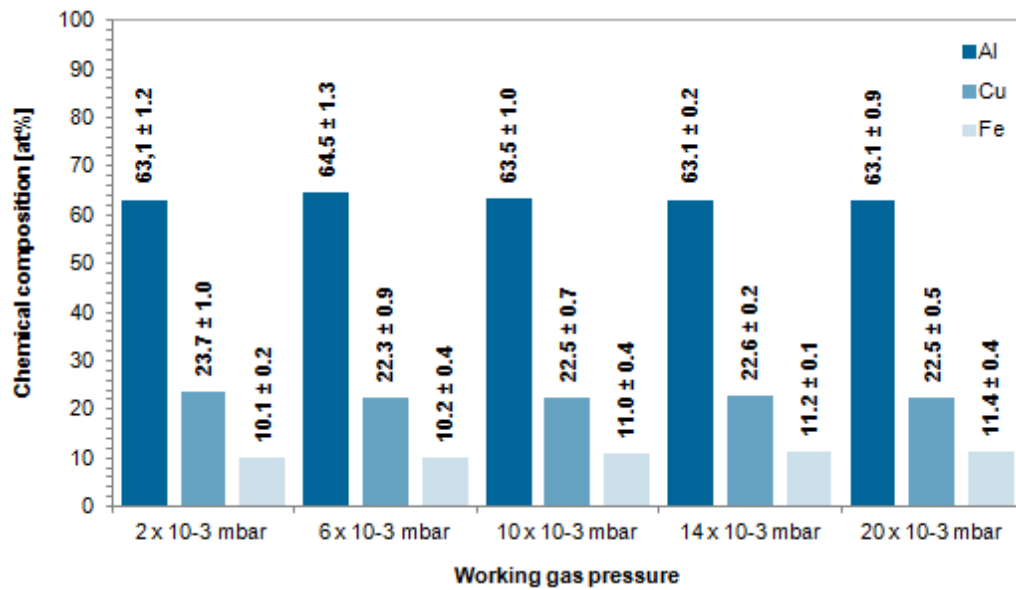


Figure 4.69 Coating composition of AlCuFeB coatings in dependence on the working gas pressure

If deposition is done on Si substrates heated to 600 °C, the intensity of the quasicrystalline AlCuFe peaks (QC) and the amount of quasicrystalline phase in the deposited coatings is maximized if a working gas pressure of  $10 \cdot 10^{-3}$  mbar is used (see Figure 4.70 and Figure 4.71).

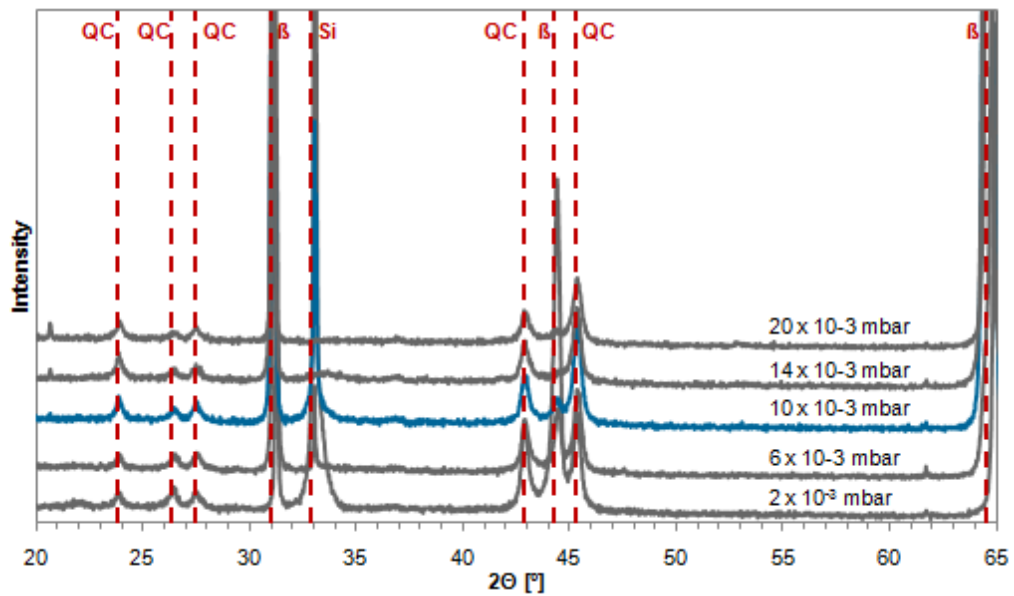


Figure 4.70 XRD pattern of AlCuFeB coatings in dependence on the working gas pressure (Cu anode  $\lambda = 1.542 \text{ \AA}$ ).

QC = quasicrystalline AlCuFe,  $\beta = \text{Al}_{50}\text{Cu}_{40}\text{Fe}_{10}$   $\beta$  phase, Si = Si substrate

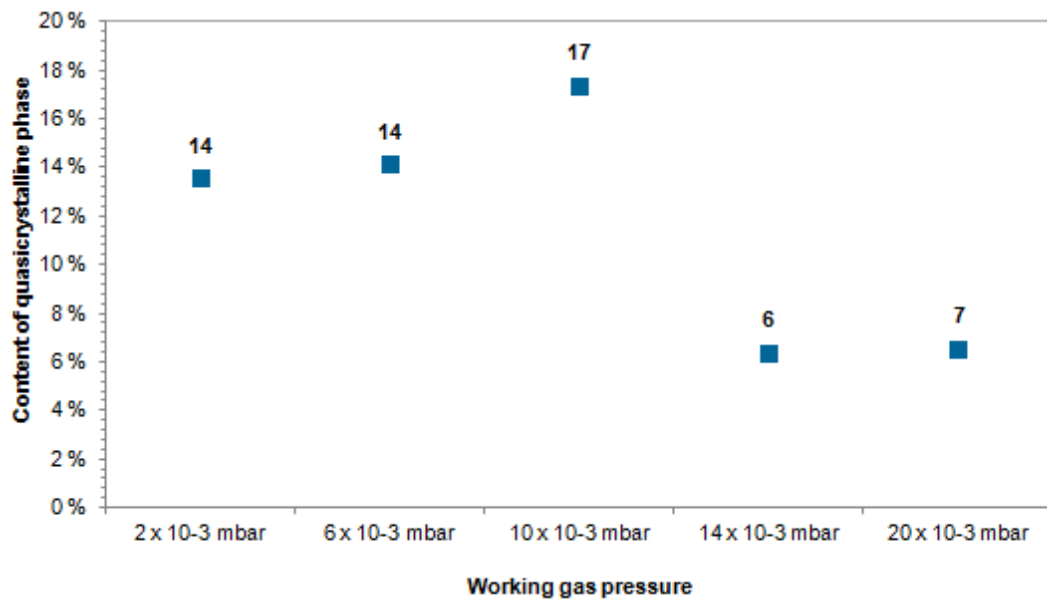


Figure 4.71 Amount of quasicrystalline phase in the deposited AlCuFeB coatings in dependence on the working gas pressure. The amount of quasicrystalline phase was estimated using the XRD peak intensities, see Relation 4.1 (Cu anode  $\lambda = 1.542 \text{ \AA}$ ).

#### 4.4.6 Bias voltage

Using a deposition power of 200 W, a working distance of 3 cm, a substrate temperature of 600 °C and a working gas pressure of  $10 \cdot 10^{-3}$  mbar (optimum deposition parameters so far), 5  $\mu\text{m}$  thick AlCuFeB coatings were deposited on Si substrates. On the substrate different bias voltages (0 V, 25 V, 50 V, 75 V, 100 V) were applied. Within this range, the deposition rate of  $\sim 130$  nm/min was not influenced by the bias voltage. Within the error of measurement, no influence of the bias voltage on the chemical composition of the AlCuFeB coatings could be detected (see Figure 4.72). In average the coating composition is:  $60.4 \pm 2.2$  at% Al,  $26.7 \pm 1.7$  at% Cu,  $9.9 \pm 0.7$  at% Fe. The O content of the coatings is about 5 at% and the C content about 2 at%.

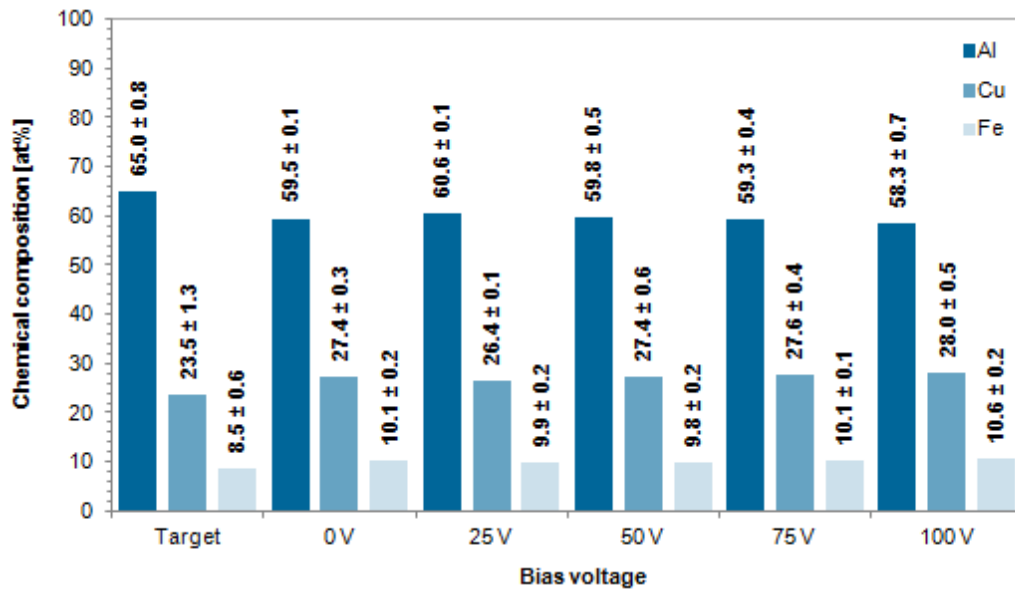


Figure 4.72 Coating composition in dependence on the bias voltage for AlCuFeB metallic targets.

If deposition is done using a bias voltage of 75 V, the intensity of the quasicrystalline AlCuFe peaks (QC) and the amount of quasicrystalline phase in the deposited coatings is maximized (see Figure 4.73 and Figure 4.74).



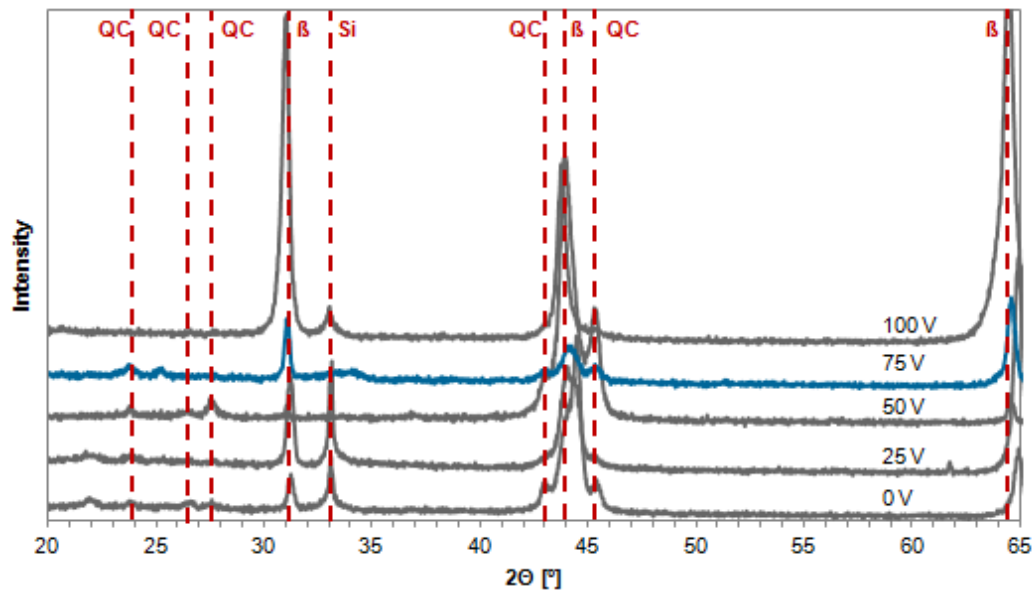


Figure 4.73 XRD pattern of AlCuFeB coatings in dependence on the bias voltage (Cu anode  $\lambda = 1.542 \text{ \AA}$ ).

QC = quasicrystalline AlCuFe,  $\beta = \text{Al}_{50}\text{Cu}_{40}\text{Fe}_{10}$   $\beta$  phase, Si = Si substrate

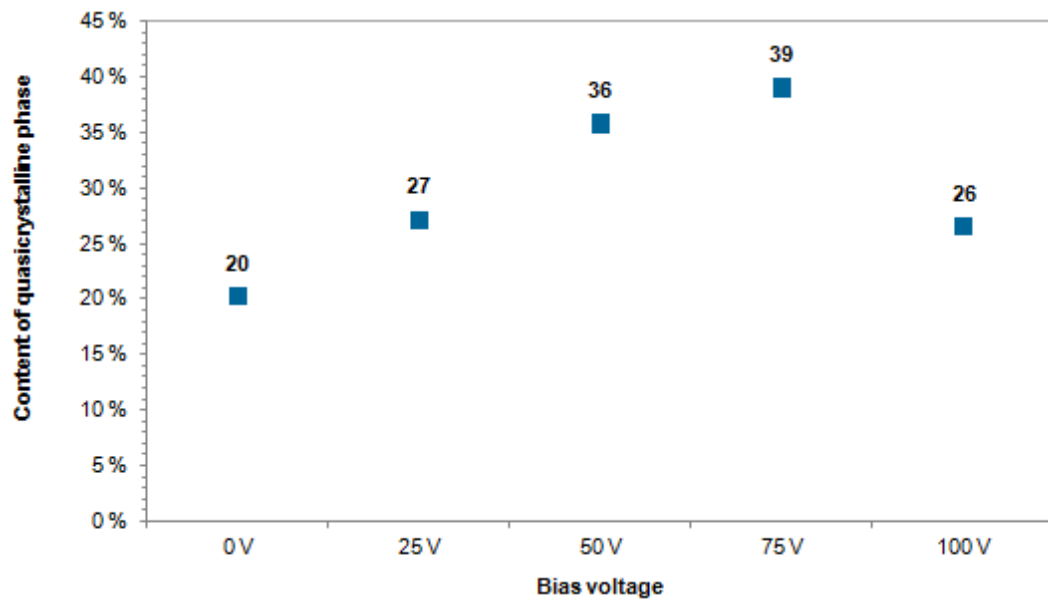


Figure 4.74 Amount of quasicrystalline phase in the deposited AlCuFeB coatings in dependence on the bias voltage, see Relation 4.1. The amount of quasicrystalline phase was estimated using the XRD peak intensities. (Cu anode  $\lambda = 1.542 \text{ \AA}$ )

#### 4.4.7 Optimised AlCuFeB coatings

Using the optimised deposition parameters (see Table 4.1) AlCuFeB coatings were deposited on different substrates (see Section 3.4): epitaxial Si, hard metal WC-Co, steel K600, steel K890 and ceramic Al<sub>2</sub>O<sub>3</sub> (99.5% Al<sub>2</sub>O<sub>3</sub>).

Table 4.1 Optimised parameters for deposition of AlCuFeB coatings using a metallic target

---

Deposition power	200 W
Working distance (target – substrate distance)	3 cm
Substrate temperature	600 °C
Working gas (Ar) pressure	10 x 10 <sup>-3</sup> mbar
Bias voltage	75 V
Deposition rate	130 nm/min

---

Adhesion of the AlCuFeB coatings is good (see Figure 4.75) for all substrates except Si.

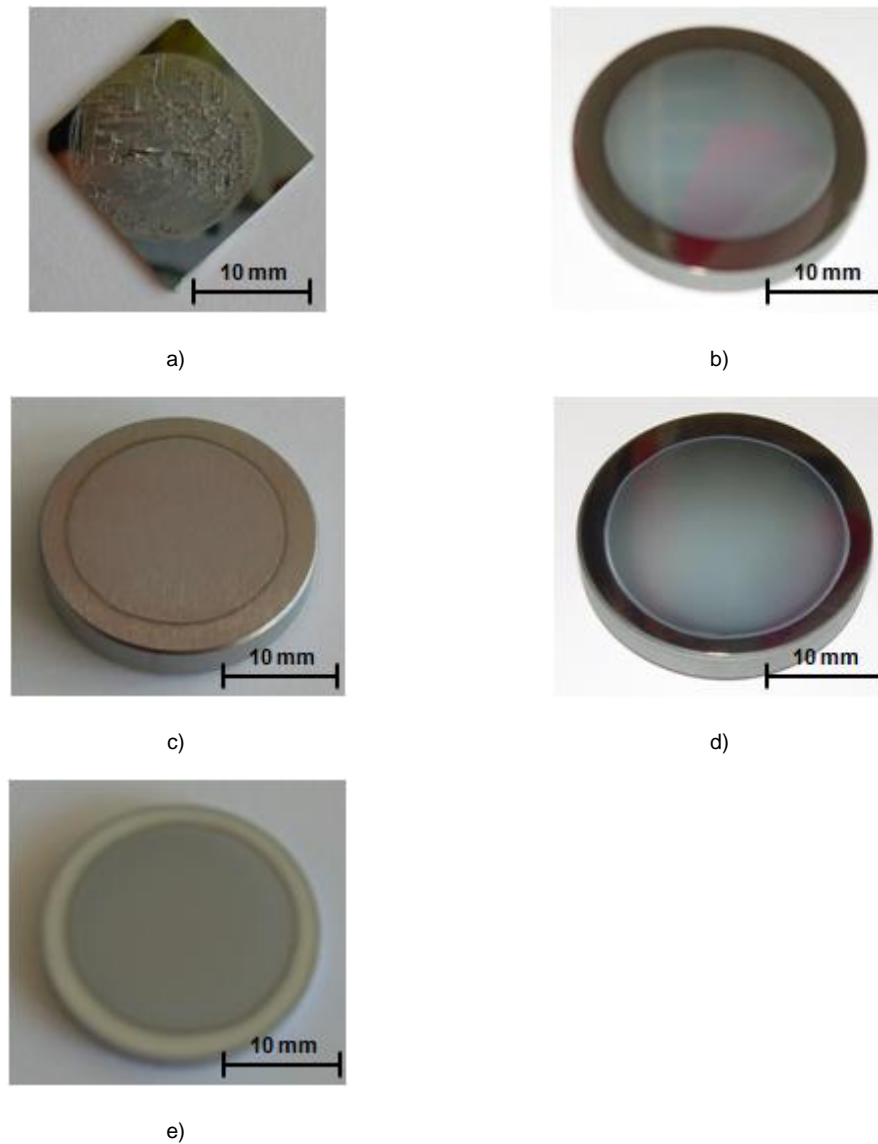
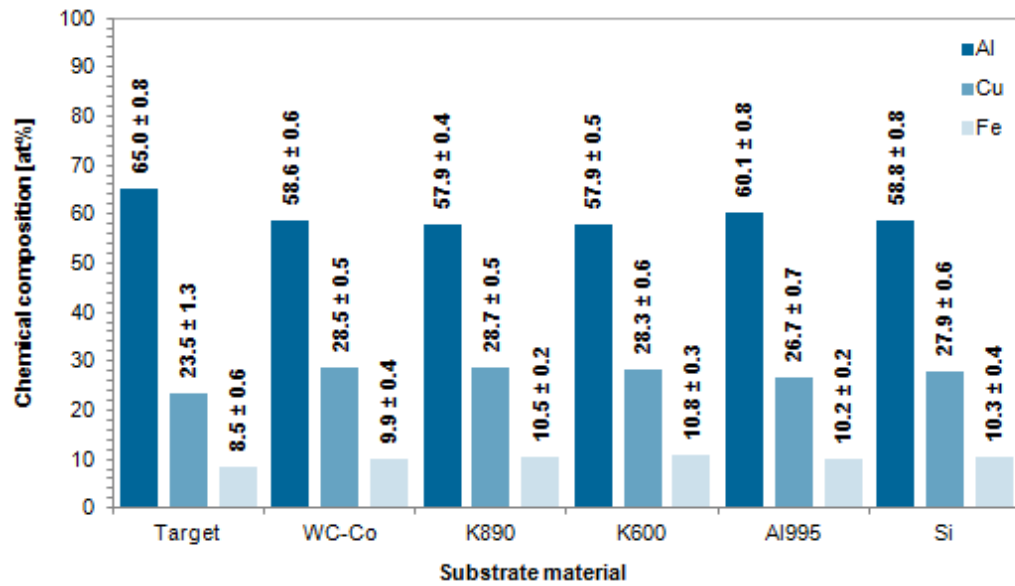
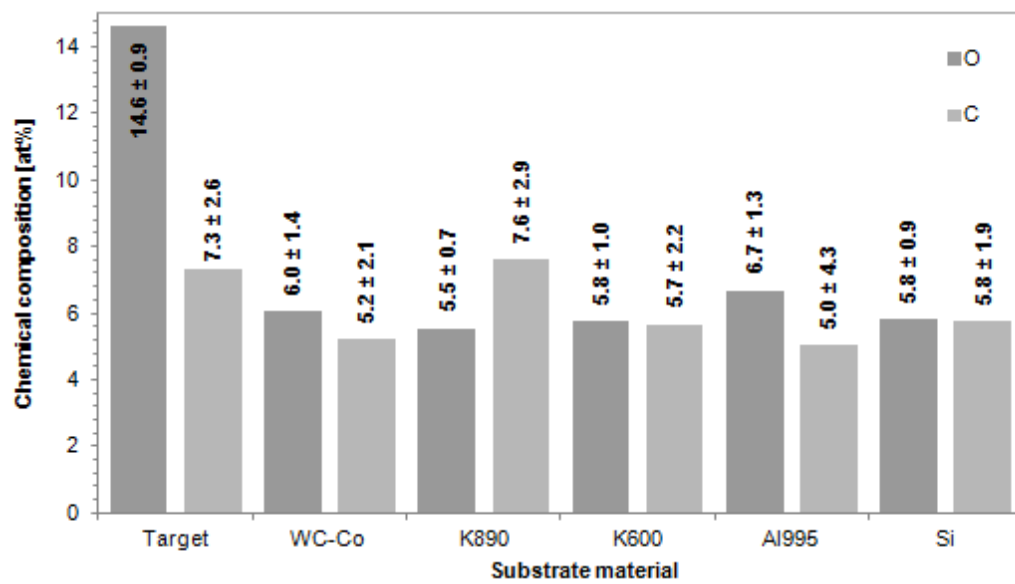


Figure 4.75 AlCuFeB coatings deposited using a metallic target and optimised deposition parameters  
a) on a Si substrate  
b) on a steel K600 substrate  
c) on a steel K890 substrate  
d) on a hard metal WC-Co substrate  
e) on a ceramic  $\text{Al}_2\text{O}_3$  substrate

Within the error of measurement, the chemical composition of the coatings is independent of the substrate material and in average:  $59.7 \pm 2.6$  at% Al,  $27.3 \pm 2.0$  at% Cu and  $10.0 \pm 0.8$  at% Fe. The O content is about 7 at% and the C content about 6 at% (see Figure 4.76).



a)



b)

Figure 4.76 Chemical composition of AlCuFe coatings deposited on different substrate materials, using a metallic target and optimised deposition parameters

a) Al, Cu and Fe content

b) O and C content

Figure 4.77 displays the average chemical composition of the AlCuFeB coatings (red dot) deposited on different substrates and the chemical composition of the metallic target (yellow dot) in the AlCuFe phase diagram. While the chemical composition of the metallic target lies a bit outside the quasicrystalline region the chemical composition of the AlCuFeB coatings is located well within the quasicrystalline region.

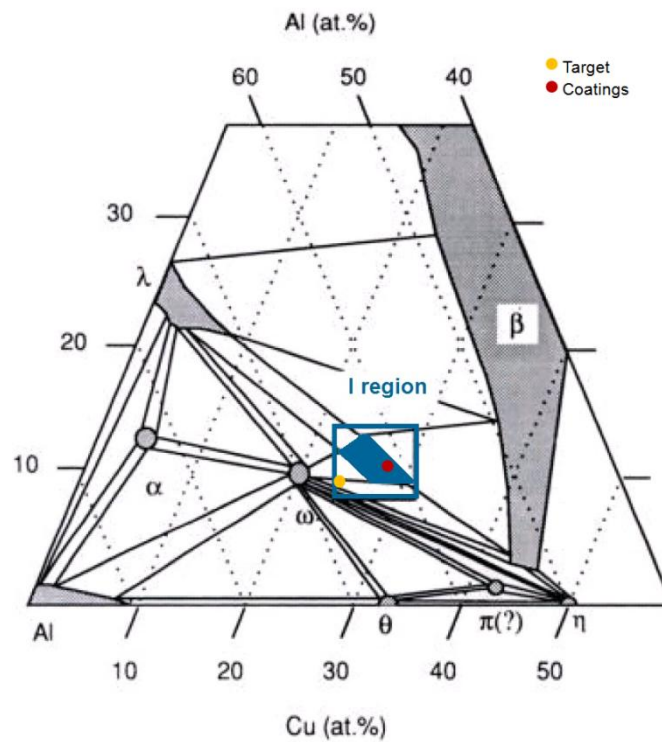


Figure 4.77 AlCuFe phase diagram including the average chemical composition of the AlCuFeB coatings deposited on different substrates and the target composition

Independent of the substrate material a quasicrystalline phase as well as a  $\beta$  phase develops (see Figure 4.78). According to XRD intensity peaks heights (see Relation 4.1), the amount of quasicrystalline AlCuFe phase can be estimated to 40 % and the amount of  $Al_{50}Cu_{40}Fe_{10}$   $\beta$  phase to 60 %.

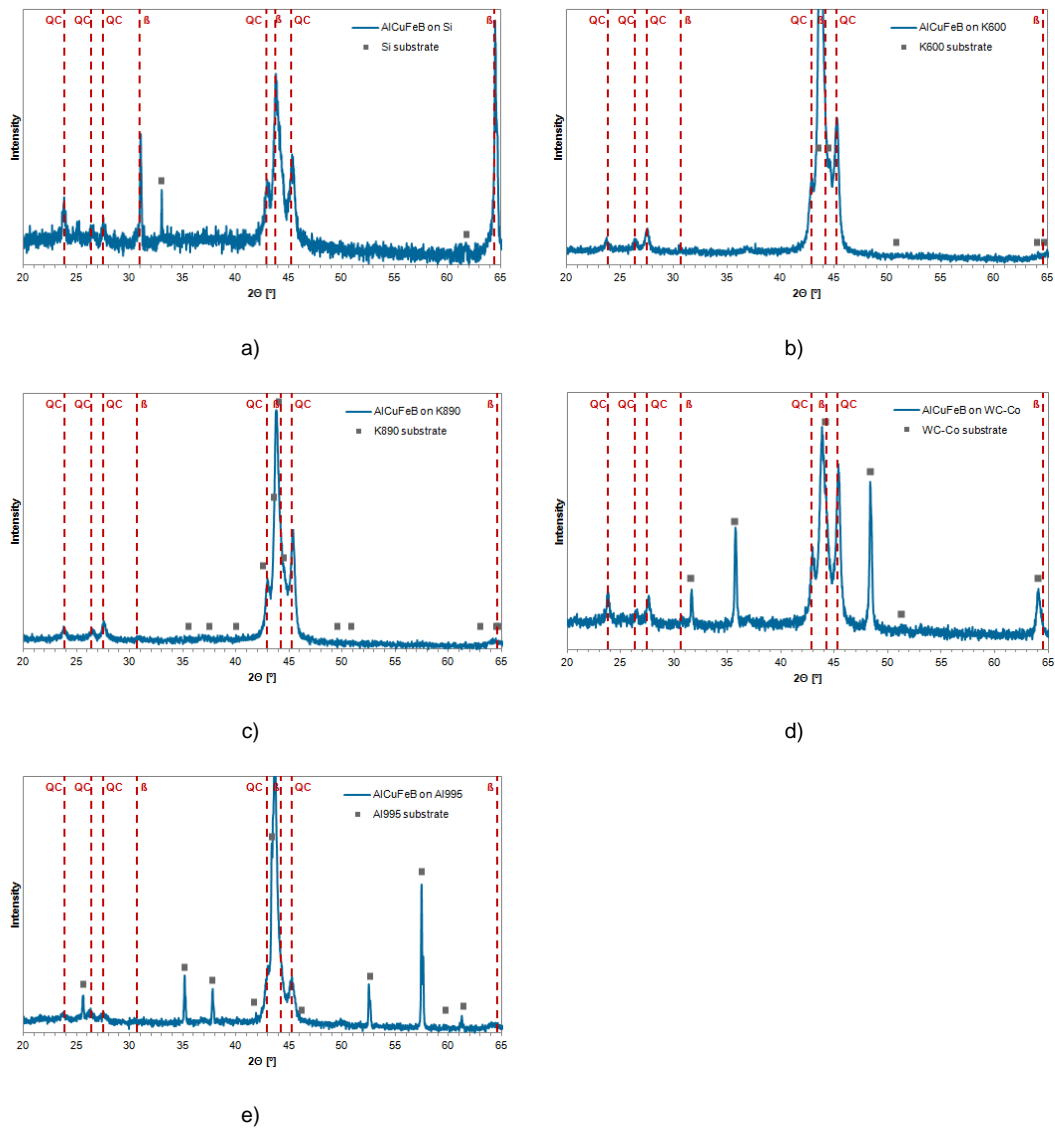


Figure 4.78 XRD pattern of AlCuFeB coatings deposited using a metallic target and optimised deposition parameters

- a) on a Si substrate
- b) on a steel K600 substrate
- c) on a steel K890 substrate
- d) on a hard metal WC-Co substrate
- e) on a ceramic  $\text{Al}_2\text{O}_3$  substrate

When deposition is done on WC-Co or on Si cracks appear all over the coating surface. For deposition on WC-Co, also delamination can be observed. For deposition on steel K600 and K890 as well as for deposition on ceramic  $\text{Al}_2\text{O}_3$ , no cracks or delamination effects occur and the surface morphology of the substrates is reproduced (see Figure 4.79).

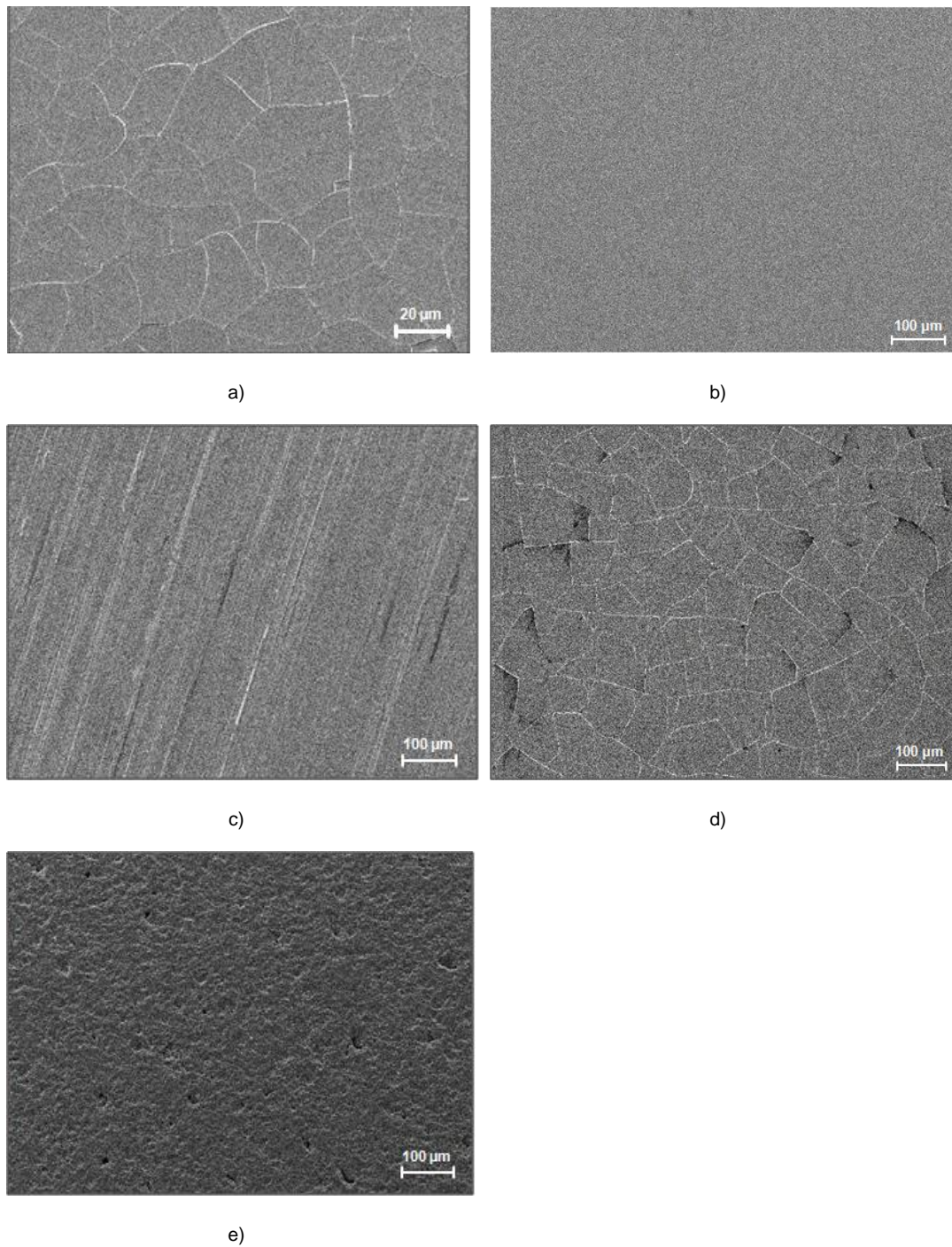


Figure 4.79 SEM surface images of AlCuFeB coatings deposited using a metallic target and optimised deposition parameters  
a) on a Si substrate  
b) on a steel K600 substrate  
c) on a steel K890 substrate  
d) on a hard metal WC-Co substrate  
e) on a ceramic  $\text{Al}_2\text{O}_3$  substrate

Independent of the substrate chosen for deposition, the deposited AlCuFeB coatings are very homogenous without any voids. For all substrates the interface appears very sharp and hardly any diffusion between the substrate and the coating material seems to take place. The coatings deposited on Si exhibit numerous cracks, which propagate throughout the whole coating and into the substrate (see Figure 4.80 a). The AlCuFeB coatings deposited on the steel K600 and steel K890 do not show any cracks (see Figure 4.80 b and c). Also for the hard metal WC-Co substrate numerous cracks and even delamination occurs all over the surface (see Figure 4.79 d) and the cracks frequently propagate throughout the whole coating and grow along the interface (see Figure 4.80 d). Because of the high surface roughness of the ceramic Al<sub>2</sub>O<sub>3</sub> substrates, the coating interface appears very rough but there are no signs of diffusion visible. Some cracks occur, which propagate from the surface to the interface where they end (see Figure 4.80 e).

Independent of the substrate material, AlCuFeB coatings consist of two different phases (see Figure 4.81), which become visible especially in Secondary Electron SEM images. One phase occurs in the form of columns and stabs (bright phase) in the matrix of the second phase (gray phase) (see Figure 4.81). The bright phase occurs significantly denser at the interface than at the regions close to the surface. These coating features could also be observed when interlayers between the Si substrate and the AlCuFeB coating are introduced (see Section 4.4.9). By EDS no difference in the chemical composition of the white stabs/columns and the gray matrix could be identified, although magnification was increased to 100.000 x and the accelerating voltage was reduced to 10 kV. The size of the grains of which the stabs/columns consist is probably too small to be resolved by EDS (excitation depth of ~1 µm). Nevertheless it can be speculated that the white phase represents the quasicrystalline AlCuFe phase, while the gray matrix consist of the Al<sub>50</sub>Cu<sub>40</sub>Fe<sub>10</sub> β phase. By using image manipulation method (threshold, pixel count), it can be estimated that the area of the white stabs/columns amounts to about 30% (see Section 4.4.9).



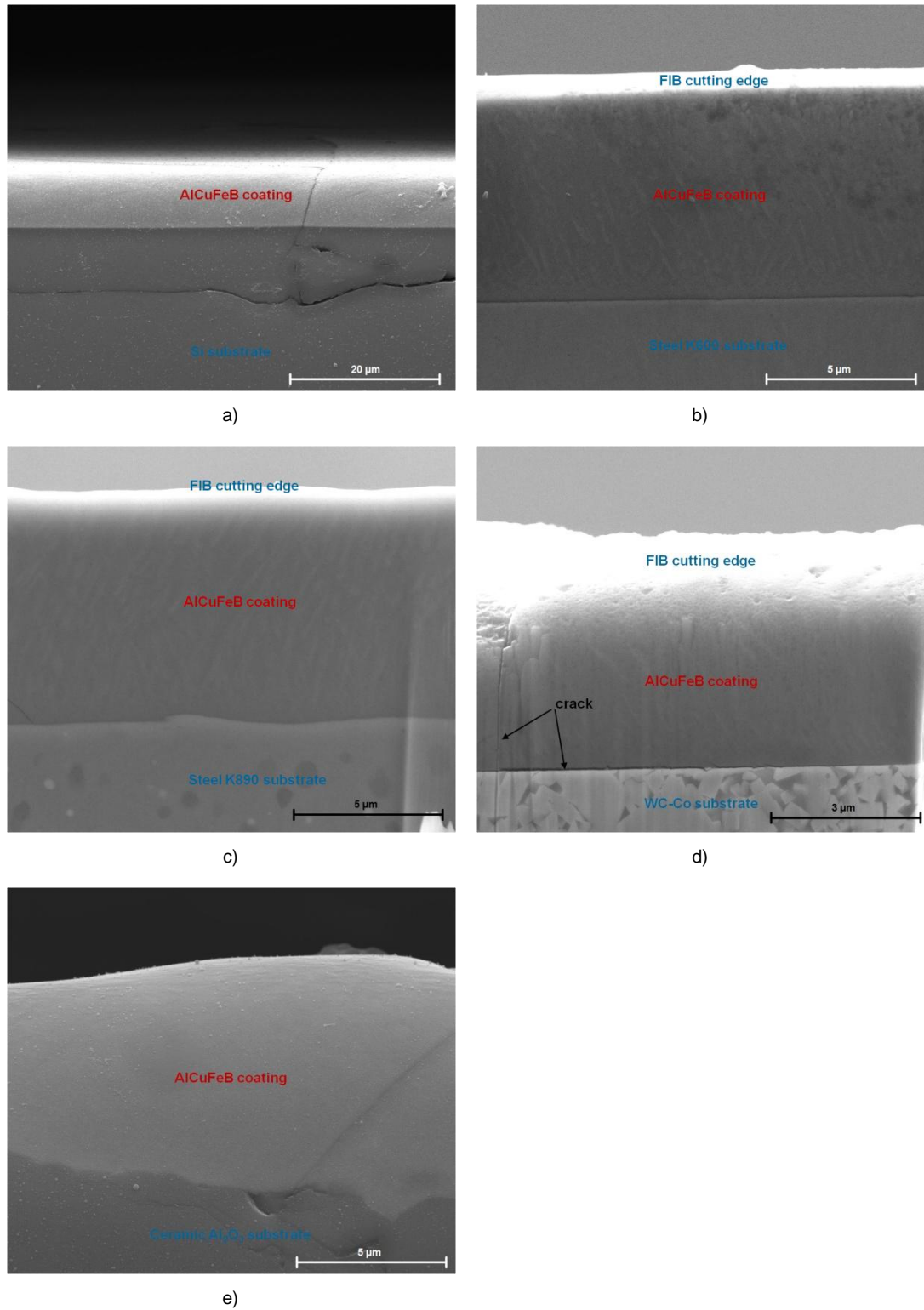


Figure 4.80 Focused ion beam (FIB) cross section of the optimised AlCuFeB coatings deposited on various substrates (secondary electron SEM)  
 a) on a Si substrate  
 b) on a steel K600 substrate  
 c) on a steel K890 substrate  
 d) on a hard metal WC-Co substrate  
 e) on a ceramic Al<sub>2</sub>O<sub>3</sub> substrate

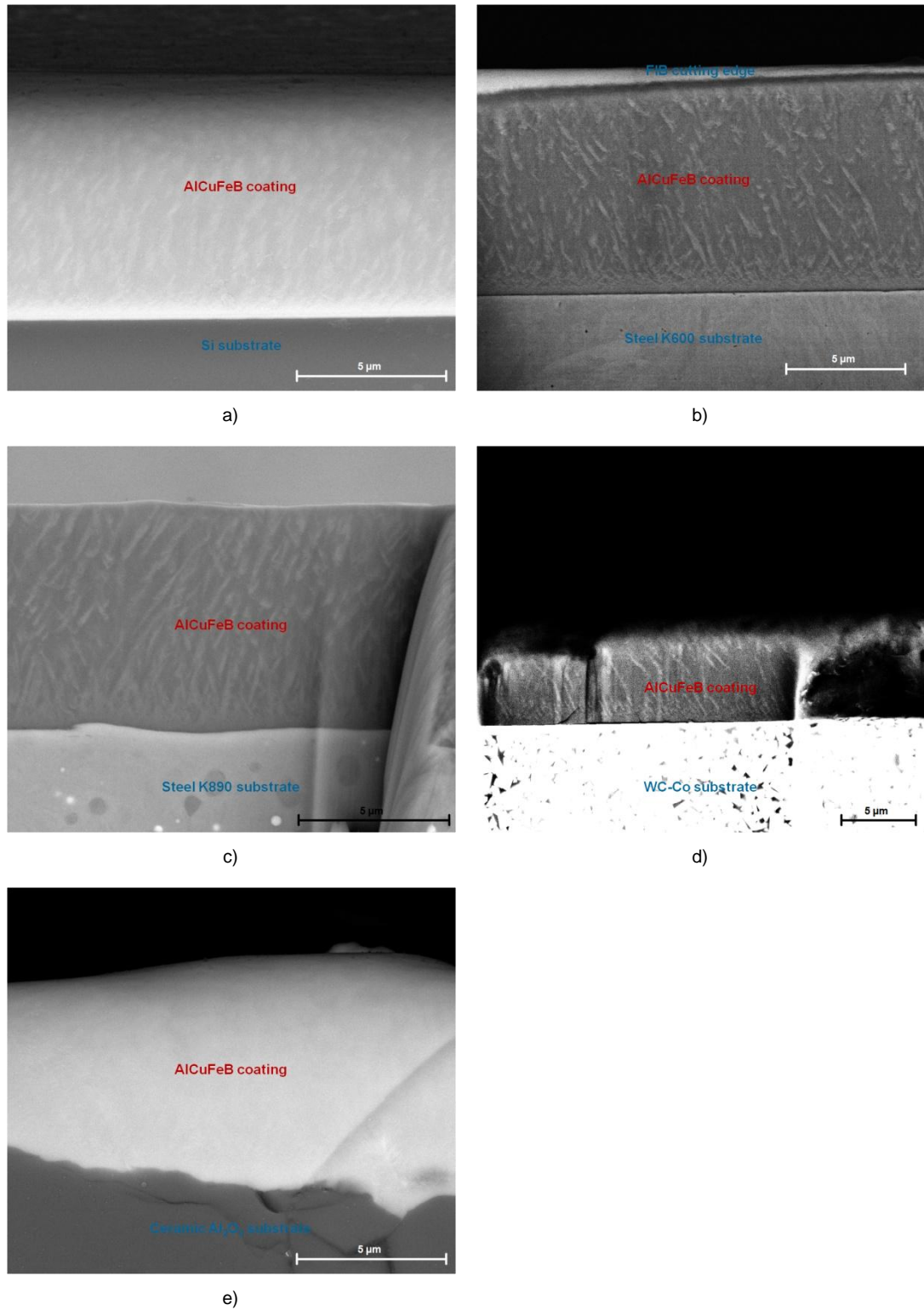


Figure 4.81 Focused ion beam (FIB) cross section of the optimised AlCuFeB coatings deposited on various substrates (back scattered electron SEM)  
a) on a Si substrate  
b) on a steel K600 substrate  
c) on a steel K890 substrate  
d) on a hard metal WC-Co substrate  
e) on a ceramic Al<sub>2</sub>O<sub>3</sub> substrate

Independent of the substrate material, Al, Cu and Fe are homogeneously distributed throughout the deposited coatings. About 8 at% C and 7 at% O can be found throughout the deposited AlCuFeB coatings. Only for the coatings deposited on the ceramic Al<sub>2</sub>O<sub>3</sub> a higher O content of more than 10 at% can be found in the coatings as well as an O enrichment on the surface. Si diffuses from the substrate to the coating, where about 5 at% can be found. While no Fe diffusion to the coating surface can be observed for the steel K600 and steel K890, Cr diffuses from the steel K890 to the coating surface, where about 2 at% can be detected. No W or Co diffuses from the WC-Co substrate to the coating surface. While for Si the interface area is about 2 μm thick, for all the other substrate materials (steel K600, steel K890, WC-Co, ceramic Al<sub>2</sub>O<sub>3</sub>) the interface is 1 μm wide (see Figure 4.82 and Figure 4.83).

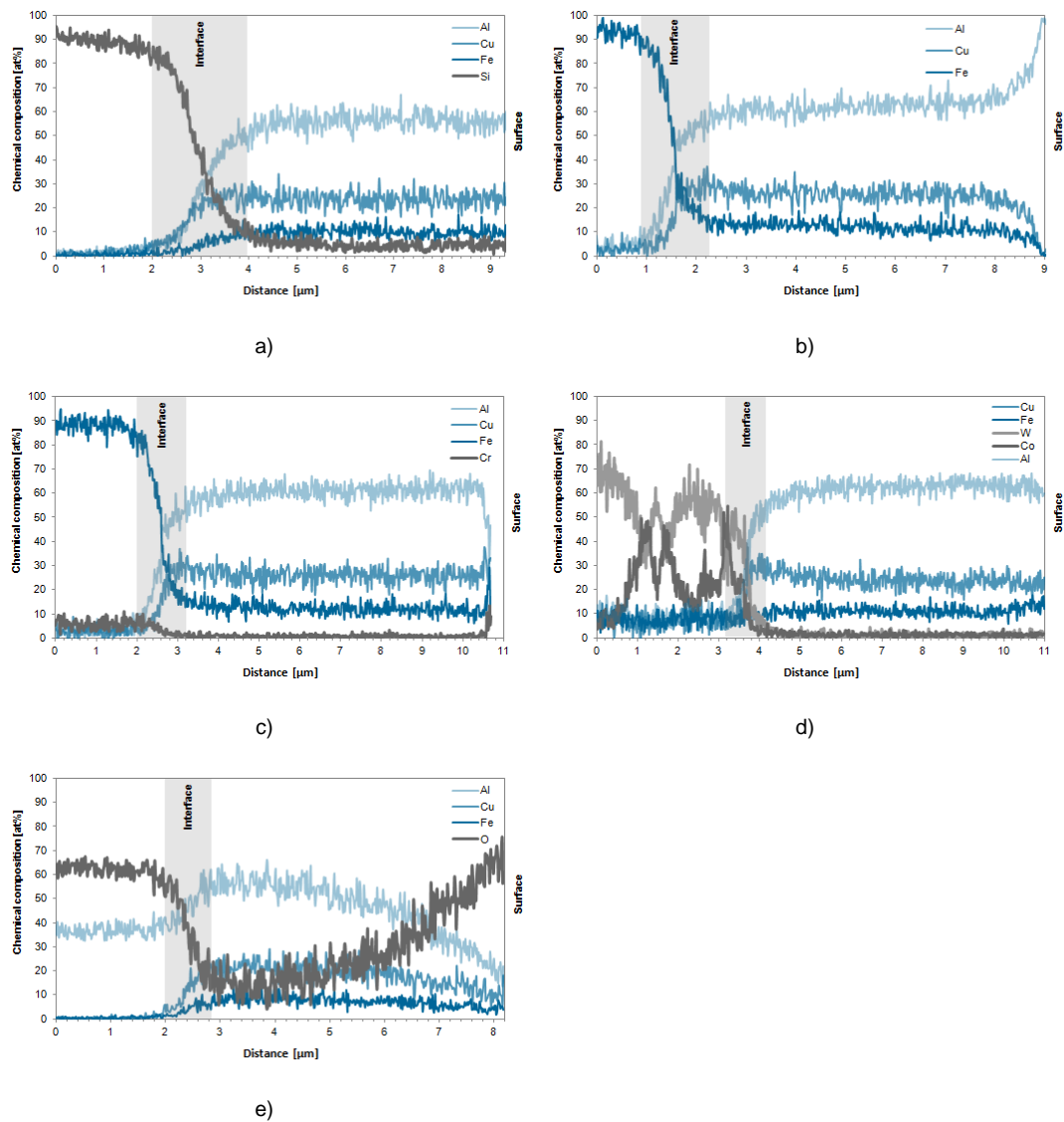


Figure 4.82 EDS line scans of AlCuFeB coating cross sections (Al, Cu, Fe). The coatings were deposited using a metallic target and optimised deposition parameters  
 a) on a Si substrate  
 b) on a steel K600 substrate  
 c) on a steel K890 substrate  
 d) on a hard metal WC-Co substrate  
 e) on a ceramic  $\text{Al}_2\text{O}_3$  substrate

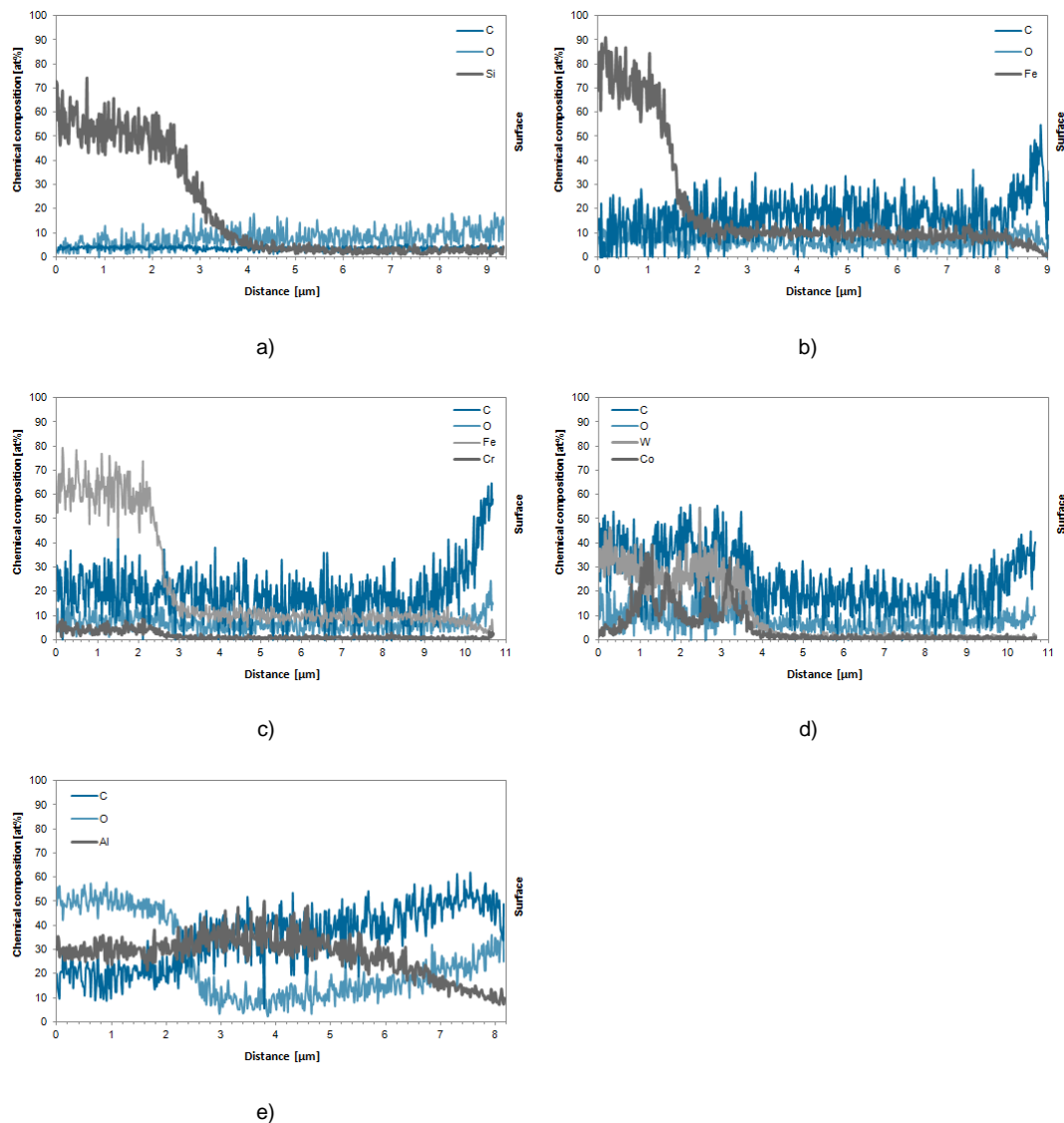


Figure 4.83 EDS line scans of AlCuFeB coating cross sections (O, C). The coatings were deposited using a metallic target and optimised deposition parameters  
 a) on a Si substrate  
 b) on a steel K600 substrate  
 c) on a steel K890 substrate  
 d) on a hard metal WC-Co substrate  
 e) on a ceramic Al<sub>2</sub>O<sub>3</sub> substrate

According to Transmission Electron Microscopy (TEM), the deposited coatings are nanocrystalline. In average the grains exhibit a diameter of about 10 nm (see Figure 4.84). The smallest grains have a diameter of about 3 nm, while the biggest grains are about 14 nm in diameter.

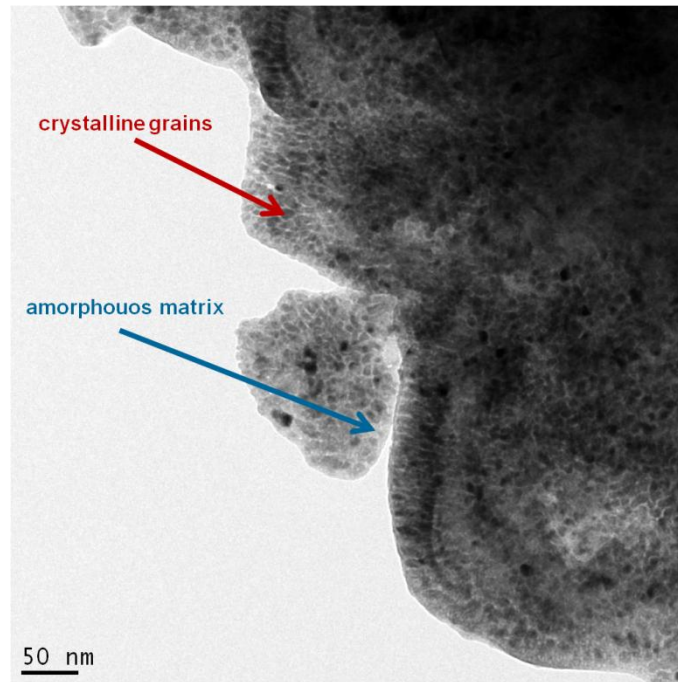


Figure 4.84 Transmission Electron Microscope (TEM) bright field image (FEI Technai G20, 29000 x magnification, 200 keV)

The grains are embedded in a matrix, which is mainly amorphous with some crystalline regions (see Figure 4.85). According to the EDS and EELS line scans, the grains and the matrix exhibit a similar composition. The diffraction image confirms that the deposited AlCuFeB coatings are nano-crystalline (almost continuous diffraction rings instead of a clear diffraction pattern). Figure 4.86 compares the diffraction pattern of the deposited AlCuFeB coating with the diffraction pattern which is expected for icosahedral AlCuFe phase [56].

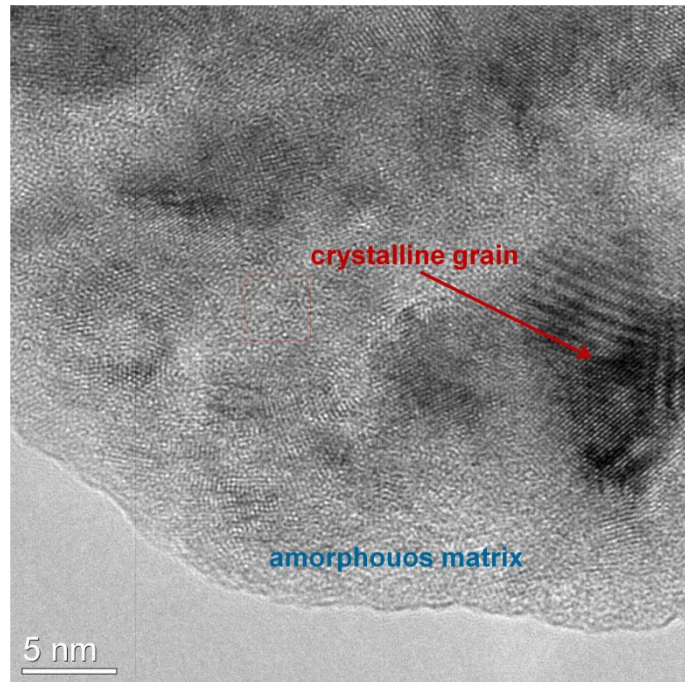


Figure 4.85 Transmission Electron Microscope (TEM) bright field image (FEI Technai G20, 29000 x magnification, 200 keV)

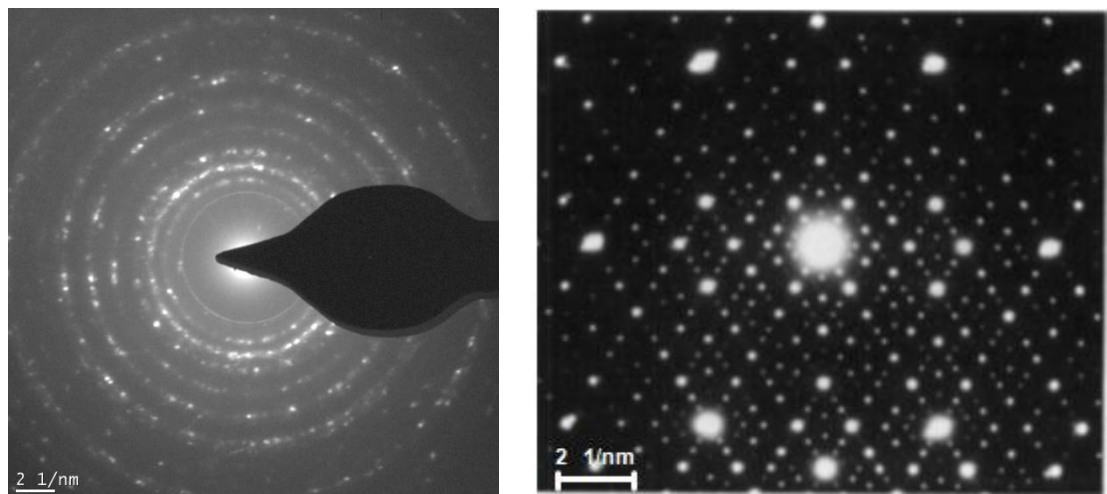


Figure 4.86 Transmission Electron Microscope (TEM) diffraction patterns (FEI Technai G20, 29000 x magnification, 200 keV)

- a) as measured for the deposited AlCuFeB coatings
- b) as found in literature [56]

#### 4.4.8 Electrical resistivity

The electrical resistivity of AlCuFeB coatings was measured using a four point probe measurement station consisting of a Jandel cylindrical probe head (tungsten carbide tips, pin-to-pin distance 0.635 mm), a Keithley 6221 DC and AC current source (1 pA to 100 mA), a Keithley 2182A nanovoltmeter and a Burster 8511-5050 load cell.

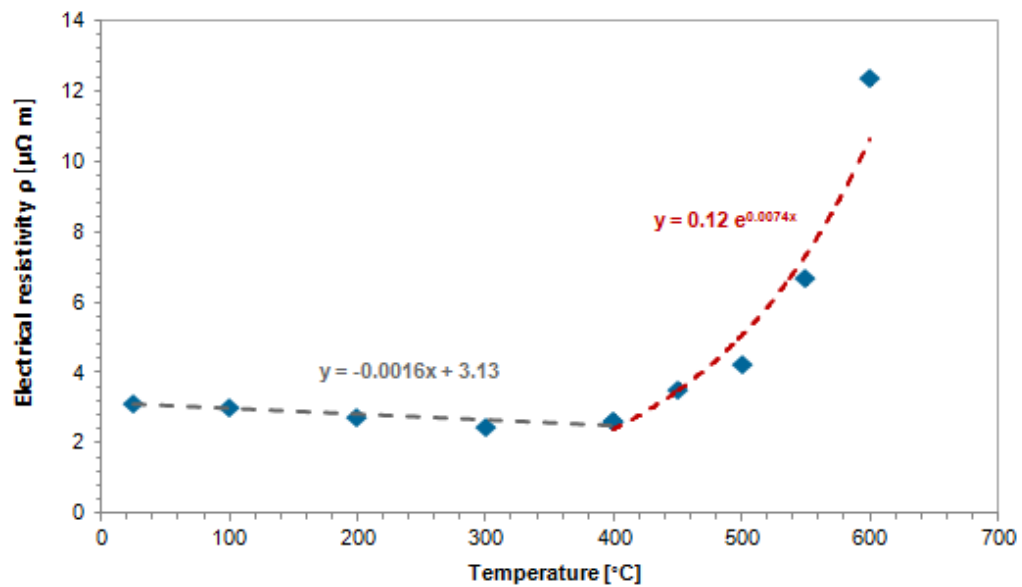
To measure the electrical resistivity in dependence on the substrate temperature during deposition and on the coating thickness, deposition was done on ceramic Al<sub>2</sub>O<sub>3</sub> substrates using the optimised parameters: 200 W deposition power, 3 cm working distance, a working gas pressure of  $10 \cdot 10^{-3}$  mbar and a bias voltage 75 V. For examining the dependence on the substrate temperature, the film thickness was 5  $\mu$ m and for examining the dependence on the film thickness, the substrate temperature was 600 °C. The measured electrical resistivity of the AlCuFeB coatings in dependence on the substrate temperature is summarised in Table 4.2.

Table 4.2 Electrical resistivity in dependence on the substrate temperature for AlCuFeB coatings deposited on ceramic substrates

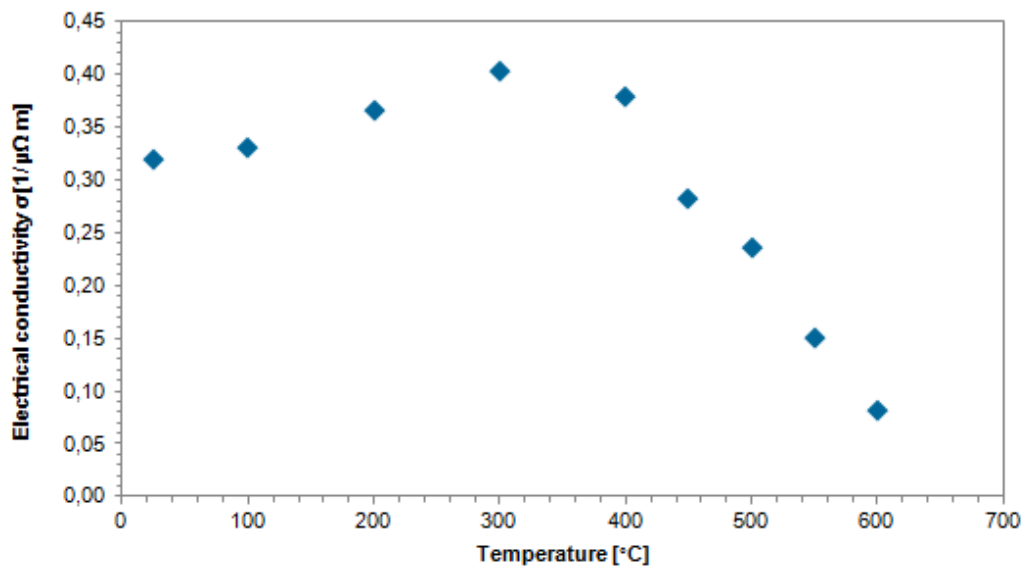
Substrate temperature [°C]	Resistivity [ $\mu\Omega$ m]	Standard deviation [ $\mu\Omega$ m]
25	3.13	$1.70 \cdot 10^{-5}$
100	3.02	$3.27 \cdot 10^{-5}$
200	2.73	$1.92 \cdot 10^{-5}$
300	2.48	$1.06 \cdot 10^{-5}$
400	2.64	$9.70 \cdot 10^{-6}$
450	3.55	$1.49 \cdot 10^{-5}$
500	4.24	$3.34 \cdot 10^{-4}$
550	6.68	$4.41 \cdot 10^{-5}$
600	12.36	$1.01 \cdot 10^{-4}$



If a substrate temperature of more than 400 °C is applied during deposition, the electrical resistivity significantly increases with temperature following an exponential law (see Figure 4.87).



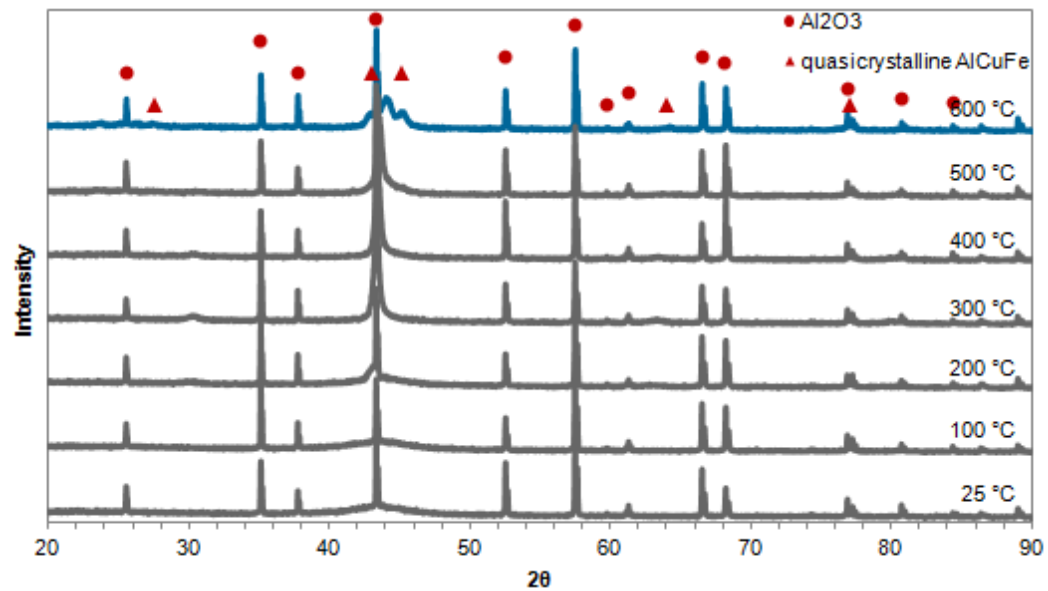
a)



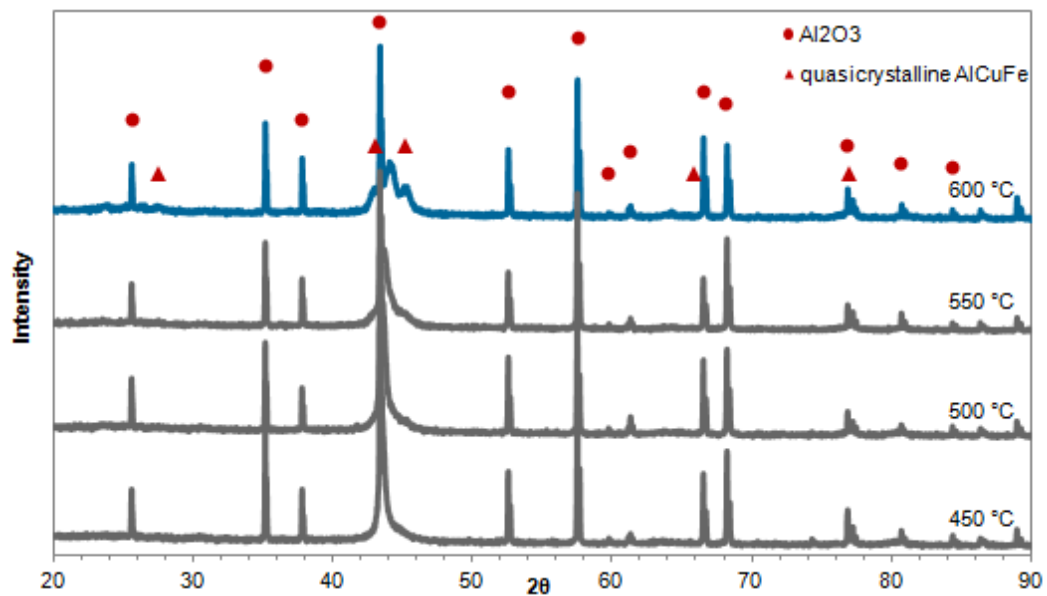
b)

Figure 4.87 Electrical conductivity/resistivity of AlCuFeB coatings in dependence on the substrate temperature  
a) electrical resistivity  
b) electrical conductivity

An increasing substrate temperature causes the development of the quasicrystalline AlCuFe phases on the ceramic Al<sub>2</sub>O<sub>3</sub> substrates (see Figure 4.88), which is in agreement with the results of Section 4.4.3.



a)



b)

Figure 4.88 XRD pattern of AlCuFe coatings deposited on ceramic Al955 substrates in dependence on the substrate temperature  
a) from 25 °C to 600 °C  
b) from 450 °C to 600 °C

The electrical resistivity of coatings deposited on ceramic  $\text{Al}_2\text{O}_3$  substrates heated to 600 °C, with a film thickness of 5  $\mu\text{m}$  (13.92  $\mu\Omega\text{m}$ ) approximately equals the electrical resistivity of AlCuFeB ceramic targets produced with the elemental powder mixture (15.0  $\mu\Omega\text{m} \pm 5.2 \mu\Omega\text{m}$ ) (see Section 4.2.1). With decreasing film thickness, the electrical resistivity decreases to about 2  $\mu\Omega\text{m}$  for a film thickness of 130 nm. For film thicknesses below 100 nm the electrical resistivity increases again up to 11.63  $\mu\Omega\text{m}$  for a film thickness of 4 nm. Table 4.3 lists the measured electrical resistivity in dependence on the film thickness and Figure 4.89 graphically displays the results.

Table 4.3 Electrical resistivity in dependence on the film thickness for AlCuFeB coatings deposited on ceramic  $\text{Al}_2\text{O}_3$  substrates heated at 600 °C

Film thickness [nm]	Resistivity [ $\mu\Omega\text{m}$ ]	Standard Deviation [ $\mu\Omega\text{m}$ ]
5200	13.92	$1.33 \cdot 10^{-3}$
2600	2.97	$1.51 \cdot 10^{-3}$
1040	1.75	$5.51 \cdot 10^{-6}$
780	2.19	$3.82 \cdot 10^{-5}$
520	1.98	$1.40 \cdot 10^{-5}$
260	1.73	$1.39 \cdot 10^{-6}$
130	2.09	$3.13 \cdot 10^{-5}$
54	2.42	$1.89 \cdot 10^{-4}$
26	2.92	$2.64 \cdot 10^{-4}$
11	5.57	$2.63 \cdot 10^{-3}$
4	11.63	$2.73 \cdot 10^{-3}$

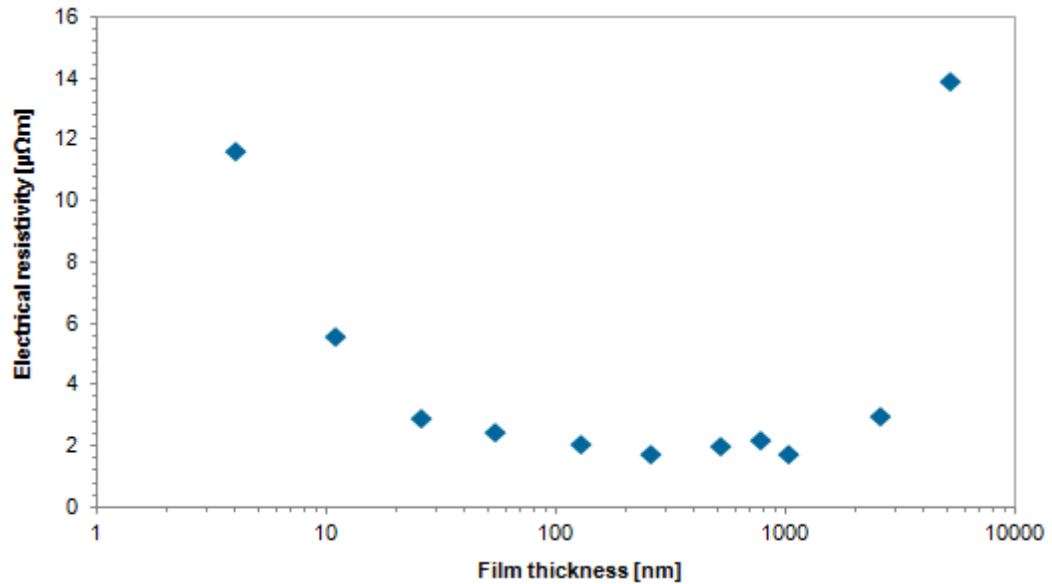


Figure 4.89 Electrical resistivity in dependence on the film thickness for AlCuFeB coatings deposited on ceramic  $\text{Al}_2\text{O}_3$  substrates heated at 600 °C

For a film thickness of more than 1  $\mu\text{m}$ , the electrical resistivity of the deposited coatings approximately equals the electrical resistivity of quasicrystalline AlCuFe bulk material ( $\sim 15 \mu\Omega$ ). For a film thickness between 50 nm and 1  $\mu\text{m}$ , the electrical resistivity is significantly lower (2  $\mu\Omega$ ) and for film thicknesses below 20 nm the electrical resistivity increases again up to 12  $\mu\Omega$ . Thus it can be speculated that the quasicrystalline structure does not develop for film thicknesses below 1  $\mu\text{m}$  if deposition is done on ceramic  $\text{Al}_2\text{O}_3$  substrates (see Section 5.4.4).

#### 4.4.9 Interlayer

To reduce the intensity of the strains at the interface (see Section 3.5), to increase adhesion and to avoid diffusion of substrate atoms into the coating, five different materials were tested as a possible interlayer: Chrome (Cr), Copper (Cu), Titanium (Ti), Manganese (Mn), Nickel (Ni). Interlayers of 200 nm and 1  $\mu\text{m}$  thickness were deposited on Si substrates at room temperature by DC magnetron sputtering. For deposition of AlCuFeB coatings on the interlayer, the samples had to be mounted on the right hand side load lock system and thus had to be brought to atmosphere (see Figure 3.5 in Section 3.1). Afterwards the AlCuFeB coatings were deposited by using an AlCuFeB metallic target (Al  $64.2 \pm 2.3$  at%, Cu  $22.0 \pm 1.5$  at%, Fe  $10.9 \pm 0.8$  at) and the following deposition parameters: 100 W deposition power, 0 V bias voltage, 5 cm target – substrate distance, 100 nm/min deposition rate,  $2 \times 10^{-3}$  mbar working gas pressure, 600 °C substrate temperature. The coatings were analysed by EDS measurements on the surface, EDS line scans and SEM images along polished cross-sections. The gray marked area in the EDS line scan profiles represents the area, in which a significant concentration of interlayer material was detected and may not correspond with the real interlayer thickness.

A Cr interlayer does not improve the adhesion of the AlCuFeB coatings (see Figure 4.90). Coating delamination occurs all over the surface. For the 1  $\mu\text{m}$  thick interlayer delamination is higher than for the 200 nm interlayer.



Figure 4.90 Images of AlCuFeB coatings with a Cr interlayer  
a) 200 nm Cr  
b) 1  $\mu\text{m}$  Cr

While Cu and Fe seems to be uniformly distributed throughout the coating, Al decreases towards the surface, O seems to be enriched at the Cr interlayer and the C impurities at

the interface Si substrate - Cr interlayer and at the interface Cr interlayer - AlCuFeB coating (see Figure 4.91 and Figure 4.92). On the coating surface no Si, no Cr, ~7 at% O and ~3 at% C can be found. Independent of the interlayer thickness, the coatings exhibit a composition of Al  $61.5 \pm 0.3$  at%, Cu  $25.7 \pm 0.3$  at%, Fe  $9.9 \pm 0.1$  at%,

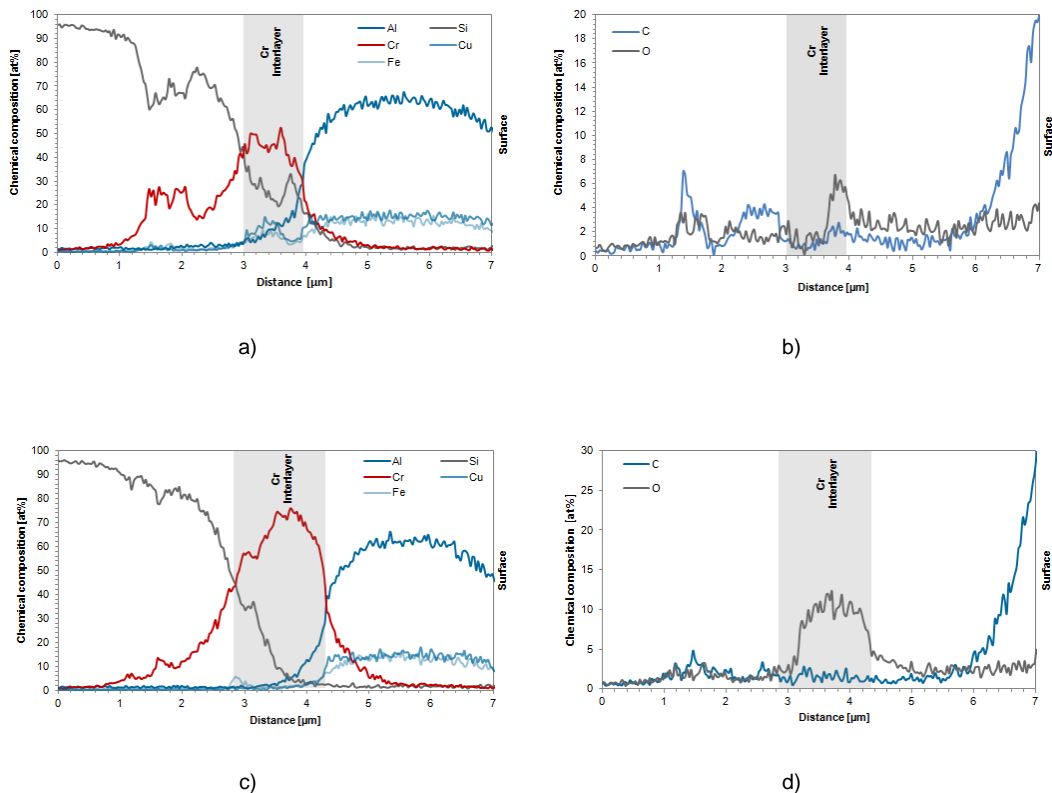
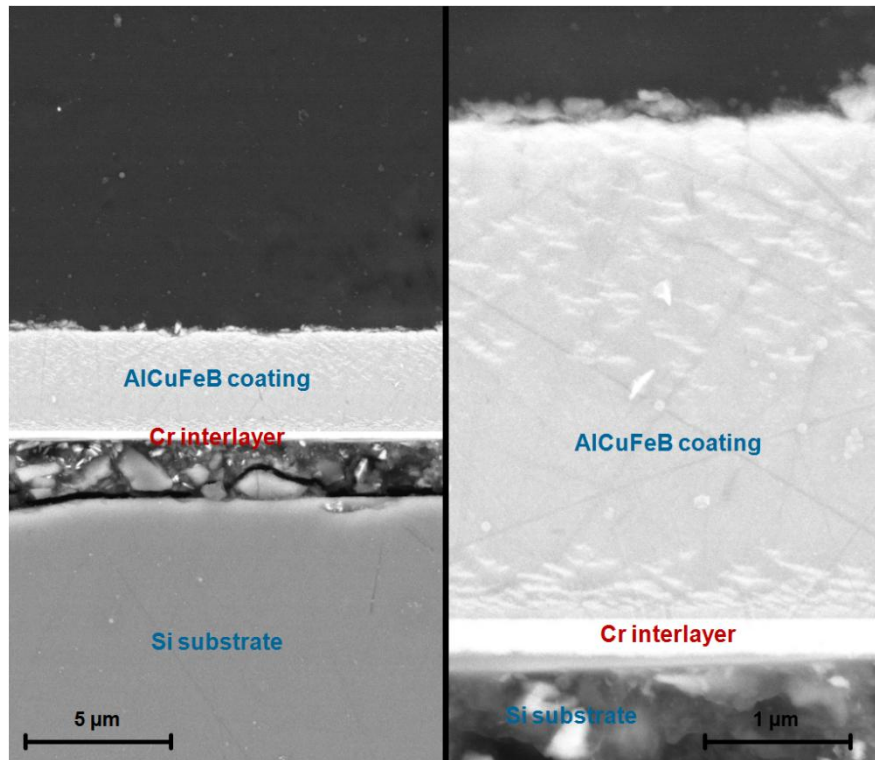
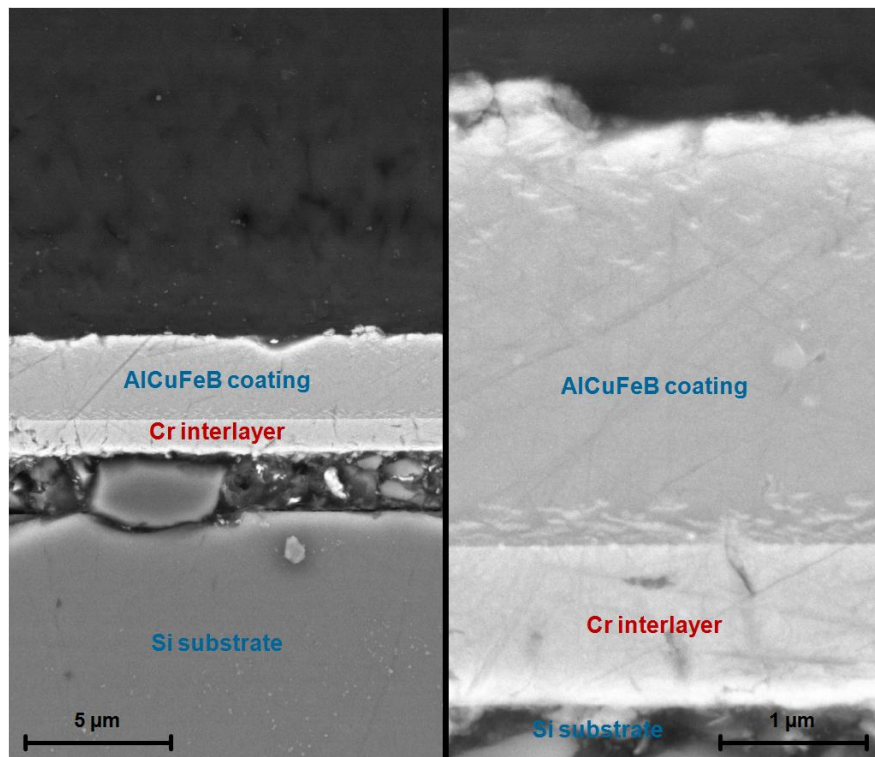


Figure 4.91 Cross section EDS line scan of a AlCuFeB coating deposited on a Si substrate with a  
 a) 200 nm Cr interlayer (Al, Cu, Fe, Si, Cr content)  
 b) 200 nm Cr interlayer (O, C content)  
 c) 1  $\mu\text{m}$  Cr interlayer (Al, Cu, Fe, Si, Cr content)  
 d) 1  $\mu\text{m}$  Cr interlayer (O, C content)

Independent of the interlayer thickness, Cr diffuses ~2  $\mu\text{m}$  into the Si substrate and about 1  $\mu\text{m}$  into the AlCuFeB coating (see Figure 4.91 and Figure 4.92). Si diffuses about 1 - 2  $\mu\text{m}$  into the Interlayer/coating. For the 200 nm thick Cr interlayer, the interlayer – coating interface shows a compact, homogenous structure and a good quality (see Figure 4.93 a). For the 1  $\mu\text{m}$  thick Cr interlayer, the interlayer – coating interface exhibits some cracks and voids (see Figure 4.93 b). The substrate – Cr interlayer interface exhibits a lot of voids in a ~2  $\mu\text{m}$  thick area (see Figure 4.93). This is in accordance with the observed AlCuFeB coating delamination (see Figure 4.90), which is more severe for the 1  $\mu\text{m}$  Cr interlayer.



a)



b)

Figure 4.93 Cross section of a AlCuFeB coating deposited on a Si substrate (secondary electron SEM)  
a) with a 200 nm Cr interlayer  
b) with a 1 μm Cr interlayer

A Cu interlayer does not improve adhesion of the AlCuFeB coatings (see Figure 4.94). Coating delamination occurs all over the surface. For the 200 nm thick interlayer delamination is higher than for the 1  $\mu\text{m}$  interlayer.

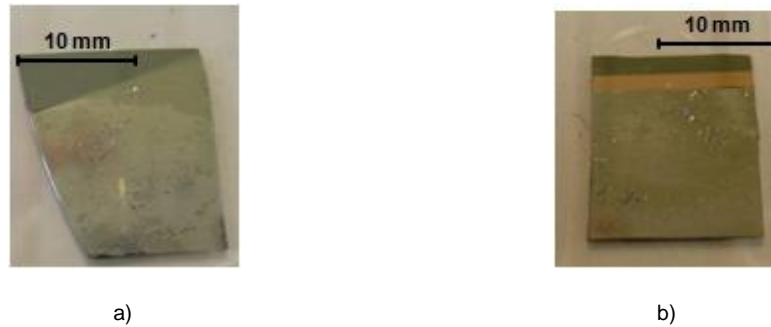


Figure 4.94 Images of AlCuFeB coatings with a Cu interlayer  
a) 200 nm Cu  
b) 1  $\mu\text{m}$  Cu

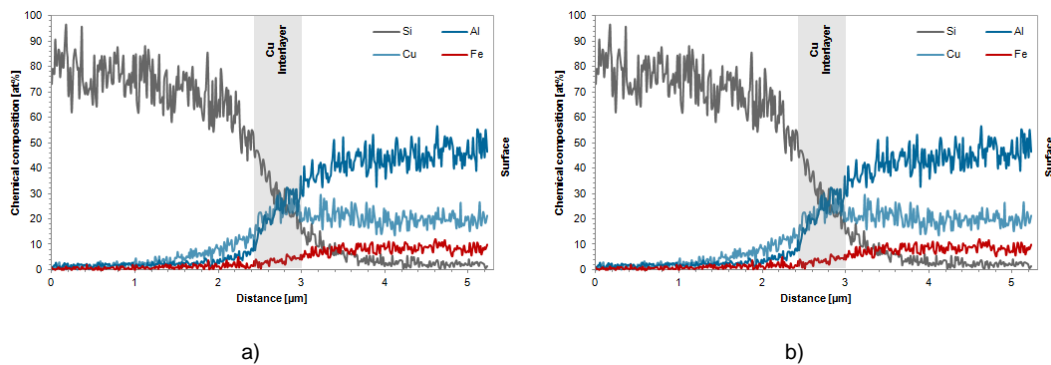
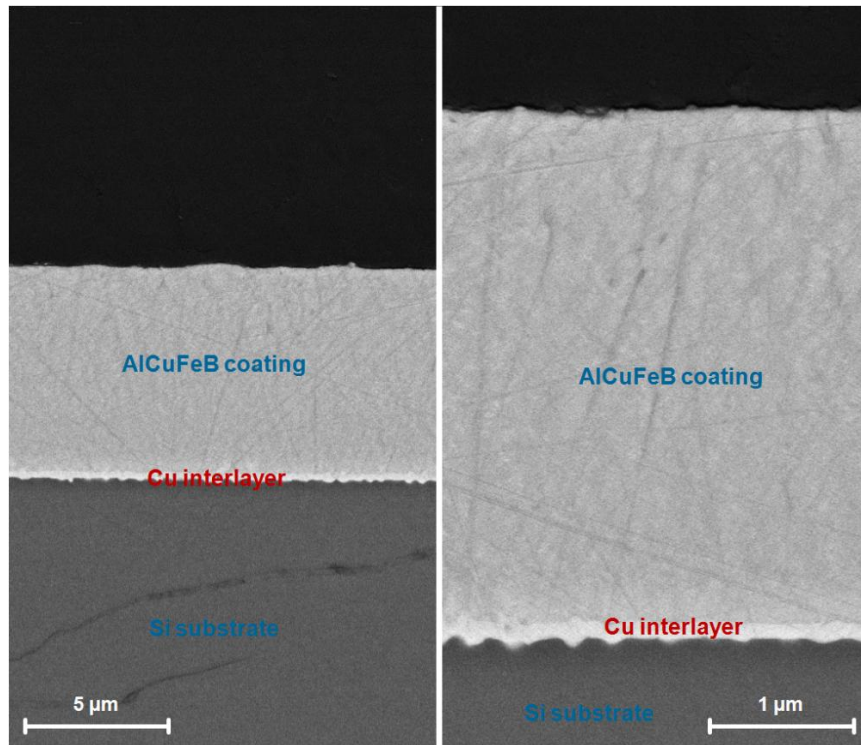


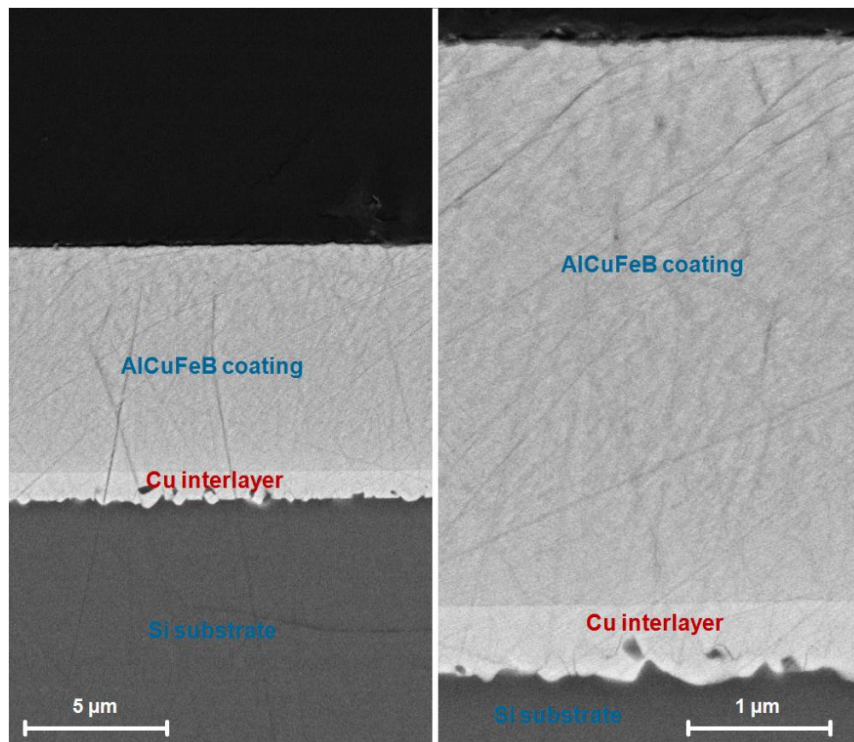
Figure 4.95 Cross section EDS line scan of an AlCuFeB coating deposited on a Si substrate with a Cu interlayer  
a) 200 nm Cu interlayer  
b) 1  $\mu\text{m}$  Cu interlayer

On the coating surface and throughout the coating  $\sim 6$  at% O and  $\sim 3$  at% C can be found. No Si could be detected on the coating surface. The coating with the 200 nm Cu interlayer exhibits a composition of Al  $60.0 \pm 0.5$  at%, Cu  $27.4 \pm 0.5$  at%, Fe  $9.6 \pm 0.2$  at%. The chemical composition of the coating with the 1  $\mu\text{m}$  Cu interlayer is: Al  $58.0 \pm 0.6$  at%, Cu  $29.1 \pm 0.3$  at%, Fe  $10.0 \pm 0.4$  at%. In comparison with the AlCuFeB metallic target (Al  $64.2 \pm 2.3$  at%, Cu  $22.0 \pm 1.5$  at%, Fe  $10.9 \pm 0.8$  at), the coatings exhibit less Al (4 - 6 at%) and more Cu (5 - 7 at%). Cu seems to diffuse from the interlayer region to the coating surface (see Figure 4.95), where the additional Cu causes the observed deviation from the target composition. Cu diffuses from the interlayer region about 1.5  $\mu\text{m}$  into the substrate (see Figure 4.95) and the substrate – interlayer interface appears very rough (see Figure 4.96). Some voids form within the Cu interlayer region. Si diffuses about 1  $\mu\text{m}$  into the interlayer/coating.





b)



b)

Figure 4.96 Cross section of a AlCuFeB coating deposited on a Si substrate (secondary electron SEM)  
a) with a 200 nm Cu interlayer  
b) with a 1 μm Cu interlayer

Adhesion of the AlCuFeB coatings is not improved by a Ti interlayer (see Figure 4.97). Coating delamination occurs all over the surface. For the 1  $\mu\text{m}$  thick interlayer delamination is higher than for the 200 nm interlayer.



Figure 4.97 Images of AlCuFeB coatings with a Ti interlayer  
a) 200 nm Ti  
b) 1  $\mu\text{m}$  Ti

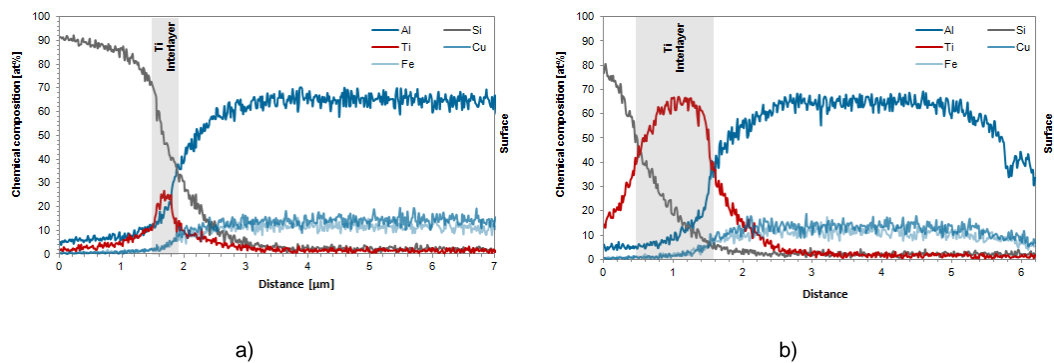
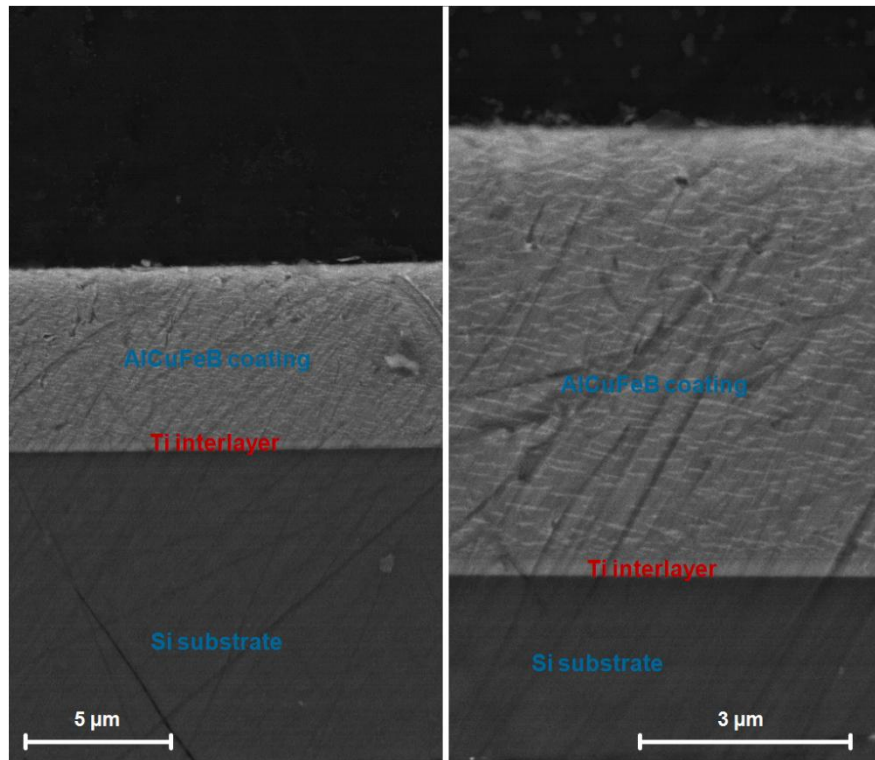
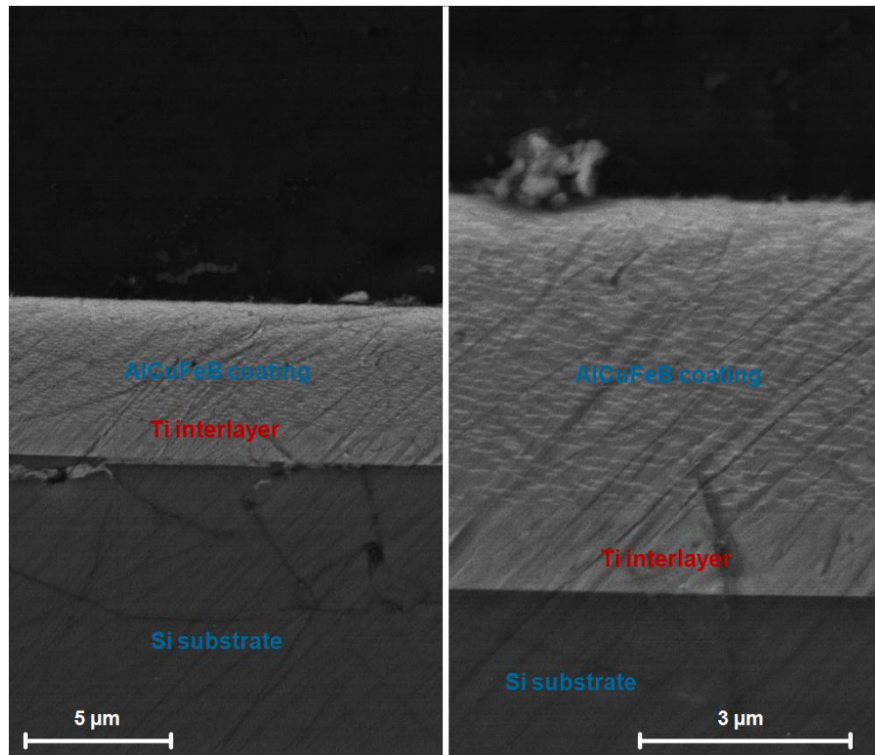


Figure 4.98 Cross section EDS line scan of an AlCuFeB coating deposited on a Si substrate with a Ti interlayer  
a) 200 nm Ti interlayer  
b) 1  $\mu\text{m}$  Ti interlayer

Al, Cu and Fe seem to be uniformly distributed and a C content of  $\sim 3$  at% and  $\sim 3$  at% O can be found throughout the coatings. For both interlayer thicknesses Si diffusion to the coating surface is prevented. On the coating surface no Si,  $\sim 3$  at% C and  $\sim 8$  at% O can be found. Independent of the interlayer thickness, the coatings exhibit a composition of Al  $63.4 \pm 0.3$  at%, Cu  $24.1 \pm 0.3$  at%, Fe  $9.5 \pm 0.3$  at%. Ti diffuses  $\sim 1$   $\mu\text{m}$  into the Si substrate and about 1  $\mu\text{m}$  into the AlCuFeB coating (see Figure 4.98). The diffusion of Si into the interlayer/coating is  $\sim 2$   $\mu\text{m}$ . The AlCuFeB coatings, the Ti interlayers and the interfaces look homogenous without cracks or voids (see Figure 4.99 a and b). Both, the substrate – interlayer as well as the interlayer – coating interface appear very sharp. The AlCuFeB coating exhibits a two phase structure consisting of a dark gray matrix and a bright, line shaped phase.



a)



b)

Figure 4.99 Cross section of a AlCuFeB coating deposited on a Si substrate (secondary electron SEM)  
a) with a 200 nm Ti interlayer  
b) with a 1 μm Ti interlayer

Independent of the interlayer thickness, complete delamination of the AlCuFeB coatings occurs if Mn is used as interlayer material (see Figure 4.100). On the surface, only Si (~41 at%), Mn (~37 at%), O (~16 at%) and C (~6 at%) can be found by EDS.



Figure 4.100 Images of AlCuFeB coatings with a Mn interlayer  
a) 200 nm Mn  
b) 1  $\mu\text{m}$  Mn

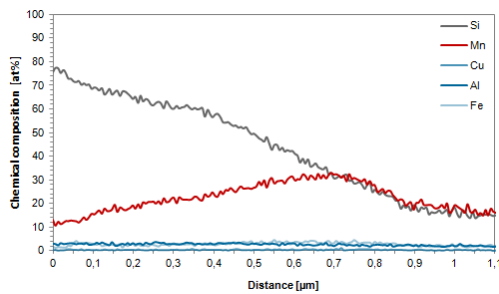
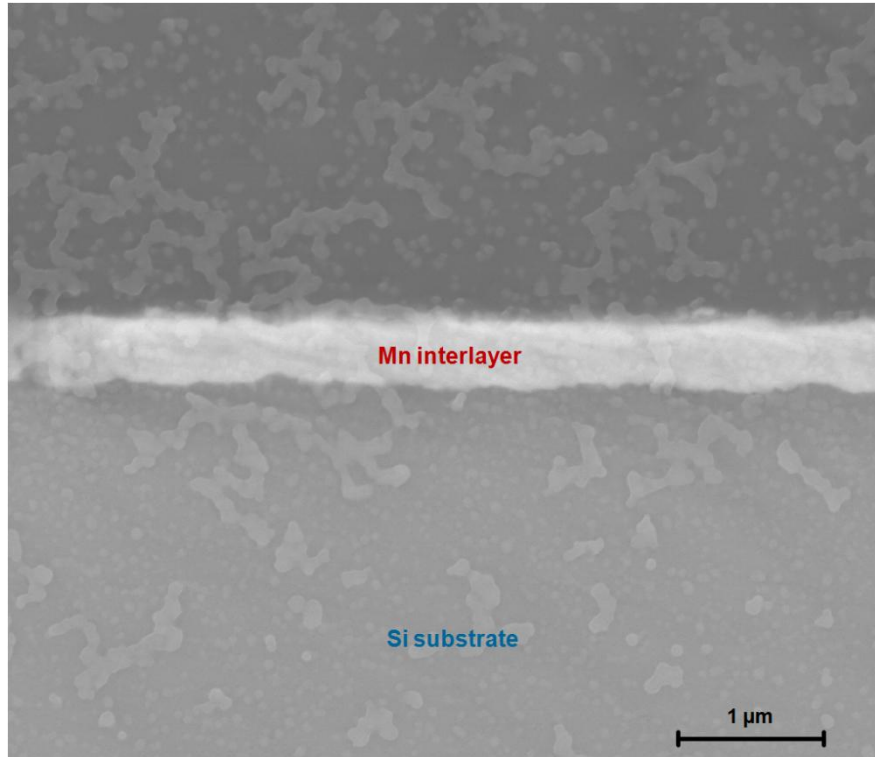
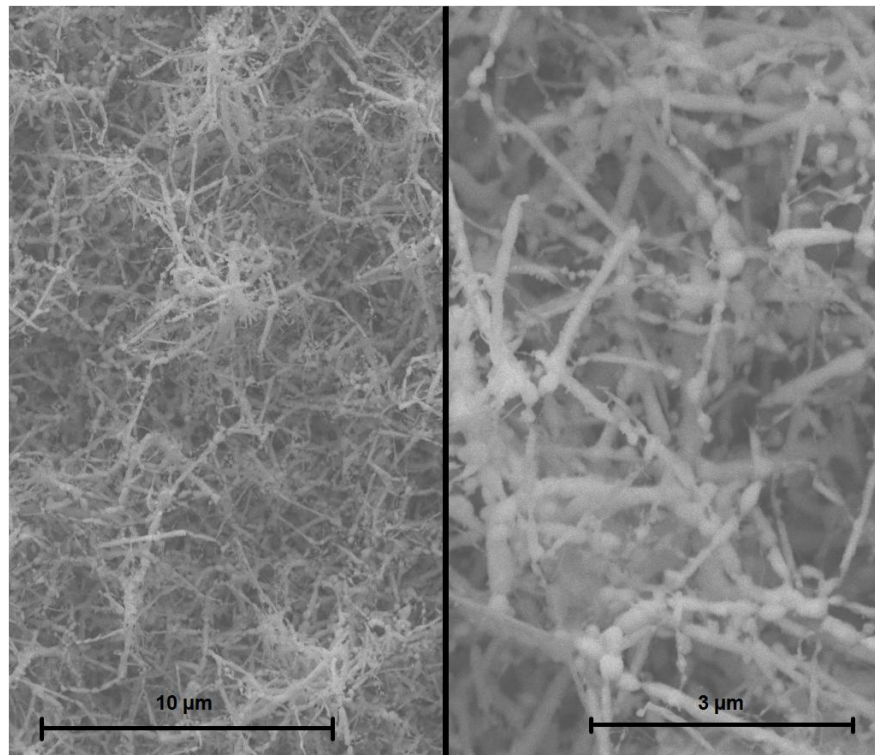


Figure 4.101 Cross section EDS line scan of an AlCuFeB coating deposited on a Si substrate with a 1  $\mu\text{m}$  Mn interlayer

Throughout the coating, no Al, no Cu, no Fe, ~4 at% O and ~7 at% C can be detected (see Figure 4.101). According to XRD measurements the coating consists of MnO and Mn suboxides. Si diffusion occurs from the substrate – interlayer interface towards the surface (see Figure 4.101). This is in accordance with the SEM cross section images (see Figure 4.102 a), which show that the AlCuFeB coating does not adhere on top of the Mn interlayer and diffusion occurs between the Si substrate and the Mn interlayer. SEM surface images show that the coatings consist of fine structured nano-tubes with a length of ~2300 nm and a diameter of ~160 nm (see Figure 4.102 b).



a)



b)

Figure 4.102 Secondary electron SEM of a 5 μm Mn coating deposited on a 600 °C Si substrate  
a) Cross section  
b) Surface

For a 200 nm thick Ni interlayer delamination of the AlCuFeB coating occurs. If the interlayer thickness is increased to 1  $\mu\text{m}$ , adhesion improves and delamination is restricted (see Figure 4.103).



Figure 4.103 Images of AlCuFeB coatings with a Ni interlayer  
a) 200 nm Ni  
b) 1  $\mu\text{m}$  Ni

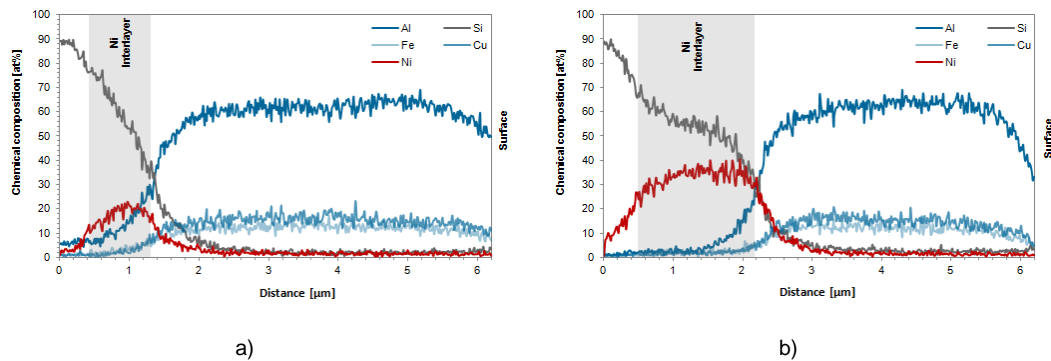
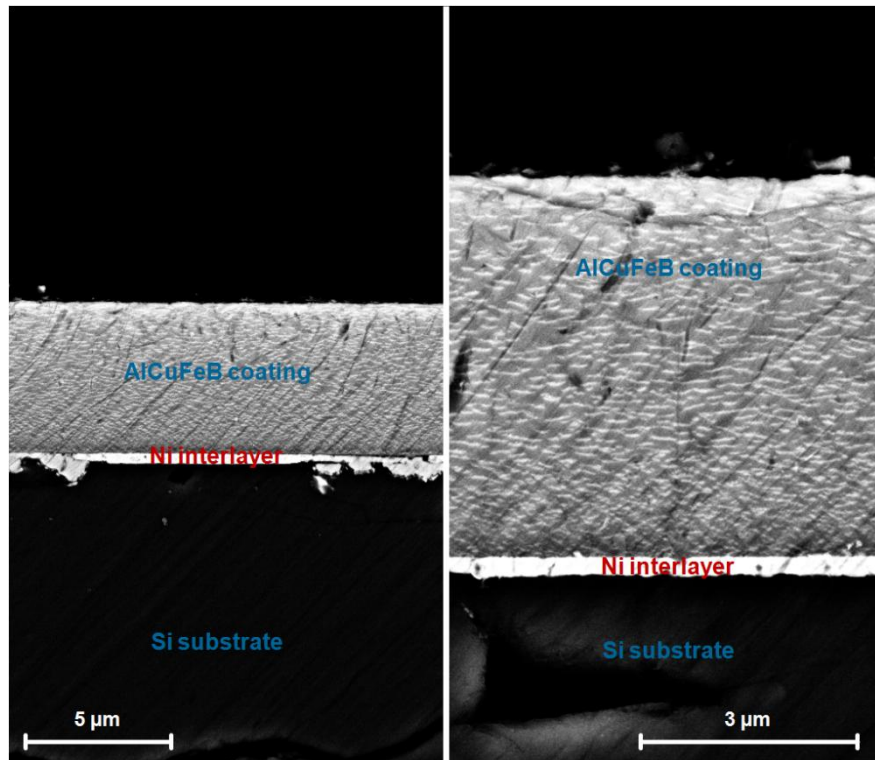
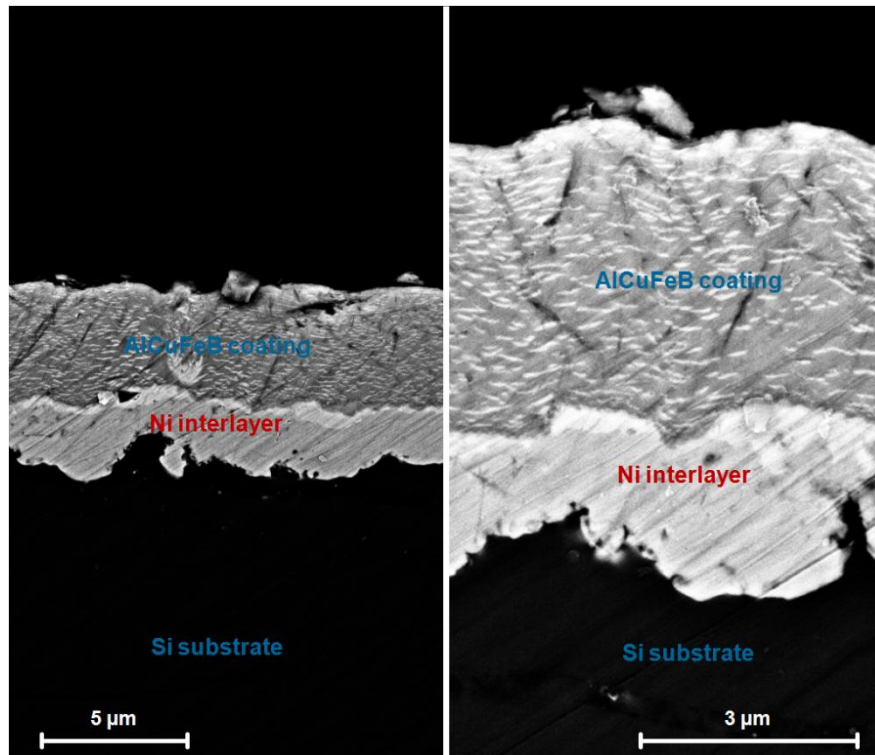


Figure 4.104 Cross section EDS line scan of a AlCuFeB coating deposited on a Si substrate with a Ni interlayer  
a) 200 nm Ni interlayer  
b) 1  $\mu\text{m}$  Ni interlayer

Al, Cu and Fe are uniformly distributed throughout the coating (see Figure 4.104). A C content of  $\sim 2$  at% and  $\sim 3$  at% O can be found throughout the coating. Si diffuses about 2 - 3  $\mu\text{m}$  into the interlayer/coating. Ni diffuses about 1  $\mu\text{m}$  into the Si substrate and  $\sim 1$   $\mu\text{m}$  into the AlCuFeB coating. Ni successfully prevents Si diffusion from the substrate to the AlCuFeB coating surface. On the coating surface no Si, no Ni,  $\sim 7$  at% O and  $\sim 3$  at% C can be found. Independent of the interlayer thickness, the AlCuFeB coatings exhibit a composition of Al  $63.1 \pm 0.1$  at%, Cu  $24.3 \pm 0.3$  at%, Fe  $9.6 \pm 0.2$  at%.



a)



b)

Figure 4.105 Cross section of a AlCuFeB coating deposited on a Si substrate (secondary electron SEM)  
a) with a 200 nm Ni interlayer  
b) with a 1 μm Cu interlayer

Independent of the interlayer thickness, the Ni interlayer and the AlCuFeB layer show some voids distributed throughout the coating (see Figure 4.105 a and b). In the AlCuFeB coating two phases can be distinguished in the SEM cross section images. A light gray matrix, in which a line shaped, white phase is homogenously distributed. The interface between the substrate and the Ni interlayer and between the Ni interlayer and the AlCuFeB coating is very rough.

Like the optimised AlCuFeB coatings deposited on different substrate types without an interlayer (see Section 4.4.7), the AlCuFeB coatings deposited on a Cr, Ti and Ni interlayer consist of two different phases. One phase occurs in the form of columns and stabs (bright phase) in the matrix of the second phase (gray phase) (see Figure 4.105). By EDS no difference in the chemical composition of the white stabs/columns and the gray matrix could be identified, although magnification was increased to 100.000 x and the accelerating voltage was reduced to 10 kV. While the white clumns/stabs seem to have a length of about 1  $\mu\text{m}$ , higher magnification SEM images show that the stabs consist of smaller grains embedded in the grain matrix (see Figure 4.106 a). The size of the grains of which the stabs/columns consist is probably too small to be resolved by EDS (excitation depth of  $\sim 1 \mu\text{m}$ ). Nevertheless it can be speculated that the white phase represents the quasicrystalline AlCuFe phase, while the gray matrix consists of the  $\text{Al}_{50}\text{Cu}_{40}\text{Fe}_{10}$   $\beta$  phase. By using image manipulation method (threshold, pixel count), it can be estimated that the area of the white stabs/columns amounts about 30% (see Figure 4.106 b). This would be in agreement with the phase ratio determined by XRD measurements (see Section 4.4.7).

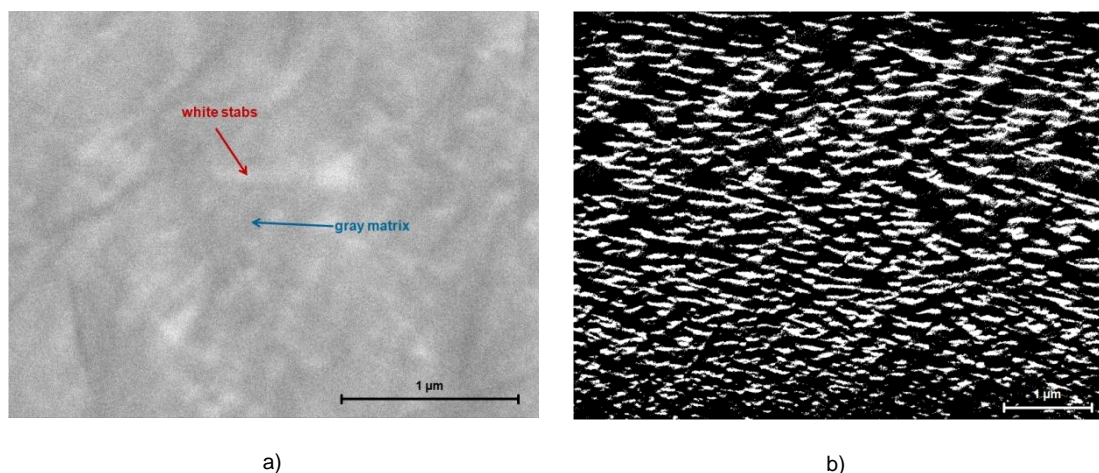


Figure 4.106 AlCuFeB coating deposited on a Si substrate with a 200 nm Ni interlayer  
a) Back scattered SEM cross section  
b) Threshold image to determine the amount of the white stabs/columns in the coating matrix



Table 4.4 shows the chemical composition of the AlCuFeB coatings deposited on different interlayer materials in comparison with a coating deposited directly on a Si substrate and with the target composition.

Table 4.4 Chemical composition of the deposited coatings and the metallic AlCuFeB target

	Al [at%]	Cu [at%]	Fe [at%]	O [at%]	C [at%]
AlCuFeB target	64.2 ± 2.3	22.0 ± 1.5	10.9 ± 0.8	6.0	3.00
No interlayer	62.8 ± 0.4	23.3 ± 2.0	9.3 ± 0.7	5.00	1.00
Cr interlayer	61.5 ± 0.3	25.7 ± 0.3	9.9 ± 0.1	7.00	3.00
Cu interlayer	59.0 ± 0.5	28.3 ± 0.4	9.8 ± 0.3	6.00	3.00
Ti interlayer	63.40 ± 0.3	24.1 ± 0.3	9.5 ± 0.3	8.00	3.00
Mn interlayer	-	-	-	-	-
Ni interlayer	63.10 ± 0.1	24.3 ± 0.3	9.6 ± 0.2	7.00	3.00

Figure 4.107 displays the chemical composition of the AlCuFeB coatings deposited on different interlayers and the chemical composition of the metallic target in the AlCuFe phase diagram. The composition of the AlCuFeB coatings deposited on Ti, Ni and Cr interlayers exhibit approximately the same chemical composition as the coating deposited directly on Si and the AlCuFeB target. The chemical composition is close to the quasicrystalline region. The chemical composition of the AlCuFeB coating deposited on the Cu interlayer is shifted to a higher Cu and lower Al content due to the diffusion of Cu into the AlCuFeB layer.

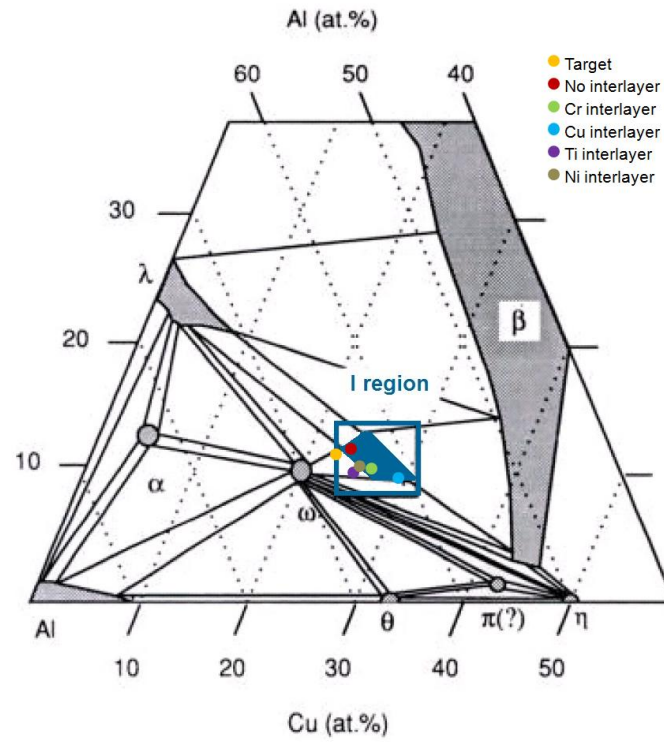


Figure 4.107 AlCuFe phase diagram including the chemical composition of the AlCuFeB coatings deposited on different interlayers

None of the test interlayer materials: Chrome (Cr), Copper (Cu), Titanium (Ti), Manganese (Mn), Nickel (Ni) could significantly reduce the intensity of the strains at the interface, increase adhesion and prevent diffusion of substrate atoms into the AlCuFeB coatings. The tested interlayer materials diffuse 1 - 2  $\mu\text{m}$  into the Si substrate and into the coating. Si diffuses about 1 – 3  $\mu\text{m}$  into the interlayer/coating. The AlCuFeB coatings deposited on Cr, Ti and Ni interlayers exhibit the same microstructure (gray matrix and white columns/stabs) as the AlCuFeB coatings deposited on different substrate materials (Si, steel K600, steel K890, WC-Co and ceramic  $\text{Al}_2\text{O}_3$ ) without any interlayer. Although no difference in the chemical composition of the white stabs/columns and the gray matrix could be identified with the methods used, it can be speculated that the white phase represents the quasicrystalline AlCuFe phase, while the gray matrix consists of the  $\text{Al}_{50}\text{Cu}_{40}\text{Fe}_{10}$   $\beta$  phase. The best result regarding adhesion, interface/coating quality and chemical composition of the AlCuFeB coatings could be achieved using a 1  $\mu\text{m}$  Ni interlayer, for which coating delamination is reduced.

#### 4.4.10 Nano-imprint-lithography (NIL)

Si molds for nano-imprint-lithography (NIL) were coated with thin AlCuFeB coatings to reduce adhesion/sticking force between the stamp and the polymer films, reduce wear and prolong lifetime and to produce repeatable, high quality imprints. The size of the stamps is about 10 x 10 mm and the patterned region is 5 x 5 mm. The structure of the stamps was produced by Prof. Zygmunt Rymuza at the Warsaw University of Technology using the reactive ion etching (RIE) Bosch process and they exhibit a half pitch of 2  $\mu\text{m}$  and a depth of 3  $\mu\text{m}$  (see Figure 4.108 a). Two different kinds of Si molds were used: one type with a 100 nm SiO<sub>2</sub> surface layer produced by thermal oxidation in dry O<sub>2</sub> at 1000 °C for 20 min and one with a pure Si surface.

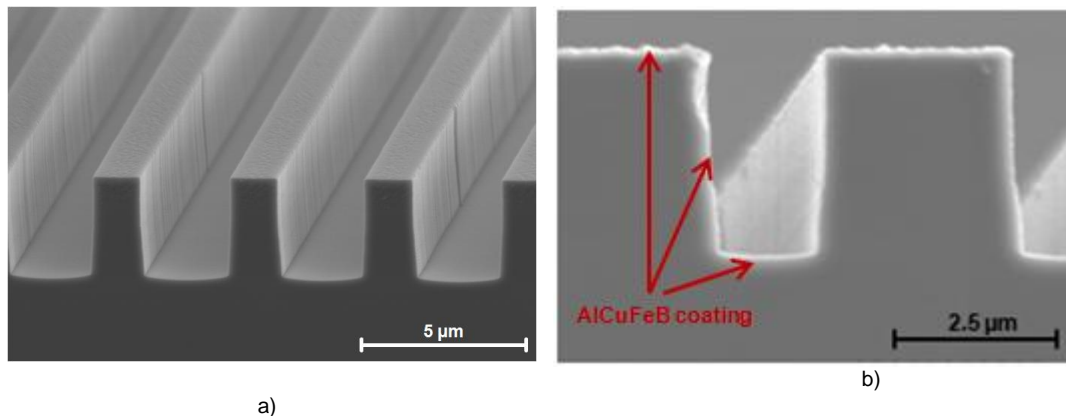


Figure 4.108 SEM image of a Si mold used for NIL, produced by reactive ion etching (RIE) Bosch process, half pitch 2  $\mu\text{m}$ , depth 3  $\mu\text{m}$  (Prof. Zygmunt Rymuza, Warsaw University of Technology)  
 a) before coating deposition  
 b) after coating deposition

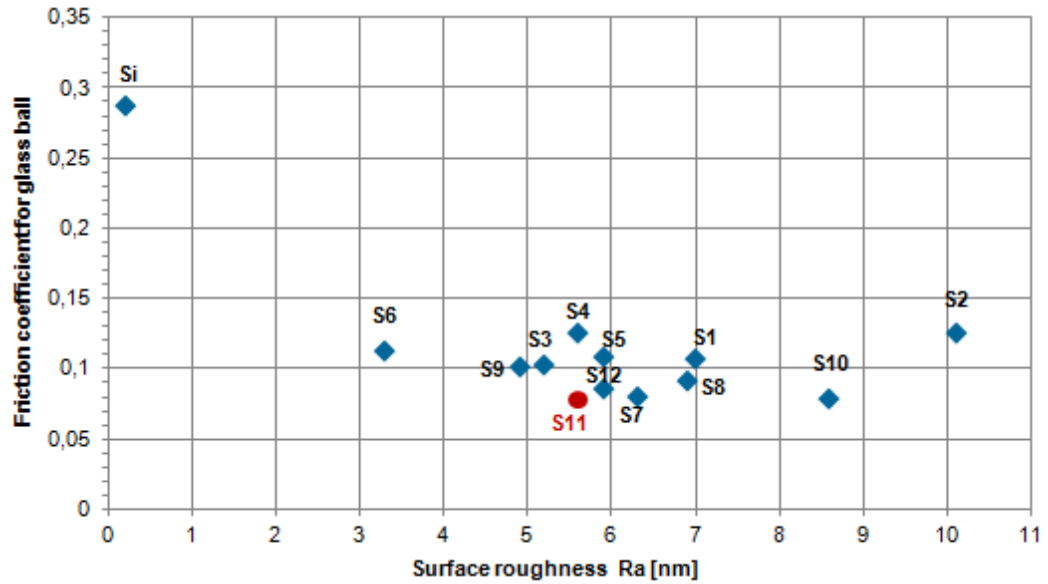
500 nm thick coatings were deposited on the stamps using a deposition power of 200 W, a working gas pressure of  $10 \cdot 10^{-3}$  mbar, a substrate - target distance of 3 cm and a deposition rate of 130 nm/min. The bias voltage was either 0 V or 75 V and the substrate temperature was varied between 500 °C and 600 °C. Table 4.5 summarizes the deposition parameters and the phases found in the deposited coatings. To deposit the AlCuFeB coatings also on the sidewalls of the Si stamps, the stamps were tilted for 40° towards the direction of the material flux and deposition was done in two runs. Between the two runs the stamps had to be brought to air and rotated for 180° so that both sidewalls are coated. Figure 4.108 b shows that the AlCuFeB coating is successfully deposited on the cavity and edges of the Si stamps.

Table 4.5 Deposition parameters and phases found in the AlCuFeB coatings deposited on the Si stamps (coating thickness: 500 nm, deposition power: 200 W, working gas pressure:  $10 \cdot 10^{-3}$  mbar, substrate - target distance: 3 cm, deposition rate: 130 nm/min)

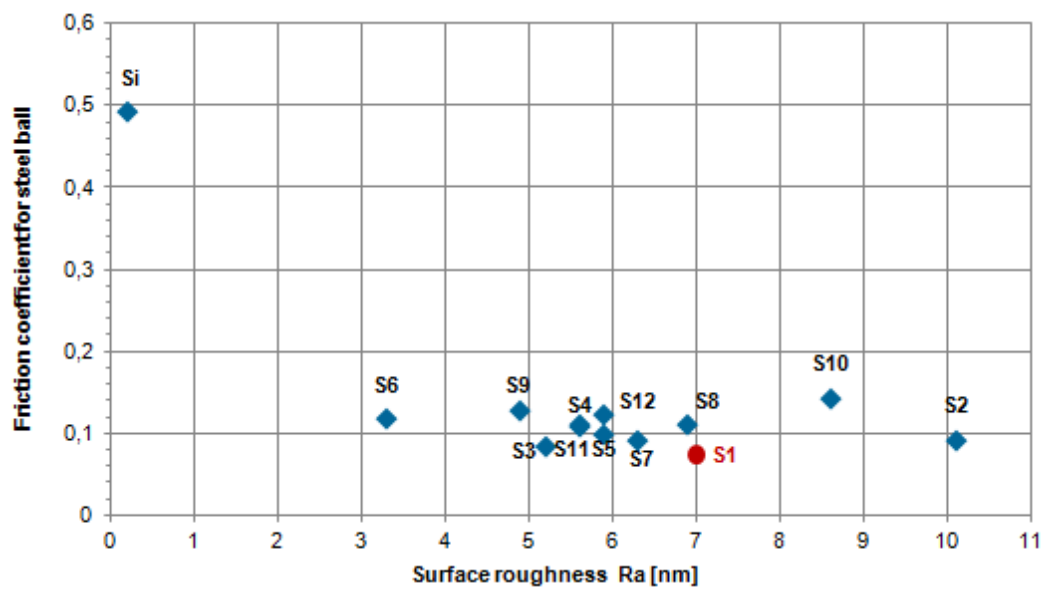
Sample Nr	Substrate type	Substrate temperature	Bias voltage	Phases
S1	SiO <sub>2</sub>	600 °C	0 V	40 % quasicrystalline AlCuFeB 60 % Al <sub>50</sub> Cu <sub>40</sub> Fe <sub>10</sub> (β phase)
S2	Si	600 °C	0 V	40 % quasicrystalline AlCuFeB 60 % Al <sub>50</sub> Cu <sub>40</sub> Fe <sub>10</sub> (β phase)
S3	SiO <sub>2</sub>	550 °C	0 V	Al <sub>50</sub> Cu <sub>40</sub> Fe <sub>10</sub> (β phase)
S4	Si	550 °C	0 V	Al <sub>50</sub> Cu <sub>40</sub> Fe <sub>10</sub> (β phase)
S5	SiO <sub>2</sub>	500 °C	0 V	amorphous Al
S6	Si	500 °C	0 V	amorphous Al
S7	SiO <sub>2</sub>	500 °C	75 V	amorphous Al
S8	Si	500 °C	75 V	amorphous Al
S9	SiO <sub>2</sub>	550 °C	75 V	Al <sub>50</sub> Cu <sub>40</sub> Fe <sub>10</sub> (β phase)
S10	Si	550 °C	75 V	Al <sub>50</sub> Cu <sub>40</sub> Fe <sub>10</sub> (β phase)
S11	SiO <sub>2</sub>	600 °C	75 V	40 % quasicrystalline AlCuFeB 60 % Al <sub>50</sub> Cu <sub>40</sub> Fe <sub>10</sub> (β phase)
S12	Si	600 °C	75 V	40 % quasicrystalline AlCuFeB 60 % Al <sub>50</sub> Cu <sub>40</sub> Fe <sub>10</sub> (β phase)

The roughness of the deposited coatings and the uncoated Si stamp was measured by Prof. Zygmunt Rymuza at the Warsaw University of Technology, using an atomic force microscope (AFM) with a NSC35 AIBS tip (conical, 10 nm radius). The friction coefficients and sticking coefficients of the coatings were also determined by AFM using a 500  $\mu\text{m}$  glass ball (IMiF beryllium bronze cantilever) and a 750  $\mu\text{m}$  steel ball (IMiF beryllium bronze cantilever). To measure the friction coefficient, a friction loop with a distance of 25  $\mu\text{m}$ , a sliding speed of 17  $\mu\text{m/s}$  and a load of 200  $\mu\text{N}$  for the steel ball and 300  $\mu\text{N}$  for the glass ball were used.

Since friction and adhesion often depend strongly on the surface roughness, Figure 4.109 shows the relationship between roughness and friction and Figure 4.110 presents the relation between roughness and pull-off force. The best samples according to friction and adhesion measurements are highlighted on the plots (red dots).

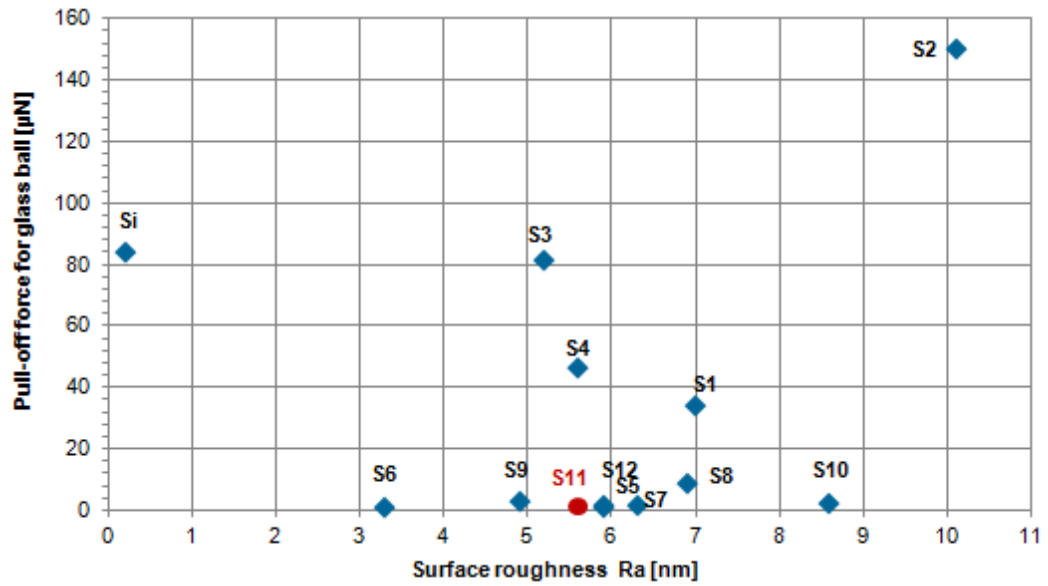


a)

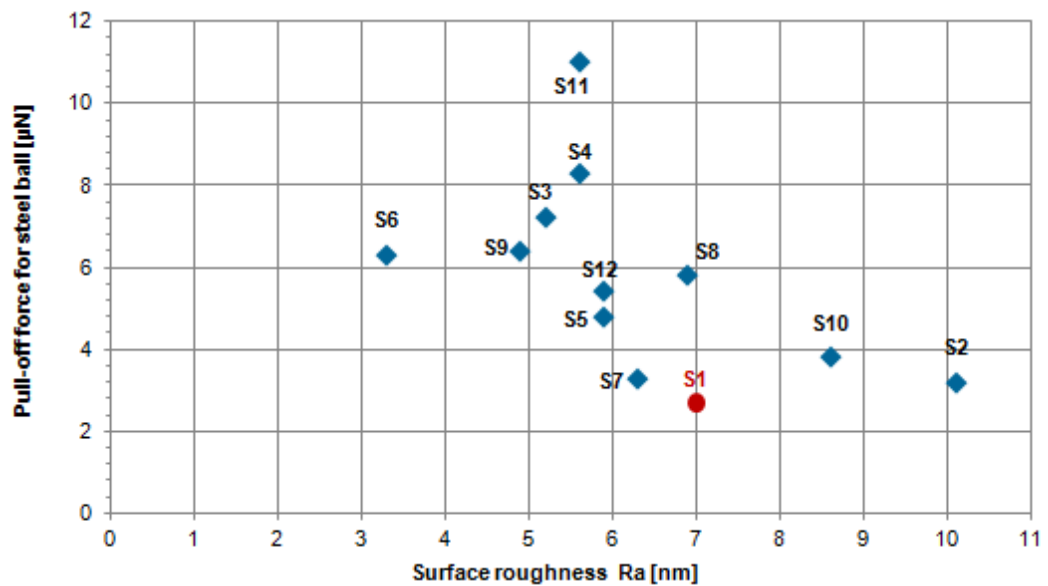


b)

Figure 4.109 Friction coefficient vs. surface roughness measured by atomic force microscope (AFM) (Prof. Zygmunt Rymuza, Warsaw University of Technology)  
 a) glass ball  
 b) steel ball



a)



b)

Figure 4.110 Pull-off force vs. surface roughness measured by atomic force microscope (AFM) (Prof. Zygmunt Rymuza, Warsaw University of Technology)  
a) glass ball  
b) steel ball

Nano-wear tests were done by Prof. Zygmunt Rymuza at the Warsaw University of Technology using an AFM with a super hard microtip DTCL-RC2060T80N (diamond tip). Two scans were performed using a scanning speed of  $11.82 \mu\text{m/s}$  with a test load of 20 nN and a scanning speed of  $39.38 \mu\text{m/s}$  with a test load of 10 nN. Figure 4.111 shows the depth of the wear track for the uncoated Si stamp and the coated samples.

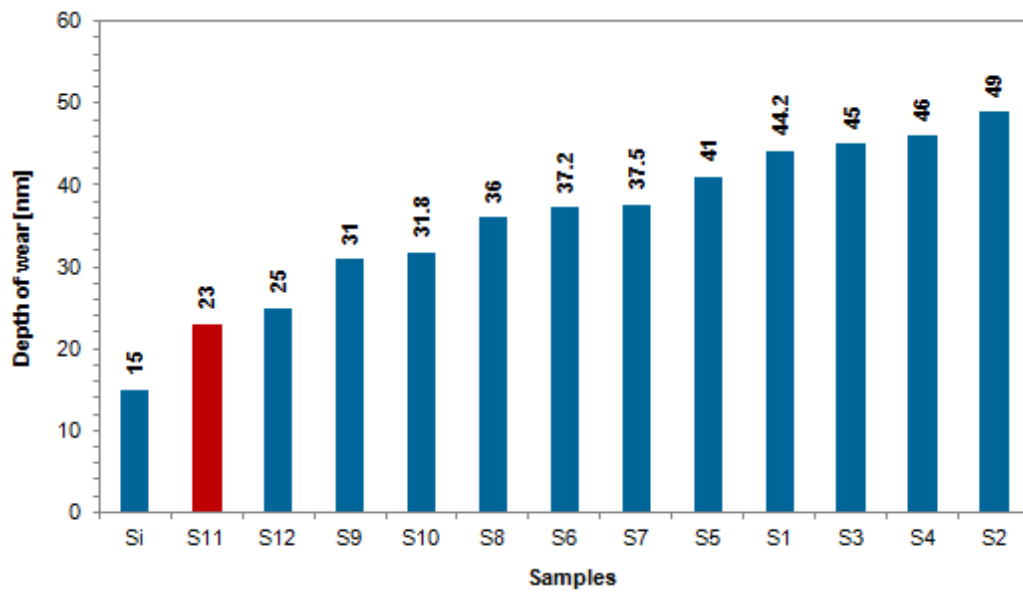
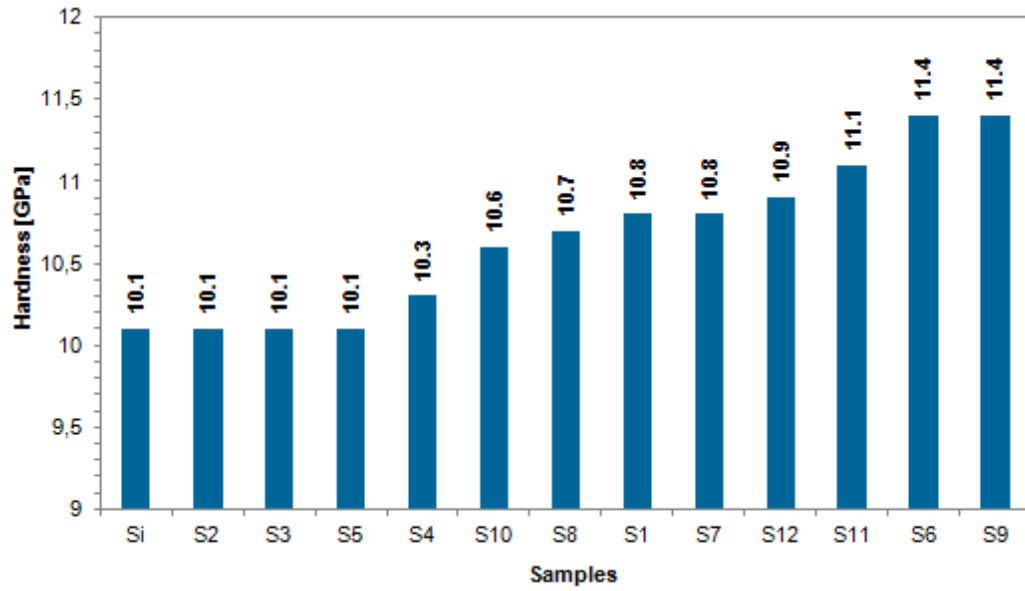


Figure 4.111 Results of the AFM nano-wear test (Prof. Zygmunt Rymuza, Warsaw University of Technology)

The hardness and Young's modulus of the samples was measured by Prof. Zygmunt Rymuza at the Warsaw University of Technology, using an AFM nano-indentation test with a Berkovich indenter and a test load between  $4000 - 10000 \mu\text{N}$ . The results are shown in Figure 4.112





a)



b)

Figure 4.112 Results of the AFM nano-indentation test  
(Prof. Zygmunt Rymuza, Warsaw University of Technology)  
a) Hardness  
b) Young's elastic modulus

Surface energy was determined by Prof. Zygmunt Rymuza at the Warsaw University of Technology using contact angle measurements with water and diiodomethane. In Figure 4.113 the polar and dispersive component of the measured surface energy are displayed.

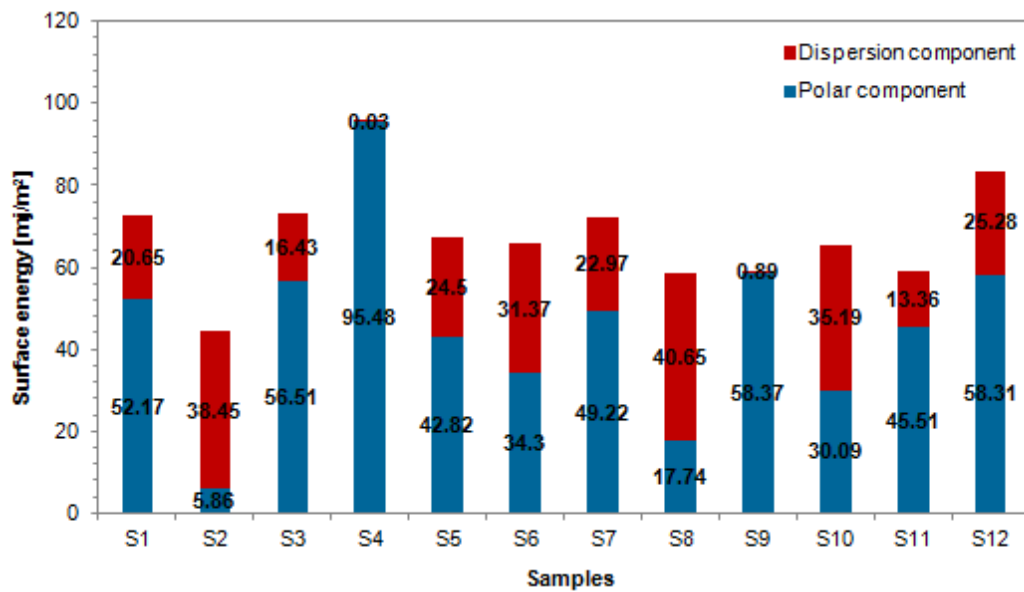


Figure 4.113 Results of the contact angle measurements using water and diiodomethane (Prof. Zygmunt Rymuza, Warsaw University of Technology)

500 nm thick, AlCuFeB coatings deposited at 600 °C with a bias voltage of 75 V and consists of 40 % quasicrystalline AlCuFeB + 60 % Al<sub>50</sub>Cu<sub>40</sub>Fe<sub>10</sub> ( $\beta$  phase), were found to exhibit favourable characteristics for nanoimprint lithography and cutting tools. These characteristics include: moderate surface roughness (Ra 5.6 nm), a very low friction coefficient (0.078 for glass, 0.111 for steel) and a very low pull-off force (1  $\mu$ N for glass, 11  $\mu$ N for steel) as well as high hardness (11 GPa) and a high Young's elastic modulus (180 GPa).

#### 4.4.11 Cutting inserts

Ceratizit (DCGT 11T308FN-25P) ISO-HW K10 cutting inserts (see Figure 4.114 a) were coated with  $\sim 1.5 \mu\text{m}$  thick AlCuFeB coatings to prolong lifetime of the cutting tools. The coatings were deposited using a deposition power of 200 W, a working gas pressure of  $10 \cdot 10^{-3}$  mbar, a substrate - target distance of 3 cm and a deposition rate of 130 nm/min, a substrate temperature of 600 °C and a bias voltage of 75 V. The coatings consist of 40 % quasicrystalline AlCuFeB and 60 %  $\text{Al}_{50}\text{Cu}_{40}\text{Fe}_{10}$  ( $\beta$  phase) (see Section 4.4.9). To deposit the AlCuFeB coatings on the top surface as well as on the cutting edge, the cutting inserts were tilted for 40° towards the direction of the material flux. After deposition, slight delamination occurs all over the cutting insert surface as well as on the cutting edge. The Film thickness is about 1.5  $\mu\text{m}$  on the surface and about 500 nm on the sidewall areas (see Figure 4.114 b - d).

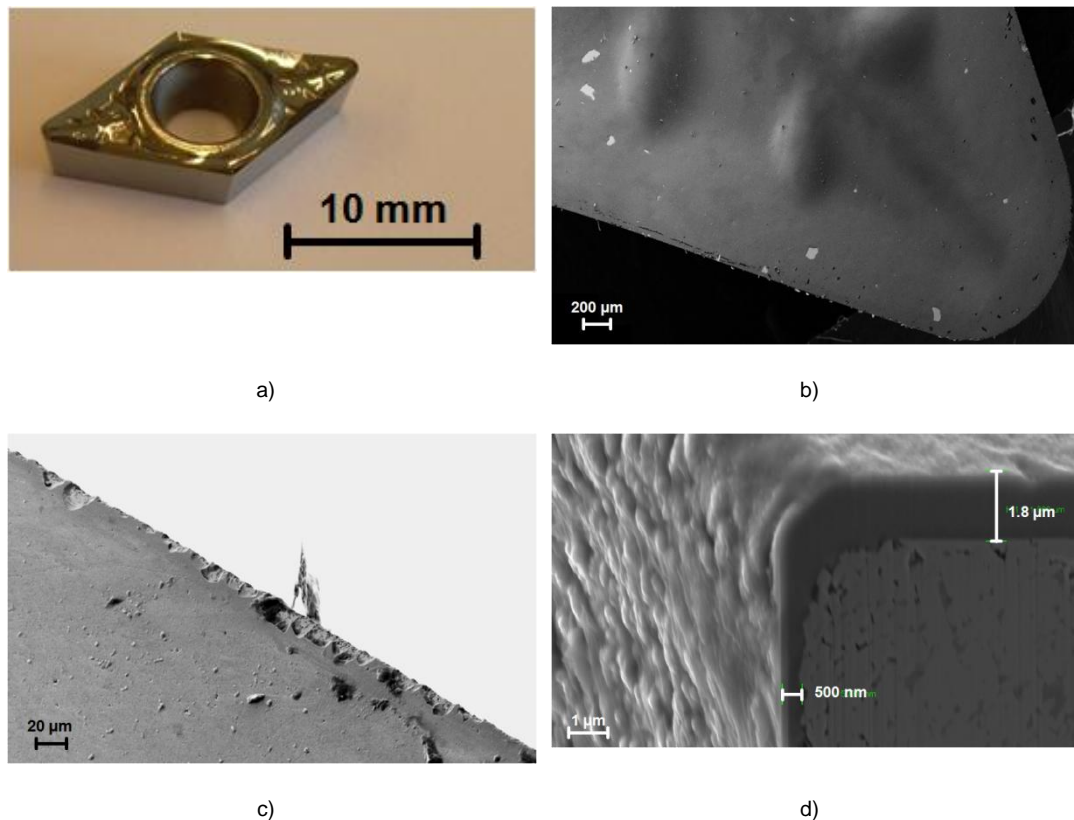


Figure 4.114 SEM image of a coated ISO-HW K10 cutting insert Ceratizit DCGT 11T308FN-25P  
b) surface  
c) cutting edge  
d) cross section (FIB)

The coated cutting inserts were tested during Aluminium (EN AW-6082) turning at Tool Consulting & Management GmbH (TCM) and compared to uncoated cutting inserts as well as with a commercially TiB<sub>2</sub> coating (Cemecon Alu Speed). While optically hardly any difference is visible between the samples (see Figure 4.115), cutting force measurements reveal that the TiB<sub>2</sub> coating breaks after about 100 Aluminium bars, while the AlCuFeB coating is still working (see Figure 4.116).

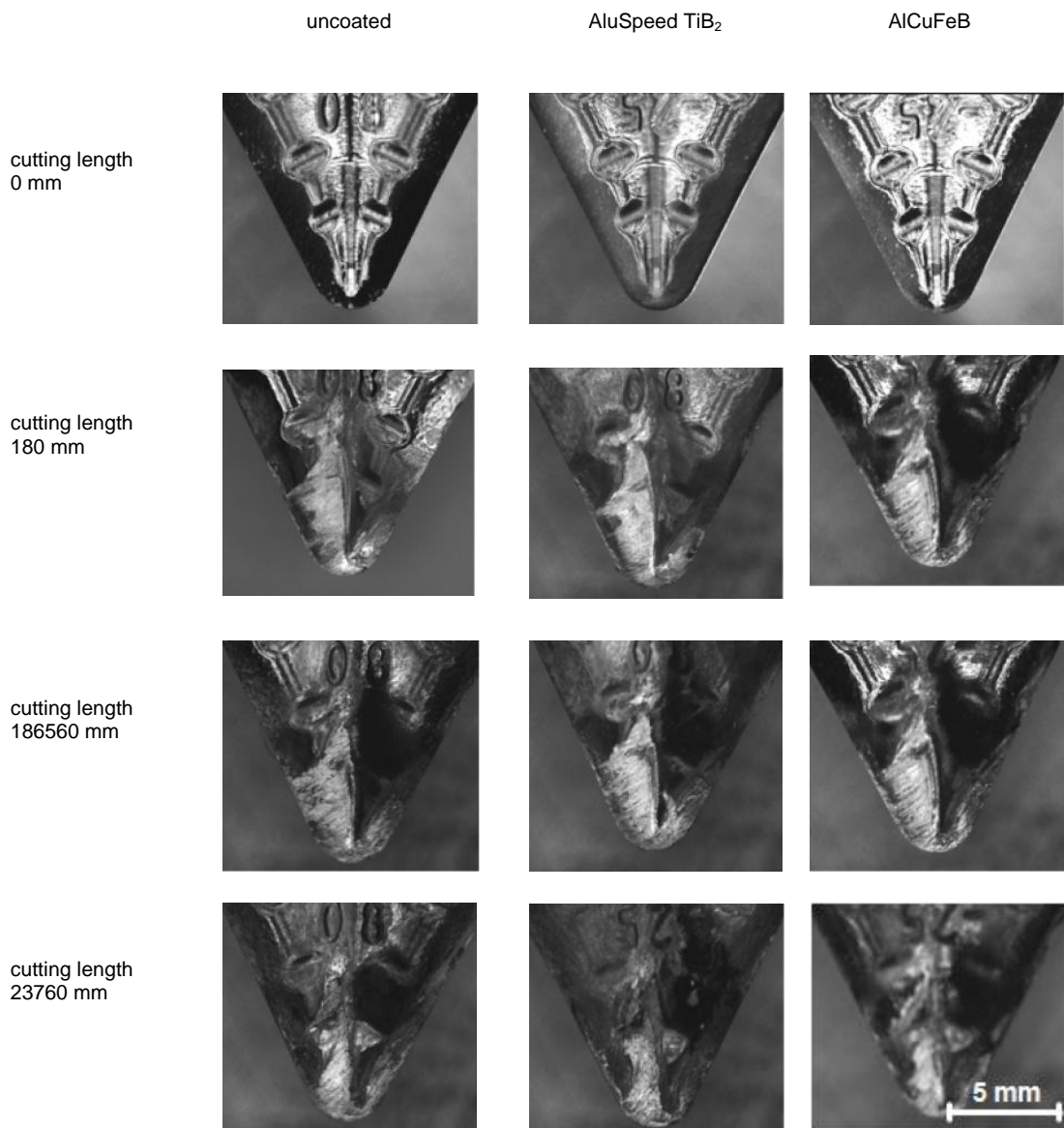


Figure 4.115 Images of uncoated and coated ISO-HW K10 cutting inserts Ceratizit DCGT 11T308FN-25P before and after turning Aluminium (EN AW-6082), cutting depth 2.5 mm, cutting speed 300 m/min, feed rate 0.25 mm/U (Tool Consulting & Management GmbH)

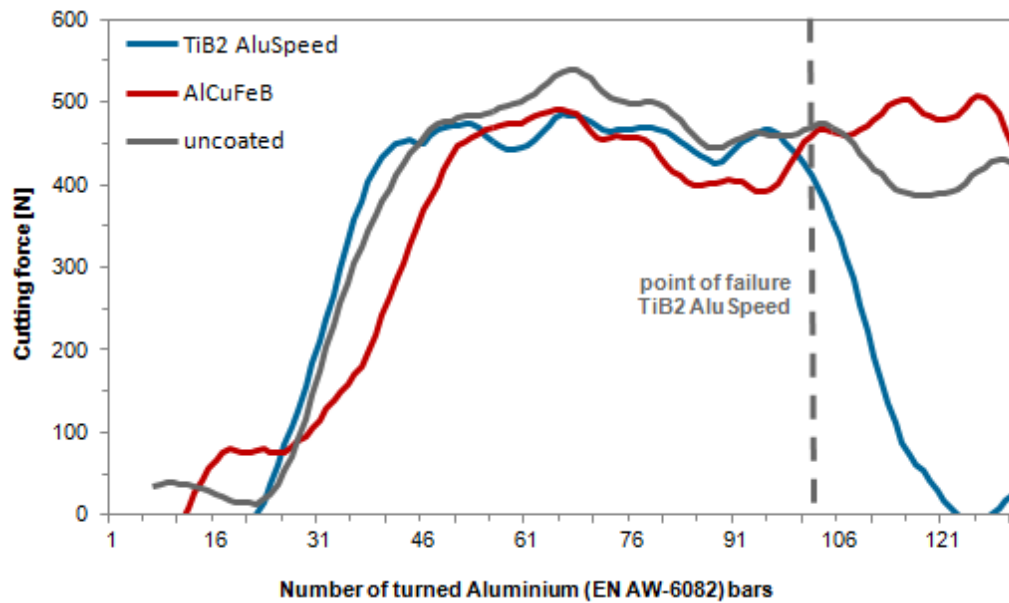


Figure 4.116 Cutting force during turning in dependence on the number of turned Aluminium (EN AW-6082) bars of 200 mm lengths, cutting depth 2.5 mm, cutting speed 300 m/min, feed rate 0.25 mm/U (Tool Consulting & Management GmbH)

Ceratizit (DCGT 11T308FN-25P) ISO-HW K10 cutting inserts coated with  $\sim 1.5 \mu\text{m}$  thick AlCuFeB coatings provide a longer lifetime during Aluminium turning compared to a commercially available TiB<sub>2</sub> coating (Cemecon Alu Speed) and thus can be regarded as a promising coating for turning tools.

## 5. Discussion

### 5.1 AlMgB<sub>14</sub>

#### 5.1.1 Targets

AlMgB targets with amorphous and with crystalline boron were produced and used for coating deposition. The density of the targets produced with amorphous B was about 1.66 g/cm<sup>3</sup> and the one of the targets produced with crystalline B was about 1.96 g/cm<sup>3</sup>. Both densities are significantly lower (38 % and 26 %) than the theoretical maximum of 2.66 gm/cm<sup>3</sup> [8,17], which suggests that the targets, especially the targets produced with amorphous B are very porous. This is confirmed by the SEM images, which reveal a very rough surface with a high density of pores. For both types of boron powder (amorphous and crystalline) the AlMgB targets show surface features, which are similar to those of the crystalline B powder (see Figure 3.9 d in Section 3.3). Thus it might be that hot pressing at 1500 °C causes crystallisation of the amorphous B powder. While the surface features of the two different targets are very similar, the SEM cross section images show that the targets produced with amorphous B exhibit a higher porosity. The densification of the AlMgB targets might be improved by optimising the hot pressing parameters or by using a hot isostatic press (HIP), where pressure is simultaneously applied from all directions to the material. Within the error of measurement the targets produced with amorphous and crystalline B exhibit the same chemical composition. The average chemical composition of the targets measured by EDS is: 4.6 ± 0.9 at% Al, 4.5 ± 0.2 at% Mg, 91.0 ± 1.0 at% B. Compared to the nominal AlMgB<sub>14</sub> composition (6.25 at% Al, 6.25 at% Mg, 87.5 at% B), the targets contain about 1-2 at% less Al and Mg, and 2-4 at% more B. As mentioned in Section 3.6 the quantification of light elements by EDS (especially B) is limited in accuracy. Thus within the error of measurement, the composition of the targets can be regarded as matching the nominal AlMgB<sub>14</sub> composition. The low standard deviation of the EDS measurements indicates that the homogeneity of the target composition is very good, which is supported by the SEM cross section images. Independent of the B powder used for target production, the AlMgB targets exhibit ~7 at% O and ~7 at% C. This approximately equals the impurity content, which has to be expected due to the impurities found in the elemental powders used for target production (~3 at% O and ~15 at% C). Thus it can be concluded that during the hot pressing process no significant amount of additional impurities is incorporated. XRD measurements show that both target types contain an AlMgB<sub>14</sub> as well as an Al<sub>2</sub>MgO<sub>4</sub> spinell phase. According to the O content of the targets, the content of the Al<sub>2</sub>MgO<sub>4</sub> phase can be estimated as 7 - 14 vol% at

maximum. The two phases are also visible in the cross section SEM images and can be identified by EDS measurements. The  $\text{Al}_2\text{MgO}_4$  is present in the form of particles with diameters less than  $3\ \mu\text{m}$ , which are homogeneously distributed throughout the targets. According to the area ratio, the content of the  $\text{Al}_2\text{MgO}_4$  phase can be estimated to be about 6 %.  $\text{Al}_2\text{MgO}_4$  can frequently be found in  $\text{AlMgB}_{14}$  bulk material, if oxygen impurities are present because oxidation is energetically more favourable than the formation of a crystalline  $\text{AlMgB}_{14}$  phase (see Section 2.2.1). Thus to avoid the formation of the  $\text{Al}_2\text{MgO}_4$  phase, the impurity content of the targets has to be reduced. The O content of the elemental powders could be minimized by using powders with bigger grains. Also hot pressing under a reducing atmosphere (e.g.:  $\text{CO}$ ,  $\text{NH}_3$  and  $\text{H}_2$ ) might help to reduce the O content of the  $\text{AlMgB}$  targets. The measured electrical resistivity of  $1.13\ \Omega\text{m}$  is within the order of magnitude of the values found for  $\text{AlMgB}_{14}$  in literature ( $50\ \Omega\text{m}$  [8,9,11,18,20]). Because an electrical resistivity of this magnitude is too high for DC magnetron sputtering, RF magnetron sputtering had to be used for coating deposition. During deposition all  $\text{AlMgB}$  targets suffer from crack formation, crack formation is more severe for the targets produced with crystalline boron. This crack formation occurs even if the applied deposition power does not exceed  $25\ \text{W}$  ( $3.8\ \text{W}/\text{cm}^2$ ). The reason is probably the high brittleness of the  $\text{AlMgB}$  targets and thermal stresses due to the low thermal conductivity of  $\text{AlMgB}_{14}$ . Since the targets produced with crystalline boron exhibit a higher density, it can be assumed that a more porous target structure reduces brittleness and thus reduces crack formation.

### 5.1.2 Coatings

$\text{AlMgB}$  coatings were deposited on Si and K10 WC-Co hard metal substrates. Since wear resistant cutting tool coatings represent the main application of  $\text{AlMgB}_{14}$  coatings, WC-Co is the substrate of major interest. The deposition rates achieved by RF magnetron sputtering are very low,  $\sim 20\ \text{nm}/\text{min}$  for a deposition power of  $100\ \text{W}$  ( $15.2\ \text{W}/\text{cm}^2$ ). Independent of the B powder used for target production and the deposition power applied, the deposited coatings show a composition of 2.2 at% Al, 1.1 at% Mg and 96.9 at% B. Since the chemical composition of the targets approximately equals the  $\text{AlMgB}_{14}$  composition, a loss of 4 -5 at% Al and Mg occurs during deposition. The loss of Al and Mg might be caused by the crack formation in the targets. Also oxidation of Al and Mg by the residual gas because of the low deposition rates might be responsible for the loss of these constituents. According to the amount of O (7 at%) and C (7 at%) impurities found on the target surfaces and the impurities incorporated in the coatings due to the residual gas (see Section 3.2), the maximum O and C content of the coatings can be estimated as: 11 at% O, 8 at% C for coatings deposited with  $5\ \text{nm}/\text{min}$  ( $25\ \text{W}$  deposition power) and 7 at% C and 8 at% O for coatings deposited with  $20\ \text{nm}/\text{min}$  ( $100\ \text{W}$

deposition power). Indeed the O and C amount incorporated in the AlMgB coatings are lower than the estimated values. In the coatings deposited with 100 W (~ 20 nm/min), about 2 at% O and 2 at% C can be found. EDS line scans show that for coatings deposited on WC-Co, at 600 °C Al, Mg, B and O are homogeneously distributed throughout the coatings. Applying post annealing at 900 °C further improves the homogeneity of the elemental distribution, but a significant amount of C (~ 40 at%) is incorporated during the post annealing process. After post annealing the AlMgB coatings exhibit approximately the same C concentration which can be found in the WC-Co substrate. Since post annealing was done under vacuum conditions, it can be excluded that such amounts of C result from the post annealing environment. EDS line scans of the coating cross section indicate that C diffuses from the WC-Co substrates into the AlMgB coating. Coatings deposited on WC-Co substrates heated to 600 °C consist of amorphous boron and exhibit a flat, featureless surface. Post annealing at 900 °C causes the development of a very rough surface with a two phase structure. Besides the amorphous boron phase, an AlB<sub>2</sub> phase forms. Additionally a CoWB phase might develop due to post annealing at 900 °C. It is reported in literature that C incorporation in coatings can inhibit crystallisation and lead to amorphous coatings and/or promotes the formation of a β-AlB<sub>12</sub> phase [14,19] (see Section 2.2.1). Besides the high C contamination, the deviation from the AlMgB<sub>14</sub> composition (4 - 5 at% less Al and Mg) and/or a too low post annealing temperature might inhibit the formation of the AlMgB<sub>14</sub> phase. Since post annealing at 900 °C alters the WC-Co substrates and causes significant C diffusion, higher post annealing temperatures were not applied. If deposition is done on WC-Co heated to 600 °C, a monolayer-to-monolayer interface develops, where little diffusion and chemical reaction between the deposited atoms and the substrate occur. The deposited coatings appear very homogenous without any cracks or pores. Although monolayer-to-monolayer interfaces usually do not indicate excellent coating adhesion, the adhesion of the AlMgB coatings on the WC-Co substrates is sufficient not to cause delamination. After applying post annealing at 900 °C, the interface still exhibits a monolayer-to-monolayer characteristic, although the interface region appears a bit less sharp. The coating still looks very homogenous without any cracks or pores. The region of W diffusion is increased causing a less sharp substrate coating interface. Nevertheless coating delamination occurs after post annealing at 900 °C. According to the estimation in Section 3.4 the thermal stresses between the AlMgB coating and the substrate increase from 0.49 to 0.83 GPa when post annealing at 900 °C is applied. The ratio of the AlMgB<sub>14</sub> melting temperature (>2000 °C [5,7,10]) and the post annealing temperature of 900 °C is about 0.52, which means that thermal stress dominates over the intrinsic coating stress (see Section 2.5.3). Therefore the significant increase of thermal stress is very likely responsible for the coating delamination. The hardness of the WC-Co K10 substrates was measured as 1550 ± 252 HV, which is a bit higher than the 1200 HV specified by the



producer. All deposited AlMgB coatings exhibit a higher hardness than the uncoated WC-Co substrate.

Exhibiting a hardness of ~2500 HV, the coatings deposited using the AlMgB target with amorphous B are slightly harder (~20 %) than the coatings deposited using the AlMgB target with crystalline B (~2000 HV). The coatings deposited on substrates heated to 600 °C, which according to XRD consist of amorphous B tend to exhibit higher (~12%) hardness values of ~2400 HV than the coatings post annealed at 900 °C (~2100 HV), see Figure 5.1.

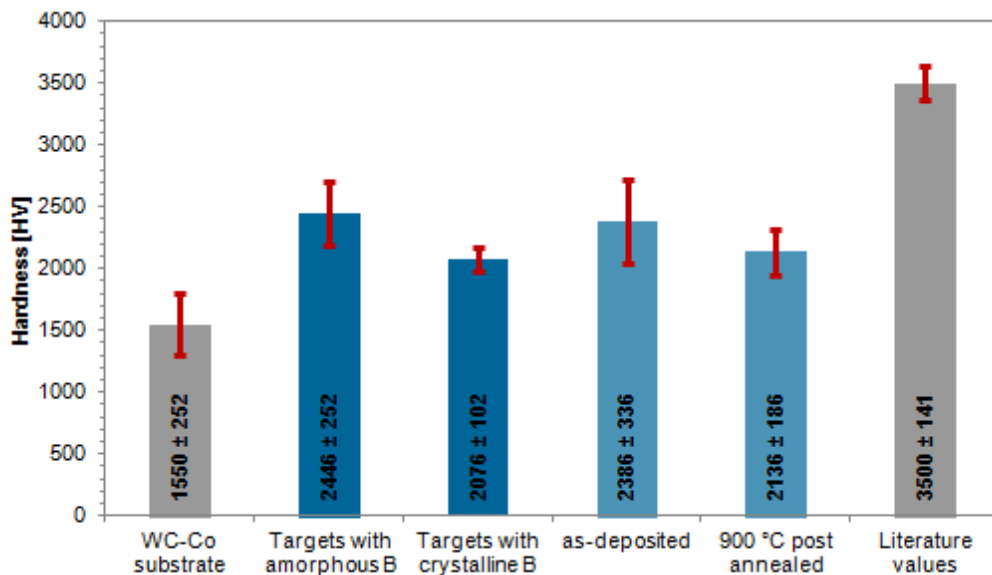


Figure 5.1 Hardness of the WC-Co substrate, the AlMgB coatings and values found in literature

This might be due to the significantly better adhesion of the as deposited coatings compared to the post annealed coatings, for which delamination occurs. Also the C incorporation might decrease the coating hardness. The hardness values measured for the coatings post annealed at 900 °C approximately correspond with the hardness of aluminium diboride  $\text{AlB}_2$  (2500 HV [56]). This is in agreement with the EDS and XRD measurements, which show that an  $\text{AlB}_2$  phase develops during the post annealing treatment. The measured hardness of the as-deposited and coatings post annealed at 900 °C is about 30 % lower than the hardness of pure, nano-crystalline  $\text{AlMgB}_{14}$ , which ranges between 32 – 35 GPa (3200 HV – 3600 HV) [6].

## 5.2 AlCuFeB ceramic targets

### 5.2.1 Targets

The quasicrystalline  $\text{Al}_{59}\text{Cu}_{25.5}\text{Fe}_{12.5}\text{B}_3$  targets exhibit ceramic characteristics like high brittleness as well as low thermal and electrical conductivity, which is likely to be caused by the quasicrystalline  $\text{Al}_{59}\text{Cu}_{25.5}\text{Fe}_{12.5}\text{B}_3$  phase that develops. The quasicrystalline  $\text{Al}_{59}\text{Cu}_{25.5}\text{Fe}_{12.5}\text{B}_3$  targets have a density between 4.66 to 4.80  $\text{g}/\text{cm}^3$ , which is close to the values found in literature of 4.7  $\text{g}/\text{cm}^3$  [45], which suggests that the densification during the hot pressing process is more or less complete. This is approved by the SEM images, which do not show any pores in the targets and show that the structure of initial powders is not preserved. Thus 700 °C Uniaxial Hot Pressing (HUP) can be regarded as an appropriate method to produce high quality quasicrystalline  $\text{Al}_{59}\text{Cu}_{25.5}\text{Fe}_{12.5}\text{B}_3$  targets. Targets with the nominal  $\text{Al}_{59}\text{Cu}_{25.5}\text{Fe}_{12.5}\text{B}_3$  composition can be produced by using *St. Gobain Cristome F1* powders with particles sizes ranging from 10 – 70  $\mu\text{m}$  and 40 – 70  $\mu\text{m}$ . The low standard deviation ( $\sim 0.5$  at%) of the chemical composition indicates that the reproducibility of the target composition is very good. The oxygen content of 4 at% is higher than the impurity content found in the *St. Gobain Cristome F1* powders (0.1 at% O). It might be that during hot pressing and/or during the finishing process (grinding/polishing) of the target additional oxygen is incorporated. The targets produced with an elemental powder mixture show small deviations ( $\sim 3$  at%) from the nominal composition. The higher standard deviation ( $\sim 3$  at%) of the chemical composition indicates a reduced reproducibility of the target composition. The higher amount of impurities found in the elemental powders and inhomogenities in the elemental distribution of the initial powder mixture might be responsible for the deviation from the nominal  $\text{Al}_{59}\text{Cu}_{25.5}\text{Fe}_{12.5}\text{B}_3$  composition and the reduced reproducibility. Mechanical milling/mixing of the single elemental powders might not be sufficient to guarantee a homogenous distribution of the single elements in the powder mixture used and/or weighting out of the single element powders could cause small composition shifts. The oxygen amount of 19 at% found in the targets produced with the elemental powder mixture is significantly higher than the amount of oxygen found in the elemental powders ( $\sim 5$  at%), which indicates that additional oxygen is incorporated during hot pressing and/or during the finishing process. Hot pressing under a reducing atmosphere (e.g.:  $\text{CO}$ ,  $\text{NH}_3$  and  $\text{H}_2$ ) might help to avoid O incorporation. Independent of the particle sizes of the *St Gobain Cristome F1* powders, Al, Cu and Fe are very homogeneously distributed in the target. B containing phases are distributed inside the grains and can be frequently found at grain boundaries as well. The targets produced with elemental powders are significantly less homogenous and the boron powder particles seem not to dissolve in the AlCuFe matrix.

All three target types show an icosahedral phase, the main diffraction peaks show shoulders. According to literature [57,58] these shoulders might be caused by approximant phases (crystalline phases nearby the composition domain of the quasicrystalline phase). Comparing the results with literature [58], it can be assumed that the shoulders could correspond to the orthorhombic approximant phase. Since approximant phases are very complex [58,59] these phases are very difficult to identify by XRD and further work would be required to determine their exact nature using High Resolution Transmission Electron Microscopy (HRTEM) or high resolution XRD [60,61]. Like the shifts of the quasicrystalline peaks visible in the XRD pattern, the shoulders of the quasicrystalline peaks could also be caused by stresses (deformation of the unit cell) due to the hot pressing / cooling process. While the targets produced with the *St Gobain Cristome F1* powders contain only the icosahedral and orthorhombic phase, the target produced with the elemental powder consists mainly of the  $\text{Al}_{50}\text{Cu}_{40}\text{Fe}_{10}$   $\beta$  phase (70 %). The  $\beta$  phase might develop due to the small deviation shift from the nominal  $\text{Al}_{59}\text{Cu}_{25.5}\text{Fe}_{12.5}\text{B}_3$  composition and/or due to inhomogenities in the elemental distribution of the initial powder mixture. It can be found in literature that the presence of C [28]; O [37,38] and N [1] strongly influences the formation the icosahedral AlCuFe phase and promotes the  $\text{Al}_{50}\text{Cu}_{40}\text{Fe}_{10}$   $\beta$  phase formation if the contamination is large enough. Thus the impurities found in the elemental powders/targets, especially the oxygen could promote the  $\beta$  phase development. The measured electrical resistivity of the targets produced with *St Gobain Cristome F1* powders ( $96.4 \mu\Omega\text{m} \pm 4.0 \mu\Omega\text{m}$ ) is of the same order of magnitude as the values found in literature for pure, high quality  $\text{Al}_{62.5}\text{Cu}_{25}\text{Fe}_{12.5}$  quasicrystalline (20 – 50  $\mu\Omega\text{m}$  [35,36]) The additionally incorporated B precipitates might be responsible for the slightly increased electrical resistivity. The lower resistivity of the targets produced with the elemental powders ( $15.0 \mu\Omega\text{m} \pm 5.2 \mu\Omega\text{m}$ ) is very likely caused by the  $\text{Al}_{50}\text{Cu}_{40}\text{Fe}_{10}$   $\beta$  phase, which exhibits a significantly lower electrical resistivity ( $\sim 1 \mu\Omega\text{m}$  [35]) than the quasicrystalline AlCuFe phase. Nonetheless these relatively high resistance values make it necessary to apply RF sputtering because they exceed values suitable for a DC sputter process. The crack formation in the target during film deposition is independent of the powders used for target production and might be caused by thermal stresses due to the low thermal conductivity of quasicrystalline  $\text{Al}_{59}\text{Cu}_{25.5}\text{Fe}_{12.5}\text{B}_3$  [23]. Using a pulsed magnetron system does not reduce the thermal load on the targets and thus does not prohibit crack formation.

## 5.2.2 Coatings

AlCuFeB coatings were deposited on Si substrates by RF magnetron sputtering of AlCuFeB targets. If a deposition power of 100 W or more is applied, reasonable deposition rates of 75 nm/min or more are achieved. The observed, linear increase of the Al content with the applied deposition power (see Figure 4.31 in Section 4.2.2) and the influence of the working gas pressure (see Figure 4.32 in Section 4.2.2) on the coating composition is probably connected with the crack formation. It is likely that small arcs develop between the cracks, especially at higher working gas pressures and favourably sputter additional Al atoms or that Al is favourably evaporated from the target due to local heating of the target. The statistical variation in the coating composition for constant deposition parameters could be caused by the crack network changing its form or developing further. A change of the crack network would change the surface exposed to the plasma causing variations in the material flux and thus in the chemical composition of the deposited coatings. The as deposited coatings show an amorphous structure, which is in agreement with results obtained for AlCuFe [57,61,64,65]. According to the XRD measurements a quasicrystalline  $\text{Al}_{59}\text{Cu}_{25.5}\text{Fe}_{12.5}\text{B}_3$  phase develops when the chemical composition of the deposited coatings is close enough to the nominal  $\text{Al}_{59}\text{Cu}_{25.5}\text{Fe}_{12.4}\text{B}_3$  composition and post annealing at 600 °C is applied for at least 30 min. The quasicrystalline diffraction peaks show shoulders, which become less significant for longer post annealing times (see Figure 4.36 in Section 4.2.3). A certain degree of peak broadening exists also after 3 h of post annealing. This might result from the formation of the rhombohedral phase [57,58] or from stresses, which deform the unit cell. High Resolution Transmission Electron Microscopy (HRTEM) or high resolution XRD would be required to gain a more detailed understanding [60,61]. According to literature [65], post annealing at higher temperatures (~750 °C) might cause the development of an almost entirely quasicrystalline phase. Since temperatures of more than 600 °C would alter the steel and hard metal substrates, post annealing at higher temperatures was not applied. Besides the quasicrystalline phase, an  $\text{Al}_{50}\text{Cu}_{40}\text{Fe}_{10}$   $\beta$  phase develops. Post annealing at 600 °C for 5 - 15 min or less leads to the development of mostly  $\text{Al}_{50}\text{Cu}_{40}\text{Fe}_{10}$   $\beta$  phase (~60 %). When the post annealing time is increased from 5 - 15 min to 30 - 45 min the content of  $\text{Al}_{50}\text{Cu}_{40}\text{Fe}_{10}$   $\beta$  phase decreases from ~60 % to ~35 %. With a further increase of post annealing time to 3 h, the amount of  $\beta$  phase can be reduced to ~25 %. Since the  $\beta$  phase can be also found when deposition is done on a WC-Co hard metal substrate, it can be excluded that the  $\beta$  phase formation is specific for the Si substrate. It is reported in literature that instead of a single icosahedral phase (i), two phases (i and  $\beta$ ) or even three phases (i,  $\beta$  and  $\omega$ ) form if a certain amount of C [28], O [37,38] or N [1] impurities is exceeded in the AlCuFe bulk. Thus it can be speculated, that the diffusion of elements from the substrates (Si/C) might promote the  $\beta$  phase development. The interface

between the Si substrate and the coatings deposited at room temperature seems to be a sharp monolayer-to-monolayer interface without any significant diffusion or mechanical interlocking. During post annealing at 600 °C high temperature Si diffusion occurs and the development of a compound interface, with chemical interaction of the film and Si substrate is observed. Si rich phases are formed not only at the interface but also close to the surface (see Figure 4.37 in Section 4.2.4). Post annealing at 600 °C causes buckle induced crack formation and coating delamination all over the coating surface. It is known from literature that buckling may occur under compressive stress for a system with weak interfacial bonding [62]. According to the estimation in Section 3.4 the thermal stresses between the quasicrystalline AlCuFeB coating and the Si substrate is about as high as 0.78 GPa (compressive) at room temperature, when deposition is done at 600 °C. The ratio of the melting temperature (~1000 °C [21]) and the substrate temperature of 600 °C is about 0.69, which means that thermal stress dominates over the intrinsic coating stress (see Section 2.5.3). Therefore thermal stress is very likely to be responsible for the buckling induced coating delamination and cracking. Besides thermal stress, also the observed Si diffusion or oxidation effects might enforce buckling. Comparing the as-deposited coatings with the films post annealed at 600 °C, it can be stated that post annealing causes a strong increase in surface roughness as well as a significantly reduced interface and coating homogeneity and quality (formation of cracks and pores).

### 5.3 AlCuFeB shifted composition targets

AlCuFeB targets with a shifted composition can be produced by either adding elemental powders to the commercially available *St. Gobain Cristome F1* powder or by using an elemental powder mixture with a shifted composition. Adding Al or AlB<sub>2</sub> to the *St. Gobain Cristome F1* powder results in target compositions with Al in excess and a lack of Cu, compared to the powder composition. If Cu and Fe powders are added to the *St. Gobain Cristome F1* powder or if a shifted powder mixture is used, the composition of the targets equals the powder composition. During coating deposition, the target composition is reproduced. The coatings exhibit the same chemical composition as the targets independent of the deposition power and the substrate temperature applied. Thus the shifted composition targets cannot be used to compensate the composition shift that occurs when deposition is done by ceramic AlCuFeB targets.

## 5.4 AlCuFeB metallic targets

### 5.4.1 Targets

By 30 MPa hot pressing at temperatures for 1 h at 500 °C it is possible to produce AlCuFeB targets which exhibit the  $\text{Al}_{59}\text{Cu}_{25.5}\text{Fe}_{12.5}\text{B}_3$  composition but not the quasicrystalline structure. These targets can only be produced with an elemental powder mixture, since the *St. Gobain Cristome F1* powder cannot be hot pressed below 700 °C and because the powder particles themselves exhibit the quasicrystalline characteristics. The density of the metallic targets is  $4.10 \text{ g/cm}^3$ , which is significantly less than that of the quasicrystalline targets. SEM cross section images reveal some small pores, which are distributed homogeneously throughout the target. Pure Al and Fe phases with similar shapes as the corresponding powder particles can be identified by EDS/SEM. The B particles do not dissolve in the target matrix and occur in the form of B precipitates homogeneously distributed throughout the target. These are indications that a hot pressing temperature of 500 °C is not sufficient to completely dissolve the elemental powders and to achieve full densification. Since the quasicrystalline phase starts to develop at about 550 °C, hot pressing temperatures cannot be increased to improve densification. An improved densification without developing the quasicrystalline phase might be achieved by using Isostatic Hot Pressing (HIP), where pressure is simultaneously applied from all directions to the material. The measured electrical resistivity of the metallic targets ( $1.12 \mu\Omega\text{m} \pm 0.06 \mu\Omega\text{m}$ ) is significantly lower than the electrical resistivity of the ceramic targets (15 – 96  $\mu\Omega\text{m}$ ). This low resistance allows to employ a DC sputter process which is more economic and efficient due to the simpler technology involved. The electrical resistivity of the metallic targets, which is of the same size as measured for simple AlCu metallic alloys is already a first indication, that no quasicrystalline phase forms during hot pressing at 500 °C. The targets also show magnetism if they are brought close to the magnetron system of the sputtering source, which suggests that the targets contain a metallic Fe phase. The average composition of:  $64.4 \pm 1.9 \text{ at\% Al}$ ,  $23.3 \pm 2.0 \text{ at\% Cu}$  and  $9.3 \pm 0.7 \text{ at\% Fe}$  deviates from the nominal composition (5 at% more Al, 2.5 at% less Cu and 2.5 at% less Fe). The standard deviation of 1 at% indicates that the reproducibility of the target composition is sufficiently good. Since hot pressing of the *St. Gobain Cristome F1* powders at higher temperatures does not cause the loss of any of the powder constituents, it has to be assumed that the composition deviation of the targets results directly from the characteristics of the elemental powder mixture. The higher amount of impurities found in the elemental powders and inhomogeneities in the elemental distribution of the initial powder mixture might be responsible. Mechanical milling/mixing of the single elemental powders might not be sufficient to guarantee a homogeneous distribution of the single elements in the powder mixture used and/or

weighting out of the single element powders could cause composition shifts. By using EDS and XRD, seven different metallic phases (Al, Fe, AlFe, AlCu, Al<sub>2</sub>Cu, Al<sub>5</sub>Fe<sub>2</sub>, Al<sub>7</sub>Cu<sub>2</sub>Fe) can be identified in the SEM images. The phases are uniformly distributed throughout the target. No crack formation occurs when the deposition power is varied between 25 W and 300 W, which is probably because of the better thermal conductivity and higher toughness of the metallic targets compared to the ceramic targets. Also the pores observed in the target allow more atomic movement/diffusion and prevent crack propagation. The results are in agreement with results found in literature [57]. AlCuFe targets produced by 22 MPa hot pressing at 400 °C for 2.5 h show similar features like absence of icosahedral and/or rhombohedral phase, intermetallic Al<sub>2</sub>Cu and elemental Al, Cu phases [57]. It could be shown that the chemical composition of the metallic target stays constant during operation and that a condition time of 5 min is required to remove most of the O and C impurities from the target surface. After 5 min of operation, the amount of O and C found on the target surface decreases from ~17 at% O and ~13 at% C to ~6 at% O and ~3 at% C, which equals the impurity content of the elemental powder mixture. The high O and C impurities located on the target surface probably result from the finishing process (grinding/polishing) and no additional O and C seem to be incorporated during the hot pressing process. Hot pressing under a reducing atmosphere (e.g.: CO, NH<sub>3</sub> and H<sub>2</sub>) might help to reduce O incorporation. For operating times below 1 h, the deposited coatings exhibit a significant excess of Al and a deficit of Cu as well as significant O and C impurities (3 times more than found on the target surface). After 1 h of operation, the coatings contain the same amount of O and C as found on the target surface and the chemical composition of the target is reproduced. High temperature diffusion of the O and C impurities incorporated inside the target to its surface and/or out-gassing through the pore network due to target heating might be responsible for the high coating contamination during the first hour of target usage. Oxidation effects might cause the deviation between coating and target composition during the 1 h of operation.

### 5.4.2 Coatings

From 25 W (3.8 W/cm<sup>2</sup>) to 200 W (30.4 W/cm<sup>2</sup>) the deposition rate  $D$  increases linearly with the applied deposition power  $P$ . If more than 200 W (30.4 W/cm<sup>2</sup>) are applied, the deposition rate starts to decrease due to energy dissipation of the incident ions deep in the target and because of ion implantation [43,67]. According to the analysis of the coating composition and microstructure, a deposition power of 200 W (30.4 W/cm<sup>2</sup>) delivers the optimum result. The deposition rate of about 160 nm/min is reasonable for industrial applications and the coatings exhibit the same chemical composition as the target used for deposition. The statistical variation of the coating composition is about 1-2 at%, which is within the accuracy of the EDS system. For deposition powers between 50 W and 200 W, the C and O content of the coatings corresponds to the amount of C and O impurities found on the target surface. If a deposition power lower than 50 W is applied, more O and C is incorporated in the coatings, probably originating from the residual gas (lower deposition rate). This is in accordance with the estimations made in Section 3.2. For a deposition power of more than 200 W, the O content increases probably due to out-gassing of the target (local heating of the target due to high energy ion bombardment). The intensity of the quasicrystalline AlCuFe peaks is maximized for a deposition power of 200 W (30.4 W/cm<sup>2</sup>). The number of sputtered atoms in the high energy region (kinetic energy > 5 eV) increases with the applied deposition power. When the sputtered atoms arrive on the substrate, their initial kinetic energy determines their mobility on the surface and the energy transferred to the substrate [43]. Both might be responsible for the enhanced growth of the quasicrystalline AlCuFe phase. If a deposition power of more than 200 W (30.4 W/cm<sup>2</sup>) is applied, the Al content significantly increases while the Cu content decreases. It is likely that Al is favourably evaporated from the target due to heating. Up to a deposition power of 150 W (22.8 W/cm<sup>2</sup>) practically no Si can be found on the coating surface. With higher deposition powers an increasing content of Si can be found on the coating surface: ~3 at% for 200 W (30.4 W/cm<sup>2</sup>) and ~15 at% for 300 W (45.6 W/cm<sup>2</sup>). In the XRD pattern peaks originating from the Si substrates appear. At these high deposition powers, the energy of the impinging ions seems to be high enough to cause physical mixing by non-diffusion type mechanisms due to implantation of high energy particles, backscattering of sputtered atoms and recoil implantation of surface atoms [43]. These mechanisms probably transport the Si atoms from the interfacial region to the coating surface. The measured deposition rate in dependence on the working distance agrees very well with the results of the geometry based simulation (see Figure 4.62 in Section 4.4.3). Deviations occur only for very small target – substrate distances of 1 cm or less, which is probably because of the neglected gas phase scattering. According to purely geometrical considerations, no atoms can reach a centrally positioned substrate if it is too close to the target, due to the ring-shaped race



track of magnetron sputtering targets. Nevertheless, gas phase scattering still allows sputtered atoms to impinge on the substrate surface. The intensity of the quasicrystalline AlCuFe peaks (QC) is maximized if the working distance is 3 cm (deposition rate 135 nm/min). The chemical composition of the target is reproduced for target – substrate distances up to 5 cm. For higher working distances, the Al content of the coatings slightly decreases, which is probably caused by gas phase scattering (gas phase scattering is stronger for the lighter Al atoms than for the heavier Cu and Fe atoms). The O and C content of the deposited coatings is independent of the working distance, which shows that the achieved deposition rates are high enough to avoid significant incorporation of residual gas atoms. The chemical composition of sputter deposited coatings does not only depend on the material flux, which arrives on the substrate, but also on the highly temperature dependent sticking coefficients of the material's components. Thus sputtered coatings may be deficient in volatile constituents at elevated substrate temperatures [43]. No influence of the substrate temperature during deposition on the coating composition could be found and the AlCuFeB coatings exhibit the target composition for substrate temperatures up to 600 °C (see Figure 4.66 in Section 4.4.4). A substrate temperature of 600 °C is necessary to develop a quasicrystalline phase. This is in contradiction with results found in literature [66] where sputter deposition on a Si wafer heated to 410 °C - 520 °C caused the development of coatings, which contain quasicrystalline AlCuFe nanoparticles with a mean diameter of 15 nm and a volume fraction of 25 %. The working gas pressure does neither influence the deposition rate nor the chemical composition of the coatings within a range of  $2 \cdot 10^{-3}$  mbar to  $20 \cdot 10^{-3}$  mbar (working distance 5 cm). The XRD measurements show that the crystalline structure can be influenced by the working gas pressure. With increasing working gas pressure, the main  $\beta$  phase peak can be shifted from 44.5° to 31°. This indicates that the texture of the  $\beta$  phase can significantly be influenced by the working gas pressure (see Figure 5.2). The ratio of the quasicrystalline peak intensities to the  $\beta$  phase peak intensity is maximized for a working gas pressure of  $10 \cdot 10^{-3}$  mbar. Applying a bias voltage up to 75 V does neither influence the achieved deposition rate nor the chemical composition of the deposited coatings. Applying a bias voltage of 75 V does maximise the quasicrystalline peak in relation to the  $\beta$  phase peak. This is in agreement with literature [43], where it is reported, that applying low energy ion bombardment during deposition can increase the temperature range over which films with the desired grain size and/or microstructure develop.

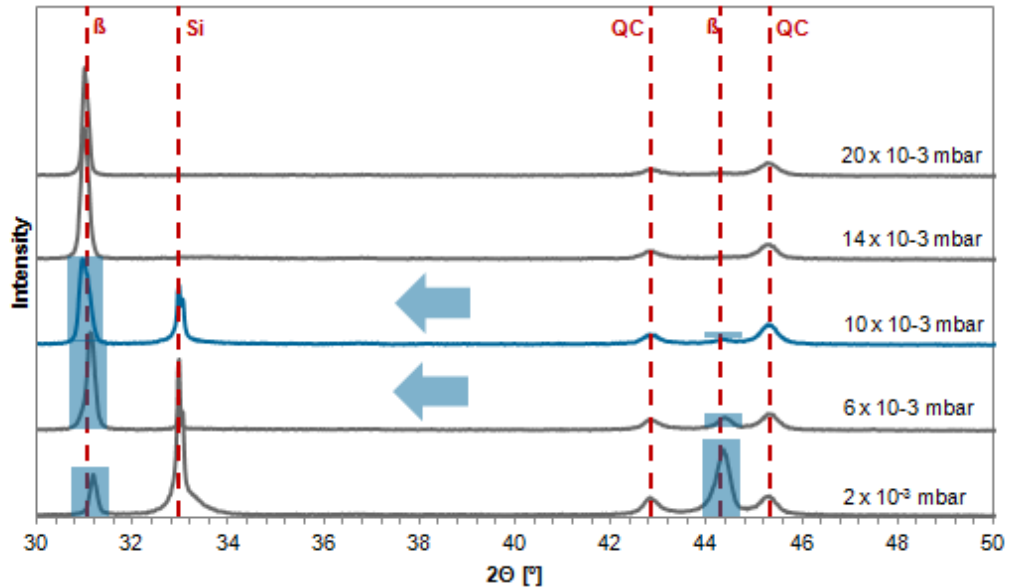


Figure 5.2 XRD pattern of AlCuFeB coatings in dependence on the working gas pressure (Cu anode  $\lambda = 1.542 \text{ \AA}$ ). As indicated by the blue boxes and arrows, the main  $\beta$  phase peak shifts with increasing working gas pressure from  $44.5^\circ$  to  $\sim 31^\circ$ . The target-substrate distance was 5 cm.

QC = quasicrystalline AlCuFe,  $\beta = \text{Al}_{50}\text{Cu}_{40}\text{Fe}_{10}$   $\beta$  phase, Si = Si substrate

The optimum deposition parameters as determined according to the variation of deposition conditions are summarized in Table 5.1.

Table 5.1 Optimised parameters for deposition of AlCuFeB coatings using a metallic target

Deposition power	200 W
Working distance (target – substrate distance)	3 cm
Substrate temperature	600 °C
Working gas (Ar) pressure	$10 \times 10^{-3}$ mbar
Bias voltage	75 V
Deposition rate	130 nm/min

### 5.4.3 Optimised coatings

AlCuFeB coatings deposited by DC magnetron sputtering using a metallic target and optimised deposition parameters (200 W deposition power, 3 cm working distance, 600 °C substrate temperature,  $10 \cdot 10^{-3}$  mbar working gas pressure, 75 V bias voltage) contain ~40 % quasicrystalline AlCuFe phase and ~60 %  $\text{Al}_{50}\text{Cu}_{40}\text{Fe}_{10}$   $\beta$  phase. The chemical composition as well as the microstructure seems to be independent of the substrate material (hard metal WC-Co, steel K600 and K890, ceramic  $\text{Al}_2\text{O}_3$  and Si). The coatings exhibit good adhesion on hard metal WC-Co, K600 and K890 steel as well as on ceramic  $\text{Al}_2\text{O}_3$ , delamination only occurs on Si substrates. Delamination is probably caused by thermal stresses due to the vast difference in thermal expansion coefficients of Si and quasicrystalline AlCuFeB and the low surface roughness of the Si substrates, which prohibits mechanical interlocking. This is in accordance with the considerations made in Section 3.4, where a compressive thermal stress at room temperature of 0.78 GPa was estimated for AlCuFeB coatings deposited on Si substrates heated to 600 °C. Interlayer coatings between the Si substrate and the AlCuFeB coating might help to improve adhesion. The chemical composition of the coatings is independent of the substrate material and in average:  $59.7 \pm 2.6$  at% Al,  $27.3 \pm 2.0$  at% Cu and  $10.0 \pm 0.8$  at% Fe, which is very close to the nominal  $\text{Al}_{59}\text{Cu}_{25.5}\text{Fe}_{12.5}\text{B}_3$  composition. The O content is about 7 at% and the C content about 6 at%, which equals the impurity content of the metallic targets (see Section 4.4.1). A deposition rate of 130 nm/min seems to be sufficient to avoid O and C incorporation from the residual gas, which is in accordance with the considerations from Section 3.2. While the chemical composition of the metallic target lies a bit outside the quasicrystalline region the chemical composition of the AlCuFeB coatings lies inside the quasicrystalline region (see Figure 4.77 in Section 4.4.7). Since the chemical composition of the AlCuFeB coatings lies within the quasicrystalline area, deviations from the nominal  $\text{Al}_{59}\text{Cu}_{25.5}\text{Fe}_{12.5}\text{B}_3$  composition cannot be responsible for the  $\beta$  phase development. It can be found in literature that the presence of C [28]; O [37,38] and N [1] strongly influences the formation the icosahedral AlCuFe phase and promotes the  $\text{Al}_{50}\text{Cu}_{40}\text{Fe}_{10}$   $\beta$  phase formation if the contamination is large enough. Thus the C and O contamination of the AlCuFeB coatings could promote the  $\beta$  phase development. Another reason might be that a substrate temperature of 600 °C is too low to achieve a pure quasicrystalline phase. Deposition at higher temperatures might help to achieve a pure quasicrystalline coating but would alter the steel substrates and thus could not be applied for practical reasons.

SEM and EDS measurements show that independent of the substrate material, the deposited AlCuFeB coatings are very homogenous without any voids. About 8 at% C and 7 at% O impurities can be found throughout the coatings. This is in agreement with the values measured on the coating surface. Only for the coatings deposited on the ceramic Al<sub>2</sub>O<sub>3</sub> a higher O content of more than 10 at% can be found in the coatings as well as an O enrichment on the surface, which might be because of oxygen diffusion from the substrate or because of the sample preparation before cross section examination (grinding and polishing was necessary for the coatings deposited on Al<sub>2</sub>O<sub>3</sub>). For all substrates the interface appears very sharp and hardly any diffusion between the substrate and the coating material takes place. Only for the Si and the steel K890 slight diffusion from the substrate to the coating surface can be observed. About 5 at% Si and 2 at% Cr can be found on the coating surfaces deposited on the respective substrates. The interface area is about 1 μm wide except for Si, for which an interface region of about 2 μm develops. Neither on the surface nor in the cross section images of the coatings deposited on steel K600 and K890 cracks or delamination effects can be observed. While the surface of the coatings deposited on ceramic Al<sub>2</sub>O<sub>3</sub> does not show cracks or delamination, the cross section images indicate some cracks, which propagate from the surface to the interface where they end (see Figure 4.80 in Section 4.4.7). Together with the high substrate roughness that promotes mechanical interlocking, the limited crack propagation results in good adhesion. The coatings deposited on Si and WC-Co exhibit numerous cracks all over the coating surface. For coatings deposited on Si, the cracks propagate throughout the whole coating and into the substrate. For coatings deposited on WC-Co the cracks frequently propagate throughout the whole coating and grow along the interface, which is likely to be responsible for the delamination effects observed. All AlCuFeB coatings except the one deposited on ceramic Al<sub>2</sub>O<sub>3</sub>, consist of two different phases. One phase occurs in the form of columns and stabs (bright phase) in the matrix of the second phase (gray phase) (see Figure 4.105 in Section 4.4.7). For the coatings deposited on ceramic Al<sub>2</sub>O<sub>3</sub> the contrast might not have been sufficient to identify the phases (extremely poor conductivity of Al<sub>2</sub>O<sub>3</sub>). By EDS no difference in the chemical composition of the white stabs/columns and the gray matrix could be identified, although magnification was increased to 100.000 x and the accelerating voltage was reduced to 10 kV. While the white columns/stabs seem to have a length of about 1 μm, higher magnification SEM images show that the stabs consist of smaller grains embedded in the grain matrix (see Figure 5.3 a). The size of the grains of which the stabs/columns consist is probably too small to be resolved by EDS (excitation depth of ~1 μm). Nevertheless it can be speculated that the white phase represents the quasicrystalline AlCuFe phase, while the gray matrix consists of the Al<sub>50</sub>Cu<sub>40</sub>Fe<sub>10</sub> β phase. By using image manipulation method (threshold, pixel count), it can be estimated that the area of the white

stabs/columns amounts to about 30% (see Figure 5.3 b). This would be in agreement with the phase ratio determined by XRD measurements.

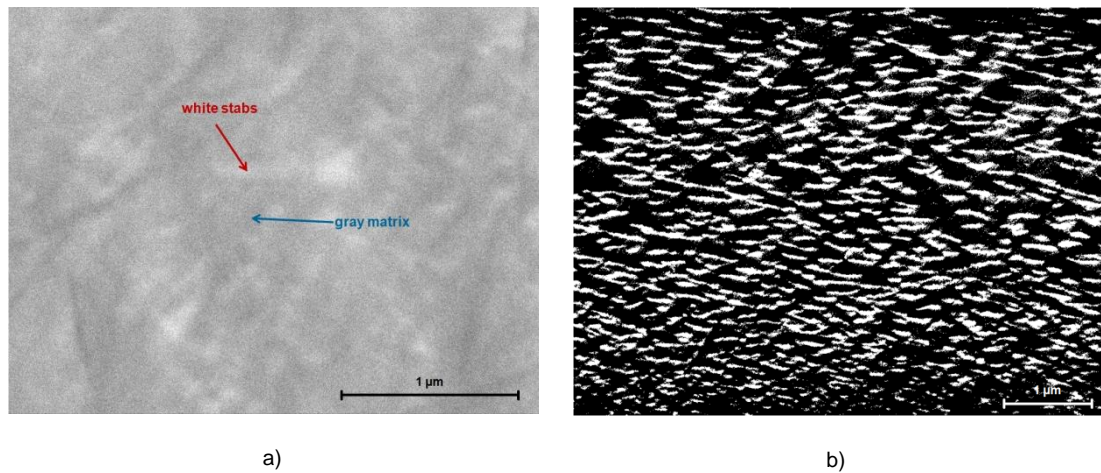


Figure 5.3 AlCuFeB coating deposited on a Si substrate with a 200 nm Ni interlayer  
a) Back scattered SEM cross section image  
b) Threshold image to determine the amount of the white stabs/columns in the coating matrix

According to Transmission Electron Microscopy (TEM), the deposited coatings are nanocrystalline, with an average grain diameter of  $\sim 10$  nm. The smallest grains have a diameter of about 3 nm, while the biggest grains are about 14 nm in diameter. This is in good agreement with results found in literature [66] for deposition of AlCuFe films on a Si wafer, which contain quasicrystalline AlCuFe nanoparticles with a mean diameter of 15 nm and a volume fraction of 25 %. The grains are embedded in a matrix, which is mainly amorphous with some crystalline regions. It can be speculated that the grains are quasicrystalline AlCuFe and the matrix consist of an amorphous Al and an  $\text{Al}_{50}\text{Cu}_{40}\text{Fe}_{10}$   $\beta$  phase.

#### 5.4.4 Electrical resistivity

The electrical resistivity of the AlCuFeB coatings strongly depends on the substrate temperature during deposition (see Figure 5.4). As described in [21,33,35,36] this depends on the development of a quasicrystalline phase and an improved structural quality with increasing substrate temperature. The coatings deposited on substrates at 600 °C exhibit an electrical resistivity of 12.36  $\mu\Omega\text{m}$ , which is in the range of the electrical resistivity found for quasicrystalline AlCuFeB with structural defects and additional phases [36]. This is in accordance with the XRD results, which show that the coatings contain 40 % quasicrystalline AlCuFe phase and 60 %  $\text{Al}_{50}\text{Cu}_{40}\text{Fe}_{10}$   $\beta$  phase. The AlCuFeB ceramic targets produced by uniaxial hot pressing at 700 °C using an elemental powder mixture possess approximately the same electrical resistivity (15.0  $\mu\Omega\text{m} \pm 5.2 \mu\Omega\text{m}$ ). Since the AlCuFeB ceramic targets produced by hot pressing of an elemental powder mixture exhibit about 30 % quasicrystalline AlCuFe phase and 70 %  $\text{Al}_{50}\text{Cu}_{40}\text{Fe}_{10}$   $\beta$  phase, this is also in good agreement with the results obtained for the AlCuFeB coatings.

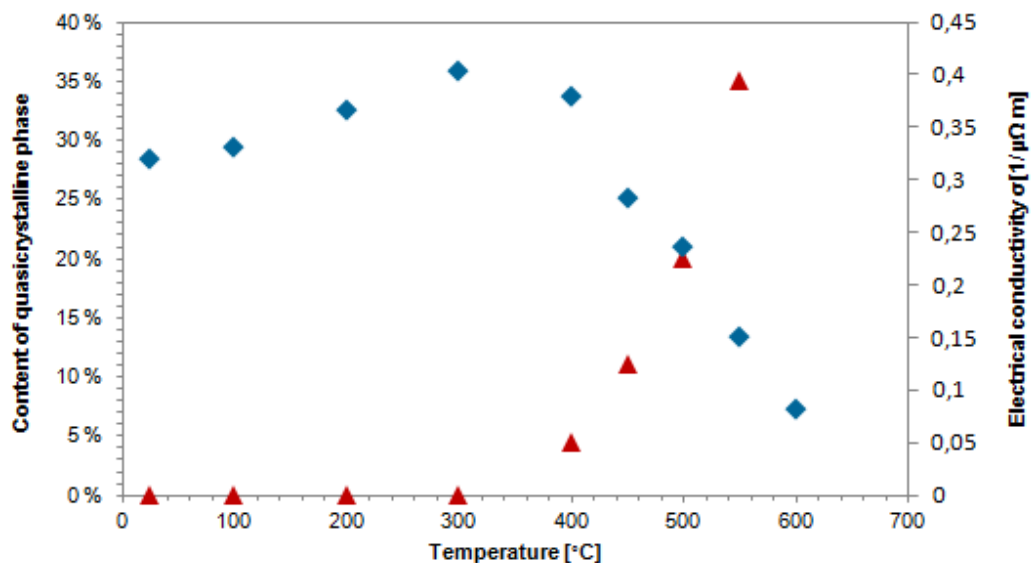


Figure 5.4 Electrical conductivity/resistivity of AlCuFeB coatings in dependence on the substrate temperature

For coatings thinner than 5  $\mu\text{m}$ , the electrical resistivity decreases with decreasing film thickness to about 2  $\mu\Omega\text{m}$  for film thicknesses of 50 nm (see Figure 5.4). This is not in agreement with the classical theory of conductivity. For metals and metal alloys the electrical conductivity increases with decreasing film thickness because of enhanced electron scattering at the coating surface and at grains [68-70]. It can be assumed that the decrease of the electrical resistivity is caused by an increasing amount of additional phases and/or because the quasicrystalline phase does not develop at all. It cannot be excluded that for film deposition on substrates, which promote crystallisation (e. g.: Si) the quasicrystalline phase is more developed also for thinner coatings. For film thicknesses below 50 nm the electrical resistivity increases again up to 12  $\mu\Omega\text{m}$  for a film thickness of 4 nm (see Figure 5.5). This increase in electrical resistivity is probably caused by the effect of enhanced electron scattering as known from metals and metal alloys and/or by a discontinuous film (island formation).

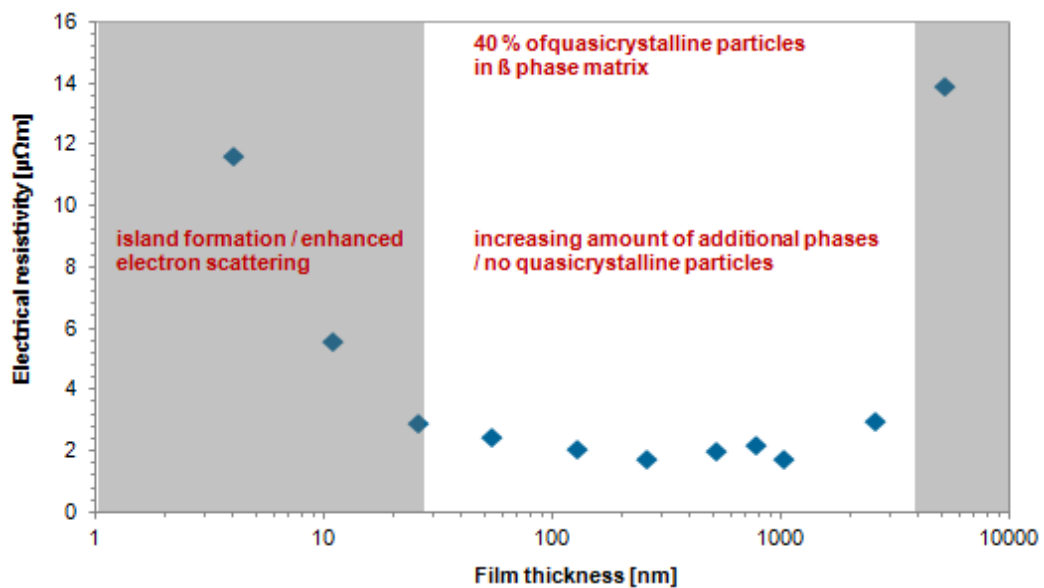


Figure 5.5 Electrical resistivity in dependence on the film thickness for AlCuFeB coatings deposited on ceramic  $\text{Al}_2\text{O}_3$  substrates heated at 600  $^\circ\text{C}$

#### 5.4.5 Interlayer

To reduce the intensity of the strains at the interface (see Section 3.5), to increase adhesion and to avoid extensive diffusion of substrate atoms into the coating, five different materials were tested as a possible interlayer with thicknesses of 200 nm and 1  $\mu\text{m}$ : Chrome (Cr), Copper (Cu), Titanium (Ti), Manganese (Mn), Nickel (Ni).

The Cr interlayer does not improve adhesion of the AlCuFeB coatings and coating delamination occurs all over the surface. The cracks and voids observed in the substrate – Cr interface are probably caused by the Cr diffusion into the Si substrate. According to the phase diagram [71] also the formation of CrSi is possible in this diffusion zone, which is  $\sim 2 \mu\text{m}$  thick. Si diffuses about 1 – 2  $\mu\text{m}$  into the interlayer/coating, but Si diffusion to the coating surface is not observed. Cr diffuses about 1  $\mu\text{m}$  into the AlCuFeB coating, the interlayer – coating interface shows some voids, especially for the 1  $\mu\text{m}$  thick Cr interlayer. O is enriched at the Cr interlayer, where about 10 at% O can be found. According to the phase diagram CrO<sub>2</sub> or CrO<sub>3</sub> might be formed [71]. C impurities are enriched at the Si - Cr interface and at the interface Cr interlayer - AlCuFeB coating. The observed voids in the interlayer – coating interface might be caused by the diffusion process, the formation of the oxide phase or because of the impurity enrichment at the interface region. The reduced interlayer – coating interface quality probably causes the more severe coating delamination for the AlCuFeB coating deposited on the 1  $\mu\text{m}$  Cr interlayer.

The Cu interlayer does not improve adhesion of the AlCuFeB coatings and coating delamination occurs all over the surface. The Cu interlayer prohibits Si diffusion to the AlCuFeB coating surface. Si diffuses about 1  $\mu\text{m}$  into the interlayer/coating. Cu diffusion from the interlayer to the coating surface causes a composition shift of the coating composition compared to the target composition. This composition shift is more extensive for the 1  $\mu\text{m}$  interlayer (-6 at% Al, + 7 at% Cu) than for the 200 nm interlayer (-4 at% Al, +5 at% Cu). This is confirmed by SEM images that show the development of voids in the 1  $\mu\text{m}$  thick interlayer, which probably result from enhanced diffusion. Cu diffuses from the interlayer region about 1.5  $\mu\text{m}$  into the substrate. The substrate – interlayer interface appears very rough, which according to the phase diagram [71] might be because of silicide formation.

Adhesion of the AlCuFeB coatings is not improved by the Ti interlayer and coating delamination occurs all over the surface. Ti diffuses  $\sim 1 \mu\text{m}$  into the Si substrate and about 1  $\mu\text{m}$  into the AlCuFeB coating. Si diffuses  $\sim 2 \mu\text{m}$  into the interlayer/coating. The AlCuFeB coatings, the Ti interlayer and the interfaces look homogenous without cracks or voids. Both, the substrate – interlayer as well as the interlayer – coating interface



appear very sharp. The AlCuFeB coating exhibits the same two phase structure consisting of a dark gray matrix and a bright, line shaped phase as observed for the optimised coatings without interlayer (see Section 5.4.3).

Although Mn exhibits a thermal expansion coefficient close to the one of quasicrystalline AlCuFeB, complete delamination of the AlCuFeB coating from the Mn interlayer coating occurs. On the surface and throughout the coating only Si and Mn can be found besides some O and C impurities. Examination of the coating reveals that fine structured nano-tubes form, which consist of Mn, MnO, MnO<sub>2</sub> and Mn suboxides. This is in accordance with results found in literature [72], which report that rod-like manganese oxide can be prepared by anodic deposition in manganese acetate solutions heated to 600 °C. The nano structure of the Manganese oxide might be responsible for the extremely poor adhesion of the AlCuFeB coating. According to the phase diagram [56] and the chemical composition of the coating surface, also the formation of MnSi is possible, although no MnSi phases could be identified with the available XRD database.

For a 1 µm thick Ni interlayer adhesion of the AlCuFeB coating improves and delamination is restricted. Si diffuses about 2 - 3 µm into the Ni interlayer/coating and Ni diffuses about 1 µm into the Si substrate and about 1 µm into the coating. Ni successfully prevents Si diffusion from the substrate to the AlCuFeB coating surface. Independent of the interlayer thickness, the Ni interlayer and the AlCuFeB layer shows some voids distributed throughout the coating. The AlCuFeB coating exhibit the two phase structure consisting of a dark gray matrix and a bright, line shaped phase as known from the optimised coatings without interlayer (see Section 5.4.3). The interface between the substrate and the Ni interlayer and between the Ni interlayer and the AlCuFeB coating is very rough, which promotes mechanical interlocking. According to the Ni – Si phase diagram [71], the chemical composition and the substrate temperature (600 °C), the formation of a αNiSi<sub>2</sub> phase is very likely. Both, the mechanical interlocking and the formation of the αNiSi<sub>2</sub> phase might be responsible for the improved adhesion, which could be observed for the AlCuFeB coating deposited on the 1 µm Ni interlayer.

It can be summarized that for metallic interlayers (Cr, Cu, Ti, Ni), the interlayer material diffuses 1 - 2 µm into the Si substrate and about 1 - 2 µm into the AlCuFeB coating. Cu is an exception because Cu diffuses from the interlayer region to the coating surface and thus causes a shift of the coating composition compared to the target composition. It can be assumed that diffusion is higher for Cu because it is also one of the coating components. Si diffuses about 1 – 3 µm into the interlayer/coating. A very rough substrate – interlayer interface seems to develop because of diffusion of the interlayer material into the Si substrate and because of silicide formation. Voids and/or cracks in the interlayer/AlCuFeB coating can be caused by diffusion of Si/interlayer material into the

interlayer/coating. Especially the formation of oxides (Cr and Mn interlayer) dramatically reduces the interface quality and adhesion of the AlCuFeB coating. Besides diffusion and oxide formation, also the formation of silicides and impurity enrichment (C) might decrease the interface homogeneity. Since delamination of the AlCuFeB coating occurs for all interlayer materials (Cr, Cu, Ti, Mn, Ni) examined, it has to be concluded that either none of these materials can eliminate the strains at the interface Si substrate - AlCuFeB coating or provide an interface of sufficient quality to guarantee good adhesion. If the AlCuFeB coatings are deposited on a Ti, Ni or Cr interlayer, the coatings exhibit about the same chemical composition as if deposition is done directly on the Si substrate and the target composition is approximately reproduced. For the Cu interlayer, the coating composition is shifted to a region with higher Cu and lower Al content. The best result regarding adhesion, interface/coating quality and chemical composition could be achieved using a 1  $\mu\text{m}$  Ni interlayer, for which coating delamination is significantly reduced. Regarding technical applications like nano-imprint-lithography stamps, for which the sticking forces between a thin AlCuFeB coating (coating thickness  $\leq 500$  nm) and polymer films has to be minimized, it is important to be aware that a certain amount of Si is present on the coating surface.

#### 5.4.6 Nano-imprint-lithography (NIL)

Nano-imprint-lithography (NIL) is a simple method of fabricating high resolution nanometer scale patterns on various materials providing low cost and high throughput. In the standard NIL process, a thin layer of imprint resist (thermoplastic polymer) is spin coated onto the sample substrate. Then the mold, which has predefined topological patterns, is brought into contact with the sample and they are pressed together under certain pressure. When heated up above the glass transition temperature of the polymer, the pattern on the mold is pressed into the softened polymer film. After being cooled down, the mold is separated from the sample and the pattern resist is left on the substrate [73]. Problems which are encountered during the NIL process are mechanical deformation, thermal expansion and wear of the stamps, which reduce repeatability and accuracy as well as adhesion between the resist and the stamp.

500 nm thick coatings were deposited on Si stamps, which according to the varied deposition parameters (substrate temperature, bias voltage) consist of different phases. Coatings which are deposited at 600 °C contain 40 % quasicrystalline AlCuFeB + 60 %  $\text{Al}_{50}\text{Cu}_{40}\text{Fe}_{10}$  ( $\beta$  phase), coatings deposited at 550 °C consist of an  $\text{Al}_{50}\text{Cu}_{40}\text{Fe}_{10}$  ( $\beta$  phase) and coatings deposited at 500 °C exhibit an amorphous Al phase. The surface roughness, the coefficient of friction and the pull-off force were measured by Prof. Zygmunt Rymuza at the Warsaw University of Technology and are independent of the substrate type (Si/SiO<sub>2</sub>). While the roughness of the coating surfaces can be regarded as

very high compared to the Si surface, the coefficient of friction and the sticking force are significantly lower for the coating surfaces than for the Si wafer. In general roughness is lower for coatings which contain only an amorphous Al phase or an  $\text{Al}_{50}\text{Cu}_{40}\text{Fe}_{10}$  ( $\beta$  phase). The coefficient of friction and the sticking coefficient are in general lower for coatings, which consist of 40 % quasicrystalline AlCuFeB + 60 %  $\text{Al}_{50}\text{Cu}_{40}\text{Fe}_{10}$  ( $\beta$  phase) than for coatings, which consist of the  $\text{Al}_{50}\text{Cu}_{40}\text{Fe}_{10}$  ( $\beta$  phase) or an amorphous Al phase. The coefficient of friction and the sticking coefficient tend to be lower for coatings that are deposited using a bias voltage of 75 V. Looking at the relationships between roughness - pull-off force and roughness - friction coefficient, it can be observed that the two coatings deposited on  $\text{SiO}_2$  (S1, S11), which contain 40 % quasicrystalline AlCuFeB + 60 %  $\text{Al}_{50}\text{Cu}_{40}\text{Fe}_{10}$  ( $\beta$  phase) deliver the best results. The results obtained for deposition of AlCuFeB coatings on ceramic  $\text{Al}_2\text{O}_3$  substrates indicated that no quasicrystalline particles develop for film thicknesses below 5  $\mu\text{m}$  (see Section 4.4.8 and Section 5.4.4). This is in contrast with the characteristics of the 500 nm AlCuFeB coatings deposited on Si wafers, which indicate that a quasicrystalline phase develops (small coefficient of friction and small sticking coefficient). The development of quasicrystalline particles in the coatings might be promoted by the crystalline surface of the Si wafer.

The best coating concerning wear is coating S11, which in contrast to sample S1 was deposited using a bias voltage of 75 V. Since the hardness of sample S11 is slightly higher than for sample S1, it can be assumed that the reduced wear might be caused by the higher hardness. Further bias sputtering probably increases adhesion of the coating, which might additionally help to reduce wear. All coatings exhibit more severe wear than the uncoated Si surface (see Figure 4.111 in Section 4.4.10) although, the average value of hardness and Young's elastic modulus of the coatings is higher than for Silicon. The best results concerning surface roughness, coefficient of friction, pull-off force, wear and hardness is coating S11, which was deposited at 600 °C with a bias voltage of 75 V and consists of 40 % quasicrystalline AlCuFeB + 60 %  $\text{Al}_{50}\text{Cu}_{40}\text{Fe}_{10}$  ( $\beta$  phase). The measured characteristics for this optimum coating are summarized in Table 5.1.

Table 5.1 Characteristics of the optimum coating S11  
(Prof. Zygmunt Rymuza, Warsaw University of Technology)

Surface roughness Ra / Rq	5.6 nm / 7.5 nm
Coefficient of Friction (glass ball)	0.078
Coefficient of Friction (steel ball)	0.111
Sticking coefficient (glass ball)	1
Sticking coefficient (steel ball)	11
Hardness (Berkovich)	11.1 GPa
Young's elastic modulus	179.2 GPa
Surface energy (polar component/ dispersive component)	58.87 mJ/m <sup>2</sup> (45.51 mJ/m <sup>2</sup> / 13.36 mJ/m <sup>2</sup> )

The measured hardness of 11 GPa and the elastic modulus of 180 GPa are higher than the values found in literature for quasicrystalline AlCuFe: hardness of 7.5 - 9 GPa [26] and elastic modulus of 100 GPa [26] [2,3]. The increased hardness and Young's elastic modulus could be caused by the additional boron, which favourably locates at grain boundaries. Since the  $\beta$  phase exhibits a lower hardness than the quasicrystalline phase, it probably does not contribute to the higher hardness. The enhanced elastic modulus might also be caused by the coating microstructure that consists of a  $\beta$  phase matrix in which the quasicrystalline grains are embedded. The surface energy of  $\sim 60$  mJ/m<sup>2</sup> equals the values found in literature of 55 mJ/m<sup>2</sup> [2,3,24]. It can be concluded, that the characteristics of the deposited AlCuFeB coatings make them very interesting as potential wear protective films in the field of nanoimprint lithography.

#### 5.4.7 Cutting insert

Ceratizit (DCGT 11T308FN-25P) ISO-HW K10 cutting inserts coated with  $\sim 1.5$   $\mu\text{m}$  thick AlCuFeB coatings provide a longer lifetime during Aluminium turning compared to a commercially available TiB<sub>2</sub> coating (Cemecon Alu Speed) and thus can be regarded as a promising coating for turning tools (see Figure 4.116 in Section 4.4.11). The slight delamination of the coating after deposition is probably caused by thermal stresses but does not seem to crucially influence the turning performance of the inserts.

## 6. Conclusion

### 6.1 AlMgB<sub>14</sub>

Targets, which contain an AlMgB<sub>14</sub> phase can be produced by 30 MPa Uniaxial Hot Pressing (HUP) at 1500 °C for 2 h 30 min. The initial powder mixture can be prepared by weighting out atomic powders of Al, Mg and B according to the nominal AlMgB<sub>14</sub> composition. The targets are very porous, whereas targets produced with crystalline B show less pores than the targets produced with amorphous B. The AlMgB targets show about 10 % Al<sub>2</sub>MgO<sub>4</sub> phase, which is probably caused by the impurities contained in the elemental powders. The O content of the elemental powders could be minimized by using powders with bigger grains or hot pressing under a reducing atmosphere (e.g.: CO, NH<sub>3</sub> and H<sub>2</sub>) might help to reduce the O content of the AlMgB targets. Because the electrical resistivity of the targets is very high (~ 1 Ωm), DC magnetron sputtering cannot be applied. The main problems encountered during deposition are the crack formation in the AlMgB targets, which occurs even for very low power densities (3.8 W/cm<sup>2</sup>) and the very low deposition rates (20 nm/min for a power density of 15.2 W/cm<sup>2</sup>). Crack formation is less severe for targets with more porous structures, because porosity might reduce brittleness. By using RF magnetron sputtering, deposition of AlMgB coatings from single targets is possible. During deposition a loss of 4 - 5 at% Al and Mg occurs, which might be caused by the crack formation (preferential sputtering/evaporation) and/or oxidation of the sputtered Al and Mg atoms by the residual gas because of the low deposition rates. The AlMgB coatings deposited on WC-Co K10 substrates heated to 600 °C do not contain a crystalline AlMgB<sub>14</sub> phase. The deposited coatings are very homogenous, without any pores or cracks and consist of mostly amorphous boron. Applying post annealing at 900 °C for 3 h causes a significant incorporation of C (~ 40 at%) because of high temperature diffusion from the WC-Co substrates. A two phase structure, consisting of amorphous boron and AlB<sub>2</sub> forms. Besides the high C contamination, the deviation from the AlMgB<sub>14</sub> composition (4 - 5 at% less Al and Mg) and/or a too low post annealing temperature might inhibit the formation of a crystalline AlMgB<sub>14</sub> phase. Since post annealing at 900 °C alters the WC-Co substrates and causes significant C diffusion, higher post annealing temperatures seem not to be applicable. After post annealing coating delamination occurs, induced by an increase of thermal stress.

## 6.2 AlCuFeB ceramic targets

High quality targets appropriate for magnetron sputter deposition can be produced by 30 MPa uniaxial hot pressing at 700 °C for 1 h using the commercially available St. Gobain Cristome F1 powder. Densification is high so that the targets exhibit no porosity. The targets are very homogenous and the reproducibility of the target composition is very good. The targets produced with the *St Gobain Cristome F1* powders exhibit a perfect icosahedral  $\text{Al}_{59}\text{Cu}_{25.5}\text{Fe}_{12.5}\text{B}_3$  phase without any residual phases but target performance is very poor. Using an elemental powder mixture, the homogeneity of the targets as well as the reproducibility of the target composition are reduced and the targets show small deviations (~3 at%) from the nominal composition. This might be caused by the impurities found in the elemental powders and inhomogeneities in the elemental distribution of the initial powder mixture. Mechanical milling/mixing of the single elemental powders and/or weighting out of the single element powders might have to be optimised. The targets produced with elemental powders exhibit an icosahedral  $\text{Al}_{59}\text{Cu}_{25.5}\text{Fe}_{12.5}\text{B}_3$  phase and an additional  $\text{Al}_{50}\text{Cu}_{40}\text{Fe}_{10}$   $\beta$  phase. The  $\beta$  phase development might be caused by the shift from the nominal  $\text{Al}_{59}\text{Cu}_{25.5}\text{Fe}_{12.5}\text{B}_3$  composition and/or by the inhomogeneities in the powder mixture. Impurities, especially oxygen can promote the  $\beta$  phase development as well. Independent of the powders used for production, oxygen is incorporated during hot pressing and/or the finishing process (grinding/polishing). Hot pressing under a reducing atmosphere (e.g.:  $\text{CO}$ ,  $\text{NH}_3$  and  $\text{H}_2$ ) might help to avoid oxygen incorporation. All quasicrystalline  $\text{Al}_{59}\text{Cu}_{25.5}\text{Fe}_{12.5}\text{B}_3$  targets produced exhibit ceramic properties like high brittleness as well as low thermal and electrical conductivity, which are characteristic for the quasicrystalline  $\text{Al}_{59}\text{Cu}_{25.5}\text{Fe}_{12.5}\text{B}_3$  phase. Therefore RF magnetron sputtering has to be applied. If a deposition power of 100 W (15.2 W/cm<sup>2</sup>) or more is applied, reasonable deposition rates can be achieved. Independent of the powders used for target production crack formation during film deposition is observed which is probably caused by thermal stresses due to the low thermal conductivity. This crack formation seems to cause a linear increase of the Al content with the applied deposition power and an influence of the working gas pressure on the coating composition. If the deposition conditions are kept constant, statistical variation in the coating composition can be observed. Usage of a pulsed magnetron system could not reduce the thermal load on the targets and thus could not prevent crack formation. A quasicrystalline  $\text{Al}_{59}\text{Cu}_{25.5}\text{Fe}_{12.5}\text{B}_3$  phase develops when the chemical composition of the deposited coatings is close enough to the nominal  $\text{Al}_{59}\text{Cu}_{25.5}\text{Fe}_{12.4}\text{B}_3$  composition and post annealing at 600 °C is applied for at least 30 min. The  $\beta$  phase is not specific for Si substrates and might be formed due to by element diffusion from the substrates. During post annealing at high temperature Si diffusion occurs and the development of a compound interface, with chemical interaction of the film

and Si substrate is observed. post annealing at 600 °C causes buckle induced crack formation and coating delamination all over the coating surface. Buckle formation is probably caused by thermal stresses between the coatings and the Si substrates and might be enforced by Si diffusion and/or oxidation. It can be concluded that post annealing at 600 °C causes a strong increase in surface roughness as well as a significantly reduced interface and coating homogeneity and quality (formation of cracks and pores).

### 6.3 AlCuFeB shifted composition targets

AlCuFeB targets with a shifted composition can be produced by either adding elemental powders to the commercially available *St. Gobain Cristome F1* powder or by using an elemental powder mixture with a shifted composition. Since the chemical composition of the coatings equals the target composition, the shifted composition targets cannot be used to compensate the composition shift that occurs when deposition is done by ceramic AlCuFeB targets.

### 6.4 AlCuFeB metallic targets

By 30 MPa hot pressing of an elemental powder mixture for 1 h at 500 °C it is possible to produce AlCuFeB targets which exhibit the  $\text{Al}_{59}\text{Cu}_{25.5}\text{Fe}_{12.5}\text{B}_3$  composition but not the quasicrystalline structure. Since these targets contain only metallic phases, they exhibit metallic characteristics like a relatively low electrical resistivity, magnetism, good thermal conductivity and a relatively high toughness. Therefore these targets can be used for DC magnetron sputter deposition and no crack formation occurs for deposition powers between 25 W and 300 W. Since the hot pressing conditions are not sufficient to achieve full densification, small pores, pure Al and Fe phases as well as B particles, which do not dissolve can be found throughout the target. Nevertheless the targets are homogenous and the reproducibility of the target composition is good. The average composition of:  $64.4 \pm 1.9$  at% Al,  $23.3 \pm 2.0$  at% Cu and  $9.3 \pm 0.7$  at% Fe deviates from the nominal composition (5 at% more Al, 2.5 at% less Cu and 2.5 at% less Fe). On the target surface a high amount of C and O is located due to the finishing process (grinding/polishing). Throughout the target the same amount of impurities is found as in the elemental powder mixture (~6 at% O and ~3 at% C). No additional O and C seems to be incorporated during the hot pressing process. The deviation from the nominal composition might be caused by the impurities of the elemental powders, inhomogenities in the elemental

distribution of the initial powder mixture, the mechanical milling/mixing process and/or weighting out of the single element powders. To reproduce the target composition in the deposited coatings, a conditioning time of 1 h is needed. For operating times below 1 h the chemical composition of the deposited coatings is altered due to excessive O and C contamination, which is caused by out-gassing effects of the target. AlCuFeB coatings, which consist of 40 % quasicrystalline AlCuFe phase and 60 % Al<sub>50</sub>Cu<sub>40</sub>Fe<sub>10</sub> β phase can be deposited by DC magnetron sputtering using the deposition parameters listed in Table 6.1.

Table 6.1 Optimised parameters for deposition of AlCuFeB coatings using a metallic target

Deposition power	200 W
Working distance (target – substrate distance)	3 cm
Substrate temperature	600 °C
Working gas (Ar) pressure	10 x 10 <sup>-3</sup> mbar
Bias voltage	75 V
Deposition rate	130 nm/min

The coatings are nano-crystalline, with an average grain diameter of ~10 nm. The grains are embedded in a matrix, which is mainly amorphous with some crystalline regions. It can be speculated that the grains are quasicrystalline AlCuFe and that the matrix consists of an amorphous Al and an Al<sub>50</sub>Cu<sub>40</sub>Fe<sub>10</sub> phase. The deposition rate of 130 nm/min is reasonable for industrial applications and the deposited AlCuFeB coatings are very homogenous without any voids, independent of the substrate material (Si, steel K600, steel K890, WC-Co and ceramic Al<sub>2</sub>O<sub>3</sub>). The coating – substrate interfaces are very sharp and hardly any diffusion between the substrate and the coating material takes place. For the steel K600 and K890 coating adhesion is excellent and no cracks or delamination effects can be observed. For the Al<sub>2</sub>O<sub>3</sub> coating adhesion is very good, although some cracks propagate from the surface to the interface where they end. The coatings deposited on Si and WC-Co exhibit numerous cracks and delamination all over the coating surface if a coating thickness of about 1 μm is exceeded. The electrical resistivity of 5 μm thick, optimized AlCuFeB coatings is about 14 μΩm and strongly depends on the



structural quality and the amount of quasicrystalline phase. Thus the electrical resistivity can be used as a very quick and easy method to estimate the AlCuFeB coating quality. None of the test interlayer materials: Chrome (Cr), Copper (Cu), Titanium (Ti), Manganese (Mn), Nickel (Ni) could significantly reduce the intensity of the strains at the interface, increase adhesion and prohibit diffusion of substrate atoms into the AlCuFeB coatings. The tested interlayer material diffuses 1 - 2  $\mu\text{m}$  into the Si substrate and into the interlayer/coating. Si diffuses about 1 - 3  $\mu\text{m}$  into the interlayer/coating. Diffusion of the interlayer material into the Si substrate and silicide formation promotes rough substrate – interlayer interfaces. The development of voids and/or cracks in the interlayer/AlCuFeB coating is promoted by diffusion of Si/interlayer material into the interlayer/coating. Especially the formation of oxides dramatically reduces the interface quality and adhesion of the AlCuFeB coating. Besides diffusion and oxide formation, also the formation of silicides and impurity enrichment (C) might decrease the interface homogeneity. The best result regarding adhesion, interface/coating quality and chemical composition of the AlCuFeB coatings could be achieved using a 1  $\mu\text{m}$  Ni interlayer, for which coating delamination is reduced. Regarding technical applications like nano-imprint-lithography stamps, where an AlCuFeB coating is deposited on a microstructure of pure Si or SiO<sub>2</sub> and for which the sticking forces between a thin AlCuFeB coating (coating thickness < 500 nm) and polymer films have to be minimized, it is important to be aware that a certain amount of Si will be present on the coating surface.

500 nm thick, AlCuFeB coatings deposited at 600 °C with a bias voltage of 75 V, which consist of 40 % quasicrystalline AlCuFeB + 60 % Al<sub>50</sub>Cu<sub>40</sub>Fe<sub>10</sub> ( $\beta$  phase), were found to exhibit favourable characteristics for nano-imprint-lithography and cutting tools. These characteristics include: moderate surface roughness (Ra 5.6 nm), a very low friction coefficient (0.078 for glass, 0.111 for steel) and sticking coefficient (1 for glass, 11 for steel) as well as high hardness (11 GPa) and a high Young's elastic modulus (180 GPa). It can be concluded, that the deposited AlCuFeB coatings are promising candidates for wear protective films in the field of nano-imprint-lithography. In the case of cutting tools, Ceratizit (DCGT 11T308FN-25P) ISO-HW K10 cutting inserts coated with ~1.5  $\mu\text{m}$  thick AlCuFeB coatings provide a longer lifetime during Aluminium turning compared to a commercially available TiB<sub>2</sub> coating (Cemecon Alu Speed) and thus can be regarded as a promising coating for turning tools.

## 7. Final summary

The thesis yielded important results in respect to applications of quasicrystalline AlCuFeB coatings. The following main points can be summarized:

- **AlMgB and AlCuFeB targets**  
More porosity might be favourable to avoid cracking of the targets during the coating deposition process.
- **AlMgB coatings**  
Although the correct AlMgB<sub>14</sub> crystallography could not be reached, the deposited coatings are homogenous and hard with low porosity.
- **AlCuFeB coatings**  
Optimum deposition parameters could be identified and runs on demonstrators for industrial applications were done successfully.
- **Upscaling**  
Using the identified process to deposit quasicrystalline AlCuFeB coatings, it was possible to successfully produce large-scale targets (Dr. Erich Neubauer, RHP-Technology GmbH) and to run the deposition process in industrial equipment (Dr. Miha Cekada, Jozef Stefan Institute, Ljubljana, Slovenia) (see Figure 7.1).

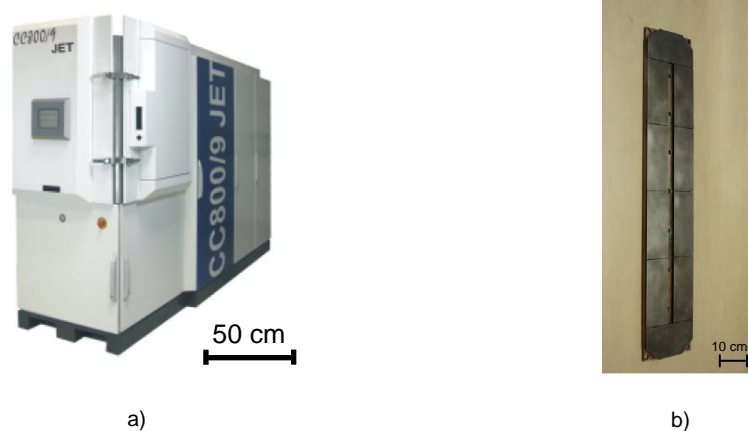


Figure 7.1 Industrial magnetron sputtering equipment and large-scale AlCuFeB target  
a) Industrial sputtering equipment CemeCon CC800/9 Jet  
(Dr. Miha Cekada, Jozef Stefan Institute, Ljubljana, Slovenia)  
b) Large-scale AlCuFeB target (Dr. Erich Neubauer, RHP-Technology GmbH)

## 8. Acknowledgements

I gratefully acknowledge the collaboration of Dr. Andreas Merstallinger (Aerospace & Advanced Composites GmbH) and thank him for fruitful discussions and for coordinating the FP7 Project appliCMA, Grant NMP3-SL-200-82 14407, which supported this work.

I also want to thank Dr. Erich Neubauer (RHP-Technology GmbH & Co. KG), Oswald Scheibenbauer (Tool Consulting & Management GmbH), Prof. Zygmunt Rymuza (Warsaw University of Technology) and Dr. Miha Cekada (Jozef Stefan Institute) for their excellent collaboration as well as the University Service Centre for Transmission Electron Microscopy (USTEM), Vienna University of Technology, where the HRSEM and EDS investigations were carried out. Furthermore I want to thank DI Harald Mahr for performing the deposition rate – working distance simulation abased on geometric considerations.

Last but not least I want to especially thank Prof. Christoph Eisenmenger-Sittner (Vienna University of Technology) for his scientific input, advices and interesting discussions.

## 9. References

- [1] S. Kenzari, D. Bonina, J.-M. Dubois, V. Fourné, *Scr. Mater.* 59 (2008) 583-586
- [2] P. Brunet, L.-M. Zhang, D. J. Sordelet, M. Besser, J.-M. Dubois, *Mat. Sci. Eng. A-Struct.* 294-296 (2000) 74-78
- [3] J.-M. Dubois, *Mat. Sci. Eng. A-Struct.* 294-296 (2000) 4-9
- [4] J.-M. Dubois, *Physica Scripta*. Vol. T49 (1993) 17-23
- [5] I. Higashi, T. Ishi, *Forma* 16 (2001) 187-207
- [6] B. A. Cook, J. L. Haringa, T. L. Lewis, A. M. Russell, *Scr. Mater.* 42 (2000) 597-602
- [7] A. Ahmeda, S. Bahadura, B.A. Cook, J. Peters, *Tribol. Int.* 39 (2006) 129-137
- [8] T. L. Lewis, B. A. Cook, J. L. Haringa, A. M. Russell, *Mat. Sci. Eng. A-Struct.* 351 (2003) 117-122
- [9] J.M. Hilla, D.C. Johnston, B.A. Cook, J.L. Haringa, A.M. Russell, *J. Magn. Magn. Mater.* 265 (2003) 23-32
- [10] Y. Tian, G. Li, J. Shinar, N. L. Wang, B. A. Cook, J. W. Anderegg, A. P. Constant, A. M. Russel, J. E. Snyder, *Appl. Phys. Lett.* 85 (2004) 1181-1183
- [11] M.i Takeda, T. Fukuda, F. Domingo, T. Miura, *J. Solid State Chem.* 177 (2004) 471-475
- [12] R. Cherukuria, M. Womacka, P. Moliana, A. Russell, Y. Tian, *Surf. Coat. Technol.* 155 (2002) 112-120
- [13] A. Ahmeda, S. Bahadur, A. M. Russell, B. A.Cook, *Tribol. Int.* 42 (2009) 706-713
- [14] V. I. Matkovich, *J. Economy, Acta Cryst.* B26 (1970) 616-621
- [15] Y. Tian, A. Constant, C. C. H. Lo, J. W. Anderegg, A. M. Russel, J. E. Snyder, P. Molian, *J. Vac. Sci. Technol. A* 21 (2003) 1055-1063
- [16] R. Schmechel, H. Werheit, *J. Phys. Condens. Matter* 11 (1999) 6803-6813.
- [17] Y. Tian, M. Womack, P. Molian, C. C. H. Loc, J. W. Anderegg, A. M. Russell, *Thin Solid Films* 418 (2002) 129-135
- [18] M. Stock, P. Molian, *J. Vac. Sci. Technol. A* 22 (2004) 670-675
- [19] V. Kevorkijan, S. D. Skapin, M. Jelen, K. Krnel, A. Medend, *J. Eur. Ceram. Soc.* 27 (2007) 493-497
- [20] Y. Tian, A. F. Bastawros, A. P. Constant, A. M. Russell, B. A. Cook, *Appl. Phys. Lett.* 83 (2003) 2781-2783
- [21] J.-M. Dubois, *J. Phys. Condens. Matter* 13 (2001) 7753-7762
- [22] J. Bellissard, *Mater. Sci. Eng.* 294-296 (2000) 450-457
- [23] D. J. Sordelet, M. F. Besser, J. L. Logsdon, *Mater. Sci. Eng. A* 255 (1998) 54-65

- [24] J.-D. Dubois, P. Brunet, W. Costin, A. Merstallinger, *J. Non-Cryst. Solids* 334-335 (2004) 475-480
- [25] A. Haugeneder, T. Eisenhammer, A. Mahr, J. Schneider, M. Wendel, *Thin Solid Films* 307 (1997) 120-125
- [26] D. J. Sordelet, M. F. Besser, J. L. Logsdon, *Mater. Sci. Eng. A255* (1998) 54-65
- [27] D. P. DiVincenzo, P. J. Steinhardt, *Quasicrystals: the state of the art, 2<sup>nd</sup> series*, World Scientific Pub Co, Singapore, 1999
- [28] G. S. Song, G. K. B. Kim, E. Fleury, W. T. Kim, D. H. Kim, *J. Mater. Sci. Lett.* 20 (2001) 1293-1296
- [29] C. Janot, M. Audier, M. De Boissieu, J. M. Dunois, *Europhys. Lett.*, 14 (1991) 355-360
- [30] V. V. Tcherdyntseva, S.D. Kaloshkina, E.V. Shelekhova, A.I. Salimona, S. Sartorib, G. Principi, *Intermetallics* 13 (2005) 841-847
- [31] B. Grushko, T. Velikanova, *Calphad* 31 (2007) 217-232
- [32] J.-M. Dubois, C. Janot, *Useful Quasicrystals*, World Scientific Pub Co, Singapore, 2005
- [33] E. Belin, Z. Dankhazi, A. Sadoc, Y. Calvayrac, T. Klein, J.-M. Dubois, *Phys: Condens. Matter* 4 (1992) 4459-4472
- [34] V. Fournée, E. Belin-Ferré, J.-M. Dubois, *J. Phys.: Condens. Matter* 10 (1998) 4231-4244.
- [35] E. Belin-Ferré, M. Klanjsek, Z. Jaglicic, J. Dolinsek, J. M. Dubois, *J. Phys.: Condens. Matter* 17 (2005) 6911-6924
- [36] T. Klein, C. Berger, D. Mayou, F. Cyrot-Lackmann, *Phys. Rev. Lett.* 66 (1991) 2907-2910
- [37] P. Weisbecker, G. Bonhomme, G. Bott, J.-M. Dubois, *J. Non-Cryst. Solids* 351 (2005) 1630-1638
- [38] B. I. Wehner, J. Meinhardt, U. Köster, H. Alves, N. Eliaz, D. Eliezer, *Mat. Sci. Eng. A-Struct.* 226-228 (1997) 1008-1011
- [39] C.V. Landauro, T. Janssen, *Physica B* 348 (2004) 459-464
- [40] A. Bilušić, A. Smontara, J. C. Lasjaunias, J. Ivkova, Y. Calvayrac, *Mat. Sci. Eng. A-Struct.* 294-296 (2000) 711-714
- [41] D. Mayou, C. Berger, F. Cyrot-Lackmann, T. Klein, P. Lanco, *Phys. Rev. Lett.* 70 (1993) 3915-3918
- [42] A. F. Prekul, N. Yu. Kuzmin, N. J. Shchegolikhina, *Mat. Sci. Eng. A-Struct.* 294-296 (2000) 527-530
- [43] R. F. Bunshah, *Deposition Technologies for Films and Coatings*, Noyes publications, New Jersey, 1982
- [44] H. Lüth, *Solid Surfaces, Interfaces and Thin Films* 5<sup>th</sup> Ed., Springer, Berlin, 2010
- [45] F. Tang, *The microstructure-processing-property relationships in an A1 matrix composite system reinforced by Al-Cu-Fe alloy particles*, PhD thesis, Iowa State University, 2004
- [46] A. M. Russell, B. A. Cook, J. L. Harringa, T. L. Lewis, *Scripta Mater.* 46 (2002) 629-633

- [47] Y. Lee, B. N. Harmon, First principles calculation of elastic properties of AlMgB<sub>14</sub>, Iowa State University, 2002
- [48] J.E. Lowther, *Physica B* 322 (2002) 173–178
- [49] Hütte – Das Ingenieurwissen, 33 Auflage, Springer, Berlin, 2007
- [50] W. H. McMaster, N. K. Del Grande, J. H. Mallett, J. H. Hubbell, Compilation of x-ray cross sections, Lawrence Livermore National Laboratory Report UCRL-50174
- [51] M. O. Krause, *J. Phys. Chem. Ref. Data.* 8, 307 (1979)
- [52] J. Als-Nielsen, D. McMorrow, *Elements of Modern X-ray Physics*, John Wiley & Sons, Ltd., 2001
- [53] B.E. Warren, *X-ray Diffraction*, General Publishing Company, 1969
- [54] B.D. Cullity, *Elements of X-ray Diffraction* 2nd Ed., Addison-Wesley, 1978
- [55] D. Keith Bowen, B. K. Tanner, *High Resolution X-ray Diffractometry and Topography*, Taylor & Francis, Ltd., 1998
- [56] W. Martienssen, H. Warlimont, *Condensed Matter and Materials Data*, Springer, Berlin, 2005
- [57] M. J. Daniels, D. King, L. Fehrenbacher, J. S. Zabinski, J.C. Bilello, *Surf. Coat. Technol.* 191 (2005) 96-101
- [58] M. Quiquandon, A. Quivy, J. Devaud, F. Faudot, S. Lefebvre, M. Bessière, Y. Calvayrac, *J. Phys. Condens. Matter* 8 (1996) 2487-2512
- [59] P. A. Bancel, *Phys. Rev. Lett.* 63 (1989) 2741-2744
- [60] T. Grenet, F. Giroud, K. Loubet, A. Bergman, G. Safran, J. Labar, P. Barna, J. L. Joulaud, M. Capitan, *J. Alloys Compd.* 342 (2002) 2-6
- [61] E. K. Widjaja, L. D. Marks, *Thin Solid Films* 441 (2003) 63-71
- [62] A. Strawbridge, H. E. Evans, *Eng. Fail. Anal.* 2 (1995) 85-103
- [63] C. Roth, G. Schwalbe, R. Knöfler, F. Zavaliche, O. Madel, R. Haberkern, P. Häussler, *J. Non-Cryst. Solids* 252 (1999) 869-873
- [64] M. J. Daniels, D. King, B. Phillips, J. S. Zabinski, J. C. Bilello, *Thin Solid Films* 440 (2003) 87-93
- [65] Y. Ding, D. O. Northwood, A. T. Alpas, *Surf. Coat. Technol.* 96 (1997) 140-147
- [66] T. Eisenhammer, A. Trampert, *Phys. Rev. Lett.* 78 (1997) 262-265
- [67] K. Wasa, S. Hayakawa, *Handbook of Sputter Deposition Technology*, Noyes publications, New Jersey, 1992
- [68] A. E. Yarimbiyik, H. A. Schafft, R. A. Allen, M. E. Zaghoul, D. L. Blackburn, NISTIR 7234, National Institute of Standards and Technology (NIST), USA 2006
- [69] A. E. Yarimbiyik, H. A. Schafft, R. A. Allen, M. E. Zaghoul, D. L. Blackburn, *Microelectronics Reliability* 46 (2006) 1050 – 1057

- 
- [70] A. E. Yarimbiyik, H. A. Schafft, R. A. Allen, M. D. Vaudin, M. E. Zaghoul, *Microelectronics Reliability* 49 (2009) 127 – 134
- [71] H. Landolt, R. Börnstein, *Numerical Data and Functional Relationships in Science and Technology: Phase Equilibria, Crystallographic Data and Values*, Springer
- [72] J.-K. Chang, Y.-L. Chen, W.-T. Tsai, *J. Power Sources*, 135 (2004) 344-353
- [73] S. Y. Chou, P.R. Krauss, P. J. Renstrom, *Science* 272 (1996), 85–87
- [74] H. Mahr, *Diplomarbeit*, Technische Universität Wien, 2009

## A. Appendix

The engineering drawings of the substrate holder's components can be found in the following figures:

Figure A.1      Copper Head Front and Side

Figure A.2      Copper Head Top and Back

Figure A.3      Macor ring Top, Side and Sectional view

Figure A.4      Pin assignment of for the temperature measurement (PT100 / type-L thermocouple) and cartridge heater



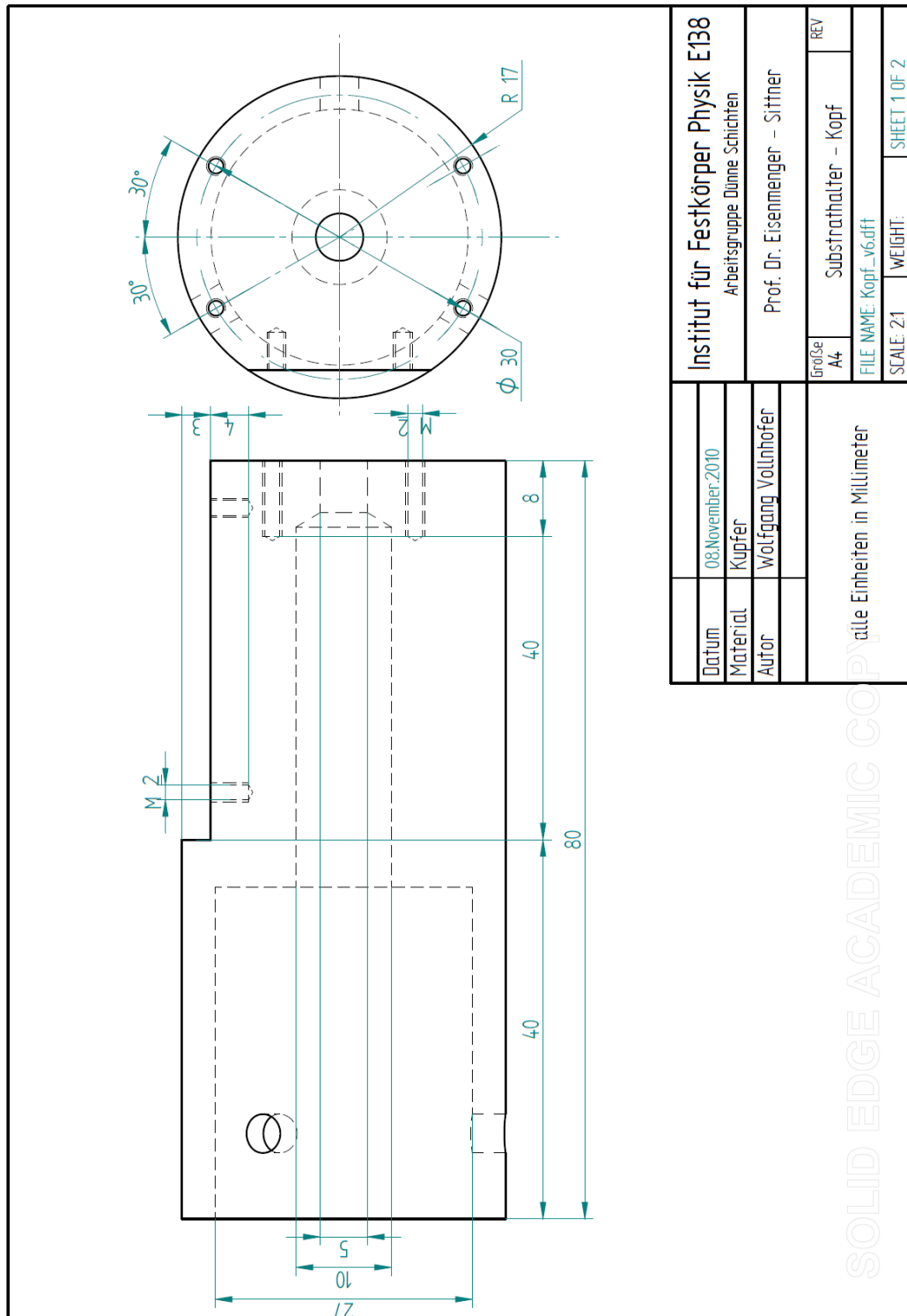


Figure A.1 Copper Head Front and Side

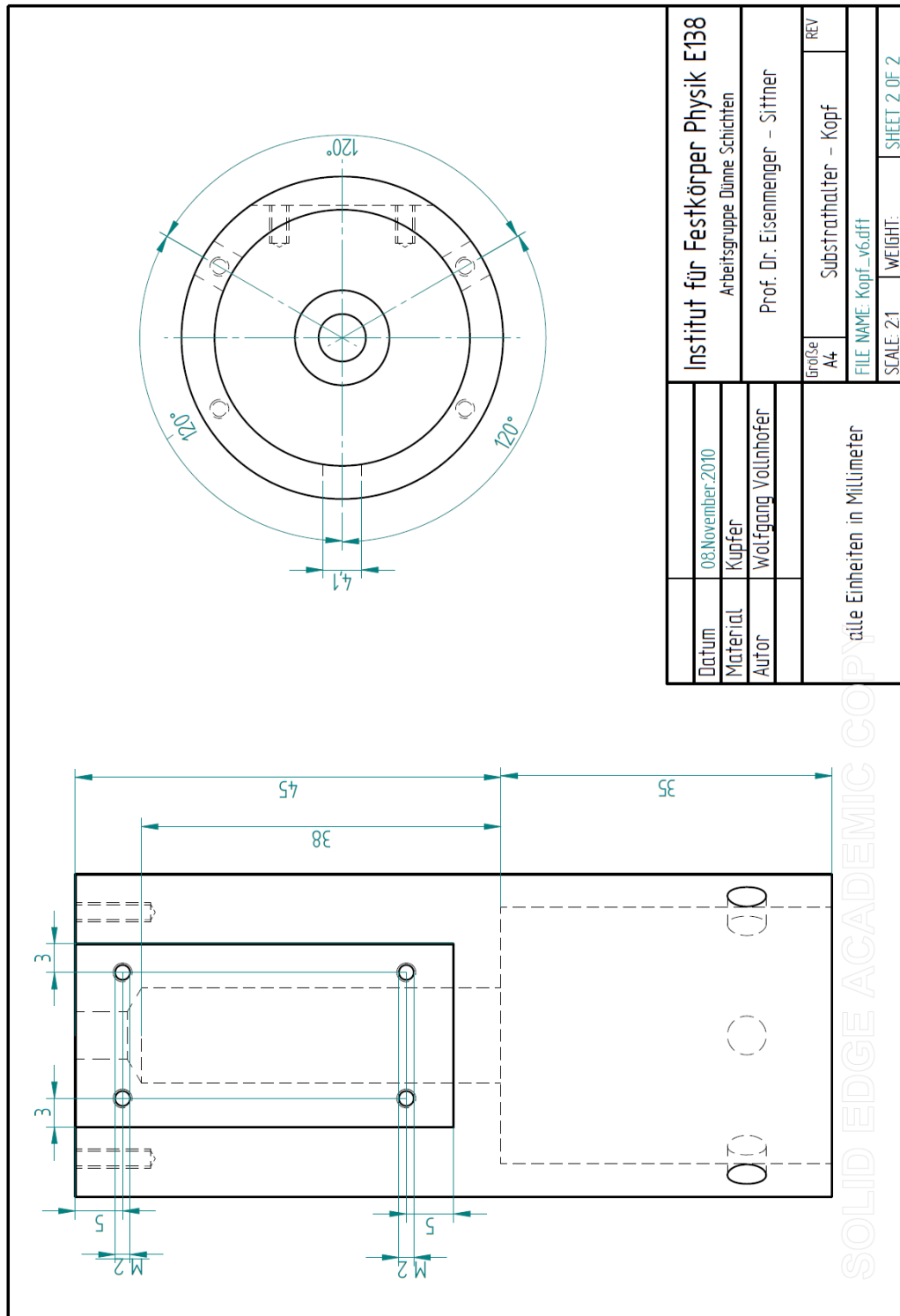


Figure A.2 Copper Head Top and Back

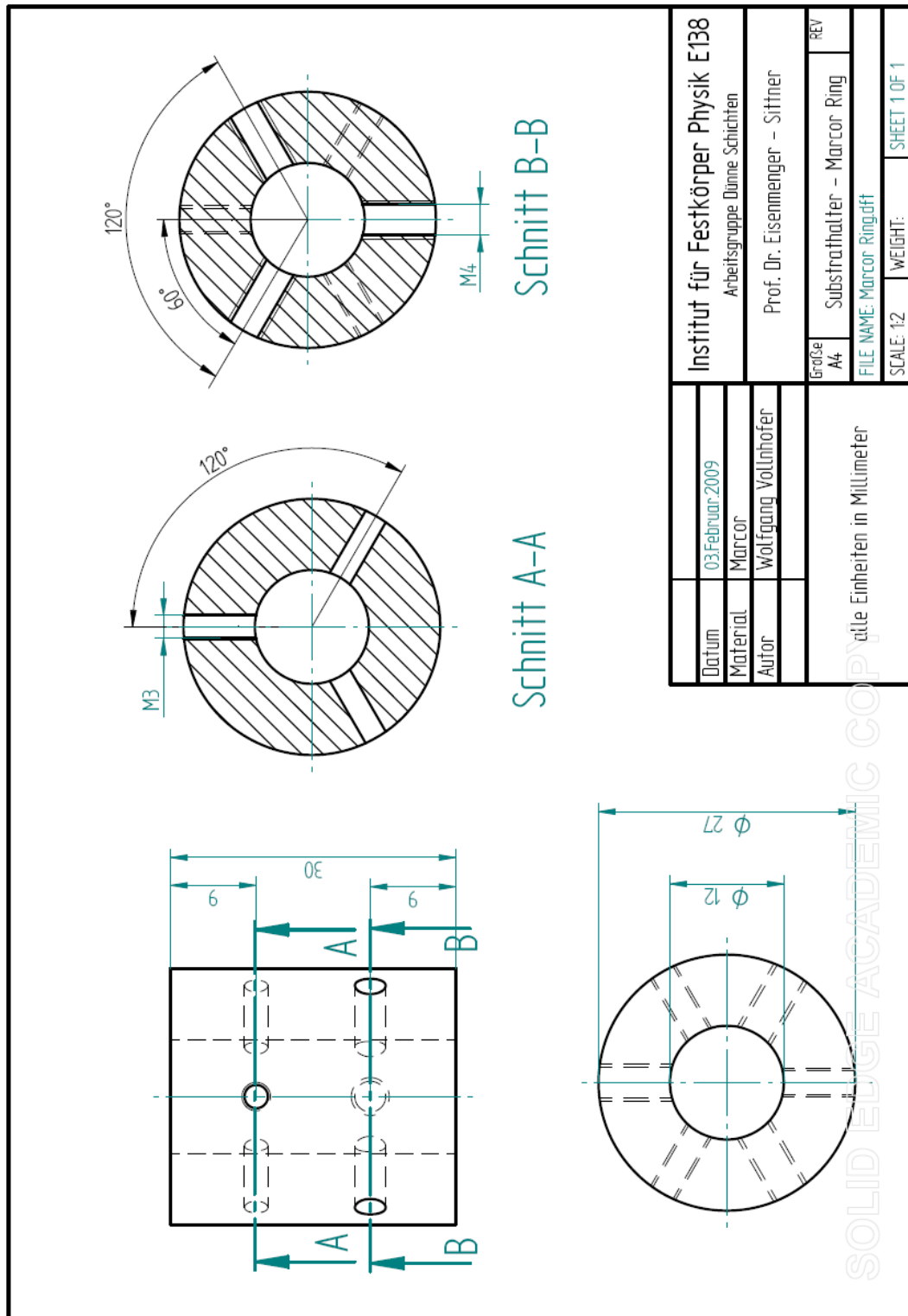


Figure A.3 Macor ring Top, Side and Sectional view

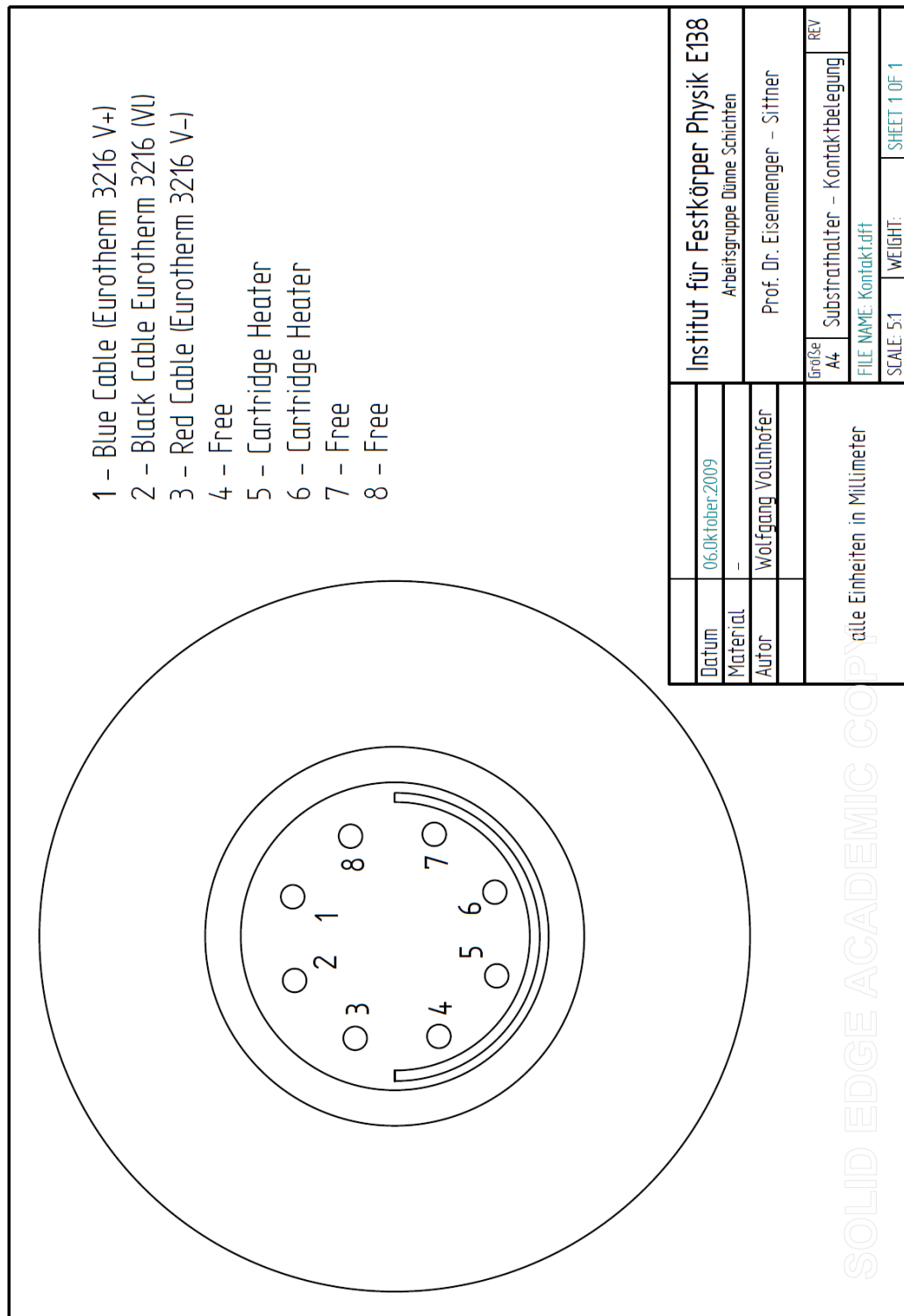


Figure A.4 Pin assignment of for PT100 temperature measurement and cartridge heater



## Lebenslauf

Dipl. Ing. Wolfgang Vollnhofer  
Zwölfergasse 8/6/17, 1150 Wien  
geboren am 27. Dezember 1983, in Wien  
Tel.: +43 664 443 75 57  
E-Mail: wolfgang.vollnhofer@gmail.com  
österreichischer Staatsbürger

## Berufserfahrung

Dez. 2008 – Nov. 2011

### **AppliCMA (EU Forschungsprojekt)**

(Partner u.a.: EADS, Genta-Platit, Gammastamp, Wolframcarb, Ernst Wittner GmbH, International Tool Consulting GmbH, Austrian Institut of Technology)

Entwicklung von Materialsystemen und Beschichtungsverfahren für industrielle Anwendungen (Metall-/Werkzeugverarbeitung, Automobil/Flugzeug-/Weltraum-Technik, Mikroelektronik und Mikroelektromechanische Systeme)

Konstruktion/Aufbau der Versuchsanlage, Implementierung der elektrischen Steuerung und Datenerfassung sowie Auswahl geeigneter chemischer und physikalischer Analysemethoden

Mitarbeit in der Entwicklung von Industrieprozessen (Materialherstellung, Beschichtungsverfahren), Optimierung der Prozessparameter, Herstellung und Analyse von Prototypen für industrielle Testläufe

Wissenschaftliche Arbeit / Publikationen / Konferenzen

Projektmanagement (Leitung eines Arbeitspaketes, Dokumentation und Präsentation des Arbeitspaketfortschrittes im Rahmen der Projektmeetings)

2008 – 2011

### **EFS Unternehmensberatung GmbH (geringfügige Beschäftigung)**

Assistenz der Projektleitung

inhaltliche Mitarbeit in verschiedenen Projekten

(z.B.: Einführung eines Produktdatenmanagement in einem internationalen Konzern, Konzeptionierung einer Plattformstrategie in der Automobilindustrie)

Programmierung in VB/VBA (MS Excel und MS Outlook)

2007 - 2011

### **Linde Gas AG (Werkvertrag)**

Entwicklung und Erprobung von Erdgas- und Wasserstoff-Betankungssystemen (Koordination der Prototypen-Testläufe, Protokollierung und Analyse der Systemfehler)

2006 - 2010

### **Technische Universität Wien**

Tutor-/Lehrtätigkeit: Betreuung des *Elektronik Labor für Technische Physiker*, des *Physikalischen Praktikum für InformatikerInnen* und der *Laborübungen II für Technische Physiker*

Projektarbeit *Entwicklung eines Ultraschallsensors zur Messung der Viskosität von Ölen*

## Ausbildung

Dez. 2008 – Nov. 2011

Projektarbeit *Wachstum von Pd Clustern auf MoO<sub>2</sub> und MgO Schichten*  
Projektarbeit *Herstellung und Charakterisierung von Mo und Mo<sub>2</sub>C Schichten*

### **Doktoratsstudium der Technischen Wissenschaften**

Technische Universität Wien

Thema: *Development of wear resistant coatings based on complex metallic alloys for functional applications.*

Schwerpunkt: Entwicklung und Charakterisierung von abnutzungsresistenten Schichten aus komplexen Metallverbindungen sowie von geeigneten industriellen Beschichtungsverfahren für verschiedene Anwendungsgebiete: Metall-/Werkzeugverarbeitung, Automobil-/Flugzeug-/Weltraumtechnik, Mikroelektronik und Mikroelektromechanische Systeme

Selbständige Erstellung des Konzeptes und Durchführung

Betreuung von Diplomanden und Projektarbeitern

Okt. 2003 - Nov. 2008

### **Diplomstudium Technische Physik**

Technische Universität Wien

Schwerpunkte: Materialwissenschaften (Entwicklung und Charakterisierung von neuartigen Werkstoffen), Beschichtungstechnologie (Tribologische Schichten für Industriewerkzeuge, Beschichtungsverfahren in Halbleiter- und Solarzellenindustrie), Sensorentwicklung

Diplomarbeit: *Deposition and characterisation of AlMgB<sub>14</sub> thin films*

Abschluss mit Auszeichnung

Sep. 1994 - Jul. 2002

Allgemeinbildende Höhere Schule Wien 6, Matura mit Auszeichnung

## Zivildienst

Okt. 2002 – Okt. 2003

Otto-Wagner Spital, Neurologisches Zentrum

Mithilfe in der Physio- und Ergotherapie

(Wiederherstellung der Bewegungs-/Handlungs-/Problemlösungsfähigkeit, die der Patient zur Bewältigung des täglichen Lebens braucht)

## Konferenzen und Fortbildung

2005 - 2011

*Tagung Festkörperanalytik (FKA)*, Wien, Österreich

*European Material Research and Science (E-MRS)* Nizza, Frankreich

Euroschool des *EU Network of Excellence for Complex Metallic Alloys*, Leibach, Slovenien

*European Conference on Applications of Surface and Interface Analysis (ECASIA)* Brüssel, Belgien

Sommerkurs *Mechanics of biomaterials and living tissues* an der Universität von Liège, Belgien

Teilnahme an den Konferenzen, Präsentationen und Vorträge sowie Veröffentlichung wissenschaftlicher Arbeiten

2009 - 2010

*European Business Competence Licence*

Stufe A (Unternehmensziele und Kennzahlen, Bilanzierung, Kostenrechnung, Wirtschaftsrecht)

Stufe B (Businessplan, Marketing und Verkauf, Investitionsrechnung, Finanzplanung)

## Außeruniversitäres Engagement

2005 – 2009

*Board of European Students of Technology (BEST)*

Aktive Mitgliedschaft und Mitarbeit

Projektleitung (europaweites Market Research Projekt und diverse kleiner Projekte)

Vorstandposition (Vice President for Public Relations 2007)

Trainer (Trainerausbildung 2008)

## Persönliche Fähigkeiten

Sprachkenntnisse

Deutsch Muttersprache

Englisch verhandlungsfähig in Sprache und Schrift  
(Doktorarbeit in Englisch verfasst, Teilnahme an internationalen Konferenzen)

Französisch gute Kenntnisse in Sprache und Schrift  
(3 Jahre Oberstufe Gymnasium und 3 Intensivkurse am Sprachinstitut der Universität Wien 2010 – 2011)

EDV Kenntnisse

MS-Office (Word, Excel, PowerPoint, Outlook), MS Project, MS Visio, MS Visual Studio, Adobe Acrobat, Photoshop, InDesign, Illustrator, Corel Draw, LabView, Mathematica, Solid Edge (CAD)

Programmiersprachen

C, C++, Visual Basic, VBA, VB-Script, Java, Fortran

Führerschein

Klasse B

## Interessen

Fachlich

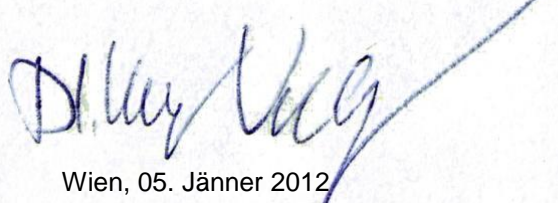
Projektmanagement, Erneuerbare Energieträger und Rohstoffgewinnung durch Recycling

Freizeit

Reisen, Lesen, Kochen

Sport

Klettern, Wandern, Laufen, Radfahren



Wien, 05. Jänner 2012